NON-INVASIVE DYNAMIC CONDITION ASSESSMENT TECHNIQUES FOR RAILWAY PANTOGRAPHS

TINGYU XIN

A thesis submitted to
The University of Birmingham
For the degree of
DOCTOR OF PHILOSOPHY

School of Engineering
The University of Birmingham
April 2019

ABSTRACT

The railway industry desires to improve the dependability and longevity of railway pantographs by providing more effective maintenance. The problem addressed in this thesis is the development of an effective condition-based fault detection and diagnosis procedure capable of supporting improved on–condition maintenance actions.

A laboratory-based pantograph test rig established during the course of the project at the University of Birmingham has been enhanced with additional sensors and used to develop and carry out dynamic tests that provide indicators that support practical pantograph fault detection and diagnosis. A 3D multibody simulation of a Pendolino pantograph has also been developed.

Three distinct dynamic tests have been identified as useful for fault detection and diagnosis: (i) a hysteresis test; (ii) a frequency-response test; and (iii) a novel changing-gradient test. These tests were carried out on a new Pendolino pantograph, a used pantograph about to go for an overhaul, the new pantograph with individual parts replaced by old components, and on the new pantograph with various changes made to, for example, the greasing or chain tightness. Through a comparison of absolute measurements and features acquired from the three dynamic tests, it was possible to extract features associated with different failure modes.

Finally, with a focus on the practical constraints of depot operations, a condition-based pantograph fault detection and diagnosis routine is proposed that draws on decision tree analysis. This novel testing procedure integrates the three dynamic tests and is able to identify and locate common failure modes on pantographs. The approach is considered to be appropriate for an application using an adapted version of the test rig in a depot setting.

ACKNOWLEDGEMENTS

I would like to thank my supervisors, Professor Clive Roberts and Dr Edward Stewart, for supporting me throughout my PhD. I have benefited a lot from their experienced guidance, continuous encouragement and the opportunities they have made available to me, for example sending me to a number of specialist academic training courses. I would like to thank my academic advisor, Dr Paul Weston, for his generous supervision, technical brilliance and help and support that he has provided throughout my PhD research.

I would also like to thank Professor Felix Schmid and Dr Charles Watson for providing me with industrial information and Mr Chris O'Donnell for his technical advice and for sending me a torsion bar. The assistance provided by Mr Adnan Zentani in the laboratory is greatly appreciated.

I would like to thank all the members of the Birmingham Centre for Railway Research and Education for their kind help and support.

Finally, I would like to thank my parents and my boyfriend, for their great love, understanding and encouragement.

CONTENTS

LIST OF FIGURES

LIST OF TABLES

ABBREVIATIONS

ADD	Automatic dropping device
ANN	Artificial neural network
CCD	Charge–coupled device
CCS	Computer Controlled Solutions
DAQ	Data acquisition
DDT	Diagnostic decision tree
DIN	Deutsches Institut für Normung
DNN	Deep neural network
DPM	Digital processing module
EN	European Norm
FFT	Fast Fourier transform
FRF	Frequency response function
HiL	Hardware-in-the-loop
HS2	High Speed Two
IEC	International Electrotechnical Commission
LM	Lumped-mass
MB	Multibody
NI	National Instrument
PANDAS	Pantograph damage assessment system
POLIMI	Politecnico di Milano
RUL	Remaining useful life
SD	Standard deviation
SMC	Softmax classifier

SMT	Simscape Multibody Toolbox
SSAE	Stacked sparse autoencoder
UIC	Union Internationale des Chemins de Fer
UoB	University of Birmingham

CHAPTER 1 INTRODUCTION

1.1 Background

As an electrified railway provides faster, quieter and more reliable journeys, and is environmentally friendly and energy efficient, railway electrification is a key trend in the modern railway (Profillidis, 2016). In the UK, the relatively new and planned railway routes are electrified, for example, High Speed Two (HS2) (Department for Transport, 2017) and Crossrail's Elizabeth Line (Wolstenholme, 2017). Moreover, some railway upgrade projects are underway or approved to electrify existing lines, such as the railway networks in Scotland and across the north of England, and the Great Western route (Network Rail Limited, 2017). Currently, two-thirds of the UK's electrified network is powered by overhead line systems, while the remainder is powered by a third rail, with some small local systems (Butcher, 2017). On these routes, pantographs or shoegear are utilised to collect power from overhead line systems or third rails (Park et al., 2003, Weston et al., 2008). Both types of current collector are supposed to slide along a conductor (contact wires or third rail) continuously; however, in the real world, the current collectors and power supply system form a coupled oscillation system, where they interact with each other, and thus contact loss may occur (Bucca et al., 2011). With an increase in the railway operating speed, the interaction issue becomes more critical, in particular where pantographs are fitted (in Figure 1.1) (Ambrósio et al., 2012). In this thesis, the dynamic behaviour of pantograph is discussed.

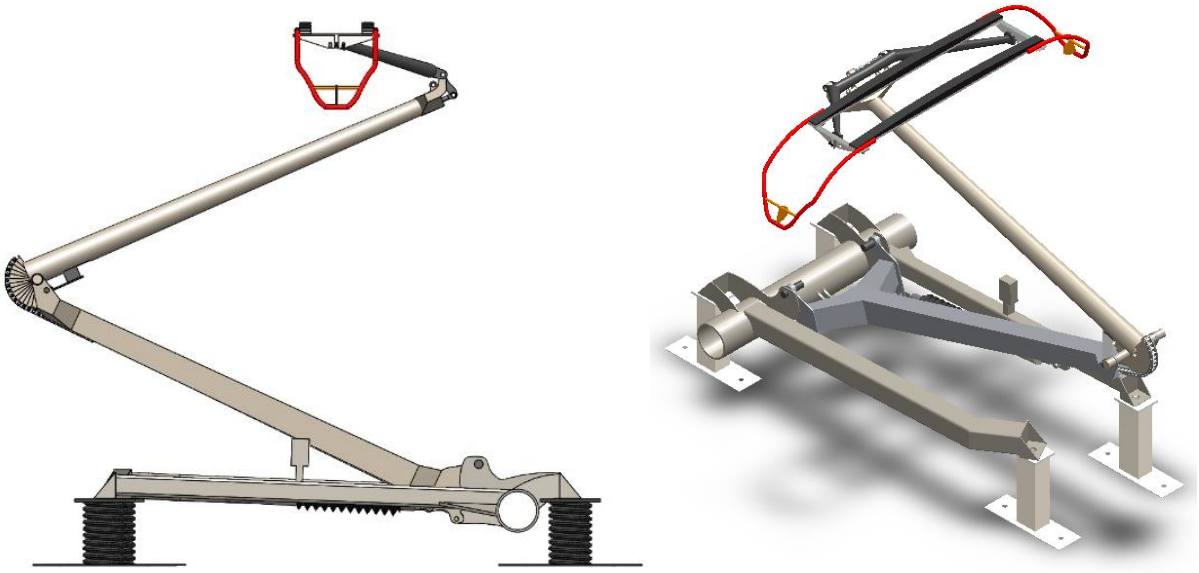

Figure 1.1 Railway pantograph

In standard EN 50119, it is defined that a high quality of current collection is realised via uninterrupted mechanical contact between the pantograph and contact wire. If the contact is not continuous, loss of contact happens, which is evaluated by the frequency and duration of electric arcing (CENELEC, 2009). Electric arcing not only impacts the quality of current collection, but also erodes the contact wire and pantograph carbon strips (Collina et al., 2007b). This thus reduces their life–cycles and the reliability of the railway network while increasing maintenance activities and cost. Railway operators are keen to minimise or even eliminate loss of contact between the pantograph and catenary (Poetsch et al., 1997).

The occurrence of contact loss is determined by the dynamic interaction between the pantograph and catenary (Pombo and Ambrósio, 2012a). Faults and degradation of the pantograph result in irregular contact forces that deteriorate the interaction and quality of current collection. This has the potential to stop the train due to lack of power; or even worse, the unhealthy condition of a pantograph may lead to railway accidents that injure people, involve time-consuming repairs, suspend railway network operation, and bring enormous economic losses to railway stakeholders (Antunes, 2012). For example, an accident happened on 5 January 2012 near Littleport, Cambridgeshire that was caused by the pantograph head

becoming dewired from and rising above the contact wire. The pantograph arms hit a catenary support mast, and then detached from the roof of the train. This accident disrupted the railway service on this route for more than 12 hours (RAIB, 2013). In order to address the factors that determine the risk of pantograph dewirement, data has been collected from fixed pantograph monitoring points at Cheddington station on the West Coast Main Line for a number of years (Evans et al., 1990). According to the monitoring evidence obtained on the network, the contact force is identified as the major factor. To ensure that pantographs generate proper contact force, and therefore that regular interaction between the pantograph and catenary is maintained, efficient maintenance of pantographs is required to achieve a safe, reliable and continuous railway network (Farrington-Darby et al., 2005).

Currently, different levels of maintenance routines for pantographs are implemented in depots on the basis of fixed operating distance or time. Most of the existing maintenance activities tend to rely on visual and manual inspection (SNCB and SNCF, 2007) , including checking lateral stability by hand, uplift force with weights, the integrity of all electrical and mechanical components, misalignment of pantograph arms, and damage or excessive wear on carbon strips (Murphy et al., 2007, Weston and Xin, 2017). At some depots, static measures of frictional hysteresis are carried out by measuring the contact force against displacement of the pantograph head at a speed of 50 mm/s as required in standard EN 50206 (CENELEC, 2010); however, the relationship between the health condition of the tested pantograph and the measurement results is not considered. Furthermore, railway operators are looking for a trade-off between reducing the likelihood of accidents, and over–maintenance that leads to unnecessary costs (Bobillot et al., 2006). Therefore, some on-board and trackside systems have been proposed to realise condition-based maintenance that provides accurate information at timely intervals using condition monitoring (RTS and TSLG, 2012). Nevertheless, on-board systems must be fitted to every pantograph to be monitored and focus particularly on the interaction between the

pantograph and catenary. Trackside systems are able to monitor the pantographs passing through; however, as these systems aim to detect the dynamic behaviour and wear of in-service (lifting) pantographs, not the parked (settled) ones, the number of pantographs that can be inspected is limited. As required by EN 50206, all the in-service pantographs should be free from any physical defect (CENELEC, 2010). More importantly, the current commercial systems can detect the incorrect contact force, excessive wear on the contact wire and the pantograph head; however, these systems cannot diagnose the faults or degradation of the pantograph or catenary that cause the abnormality.

1.2 Motivation and objective

Considering the disadvantages of the current maintenance and condition monitoring approaches for pantographs, to reduce the variability in pantograph performance as part of a higher purpose to maintain the performance and reliability of the pantograph-catenary system, a depot-based pantograph test rig should be developed to detect faults and degradation in all pantographs in the depot by testing their dynamic behaviour (Weston and Xin, 2017).

A pantograph is mounted on the roof of a train and is utilised to transmit electrical current from the catenary to the train through contact. The current is collected by carbon strips on the top of the pantograph head, and then transferred to on-board systems through the pantograph arms. The pantograph and catenary form a coupled oscillation system in which each part interacts with the other via contact force (Collina et al., 2007a). To achieve proper interaction, the primary design purpose of pantographs is to keep contact with the contact wire to achieve a satisfactory quality of current collection; this goal is more difficult to reach for high-speed trains, as the higher operating speed exacerbates the variation in the contact force (Collina et al., 2007b). High levels of contact force result in excessive uplift and mechanical wear of the pantograph and contact wire, whereas weak contact forces lead to a greater percentage of

contact loss that generates electric arcing and abrades the pantograph carbon strips and contact wire (Balestrino et al., 2000). It is concluded in standard EN 50367 that the safety and performance of a pantograph and wear of the carbon strips and contact wire are influenced by the dynamic interaction between the pantograph and catenary (CENELEC, 2012b). Accordingly, the correct force and response to the oscillation between the pantograph and catenary should be produced by the pantograph to achieve a balance between the degree of wear and the quality of current collection (Karakose et al., 2017). Other than the original design of the pantograph, the health status of pantograph components is another important factor that determines its dynamic behaviour (Qin et al., 2014). Therefore, it is necessary to develop an efficient pantograph maintenance procedure to maintain the healthy condition of in-service pantographs.

The motivation of this work is to economically incorporate realistic dynamic tests into an intelligent maintenance routine for pantographs; it is therefore necessary to develop a depot-based system that can be used to test the condition of every pantograph on a basis. As part of this work, a laboratory-based test rig was developed and located at the University of Birmingham. This laboratory-based system is intended to be developed further in the next stage for use in a depot environment to inspect and remove faulty pantographs from service.

Consequently, this thesis consists of the following research tasks:

- Understanding the dynamic behaviour of pantographs through the use of multibody modelling and dynamic simulation.
- Development of a laboratory-based pantograph test system that is able to diagnose faults on the tested pantograph based on a proposed testing routine.

- Developing the fault detection and diagnosis routines, testing pantographs in normal and various faulty conditions using different dynamic tests; measure critical parameters and analyse using different algorithms.
- Various pantograph faults are characterised by extracting features from the measurements obtained by different dynamic tests. Algorithms including conventional approaches, such as system identification using lumped-mass models and calculation of the standard deviations, and advanced methods, such as deep learning algorithm, are applied.
- By considering the efficiency and time consumption of the different dynamic tests for detecting pantograph faults, a rapid pantograph fault detection and diagnostic test routine are proposed by combining the dynamic tests with decision tree analysis.

The thesis addresses the following hypothesis: is it possible to develop a pantograph dynamic behaviour measurement device that is able to implement condition-based fault detection and diagnosis.

The aim of this work is to characterise the common faults of pantographs, and thus to evaluate the condition of a tested pantograph by detecting and diagnosing the faults on it using the proposed testing procedure. Knowledge of the common pantograph faults has been gathered from the railway experts and depot managers. In order to address the most effective testing procedure for investigating pantograph faults, different dynamic tests are implemented based on the experience of previous studies and understanding the dynamic behaviour of Brecknell Willis high-speed pantographs. In this thesis, the pantograph can be tested innovatively with a full extension scale; its dynamic behaviour is measured by various external and internal sensors, then the data measured is transmitted to a PC via National Instrument (NI) data acquisition modules for further analysis and storage. The measurements collected from a new pantograph

are considered as references; the faulty data is collected by emulating faults on the pantograph under test. By comparing the faulty features with the references, the faults are characterised.

According to the faults detected in the pantograph, related maintenance activities can be carried out; therefore, condition-based pantograph fault detection and diagnosis is realised. Condition-based fault diagnosis for pantographs is expected to improve the current fixed-term and low-tech maintenance in depots, and therefore to enhance the safety and reliability of the railway network.

1.3 Thesis outline

The problem of developing condition-based fault detection and diagnosis for pantographs is discussed in the following manner:

- In Chapter 2, an overview of studies related to the dynamic behaviour of pantographs is provided. These studies investigated the interaction between pantograph and catenary to evaluate the performance of pantographs. The types of technique that have been previously considered for pantograph-catenary interaction include theoretical mathematical model-based approaches, hybrid simulations that combine an actual pantograph with a virtual catenary model, and the development of on-board and trackside condition monitoring systems. This chapter is concluded by assessing the advantages and disadvantages of the methods developed that inspire the development of pantograph fault detection and diagnosis approaches proposed in this work.
- In Chapter 3, the structure of the Pendolino pantograph is provided; common pantograph faults are listed, followed by an analysis of the working principle of a pantograph and conversations with railway operators and depot managers. In order to detect and diagnose the common faults, a pantograph test rig has been developed at the University of Birmingham. Furthermore, to understand the dynamic behaviour of

pantographs, a 3D multibody model of a Pendolino pantograph was developed using SolidWorks software and simulated within the MATLAB Simscape Multibody Toolbox.

- Chapter 4 is used to outline the concept and feasibility of the three dynamic tests considered in this thesis for pantograph fault detection and diagnosis. In order to investigate the dynamic behaviour of the tested pantograph under various circumstances, an extended hysteresis test, a frequency-response test and a novel changing-gradient test are developed.
- Chapter 5 is used to highlight the relation between measurements from the hysteresis tests and the condition of the tested Pendolino pantograph. Inspired by the static hysteresis test that is currently being carried out at some depots at a speed of 50 mm/s, in this thesis, this existing test is extended to accomplish testing at speeds from 50 to 400 mm/s with 50 mm/s step to excite different pantograph nonlinearities. By emulating various faults to critical components of the pantograph, including the head and frame suspension and the elbow joint, the faults that can be detected and diagnosed by the hysteresis test are characterised.
- In Chapter 6, a second dynamic test, the frequency-response test, is implemented by emulating different faults in the pantograph. As a pantograph is a nonlinear system, the appearance of its dynamic behaviour varies with excitation. In this chapter, different excitation strategies are proposed to work out the most appropriate testing approaches for various pantograph faults.
- Chapter 7 presents the results of a novel changing-gradient test. The development of such a rapid test aims to reproduce the trajectory of the pantograph when it passes a trackside mast supporting the catenary. In order to classify different faults, both conventional and deep learning algorithms are applied.

- Chapter 8 builds on the previous studies of the three dynamic tests to identify a method that is effective and rapid to detect and diagnose pantograph faults. A decision tree analysis approach is applied to detect the potential faults in pantographs by combining the three tests carried out in this thesis. This condition-based maintenance method will be applied at maintenance depots in the next stage of this project.
- In Chapter 9, the author draws conclusions from the work presented and discusses areas of future work.

This thesis represents a number of collaborative industry condition monitoring initiatives undertaken at the University of Birmingham. The collaborating companies include:

- Computer Controlled Solutions Ltd (CCS) – a company specialising in the development of software systems for data acquisition and analysis.
- Motion Drives & Controls Ltd – a company specialising in integration of drive systems.

CHAPTER 2 PREVIOUS RESEARCH TO UNDERSTAND THE DYNAMIC BEHAVIOUR OF PANTOGRAPHS

2.1 Introduction

In this chapter, an overview of previous research focussing on the dynamic behaviour of pantographs is provided.

The pantograph and catenary form a coupled oscillation system. Undesirable contact loss happens between the pantograph and catenary that resulting in interruption of current collection and wear on pantograph carbon strips and contact wires (Morris, 1964). As the operational speed increases, improving the interaction between the pantograph and catenary is a key issue towards developing faster and safer railway operations while reducing maintenance costs for both rolling stock and infrastructure (Bruni et al., 2017). Most of the studies concerning the dynamic behaviour of pantographs analyse the interaction within this system. The methods applied can be categorised into three groups: computational simulations, laboratory-based tests, and on-board and trackside inspections.

Research in the field of pantograph-catenary interaction started with the development of numerical models and simulations (Wann, 1980). Presently, computational methods are still commonly used, as they are able to prequalify and optimise the design of pantographs and active control strategy prior to expensive line tests. Two types of pantograph model are widely used: lumped-mass and multibody models (Lopez-Garcia et al., 2007). Various nonlinearities were included in the mathematical models, which improves the accuracy of the simulation results

(Pombo and Antunes, 2013, Gregori et al., 2017). However, the mathematical models can only reproduce the dynamic behaviour of the pantograph with certain nonlinearities; they cannot be used to inspect the real condition of the pantograph with unknown degradation or faults. In order to inspect and reproduce the dynamic behaviour of pantographs more practically, laboratory-based testing systems, so-called 'hybrid' or 'hardware-in-the-loop' simulations, were proposed by combining an actual pantograph with a virtual numerical model of the overhead line. Furthermore, to explore the values of the critical parameters during railway operation, some on-board and trackside systems have also been developed (Bruni et al., 2017).

Common approaches to research the dynamic behaviour of a pantograph are discussed in this chapter. Some of these methods are developed further in later chapters through the use of real-world case studies.

2.2 Pantograph-catenary interaction

The catenary and pantograph form a dynamically coupled oscillation system. The main reason for the oscillation is the variation in the effective stiffness of the overhead line system within a span (Baxter, 2015). Railway catenaries are periodic structures that supply electrical energy to trains and locomotives. A typical catenary includes masts that support the arms which fix the messenger and contact (Ambrósio et al., 2012). The contact wire is in tension between support masts and hung via droppers from a messenger wire that is periodically attached to trackside masts (Baxter, 2015), a 3D sketch of the catenary consisting of two spans is shown in Figure 2.1.

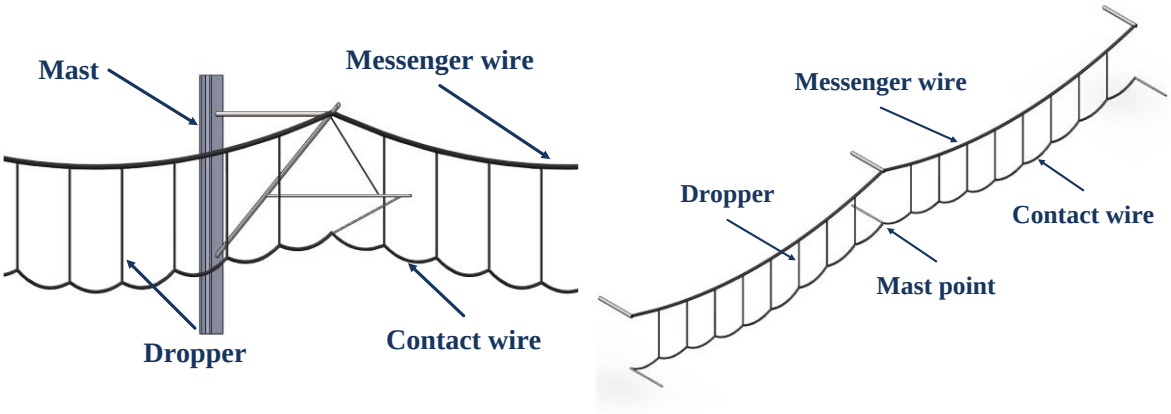

a. *b.*

Figure 2.1 Sketches of catenary

The main reason for the pantograph oscillation is the stiffness variation of the contact point. As the beginning and end of a span are supported at the masts, the stiffness of the catenary near the masts is at a maximum; in the middle of a span, it is at its minimum (Wu and Brennan, 1999). While the pantograph is sliding along the contact wire, variation in the stiffness of the contact wire produces periodic excitations to the pantograph head which result in fluctuation of the contact force, and oscillation between the pantograph and catenary. A consequence is that disturbances of the contact wire by a pantograph may result in relatively large or high-frequency movements of the catenary (Gostling and Hobbs, 1983).

The key parameters to evaluate the oscillation between the pantograph and catenary are contact force, displacements and accelerations of different pantograph parts and catenary, percentage occurrence of contact loss, etc. (Bolton and Dyne, 1984). Therefore, studies related to the dynamic behaviour of pantographs mainly focus on the variation of these parameters under different circumstances.

2.3 Pantograph modelling and simulation

To reproduce the interaction between pantograph and catenary, and therefore to improve the quality of current collection and reduce wear on the pantograph and particularly the contact

wire in a relatively low-cost computational environment, some numerical simulation methods are well established. In most cases, the pantograph and catenary are modelled as two separate parts, and then coupled by applying a contact model (Wann, 1980). The catenary is normally modelled by the finite element method (FEM) or finite difference method (FMD) (Shin et al., 2006). Meanwhile, pantograph models are generally developed in the form of lumped-mass models (Eppinger, 1984) or multibody models (Ambrósio et al., 2012). In this section, the development and typical application of pantograph lumped-mass and multibody models are provided, and their advantages and shortcomings in use are also discussed hereafter.

2.3.1 Lumped-mass models of pantographs

2.3.1.1 Lumped-mass modelling

Lumped-mass models are simplified representations of actual pantographs. They simplify the pantograph to a few masses connected by springs and viscous dampers according to its fundamental kinematics (Seering et al., 1983). The springs and dampers represent the stiffness and damping on the connections between different pantograph parts (Poetsch et al., 1997). Due to the simplicity of their architecture and fidelity for reproducing pantograph-catenary dynamics, lumped-mass models are commonly used by train operators, manufacturers and researchers to approximate the dynamic behaviour of pantographs (Antunes et al., 2012). Different degrees of lumped-mass models are shown in Figure 2.2.

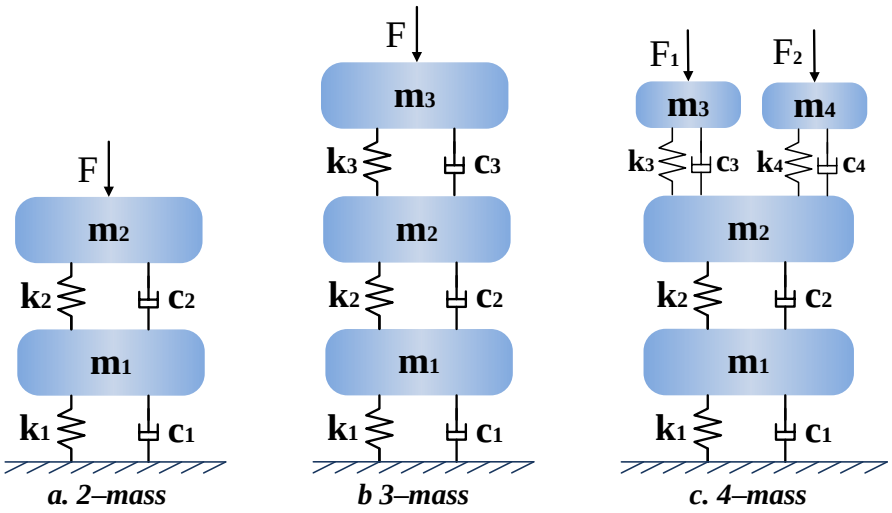

Figure 2.2 Lumped-mass models: *a*. 2–mass; *b*. 3–mass; *c*. 4–mass

Two-mass models were developed first by considering the pantograph head as the upper mass and other arms as the lower mass (O'Connor, 1984). However, as the structure of physical pantographs can be decomposed into three main parts: head, upper arm and lower arm, two-mass models that combine the upper and lower arm as one mass are not able to represent the behaviours of the two joints linking the upper and lower arms, and the lower arm and support frame separately. Therefore, three-mass models (Figure 2.2 *b*) came into being (Galeotti et al., 1993) by considering the upper and the lower arm as two separate masses. In some cases, four-mass models were established to reproduce more degrees of freedom. For example, a four-mass model (Figure 2.2 *c*) was developed by separating the top mass into two individual ones to represent the two contact strips on the top of the pantograph head (Schaub and Simeon, 2001); thus, rotation of the head could be reproduced by analysing the force and displacement on the two masses (Kumaniecka and Prącik, 2003). As real pantographs contain nonlinearities which are mainly generated by the pneumatic actuator and the effects of friction, the linear models are only valid for a pantograph under one operational circumstance (Poetsch et al., 1997). In order to develop models which are able to reproduce pantograph dynamics in various conditions of concern, nonlinear terms were added into the lumped-mass models (Collina and Bruni, 2002).

According to the structure of the lumped-mass models shown in Figure 2.2, the state–space model of a p–mass model can be described as:

$$[m_p]\ddot{x}_p+[C_p]\dot{x}_p+[k_p]x_p= F_p\,(x_p) \tag{2.1}$$

where x_p and F_p represent the displacement and the force acting on the p^{th} mass, respectively; m_p is the diagonal matrix of the masses of each block, and can be described as $m_p = diag\{m_1, \dots, m_p\}$; and C_p and k_p are the damping and stiffness matrices, respectively.

By identifying all parameters in Equation (2.1), the lumped-mass model of a pantograph is fully defined. In general terms, an identification experiment is performed by exciting the system and observing its input and output (Soderstrom and Stoica, 1989). The parameters in the lumped-mass model are obtained by an identification process using measurements collected via a frequency-response test (Collina and Bruni, 2002). By fitting the frequency-response function (FRF) for the lumped-mass model to the measured one, the values of the parameters are resolved.

The transfer function of a higher-degree lumped-mass model can be written as Equation (2.2):

$$G(s)=\frac{b_0 s^m+b_1 s^{m-1}+\cdots+b_{m-1}s+b_m}{a_0 s^n+a_1 s^{n-1}+\cdots+a_{n-1}s+a_n}\ (m \le n) \tag{2.2}$$

The behaviour of a higher-order system can be seen as the sum of the responses of first-order and second-order systems, and then the transfer function $G(s)$ can be written in as Equation (2.3):

$$G(s)=\frac{a}{s}+\sum_{j=1}^{q}\frac{a_j}{s+p_j}+\sum_{k=1}^{r}\frac{b_k(s+\zeta_k\omega_k)+c_k\omega_k\sqrt{1-\zeta_k^2}}{s^2+2\zeta_k\omega_k s+\omega_k^2}\ \ (q+2r=n) \tag{2.3}$$

However, for all the parameters in the lumped-mass model, only the characteristics of the top mass correspond to the physical properties of the pantograph head; the parameters of other masses in the model do not relate to real structures (Antunes, 2012).

Lumped-mass models were used initially to identify real pantograph parameters and to explore nonlinear effects (Seering et al., 1983). Then, some other applications were proposed, including supporting the design of pantograph-catenary models and active pantograph control (Facchinetti and Marco, 2008, Walters et al., 2011, Lopez-Garcia et al., 2007). These applications are detailed in the following sections.

2.3.1.2 Optimisation of pantograph and catenary design using lumped-mass models

Optimisation of the design of the pantograph and catenary is a key approach to improve the interaction between the pantograph and catenary, and therefore increase the limit of the operational speed of a high-speed railway (Harell et al., 2005). Pantograph-catenary modelling and simulation, where lumped-mass models of pantographs are commonly used, are able to solve this problem economically and safely.

To determine the performance of a new type of high-speed pantograph before applying it into practical use, Park et al. (2003) adopted a three-mass pantograph model that works in conjunction with a FEM catenary model. By varying the stiffness of the contact wire on the basis of a real railway line, parameters in the pantograph model were optimised under different conditions of operation by minimising the percentage of contact loss. Ambrósio et al. (2013) applied lumped-mass models of a pantograph to optimise the design parameters of the head and head suspension. Then, lumped-mass models were applied into more complicated scenarios with double pantographs operating under a catenary at a speed of 350 km/h (Han et al., 2013). Karakose and Gencoglu (2014) developed a lumped-mass pantograph model in MATLAB–Simulink to improve the interaction between the pantograph and catenary by varying one

parameter in the model at each time. Therefore, the impact of the parameters on the contact force could be understood.

Lumped-mass models have also been applied for designing and optimising the structure of the catenary. When the pantograph passes through special catenary sections, including section overlaps and insulated sections, its performance varies significantly. Seo et al. (2005) used lumped-mass pantograph models to check the impact of large deformation of the catenary on the interaction between the pantograph and catenary. To maintain the variation of contact force and decrease the percentage of contact loss, Harell et al. (2005) proposed simulations of a scenario with multiple pantographs passing section overlaps and insulated sections. The simulations reproduced the performance of the pantographs at different operational speeds under various catenaries. By using two-mass pantograph models, the authors worked out better plans for designing the catenary in special areas. Benet et al. (2007) applied a more detailed pantograph model, a four-mass model, to simulate the behaviour of a pantograph while running in an overlapping span area where the pantograph interacts with two contact wires at the same time. Then, lumped-mass models of the pantograph were used to determine the performance of nonlinear droppers in Korea (Cho, 2008), and to optimise the structure of high-speed railways with a maximum speed of 360 km/h in Japan (Ikeda, 2008) and in France (Van et al., 2017).

2.3.1.3 Active control of pantograph

The active control of a pantograph is realised by adding one or more controlling devices to modify the interaction between the catenary and pantograph by improving the consistency of contact force. Before the control strategies are implemented on a train, simulations are used to check their performance. O'Connor et al. (1997) proposed a frame-actuated controller for a two-mass pantograph model to diminish fluctuations in contact force. In this work, the relative velocity between the frame and head mass was monitored and used to trigger a controller. The

frame-actuated controller then modifies the speed of the pantograph in the vertical direction when loss of contact occurs, and therefore the pantograph is able to move appropriately to accommodate the contact wire. The simulation result showed that active control of the pantograph reduces the variation in contact force by 50%. Following this, Resta et al. (2001) proposed another active pantograph design by controlling the rotation of the pantograph head. It was found that by controlling the motion of the top masses in a four-mass model, the highest operational speed of the existing railway can be improved significantly, and the simulation results were verified through laboratory-based tests (Collina et al., 2005). This controlling system was also applied to another type of pantograph to improve the dynamic behaviour (Benedetto et al., 2008). Later, Tieri et al. (2013) proposed a pneumatic actively controlled pantograph by adjusting the pressure level of the pneumatic actuator to maintain the uplift force. As the variation in force is reduced, the maximum operational speed increased from 170 to 300 km/h.

2.3.2 Multibody models of pantographs

In lumped-mass models, the parameters of the masses below the top one have no relationship to the physical quantities of the pantograph (Antunes, 2012). In order to describe the characteristics of each critical component of the pantograph, multibody models have been developed (Rauter et al., 2007b). A typical multibody model consists of interconnected rigid or deformable parts that have relative motion constrained kinematically by different kinds of joints (Shabana, 2013). In the multibody pantograph model, the actual pantograph parts are replaced by equivalent models that are made up of the corresponding components. Compared to lumped-mass models whose parameters are identified by a frequency response test, the multibody pantograph models can be built with the design data alone (Ambrósio and Pombo, 2013). Development of a multibody model of a pantograph helps to enhance the understanding of the pantograph dynamic behaviour.

In order to investigate the interaction between the pantograph and catenary, the multibody pantograph models were coupled to finite element catenary models by contact force models (Rauter et al., 2007a). As the models of pantograph and catenary were built using different software, a co-simulation approach was applied (Veitl and Arnold, 1999): the multibody model provides the displacement and velocity of the contact point to the catenary model; using this information, the catenary model resolves the contact force at the contact point and sends it back to the multibody model to actuate the pantograph. The simulation results were validated using line measurements collected in the field (Rauter et al., 2007b). The scenario of a high-speed train with multiple pantographs was simulated by applying the method described above (Ambrósio et al., 2009). Then, Pombo et al. (2009) used this co-simulation approach to investigate the influence of aerodynamic forces on pantograph and catenary interaction, with the purpose of defining the maximum operational speed for a high-speed line.

In order to investigate the influence of deformation of pantograph components on the dynamic behaviour, an improvement was made by developing a flexible multibody model that describes each pantograph body using a floating frame of reference (Ambrósio et al., 2010). Then, several multibody models were proposed with various bending and rotational movements of different pantograph components to inspect the performance of the pantograph (Ambrósio et al., 2011). Multibody models were also adopted to improve the design of pantographs (Pombo and Ambrósio, 2012a), and to check the performance of different configurations of catenaries with multiple pantographs operating at 300 km/h (Pombo and Ambrósio, 2012b). As mentioned in EN 50367, the minimum distance between two in-service pantographs on one train is limited by the dynamic performance of the pantograph and catenary (CENELEC, 2012b); the multibody pantograph models were also adapted to work out the optimal distance between two in-service pantographs (Pombo et al., 2012). Furthermore, the influence of track and environment on pantograph-catenary interaction has also been addressed with multibody

models (Pombo and Ambrósio, 2013). Then, commercial software was developed by combining the applications of the multibody models mentioned above (Ambrósio et al., 2013). In order to validate the multibody models of the pantograph, the simulation results were compared to those of a linear two-mass pantograph model that had been verified according to EN 50318 (CENELEC, 2002).

Multibody models have also been used for simulating the performance of active pantograph control with a PID controller (Song et al., 2017). As the structure of multibody models is similar to that of a physical pantograph, simulations using this type of model provide preliminary experience prior to laboratory-based and line tests.

2.3.3 Pantograph-catenary interaction simulation tools

Based on the models of the pantograph and catenary demonstrated above, user–friendly software to reproduce the interaction between the pantograph and catenary has been developed by different institutions, including PrOSA (Finner et al., 2015), PantoCat (Ambrósio et al., 2015), SPOPS (Cho, 2015), PCaDA (Collina et al., 2015), OSCAR (Massat et al., 2015), PCRUN (Zhou et al., 2015), CANDY (Sánchez-Rebollo et al., 2015) and PACDIN (Tur et al., 2015). A benchmarking exercise was conducted by Politecnico di Milano to verify the efficiency of these software and to identify the modelling approaches best suited to studying pantograph-catenary interaction (Bruni et al., 2015).The types of pantograph model used for developing these tools are detailed in Table 2.1, where LM and MB are abbreviations for lumped-mass and multibody models, respectively. Table 2.1 shows that all interaction simulation tools support lumped-mass models, and some also support multibody models.

Table 2.1 Numerical pantograph models used in different software

Software	PrOSA	PantoCat	SPOPS	PCaDA	OSCAR	PCRUN	CANDY	PACDIN
Pantograph models	LM MB	LM MB	LM	LM	LM MB	LM MB	LM	LM

In most of the studies reviewed above, the authors focused on improving or maintaining appropriate interaction between the pantograph and catenary; therefore, the responses of the pantograph head in various scenarios need to be understood. The works reviewed in §2.3.1 have shown that the lumped-mass models are able to reproduce the interaction between the pantograph and catenary reasonably; meanwhile, as their architectures are simple, they are commonly used in different simulation tools. The multibody models are able to reproduce the dynamic behaviour of each pantograph part; however, their architecture is complicated. The multibody models are used less frequently.

Considering the advantages and shortcomings of pantograph lumped-mass and multibody models, in this work the lumped-mass and multibody models are used to detect the faults on the pantograph head and understand the dynamic behaviour of each pantograph component in various conditions, respectively.

2.4 Laboratory-based pantograph rest rigs

2.4.1 Hardware-in-the-loop test rigs

Even though the numerical models of pantographs can include the nonlinearities that are inherent in the design, they cannot model degradation over the pantograph lifetime because there is not enough data has been collected. In order to inspect the dynamic behaviour of the pantograph in various conditions, laboratory-based hardware-in-the-loop (HiL) test rigs have been developed that apply an actual pantograph interaction with a virtual catenary. According

to whether the pantograph is coupled to the catenary model in real-time, the existing test rigs can be divided into two groups: open-loop and closed-loop HiL systems.

2.4.1.1 Open-loop HiL test rig

An open-loop HiL test rig was built by Deutsche Bahn AG in Germany (shown in Figure 2.3) that aimed to improve the contact quality between the pantograph and catenary and to optimise the design of pantographs (Deml and Baldauf, 2001). The actuators of the test rig apply pre-defined excitations to the pantograph head in both horizontal and vertical directions. The horizontal movement emulates the stagger effect of the catenary, and the vertical movement duplicates oscillation of the pantograph and catenary at different frequencies. The excitation profiles were deviated from either line tests or numerical simulations. Static and dynamic tests carried out using this open-loop HiL system were validated by related DIN (Deutsches Institut für Normung), EN (European Norm), UIC (Union Internationale des Chemins de Fer) and IEC (International Electrotechnical Commission) standards. This test rig was used to identify the parameters of linear three-mass lumped models for different types of British high-speed pantographs through frequency-response tests (Conway, 2016).

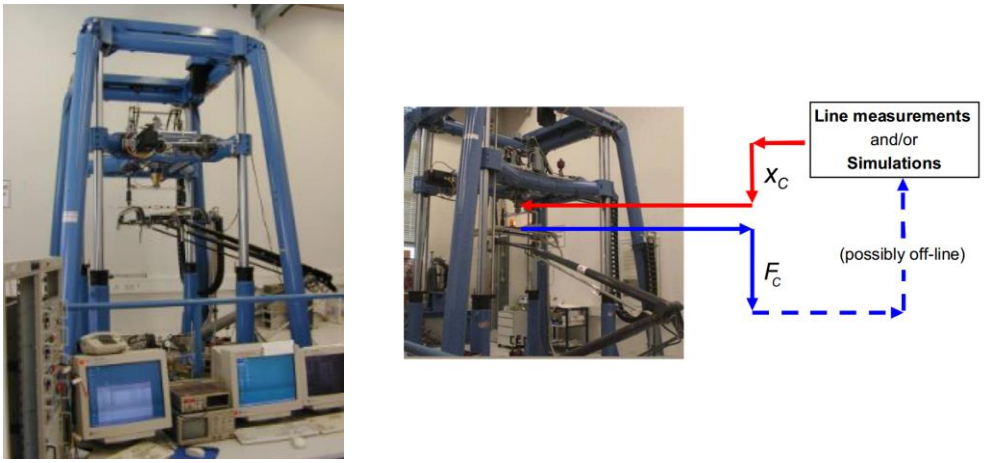

Figure 2.3 Laboratory-based test rig: open-loop HiL system (Deml and Baldauf, 2001)

However, as the pantograph-catenary is a coupled system, the interaction between the two parts varies not only with the design of the pantograph and catenary, but also with their real health

conditions, as pantographs and the catenary degrade during operation. Therefore, such a hybrid simulation using the parameters to actuate the pantograph cannot reproduce practical scenarios accurately.

More recently, Schirrer et al. (2017) proposed an alternative HiL pantograph test rig by applying a robot arm which is controlled by a linear drive, as shown in Figure 2.4. A complicated control strategy was used to generate the displacement with fewer errors (Aschauer et al., 2017).

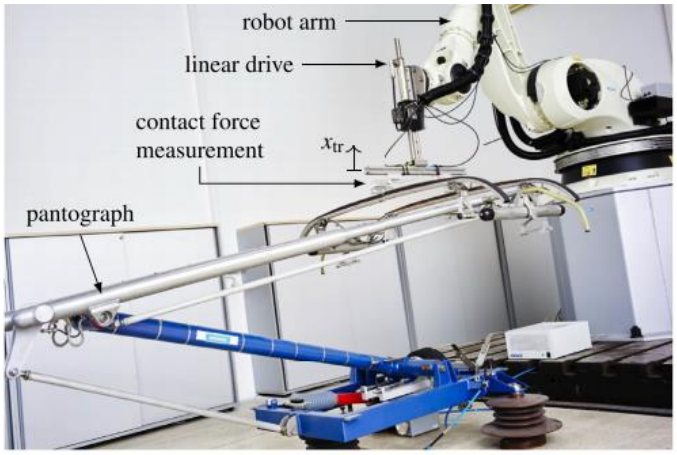

Figure 2.4 Pantograph test rig using a robot arm (Schirrer et al., 2017)

2.4.1.2 Closed-loop HiL test rigs

To overcome the drawback mentioned above, a closed-loop HiL with coupling of the pantograph and catenary model was first proposed by Zhang et al. (2002), and then further developed by Collina et al. (2004); the system is shown in Figure 2.5. It consists of two parts: hardware test facilities, including a pantograph, actuators and supporting frames that are similar to the open-loop HiL system; and a numerical linear catenary model that is capable of working out the displacement of the catenary using the contact force measured in real-time. A load cell is placed between the pantograph head and the hydraulic actuator to obtain the contact force. The force measured is sent to the virtual catenary model and used to compute the dynamic displacement of the contact wire. This displacement is then applied to actuate the pantograph to accomplish a closed-loop control. Compared to an open-loop HiL system, a closed-loop HiL

system provides a more realistic way to reproduce pantograph-catenary interaction in a laboratory environment.

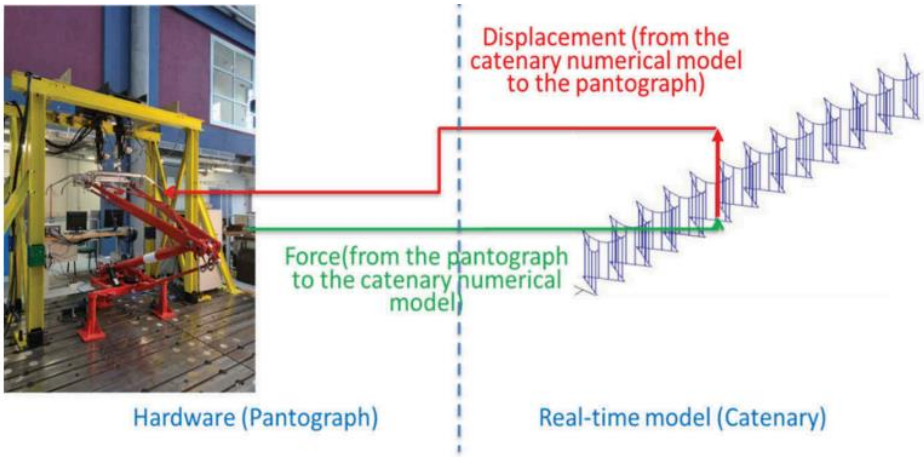

Figure 2.5 Laboratory-based test rig: closed-loop HiL system (Bruni et al., 2017)

By comparing the experimental measurements with the results of numerical simulations that had been verified with by line test data (Collina and Bruni, 2002), the ability of this laboratory-based closed-loop HiL to reproduce the dynamic behaviour of the pantograph-catenary system was validated according to EN 50317 (CENELEC, 2012a). This test rig has been applied to assist the design of a new type of pantograph (Collina et al., 2004). Following this, the numerical catenary model was improved by considering complex nonlinearities such as dropper slackening (Resta et al., 2008). The improved test rig was applied to verify the active control of pantographs by placing an actuator parallel to the head suspensions (Collina et al., 2005, Facchinetti and Marco, 2008) and the bottom of the lower arm to control the motion of the pantograph head and lower upper (Pugi et al., 2008), respectively. A further improvement to the catenary model was accomplished by adding an extended Kalman filter (EKF) to estimate the contact force more efficiently (Facchinetti and Mauri, 2009).

Later, the test rig was modified again by introducing two independent actuators to excite the two carbon strips independently, and the stagger effect was taken into account. Furthermore, the measurements obtained by this laboratory-based system were assessed by those obtained

from line tests for the first time, and acceptable agreements were achieved (Facchinetti and Bruni, 2012). Bruni et al. (2012b) applied this system to design a catenary for use at 360 km/h and above. The results of the experiments were validated by comparing to those of the theoretical numerical simulation.

The measurements obtained using open– and closed-loop HiL systems were compared to those collected from line tests. The results demonstrated that the matching errors of both HiL devices with respect to the line measurements are calibrated as ±10%; moreover, the contact forces worked out by the HiL systems are more accurate as they are closer to those measured on a testing train than those calculated with numerical simulation (Bruni et al., 2011). The use of open– and closed-loop laboratory-based HiL systems helped to reduce the number of costly line tests significantly (Bruni et al., 2017).

2.4.2 Spinning test rigs

In Europe, the designed lifespan of the overhead line system is 30–50 years or even longer. Therefore, wear is expected to occur mostly on the pantograph, rather than on the contact wire (O'Donnell et al., 2006). In order to ensure the healthy condition of the pantograph-catenary system and predict the remaining useful life (RUL) of the contact strips, wear on the contact strips of the pantograph and contact wire can be simulated by some laboratory-based spinning test rigs. The first spinning test rig was proposed at Politecnico di Milano to monitor abrasion on the pantograph carbon strips and contact wire by Bruni et al. (2004), as shown in Figure 2.6. The spinning element of this test rig is a 4.3 m diameter disk rotating around a vertical axis that is driven by a motor with a maximum rotation speed equivalent to 200 km/h at the contact point. A metal wire with a cross section of 120 mm^2 (the same as the Italian contact wire) is attached to the bottom edge of the rotating disk that acts as the contact wire. A full-scale pantograph is mounted on a platform which moves along the radial direction of the rotating disk to produce

the effect of stagger. Important parameters, including the sliding speed of the pantograph head, contact force, temperatures of contact strips, and current flow through the contact, are measured by contact sensors. Furthermore, the thickness of the contact wire and strips are measured by a non-contact laser-optical device. As the intensity of the electrical current is up to 1200 A DC during the test, insulation of the sensors is challenging. Boffi et al. (2009) measured the contact force using optical fibre sensors that are immune to electromagnetic interference. The Italian test rig shown in Figure 2.6 was used to measure the wear of the pantograph collector strip and contact wire as a result of both electrical and mechanical interactions. Different contact strip materials were tested at different sliding speeds; then, solutions to reduce wear under various operational scenarios were addressed (Bucca and Collina, 2009).

Figure 2.6 Sniping test rig at Politecnico di Milano (Bucca et al., 2017)

Similar test rigs have also been established by other institutions, including the Chinese Academy of Railway Sciences (Wei et al., 2013), the Japanese Railway Technical Research Institute (Stoten et al., 2016), and the Korean Railway Research Institute (Park et al., 2003).

Figure 2.7 Sniping test rig at the Chinese Academy of Railway Sciences (Wei et al., 2013)

The Birmingham test rig developed and used in this work is inspired by the existing systems reviewed in this section (Weston and Xin, 2017).

2.5 On-board and trackside monitoring systems

As the modern railway system operates at high speeds, improving the reliability and safety of railway operation while reducing the cost of maintenance has become increasingly important. Therefore, preventative and predictive maintenance needs to be accomplished (Barmada et al., 2014), which requires monitoring of the conditions of the pantograph and catenary accurately. As the electrical and mechanical interaction between the pantograph and catenary is complicated, it is difficult to simulate or reproduce all phenomena with high accuracy (Masini et al., 1998). In order to inspect the interaction accurately, on-board and trackside monitoring systems have been developed in different countries. The on-board and trackside monitoring systems evaluate the dynamic interaction between pantograph and catenary and current collection quality by monitoring contact loss, contact force and the motion of the pantograph and contact wire, etc. In this section, details of existing on-board and trackside systems are provided.

2.5.1 On-board systems

According to the types of sensors applied in the on-board systems, these systems are categorised into conventional and contactless systems. The devices adapted in the conventional systems include contact sensors such as load cells and accelerometers, whereas contactless systems only use cameras or other non-contact devices.

2.5.1.1 Conventional on-board systems

For conventional on-board systems, some of the sensors used for detecting the critical parameters relating to pantograph-catenary interaction are instrumented on the pantographs. In the 1990s, Masini et al. (1998) proposed an on-board system with various contact sensors and a camera to monitor the condition of a pantograph-catenary system on a live train in Italy. The information surveyed included mechanical variables such as contact force, catenary stagger, the height of the contact point, the dynamic raising of the catenary wire, etc., and electrical specifications such as the voltage and current supplied by the contact wire. The measurements were processed by a programme developed to evaluate the dynamic behaviour of the pantograph-catenary system. Based on the fundamental design of this system, Fumi and Forgione (2001) developed an integrated measurement train, named the Geocat system (shown in Figure 2.8), to examine the quality of the current collection. Information collected by this measurement train was not only used for real-time inspection and fault prevention, but also stored in a server for further processing to optimise the catenary maintenance plan. Compared to checking the status of the catenary manually, the Geocat system developed by Fumi and Forgione (2001) reduced the maintenance time by 95%.

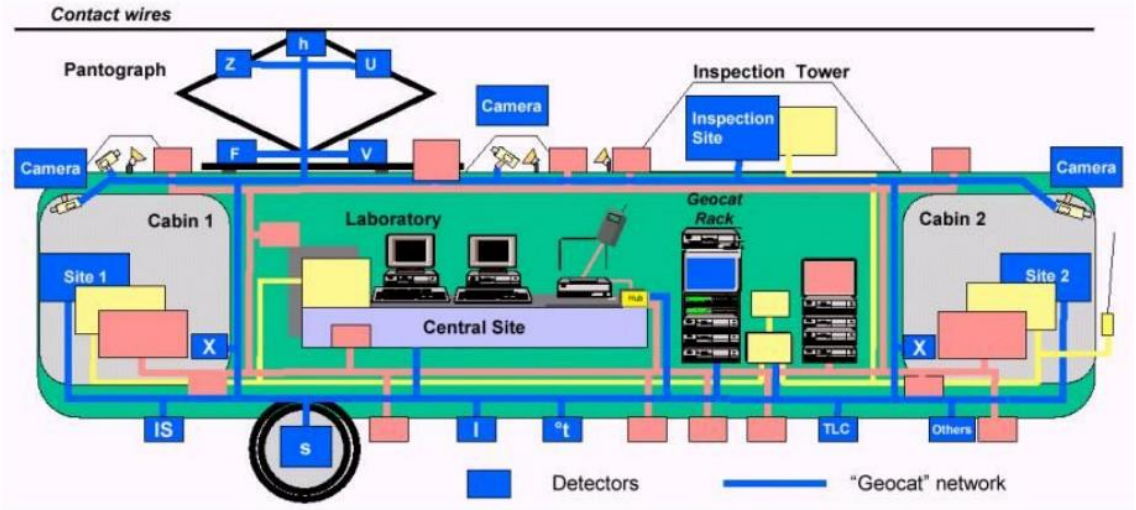

Figure 2.8 Measurement train: Geocat system (Fumi and Forgione, 2001)

Another on-board condition monitoring system for investigating the interaction between the pantograph and catenary was developed by Kolbe and Baldauf (2001) in Germany. By mounting force sensors and accelerometers underneath the pantograph carbon strips, real-time analysis can be implemented for inspecting the pantograph-catenary interaction over short distances and online diagnosis. The decision for evaluation and location of the train were transmitted to railway operators and maintainers via radio for scheduling and optimising maintenance activities.

Bobillot et al. (2006) proposed an on-board system called OSCAR, which aimed to detect the interaction of pantograph and catenary at a speed of 300 km/h. By analysing the contact force measured using the OSCAR platform (Massat et al., 2015), defects in the catenary were examined. To validate this proposed system, some defects were created on French high-speed lines, including missing droppers and the wrong tension in contact wires. The results proved that the system was able to identify some of the faults in the catenary.

O'Donnell et al. (2006) established an on-board system, named the PANtograph Damage Assessment System (PANDAS), that was used to detect damage and wear in pantographs travelling up to 125 mph (200 km/h) in the UK. Contact force and accelerations of the

pantograph head and arms were monitored; meanwhile, the train was located by GPS. The PANDAS initially powered the sensors using a long-life lithium battery, rather than from the power supply of the train. A prototype of the PANDAS was installed on a British Class 310 train for system validation and line testing. Then, Daadbin and Rosinski (2010) enhanced this system by introducing a solar-powered digital processing module (DPM) that interfaces with the accelerometers on the pantograph arm. The processor now transmits the analysis results to a receiver inside the coach via Bluetooth; meanwhile, high-level alert events are also sent to the control centre instantly for further activities.

Based on the prototypes proposed above, some other on-board systems were developed to improve the existing ones. To avoid influences generated by the instrumented sensors on a pantograph, the sensors were miniaturised; meanwhile, all cables went inside the pantograph body instead of outside (Keen et al., 2008). Regarding the high-level voltage supplied by the contact wire (25 kV in the UK), these sensors should be protected against voltage and EMI. Considering this, Bocciolone et al. (2012) replaced the conventional load cells with fibre Bragg grating (FBG) sensors which are insulated intrinsically. This new approach was validated by comparing the measurements with those of the traditional systems, and then using it in underground scenarios (Bocciolone et al., 2013). A further improvement was to embed the fibre in the carriers of the carbon strips (Schröder et al., 2013); therefore, the sensors did not vary the aerodynamics of the pantograph significantly. Other than improving the force sensors, Giuseppe et al. (2016) replaced the traditional accelerometers with fibre ones.

These systems can evaluate the dynamic behaviour of the pantograph-catenary system and detect faults in the pantograph and catenary, which improve the current fixed-term scheduled catenary and pantograph maintenance. However, conventional on-board systems using contact sensors affect the dynamic characteristics of the pantograph. Additionally, these systems

require relevant devices or techniques to realise data transmission and device insulation. Moreover, it is difficult to address the sensor installation plan on some types of pantograph because of structural limitations (Koyama et al., 2014).

2.5.1.2 On-board systems using contactless sensors

To overcome the disadvantages of conventional on-board systems, some on-board systems using contactless detection techniques have been developed using phototube sensors or cameras to monitor the condition of the pantograph and catenary. By using phototube sensors, Bruno et al. (2001) set up a non-invasive and low-cost on-board system to inspect the quality of pantograph current collection by detecting the occurrence of arcing. The phototube sensors were mounted on the roof of locomotives which operate on Italian high-speed lines, to measure the duration of the ultraviolet emission caused by electric arcing. The data collected by the phototube sensors was processed to obtain a definition of a pre-defined index for evaluating current collection quality and to organise maintenance priority. Based on this system, Landi et al. (2003) utilised infrared cameras to monitor the temperature gradient on the carbon strip and contact wire to investigate the occurrence of contact loss. Then, the image processing algorithm was used to work out the contact loss was further developed by Landi et al. (2006) to predict the wear on pantographs caused by arcing. Accordingly, it was possible to implement predictive maintenance.

As digital cameras and image processing techniques have been widely used in monitoring the wear and damage on pantograph carbon strips, Hamey et al. (2007) applied two charge–coupled device (CCD) cameras to obtain side and top views of the carbon strips. Aydin et al. (2012) applied digital cameras to detect the occurrence of arcing, by analysing the relative position of the contact wire to the edges of pantograph carbon strips. This system was also used to detect the height of the pantograph in real time. Based on this, active pantograph control was

implemented by controlling the contact force with respect to the height measured in real-time (Aydin et al., 2013). Then, the function of this system was extended to investigate some pantograph faults, such as overheating and excessive wear of the carbon strips (Aydin et al., 2014).

As the contact force is an important parameter to evaluate the performance of the pantograph-catenary system, Koyama et al. (2012) proposed an on-board system with line sensor cameras to work out the contact force based on an image processing technique. The system was validated by EN 50317 (CENELEC, 2012a) in a laboratory environment before line testing. Following this, the verified system was installed on a high-speed train with a maximum speed of 300 km/h (Koyama et al., 2014). The above systems inspect the interaction between and the conditions of pantograph and catenary based on pictures taken by high-speed cameras.

Cho and Park (2016) detailed a video-based monitoring system installed on a train with an operational speed of up to 400 km/h. A camera was applied to work in conjunction with an arc sensor for detecting arcing accurately at very high operational speeds. Karakose et al. (2017) proposed another video-based monitoring system with the target of assessing the wear on pantograph carbon strips. By detecting the most worn points on the carbon strip, the RUL can be predicted.

2.5.2 Trackside monitoring systems

To detect the condition of each in-service pantograph, an on-board system must be fitted to every pantograph, which results in a high cost. Considering this, some trackside systems have been developed with sensors and cameras fixed to the catenary system or trackside masts to observe all the in-service pantographs that pass the systems.

Cléon et al. (2006) proposed a trackside monitoring station to automatically evaluate the performance of pantographs at speeds up to 300 km/h using the sensors that are mounted on the support of the catenary and contact wire. End users can assess the trackside measurements and evaluation results at any time. However, as the contact wire is relatively flexible, attaching sensors to contact wires involves some safety issues; with consideration of this, other trackside systems have been developed with devices fixed to the supports that are relatively rigid.

An image-based trackside system was proposed by (Jarzebowicz and Judek, 2014) for inspecting the health condition of pantograph carbon strips. By fixing a camera and a line laser onto the support (in Figure 2.9), the system is able to generate 3D scans for the carbon strips when a train passes the inspection point. Then, wear and thickness of the carbon strips can be calculated and evaluated to prevent a faulty pantograph from being used (Judek and Jarzebowicz, 2014). Koyama et al. (2016) developed a more specific system for inspecting uneven wear on pantograph carbon strips by inspecting irregularities in the contact force.

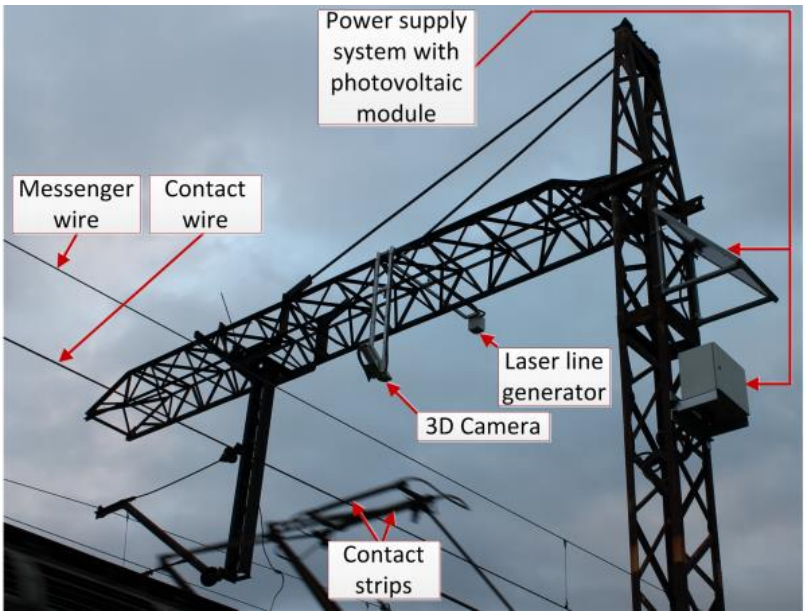

Figure 2.9 Trackside monitoring system (Judek and Jarzebowicz, 2014)

The on-board and trackside systems detailed in this section inspect and evaluate the performance of the pantograph and catenary by monitoring the electrical and mechanical

interactions. In the real operating circumstances, electric arcing is an important factor to evaluate the electric interactions between the pantograph and catenary; meanwhile, the contact force, accelerations and displacement of different pantograph parts can be used to evaluate the mechanical interactions. As the electrical effects are not considered in this work, in order to detect the mechanical behaviour of the pantograph, the contact force, accelerations and displacement of different pantograph parts are collected by the Birmingham test rig developed in this work.

2.6 Conclusions

As the pantograph and catenary compose a coupled oscillation system, in most studies, analysis of pantograph dynamics is from the point of pantograph-catenary interaction. The methods for analysing the dynamic behaviour of pantographs considered in this chapter range from numerical simulations to laboratory-based and online monitoring. Each technique has its own advantages and disadvantages.

Numerical simulations with lumped-mass or multibody models of pantographs provide a safe and rapid way to validate strategies for active pantograph control and optimisation of pantographs and catenaries. However, numerical simulations are not able to represent the degradation of the pantographs as there is no data available for modelling. A relatively new approach, hybrid simulation, has been proposed to study pantograph-catenary interaction by integrating an actual pantograph to a numerical catenary model in the laboratory. The hybrid simulations that were carried out using the HiL system can observe the performance of pantographs under various circumstances practically; furthermore, the wear and life-cycle of the pantographs can be monitored and predicted, which helps to optimise maintenance. In order to realise reliable preventative and predictive maintenance, line measurements are obtained using on-board and trackside monitoring systems.

Most of the previous studies evaluated the performance of pantographs by investigating the interaction between the pantograph and catenary. However, the performance of pantographs varies with their health conditions and degradation. The studies concerned with monitoring the status of pantographs concentrate on the wear of the carbon strips, but not on faults in other critical components of pantographs. In order to maintain every in-service pantograph working in healthy condition, and therefore to ensure the reliability of railway operation, economical condition monitoring for pantograph fault detection and diagnosis needs to be realised. To incorporate realistic dynamic tests into a scheduled maintenance routine for pantographs, it is therefore necessary to develop a depot-based system that can be used to test every train in a fleet on a scheduled basis (either operating time- or distance-based). The following chapters consider a pantograph fault detection and diagnosis testing routine where a hybrid approach is developed. The development of the test rig is inspired by the existing laboratory-based systems. The numerical modelling and selection of the parameters to evaluate the dynamic behaviour of the tested pantograph are also inspired by the techniques reviewed in this chapter.

CHAPTER 3 DEVELOPING A LABORATORY-BASED PANTOGRAPH TEST RIG

3.1 Introduction

In this chapter, the structure and working principle of pantographs and details of a laboratory-based pantograph test rig are provided. Through discussions with railway industrial experts, operators, depot managers and academic researchers, details of common pantograph faults were identified. The reasons for and impacts of these faults were also discussed. In order to detect and diagnose these faults using dynamic tests, in this work, a laboratory-based pantograph test rig has been developed at the Birmingham Centre for Railway Research and Education at the University of Birmingham. This test rig is able to excite the pantograph in various ways. To understand and inspect the dynamic behaviour of a pantograph under various conditions prior to actual laboratory-based tests, a 3D multibody model of a Pendolino pantograph and a simplified test rig were developed.

3.2 Overview of the Pendolino pantograph

3.2.1 Structure of a pantograph

Pendolino high-speed pantographs were designed and manufactured by Brecknell Willis Ltd. It is designed based on a one-degree-of-freedom mechanism which is essentially a four-bar linkage, referred to as an articulated frame (Carnevale et al., 2017). According to EN 50206, a common pantograph consists of four parts: a base frame, an operating

system, an apex frame and a head (CENELEC, 2010). The operating system composes of a lower arm with a fourth bar running inside, an upper arm with a control rod running inside (Gil-Vera, 2000). A pneumatic actuator that links the lower arm and the base frame supplies uplift force to raise the pantograph head to the contact wire. The 3D model of the Pendolino high-speed pantograph developed in this work is shown in Figure 3.2. Insulators are used to mount the pantograph on the roof of the train and to provide electric isolation between the train and the high-level voltage (25 kV in the UK) from the overhead line system. As the electrical effects are not considered in this work, the insulators are simplified in the 3D model.

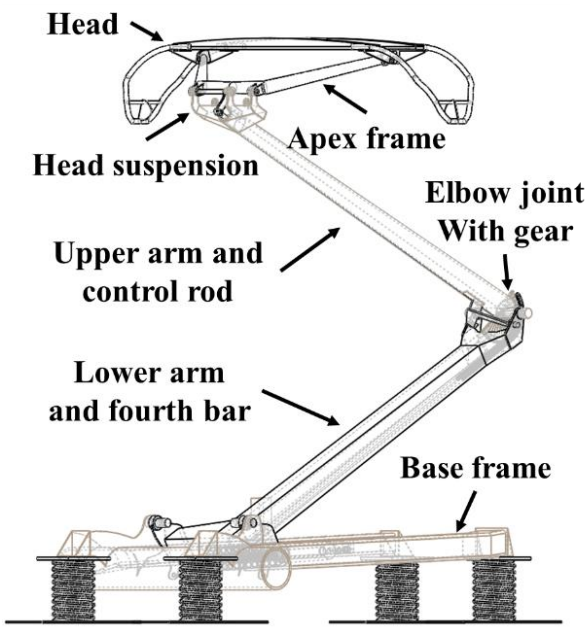

Figure 3.1 Pendolino pantograph

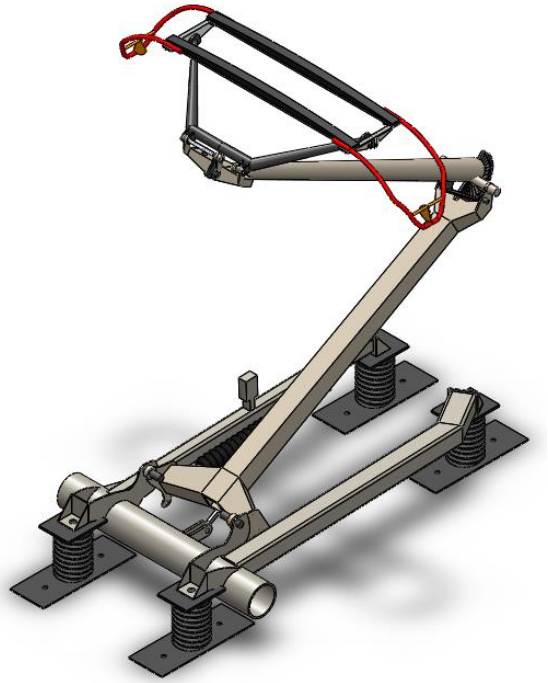

Figure 3.2 Pendolino pantograph

The pantograph base frame (Figure 3.3 *a*) is mounted on the roof of a train via insulators, to support the parts above. The pneumatic actuator (Figure 3.3 *b*), the lower arm and the fourth bar (Figure 3.3 *c* and *d*), connect directly to the base frame. One end of the pneumatic actuator pivots on an arm of the base frame, and the moving end of the pneumatic actuator connects to the bottom of the lower arm. It works as a lever with a specific design ratio; the ratio of the Pendolino pantograph tested in this thesis is 1:17. Therefore, a small displacement generated by the piston of the pneumatic actuator is able to move the pantograph upwards significantly. The bottom of the lower arm also pivots on two needle roller bearings fitted to the base frame. The pneumatic actuator and these bearings make the pantograph frame suspension.

a. Base frame

b. Pneumatic actuator

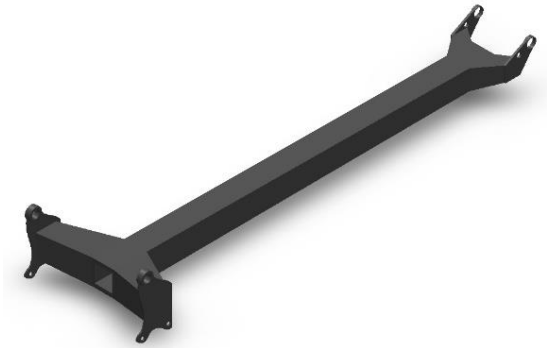

c. Lower arm

d. Fourth bar

Figure 3.3 Pantograph components I

A bar, so–call ‘fourth bar’, runs inside the lower arm. Its lower end pivots around a needle bearing fitted to the base frame. There are three chains at its top end: one centre chain and two outer chains lying on an eccentric cam (gear) fitting at the lower end of the upper arm, shown in Figure 3.4. When pressure acts on the pneumatic actuator, the gear (in Figure 3.4) rotates anticlockwise, and the upper arm is lifted. The angle of the upper arm above a horizontal plane is designed to be approximately the same as the angle of the lower arm below the horizontal plane. The joint connecting the upper and lower parts of the pantograph is called the elbow joint.

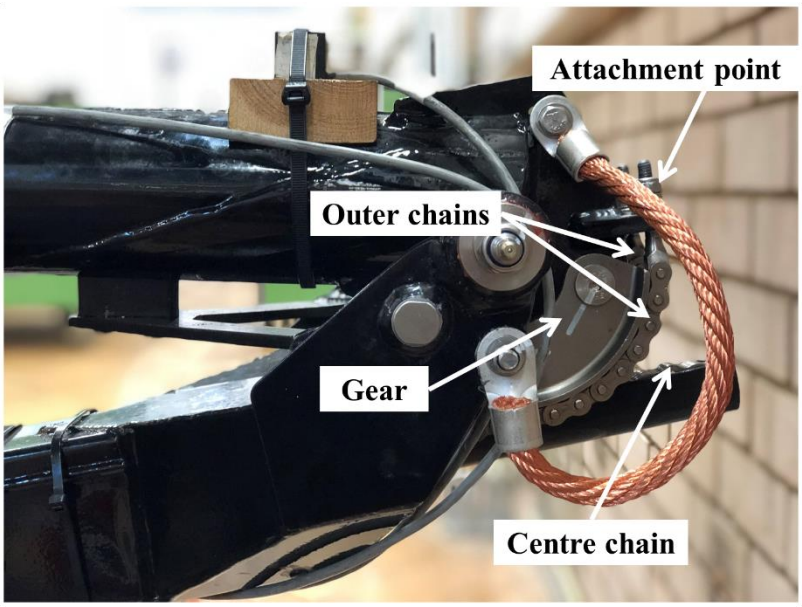

Figure 3.4 Pantograph elbow joint

The upper arm (Figure 3.5 *a*) is made as a hollow tube to reduce the mass (Hobbs, 1977). The apex frame (Figure 3.6 *b*) is fitted on the top of the upper arm. The control rod (Figure 3.5 *b*) runs through the upper arm. The top and bottom ends of the control rod connect to the apex frame and the top of the lower arm, respectively. The control rod governs the extension angle of the apex frame, to control the rising height of the pantograph head.

a. Upper arm ***b. Control rod***

Figure 3.5 Pantograph components II

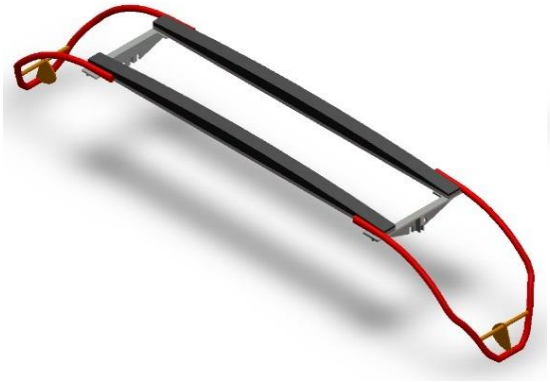

a. Head

b. Apex frame

Figure 3.6 Pantograph components III

The pantograph head is placed on top of the apex frame (Figure 3.6 *b*). For the Pendolino pantograph studied in this work, the pantograph has two carbon strips. Horns are formed at the ends of the pantograph head for an easier transition from one contact wire to another, and to avoid snagging in special areas such as crossing lines and overlaps. A torsion bar (Figure 3.7) is placed between the upper arm and apex frame, which generates a head suspension.

Figure 3.7 Pantograph torsion bar

In this thesis, the lower part of the pantograph is considered to be made up of the pneumatic actuator, the base frame, the lower arm and the fourth bar; the upper part contains the upper arm and the control rod.

3.2.2 Pantograph important components

3.2.2.1 Head suspension

A pantograph consists of two suspension systems: head and frame suspensions. The characteristics of the two suspensions vary the pantograph-catenary interaction. The head suspension is placed between the apex frame and the upper part, acting as a spring-damper system, which allows the pantograph to track high-frequency irregularities of the contact wire rapidly and smoothly and reduce the possibility of contact loss (Gil-Vera, 2000). Therefore, this 'soft' mechanism is equivalent to a high-frequency excitation absorber (Gostling, 1979). To achieve a high-frequency response, the travel excursion of the head suspension is designed as a relatively small value (Cullingford, 1993). For example, the pneumatic actuator is able to extend the pantograph to full scale (around 3 m); however, the maximum distance travelled by the head suspension of a type of Brecknell Willis high-speed pantograph fitted on Class 91 trains is only 70 mm (Gil-Vera, 2000). Normally, a small linear spring or a torsion bar is used to form the head suspension. For the type of pantograph tested in this work, a C-shaped torsion bar is applied, as shown in Figure 3.7. The torsion bar shown in Figure 3.7 belonged to the pantograph that was damaged in the Cambridgeshire accident (RAIB, 2013) mentioned in Chapter 1.

The material properties of the torsion bar and the stiffness of the bearings in the head suspension affects the performance of the head suspension. As the pantograph operates longer, the conditions of the bearings change due to wear and dirt; meanwhile, the properties of the torsion bar also vary as it degrades, for example, if cracks occur. The pantograph head is expected to slide along the contact wire without losing contact. However, if the head suspension is not able to absorb the high-frequency oscillations as it is designed, it increases the likelihood of contact loss. Therefore, in order to maintain the pantograph behaviour, it is necessary to detect variations in the head suspension.

3.2.2.2 Frame suspension

The behaviour of the frame suspension is mainly dominated by a pneumatic actuator. The function of the frame suspension is different from that of the head suspension. It is designed to cope with the relatively low-frequency and high-level displacement, which is mainly caused by variation in the height of the contact wire and strong oscillation between pantograph and catenary (Van, 2016). The pneumatic actuator behaves in two ways: as a constant uplift force supplier and as a spring-damper system.

The uplift force provided by the pneumatic actuator, F_{lift}, can be worked out by Equation (3.1):

$$F_{lift} = p \cdot A \tag{3.1}$$

where *p* and *A* are the pressure inside the pneumatic actuator and the cross-section of the piston, respectively.

A sketch of a Pendolino pantograph and the pantograph mechanism are shown in Figure 3.8 and Figure 3.9, respectively. When the air compressor is on, the piston of the pneumatic actuator moves towards the right; meanwhile, the moving end of the actuator pulls the lower bottom of the lower arm to rotate anti-clockwise and so the pantograph rises. If the air compressor is turned off, the pneumatic actuator cannot hold up the pantograph, so the pantograph drops down to the parked position while the lower bottom of the lower arm rotates clockwise, and the piston moves to the left.

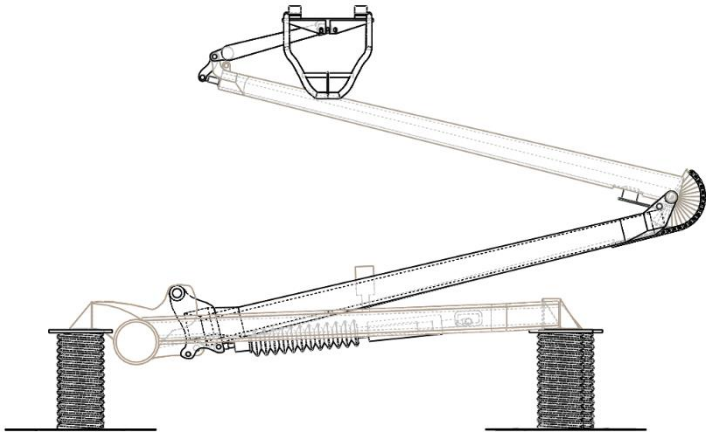

Figure 3.8 Sketch of a Pendolino pantograph

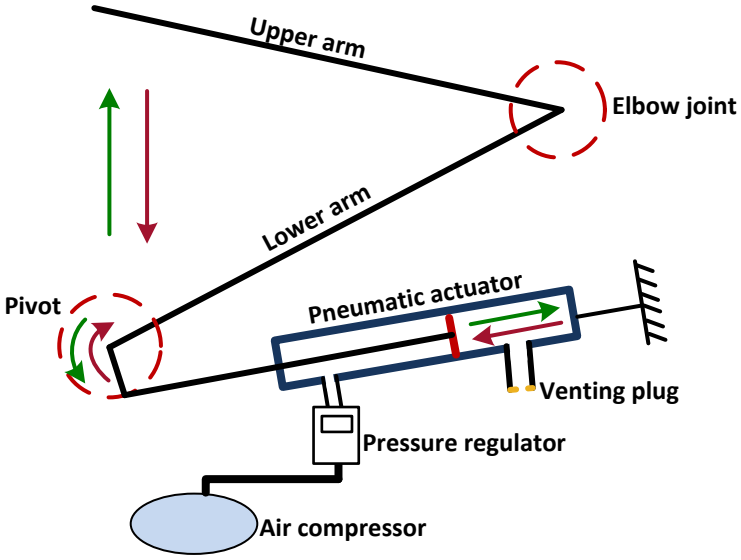

Figure 3.9 Pantograph mechanism

When the motion of the pantograph is relatively slow, the air pressure in the pneumatic actuator is kept roughly constant by venting air through a plug or pumping air from an air reservoir via a pressure regulator. According to Equation (3.1), the uplift force is maintained at a constant value under this circumstance. However, the pneumatic system cannot respond to the sudden changes in pressure caused by the rapid movement of the pantograph head that cannot be taken up by the head suspension. This varies the pressure in the pneumatic actuator, therefore varies the uplift force. Air goes through the venting plug rapidly resulting in the frame suspension behaves like a spring-damper system.

Considering the requirements in EN 50119 (CENELEC, 2013), the height of the contact wire differs due to local conditions. For example, due to the limited space inside tunnels, the height of the catenary falls in the tunnel (O'Connor et al., 1997); to prevent damage caused tall by heavy goods vehicles, the contact wire above level crossings is required to be high at such locations (Gabbott, 2007). When the pantograph passes these areas, a relatively large movement is required in the frame suspension; meanwhile, to avoid loss of contact with the contact wire, high stiffness is needed. Normally, the height of the contact wire changes gently and smoothly. Therefore, air flows relatively slowly inside the actuator, and does not affect the pressure inside the pneumatic actuator. The pneumatic supplies constant uplift force under this circumstance.

If strong oscillation happens between the pantograph and catenary, the head suspension cannot fully absorb the motion, and the dynamic behaviour of the pneumatic actuator is excited. In this situation, relatively rapid reciprocating motion acts on the pneumatic actuator. Air flows in and out of the pneumatic actuator through orifices. This results in changes in the equivalent damping and stiffness of the pneumatic actuator, and therefore varies the dynamic performance of the frame suspension; under this circumstance, the pneumatic actuator operates as a spring–damping system, and absorbs and releases energy (O'Donnell, 2003). Accordingly, the behaviour of the frame suspension also varies with the size of the orifice.

Figure 3.10 Venting plug

The orifice that allows air flowing out of the pneumatic actuator is covered by a venting plug (in Figure 3.10) to protect it against dirt. The material of the yellow part on the top of the venting plug is air permeable. As the pantograph operating time and distance increases, the yellow part on the top of the venting plug could be blocked by dirt, even though the cleanliness of the venting plug is checked regularly in depots. The degradation of the venting plug lowers the air flow rate, and therefore the pneumatic actuator becomes more resistant to motion. Furthermore, the lower permeability of the venting plug decreases the damping ratio of the pneumatic actuator; accordingly, the pantograph becomes more oscillatory and lightly damped (Murphy et al., 2007). The impact of the degradation of the venting plug on the dynamic behaviour of the frame suspension is discussed in this work. Another common fault on the frame suspension that will be considered in this thesis is the wrong levels of pressure supply (Betts et al., 1989). In this thesis, the impacts of the above factors, as well as leakage in the pneumatic actuator, on the dynamic behaviour of pantograph are considered.

3.2.2.3 Elbow joint

The elbow joint connects the upper and lower parts of the pantograph and governs the extension rate of the upper arm through three chains lying on the eccentric cam (gear):

one centre and two outer chains (in Figure 3.4). The elbow joint also transfers the relatively large displacement and low-frequency oscillation that is not taken up by the head suspension to the lower part. The tightness of the chains' attachment points changes the extension ratio of the upper part and vibration transmission from the upper to the lower part. Faults and changes in the elbow joint are generally caused by stiff or loose chains.

In the real operating circumstances, the carbon strips are worn by the contact wire while sliding along, and some carbon dust falls into the elbow joint. The carbon dust mixes with the lubricant making the chains stiffer. If the stiffness of the chains is higher than normal, the chains do not bend so well around the eccentric cam; and, therefore, the angle between the upper and lower arms can become locked, and the pantograph cannot return to its parked position. This extreme case is not considered in this thesis, as it is too dangerous to reproduce in the laboratory.

The chains are highly likely to become loose to some extent over time (ERG, 2012b). If the chains are loose, the extension ratio decreases which results in less excitation of the upper arm. In this work, different degrees of the tightness of the elbow joint chains is considered in the following chapters.

3.2.2.4 Automatic dropping device (ADD)

An Automatic Dropping Device (ADD) is installed to lower the pantograph in the event of head failure or damage (CENELEC, 2012c). The ADD must be employed for lines with operational speeds of 160 km/h or more (CENELEC, 2012b). For the lines with the speed lower than 160 km/h, the installation of the ADD is determined by train operators. The ADD incorporates an air pipe that passes along the pantographs and goes into one of the carbon strips. If the damage on the carbon strip rupture the pipe or the pantograph

head extends more than the maximum height, the ADD operates and realises the air pressure inside the pneumatic actuator to zero rapidly (RAIB, 2013). Without the uplift force supplied by the pneumatic actuator, the pantograph drops to its parked position. This action is also meant to prevent further possible damage to the catenary (Phillpotts, 1995). The ADD should not be mobilised during any tests in this work.

3.2.3 Comments

The dynamic behaviour of a pantograph is related to the characteristics of the head and frame suspension and the elbow joint. The behaviour of the head suspension is determined by the stiffness of the bearings and material properties of the torsion bar. The performance of the frame suspension is related to several factors, including the pressure supply level, the sizes of orifices, leakage in the pneumatic actuator, and the degradation of the venting plug. Problems associated with the elbow joint are generally due to loose or high stiffness chains. The pantograph faults and changes considered in this worked are listed in Table 3.1. In the following chapters, these common faults are investigated through different dynamic tests to support the realisation of pantograph fault detection and diagnosis.

Table 3.1 The pantograph faults and changes considered in this work

Location	Types of fault or change
Head suspension	Varying the greasing level of the head suspension
	Replacing the torsion bar
Elbow joint chain	Varying the degree of tightness of the elbow joint chain
Frame suspension	Varying pressure levels
	Leakage within the pneumatic actuator
	Degradation of the venting plug

3.3 A test rig for pantograph diagnosis

3.3.1 Introduction

In order to accomplish various tests for inspecting pantograph dynamics and realise fault detection and diagnosis without removing the pantograph from the roof of the train, a laboratory-based pantograph test rig has been developed in this work. The test rig is funded by RSSB and now located at the University of Birmingham. To collect parameters during various tests, additional load cells and accelerometers were fitted on the test rig and pantograph to work in conjunction with a built-in tachometer. Using this test rig, various dynamic tests are able to be carried out on an actual pantograph under control. The developed test rig is able to move the pantograph head at any pantograph working (extension) height, and the vertical oscillations can be varied in frequency and amplitude in a controlled way. The vertical displacement can be applied at any lateral position across the pantograph head. Critical parameters are measured during the tests by sensors, and then data is transferred to a computer via the data acquisition system. The measurement data is also stored in the computer for further analysis.

3.3.2 Laboratory-based pantograph test rig

The development of the test rig is inspired by some existing test rigs including those developed by POLIMI (Collina et al., 2004) and DB (Deml and Baldauf, 2001). The architecture of the test rig is similar to these test rigs as it is composed of an actuation system, data acquisition system and a PC for data analysis and storage, as shown in Figure 3.11. However, as the existing test rigs were developed for accomplishing pantograph frequency-response tests, they are only able to excite the pantograph at one extension height; meanwhile, the lateral motion of the existing rigs are also limited. Furthermore, the POLIMI and DB test rigs utilise hydraulic actuators that have difficulty

achieving high-frequency excitations (Rosero et al., 2007). Regarding these disadvantages of the developed test rigs, the Birmingham test rig is developed with large-scale vertical and lateral movement; meanwhile, electric actuators that are more suitable for high-speed and high-frequency control are used (Boglietti et al., 2009).

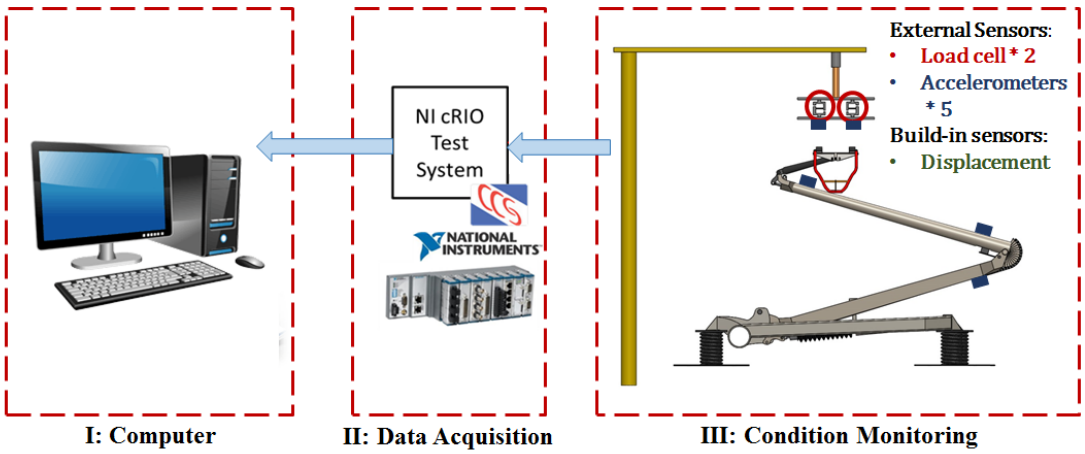

Figure 3.11 Architecture of the Birmingham pantograph test rig

The development of the Birmingham test rig meets the relevant requirements in European standard EN 50317 (CENELEC, 2012a) and concerns elicited from managers of maintenance depots during the requirements gathering stage. In EN 50317, it is demanded that in order to present the dynamic behaviour of pantographs, critical parameters should be measured with the sampling rate greater than 200 Hz, and the excitation of frequency-response test should up to 20 Hz. The parameters related to the objective of this thesis are the contact force and the vertical displacement of the contact point. The Birmingham rig is capable of sampling at 1 kHz, and the excitation frequency extends up to 50 Hz. Furthermore, the accelerations of different pantograph parts have been proved as important factors to investigate the dynamic behaviour of the pantograph in the previous studies reviewed in Chapter 2 (Bolton and Dyne, 1984, O'Donnell et al., 2006), therefore the accelerations are also recorded by additional accelerometers attached to the test rig.

One of the concerns from the industry is that the test rig should be calibrated carefully and provide reliable measurements. Thus, the test rig was calibrated according to the same standard, EN 50317 (CENELEC, 2012a).

3.3.2.1 Actuation Subsystem

The actuation subsystem of the Birmingham test rig (Figure 3.12 *a*) stands on two supporting legs, between which a horizontal linear guide is mounted. The horizontal guide has a working stroke of 2.8 m, which allows force input to be applied anywhere across the full width of the pantograph contact strips. A vertical axis is mounted on and perpendicular to the horizontal guide. A triangle actuator arm is attached to and moves along the vertical axis to perform vertical excitation. To excite two contact strips evenly, an excitation bar is mounted under the actuator arm. The vertical guide provides a 3 m working stroke to achieve a high extension level of the pantograph. Therefore, the hysteresis test and a novel changing-gradient test can be implemented; furthermore, the frequency-response test can be carried out at different heights, whereas, other existing rigs only work at one single height (Facchinetti and Mauri, 2009). In the next stage of this project, the supporting legs of the Birmingham test rig will be lengthened to allow the trains passing underneath it; therefore, it will be possible to test the pantographs without removing them from the roof of the trains.

Two three-phase servo actuators are used to control the vertical and lateral motion independently through user–friendly software. Accordingly, the test rig is able to exercise the pantograph at different extension heights and lateral positions across the pantograph head. Various control strategies can be applied in controlled ways. The highest excitation frequency that can be generated by the test rig is 50 Hz, which is higher than the requirement of 20 Hz in EN 50317 (CENELEC, 2012a). However, the existing test rigs

that driven by the hydraulic actuators only can generate small vertical displacements at high frequencies. These test rigs do not allow the excitations with high amplitudes that are required for pantograph dynamic testing in the future. In addition, hydraulic actuators can leak and cause a considerable mess.

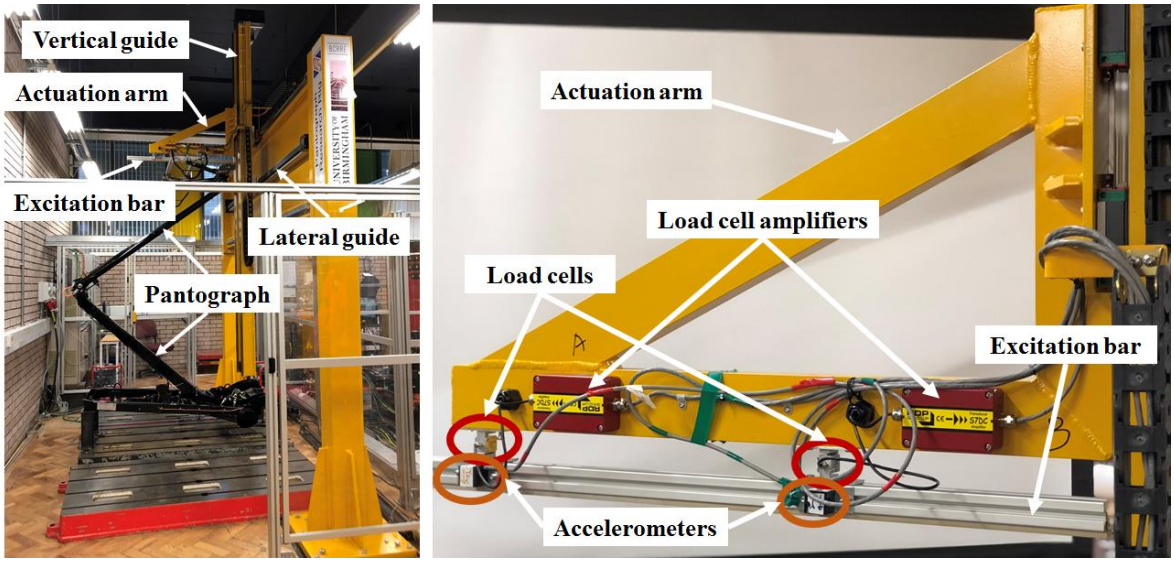

a. ***b.***

Figure 3.12 Birmingham pantograph test rig

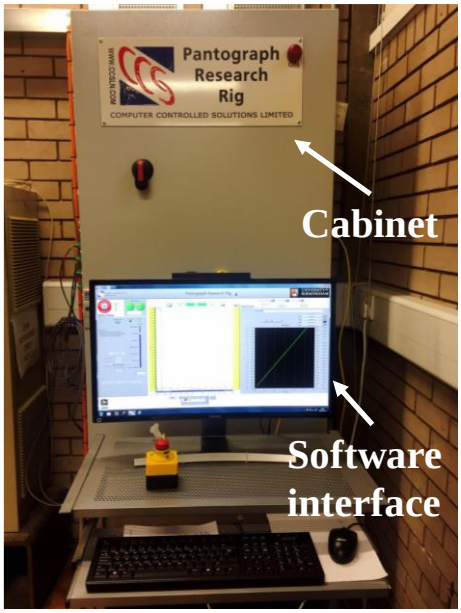

Figure 3.13 Cabinet and software interface

The electronic control of the motion is achieved with a PC using bespoke control software written in LabView. Different control modes such as manual and pre-defined profile

control can be accomplished for different dynamic tests (Weston and Xin, 2016). The cabinet and software interface are shown in Figure 3.13.

3.3.2.2 Data Acquisition System and Analysis Server

In order to address the dynamic behaviour of a pantograph, useful parameters need to be recorded and logged on the computer for further analysis while the dynamic tests are carried out. The data acquisition system consists of various sensors and data acquisition (DAQ) measurement hardware with a sampling rate of 1 kHz to reduce the noise. The lowest sampling rate required in EN 50317 is 200 Hz(CENELEC, 2012a).

The plan of the chosen sensors is inspired by some previous studies. The parameters related to the performance of pantograph include the contact force and the displacement of the pantograph head (Morris, 1964) and accelerations of different pantograph parts (Gostling and Hobbs, 1983). Theoretically, the pantograph only has one degree of freedom in the vertical direction. However, in the real world, due to the vibration of rolling stock, crosswinds and other external factors, the pantograph generates unexpected motion in the lateral direction. In this work, these external influences are not taken into consideration. The stagger arrangement of the catenary is not considered either, as lateral excitation generates excessive lateral friction on the pantograph head in the laboratory. However, while the train is moving along the contact wire in the real world, the lateral force on the pantograph head is small, as most of the friction force is in the longitudinal direction. The excessive lateral force generated by the laboratory-based test may damage the pantograph.

In order to measure the contact force, two load cells are fitted between the excitation bar and excitation arm (in Figure 3.12 *b*). The contact force collected in this work is the force between the pantograph head and the excitation bar. The ‘S’ beam load cells (in Figure

3.14) are manufactured by Omega Sensors; the model number is LCM101–50. Referring to previous work, the maximum value of the contact force obtained through numerical simulation, laboratory-based test and online measurement is normally less than 350 N (Facchinetti et al., 2013, Facchinetti and Bruni, 2012, Bobillot et al., 2006). In this work, a trade-off is made between measuring the contact force with relatively high accuracy and ensuring the load cells are not overloaded due to an unexpected testing condition. The measurement range of the load cells are chosen as ± 50 kgf (490.33 N) with a safe overload of 150% and an accuracy of 0.1 N. A built-in tachometer is used to acquire the rotational speed of the rig's drives, therefore the displacement of the excitation arm can be worked out.

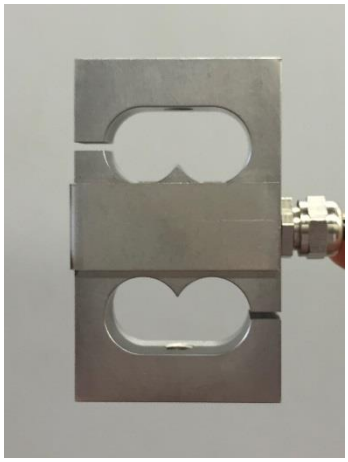

Figure 3.14 Load cell

The dynamic behaviour of the pantograph varies significantly with the condition of the head and frame suspensions and the elbow joint (Morris, 1964). Therefore, it is desirable to measure the accelerations at locations close to each connection. The POLIMI test rig measures the accelerations of the head, and the top ends of the upper and lower arms (Bruni et al., 2012a). Compared to the work carried out at POLIMI, in this work, one more accelerometer is mounted on the bottom end of the upper arm to fully investigate the behaviour of the elbow joint under various conditions. On the Birmingham test rig, five accelerometers are used: two one-axis and three two-axis accelerometers; the

configuration of installation is shown in Figure 3.15. The two one-axis accelerometers are mounted on the excitation bar immediately under the load cells, to measure the vertical acceleration of the pantograph head. The other three accelerometers measure accelerations parallel and perpendicular in a vertical plane to the arms. From these accelerations, the vertical acceleration of each monitoring location at any extension height can be worked out as shown in the right figure of Figure 3.15. Two of the two-axis accelerometers are attached to the top and bottom end of the upper arm, respectively; the last accelerometer is fitted on the top end of the lower arm. The accelerometers have a full-scale range of ±3g, and the bandwidths have a range of 0 to 1600 Hz.

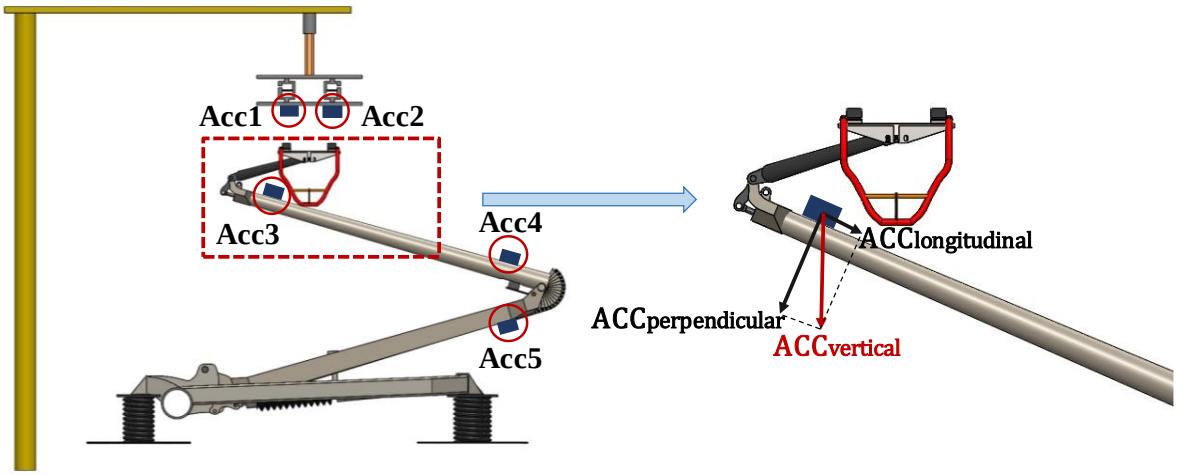

Figure 3.15 Configuration of the accelerometers

The acquired data is logged on a PC. Data streaming is managed by the controlling software. The data is saved in the National Instrument (NI) TDMS format which can be loaded into Excel or MATLAB for further analysis.

It is assumed that the displacement of the excitation bar is the same as that of the pantograph head. If the pantograph and excitation bar lose contact, then the force is valid, but the displacement is not. Therefore, the loss of contact results in unusable data. Contact loss is unexpected during any test.

In the following chapters, this test rig is used to carry out various dynamic tests, and therefore to achieve the final target of this research: establishing a rapid testing procedure for pantograph fault detection and diagnosis. In the next section, multibody modelling of a Pendolino pantograph is described to understand the behaviour of the pantograph and support the design of the test rig.

3.4 Multibody modelling of a Pendolino pantograph

3.4.1 Introduction

As discussed in Chapter 2, two types of pantograph models, namely, lumped-mass and multibody models, are widely applied to study the dynamic behaviour of pantograph (Sidorov et al., 2016). A 3D model is able to provide a more realistic way to understand the working principle of a pantograph (Benet et al., 2013). In this section, a 3D multibody model of a pantograph is presented. This model was used to support the design of the Birmingham test rig. Different from the multibody models reviewed in Chapter 2 that were built using mathematical equations (Ambrósio and Pombo, 2013), here, a new modelling method was applied: firstly, a 3D pantograph model was developed in SolidWorks, then this model was imported into MATLAB Simscape Multibody Toolbox for further simulation analysis. The 3D multibody model introduced in this work is built based on the actual geometry of a Pendolino pantograph.

3.4.2 3D modelling

The 3D modelling was carried out in SolidWorks software. Dimensions for the pantograph components were obtained from physical measurements and manufacturer data. Firstly, each critical component of the pantograph, including the base frame, pneumatic actuator, lower arm with a fourth bar running inside, upper arm with a control rod running inside, apex frame and head, were modelled separately, as shown in Figure

3.3, Figure 3.5 and Figure 3.6. Then, the correct material properties were determined for each of the components. The individual components were connected together to form a complete model through the use of different mechanical joints that represent the physical kinematic constraints. The complete pantograph model is shown in Figure 3.16.

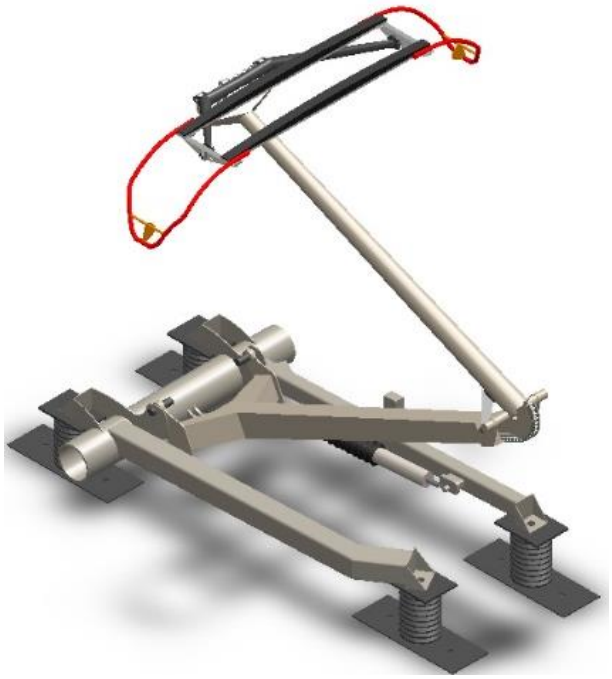

Figure 3.16 3D model of a Pendolino pantograph

A simple test rig model was also developed. The final 3D model of the complete system is shown in Figure 3.17.

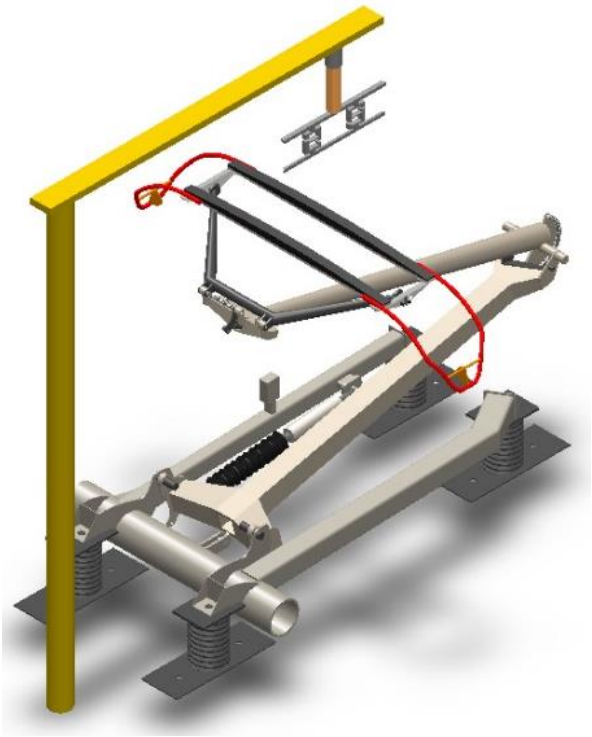

Figure 3.17 3D models of pantograph and test rig

3.4.3 Development of multibody model and simulation

A multibody model of the pantograph and test rig is generated by importing the 3D model developed within SolidWorks in Figure 3.17 into the MATLAB Simscape Multibody Toolbox (SMT). Simscape Multibody™ is a multibody simulation tool for 3D mechanical models. There two ways to build the 3D multibody model: (i) developing the model uses blocks representing bodies, joints, constraints, force elements, and sensors within Simscape Multibody Toolbox; or, (ii) importing a complete CAD assembly. If a CAD assembly is imported to the SMT, all masses, inertias, joints, constraints, and 3D geometry that have been included into the model are automatically mapped to equivalent joints in the SMT. Following this, the SMT formulates and solves the equations of motion. It can also generate a 3D animation that allows the users to visualise the system dynamics (MATLAB, 2018).

The joints of the pantograph built in the SolidWorks are automatically replaced by equivalent joints in the SMT. For the convenience of simulation control, the multibody model developed in this work is organised as three main parts: a pantograph, a pneumatic actuator, and a simplified test rig, as shown in Figure 3.18.

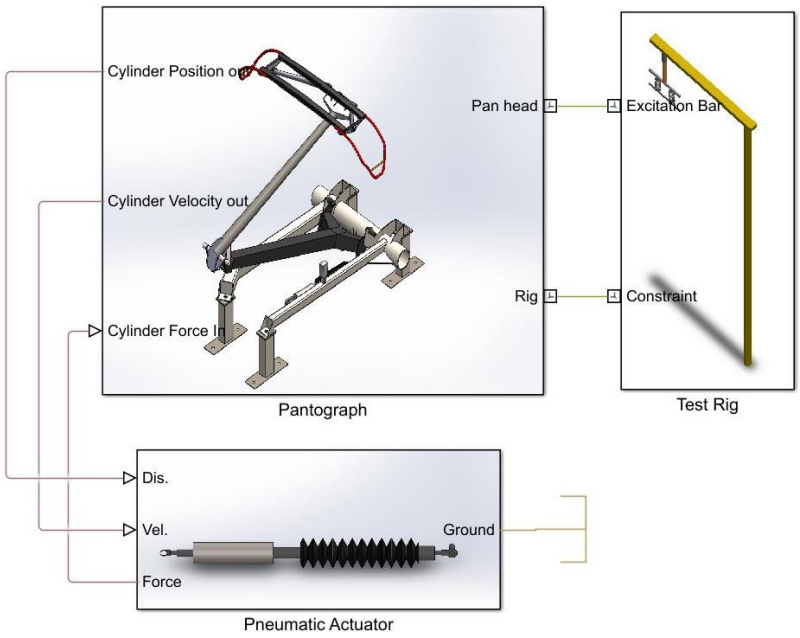

Figure 3.18 3D multibody pantograph model: the overall system

The composition of the multibody pantograph model is shown in Figure 3.19; components are linked by the MATLAB SMT built-in joints and constraints.

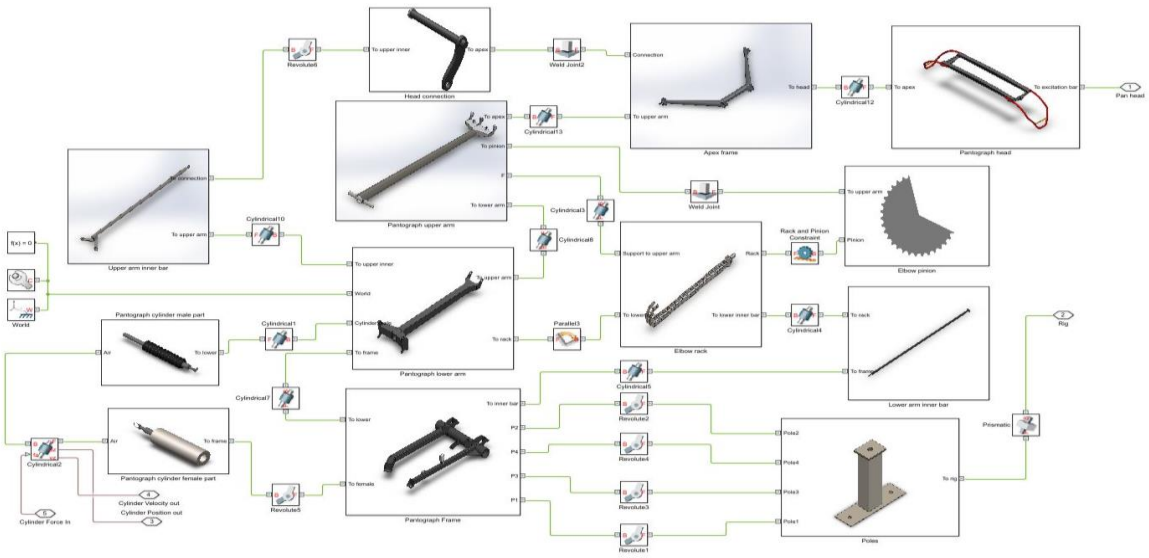

Figure 3.19 3D multibody pantograph model: pantograph components

To support the design of the test rig, the pantograph multibody simulation was configured so that it had a fault on the eccentric cam. There are three chains on the eccentric cam, linking the fourth bar and the upper arm. The three chains work in conjunction to govern the excitation of the upper arm. The trajectory of the pantograph head is designed to be a vertical line when the pantograph rises and lowers. However, if the chains are loose, the shape of the trajectory becomes curved; in extreme circumstances, all three chains could be loose. Here, the extension angle of the upper arm will be less than expected, and the pantograph head will not elevate vertically. The simulation result is shown in Figure 3.20, where the black dashed line is the trajectory of the pantograph head under normal condition, and the red curve is that when the chains are loose. As the pantograph rises more, the centre of the pantograph will move more to the left. In this case, the carbon strips may slip off the excitation arm of the test rig. To avoid this phenomenon, the length of the excitation arm is designed carefully.

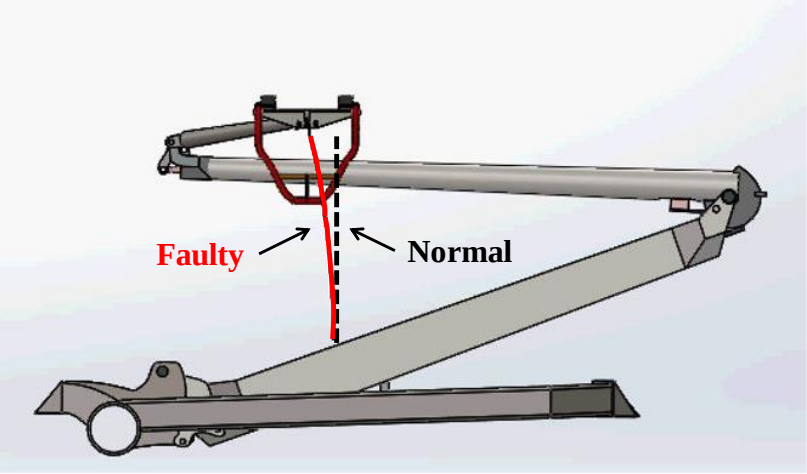

Figure 3.20 Pantograph faulty condition simulation

3.5 Summary

In this chapter, the structure and working principle of the Pendolino pantographs are discussed. Common faults in the pantograph head and frame suspension and the elbow joint are described. In order to identify pantograph diagnosis approaches under controlled

conditions, a laboratory-based test rig has been developed. This test rig is designed in line with European standard EN 50317–Railway applications–Current collection systems–Requirements for and validation of measurements of the dynamic interaction between pantograph and overhead contact line (CENELEC, 2012a), and also by taking account of requirements given by depot managers. Furthermore, a 3D multibody model consisting of a pantograph and a simplified test rig was developed in SolidWorks; by importing this 3D model to the MATLAB SMT, further simulations were carried out to support the design of the test rig and obtain a better understanding of the dynamic behaviour of the pantograph in normal and faulty conditions priors to carry out the dynamic tests.

CHAPTER 4 DYNAMIC TESTS FOR PANTOGRAPH FAULT DIAGNOSIS

4.1 Introduction

Pantographs mounted on the roofs of trains are used to collect current from the overhead line equipment. By sliding along the contact wire, the pantograph collects traction current via carbon strips on the pantograph head and transfers the power to the on-board systems. The pantograph and the catenary interact with each other to form a coupled dynamic oscillating system where contact loss may occur (Bocciolone et al., 2006). Contact loss results in electric arcs and sparks that adversely affects the current collection quality, and increases wear of the OHL and contact strips (Mochizuka et al., 2000). The interaction between the pantograph and catenary is mainly associated with the contact force that varies according to the health of the pantograph, assuming that the catenary is in good condition (Resta et al., 2001). Accordingly, the condition of pantographs should be inspected to maintain the current collection quality and safe operation of the pantograph-catenary system.

Currently, the maintenance activities carried out at depots mainly relies on visual and manual checks based on either operating time or distance. Measurement of static hysteresis is carried out at some depots; however, the results tend not to highlight faults and degradation directly. Therefore, it would provide significant benefit to develop an intelligent pantograph maintenance procedure, which allows the condition-based fault detection and diagnosis of pantographs to be carried out. To this end, a laboratory-based pantograph condition monitoring system has been developed as detailed in Chapter 3.

In order to realise condition-based fault detection and diagnosis, three dynamic tests are proposed in this work: (i) a dynamic hysteresis test; (ii) a frequency response test; and (iii) a novel changing-gradient test. The static frictional hysteresis (50 mm/s) test is carried out at some depots. However, the nonlinearities in joints and pneumatic actuators that affect the dynamic behaviour of pantographs cannot be inspected using this test. In this work, one way to excite the nonlinearities of pantograph is by using 'extended hysteresis tests' which are carried out at various speeds in the range of 50 to 400 mm/s.

In order to analyse the behaviour of a nonlinear system, the steady–state and transient response are both have to be measured (Ogata, 1970). The frequency-response and changing-gradient tests were used to detect and identify the steady-state and transient response of the pantograph, respectively. A sinusoidal signal is commonly used to excite the steady-state response of a nonlinear system (Storer, 1991). In this work, the frequency-response test is carried out by varying the frequency of the sinewave excitation in the range specified in EN 50317 (CENELEC, 2012a). In order to investigate transient responses, step and impulse inputs are widely used (Burgess, 1988). The test rig is able to apply input to the pantograph with controlled displacement or speed. However, for a mechanical system, it is difficult to generate a step change in displacement so, instead, the changing-gradient test is carried out using stepped vertical speed input signals. Various excitation speeds were applied to investigate the responses at different operational speeds.

The feasibility of these three dynamic tests for detecting and diagnosing pantograph faults is considered. The measured data from a new pantograph is used as a reference; by comparing data collected from pantographs in various states of health to the reference data, the features that can be used to detect and diagnose various faults can be identified and extracted. Different system identification techniques are applied to extract the fault characteristics from the

measurements using frequency-response and changing-gradient tests. Furthermore, to classify and diagnose various faults, a type of deep learning algorithm, a stacked sparse autoencoder (SSAE) is utilised to analyse the data collected by the novel changing-gradient test.

4.2 Hysteresis test

4.2.1 Introduction of hysteresis test

Frictional hysteresis occurs in all real-world mechanical systems. In the railway industry, maintainers and manufacturers consider static frictional hysteresis as one of the important criteria for evaluating the performance of pantographs (Conway, 2014). Hysteresis of a pantograph tends to vary as the condition of the pantograph degrades with an increase in operating time and distance. The hysteresis test has been carried out in depots since the 1990's (SNCF, 1991). Commercial equipment is available to measure the static frictional hysteresis of pantographs at a standard excitation speed of 50 mm/s according to one of the requirements in standard EN 50206 (CENELEC, 2010). The decision as to whether the pantograph has 'passed' or 'failed' the test is made by comparing the hysteresis measured and the mean force with a manufacturer-specified threshold. The measurement of hysteresis is relatively straightforward with low technical requirements; however, it is not implemented commonly at depots, as the relationship between the information obtained by the tests and the condition of the pantograph is not fully understood.

In this work, the relationship between hysteresis and the health status of the pantograph is addressed by carrying out the static hysteresis test on a Pendolino high-speed pantograph under various conditions using the test rig. Furthermore, the hysteresis test is also carried out at additional higher speeds to accentuate and inspect different nonlinearities. By understanding the relationship between the test results and the pantograph status, it might be possible to use the hysteresis test for pantograph fault detection and diagnosis.

4.2.2 Measurement of the hysteresis

The hysteresis test starts with the pantograph at its lowest position. Then, the pantograph travels upwards under the control of the measurement device. When the pantograph reaches the maximum height, the test rig pushes the pantograph back down to the starting point, maintaining a constant speed. Critical parameters, including contact forces, displacement of the pantograph head, accelerations of different pantograph parts, are recorded during this process. Four cycles of pantograph hysteresis were obtained to ensure the measurements used for fault detection and diagnosis are not affected by random disturbances and noise, the excitation profile of the static hysteresis test (50 mm/s) is shown in Figure 4.1. The 'zero' height position is considered to be where the pantograph is in its parked position.

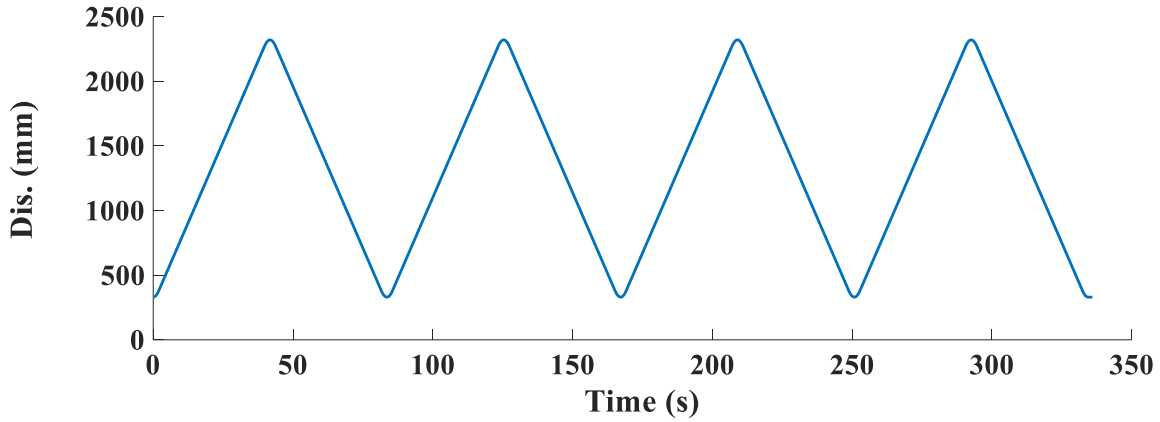

Figure 4.1 Excitation profile of hysteresis test

To avoid contact loss between the pantograph head and the excitation bar when the pantograph reverses direction, the change of speed is smoothed over about 1 second. Due to a safe–operating limitation on the speed of the excitation arm when operating below 330 mm, the starting position of the hysteresis measurement is set to 330 mm. The greatest extension height is limited to 2320 mm, where the automatic dropping device (ADD) starts to be triggered. The function of the ADD was detailed in §3.2.2.

4.2.3 Static hysteresis comparison: a new and a pre-overhaul pantograph

In order to explore the impact of changes to the pantograph on the static hysteresis, a new pantograph and a pre-overhaul pantograph of the same type were tested at the standard excitation speed of 50 mm/s. In line with the requirement in EN 50317 (CENELEC, 2012a), the frequency range of interest for the measurement of pantograph dynamics is only up to 20 Hz; so, all signals were filtered with a low-pass filter with a cut-off frequency of 20 Hz.

The hysteresis loops measured using the four excitation cycles (in Figure 4.1) are plotted in Figure 4.2. The hysteresis loops measured by four consecutive excitation cycles show very good repeatability.

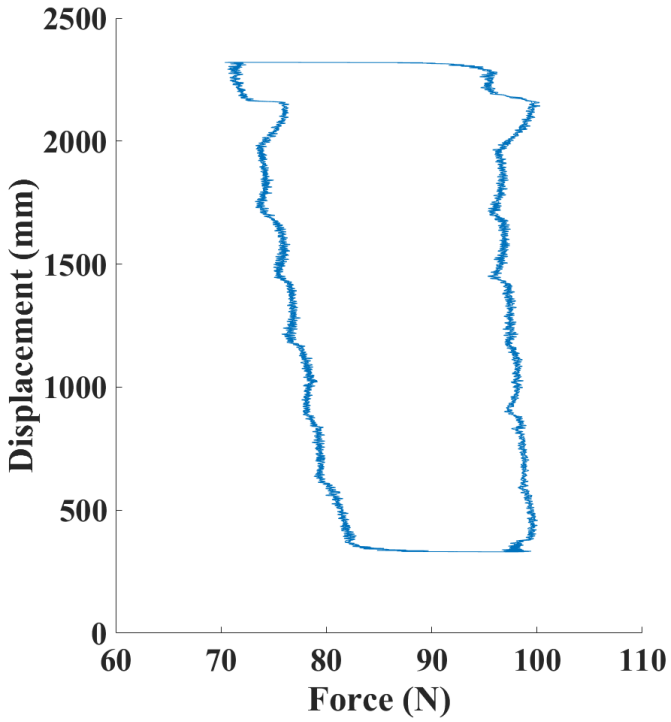

Figure 4.2 Four Hysteresis loops

In order to evaluate the repeatability of the results obtained by the four hysteresis tests, the differences between the mean of the four tests and each individual test are worked out. The histogram of the differences is shown in Figure 4.3. The mean and standard deviation of the differences in force are 0 N and 0.19 N, respectively; the corresponding normal distribution is

the red line in Figure 4.3. Accordingly, the results of the four hysteresis tests achieve good repeatability, and the mean force measured of the four tests can be used in this work for further analysis.

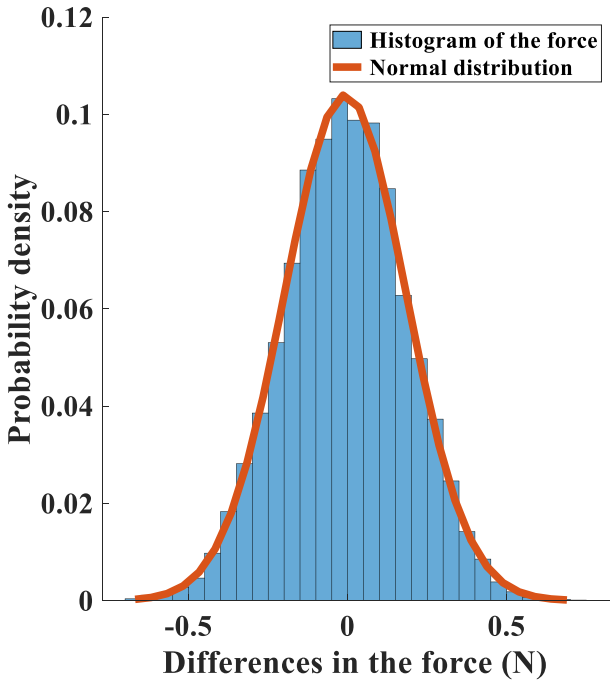

Figure 4.3 Histogram of the differences in the measured force

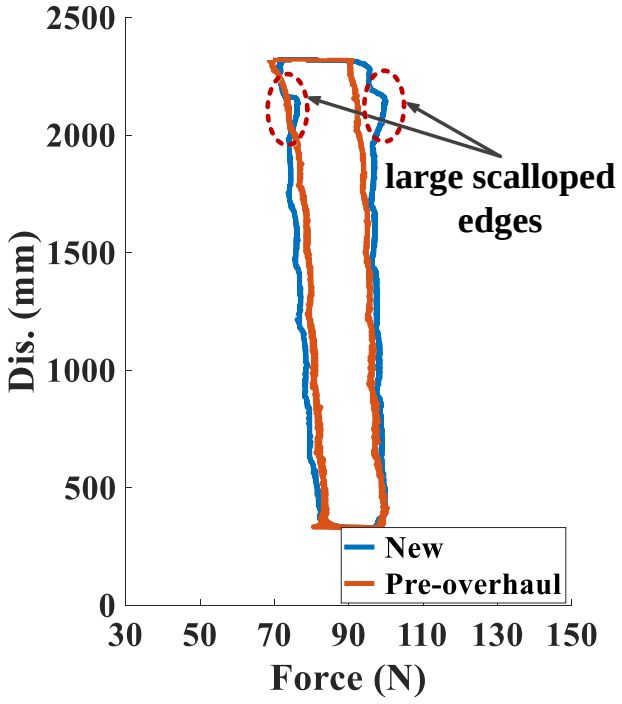

Figure 4.4 Comparison of static hysteresis: new and pre-overhaul pantographs

The static hysteresis of the new and pre-overhaul pantographs are presented with blue and red profiles, respectively, in Figure 4.4.

In this figure, the left side of the hysteresis loop is the contact force measured while the pantograph is rising and is referred to as the 'up force', while the right side of the loop is measured while the pantograph is pressed downwards and is called the 'down force'. The mean value of the up and down forces is referred to as the 'uplift force'. The average gap between the up and down forces is the hysteresis of the pantograph. When the pantograph is excited at 50 mm/s, the hysteresis is defined as static hysteresis. The values of these parameters collected from the two pantographs are presented in Table 4.1.

Table 4.1 Measurement of pantograph hysteresis

Conditions	Avg. up force (N)	Avg. down force (N)	Uplift force (N)	Hysteresis (N)
New	79.6	100.6	91.1	20.9
Pre–overhaul	81.7	99.0	90.4	17.3
Difference	−2.1	1.6	−0.7	3.6

The uplift force and the maximum allowed hysteresis of the Pendolino pantograph are specified as 90 ± 3 N and 24 N, respectively (ERG, 2012a). Based on these criteria, both pantographs pass the hysteresis test. However, in Figure 4.4, compared to the new pantograph, the hysteresis loop of the pre-overhaul pantograph bends to the left gradually as the extension height increases. This indicates that the pre-overhaul pantograph cannot maintain the contact force at relatively constant levels while it is rising and being compressed as the extension height varies. Furthermore, large scalloped edges (or irregular ripples) appear on the hysteresis loop for the new pantograph at extension heights between 1970 and 2180 mm, but do not show up on that of the pre-overhaul one. These two traits could be considered as the features to detect and diagnose faults. However, the current pantograph examination criteria does not include this

level of detail. Accordingly, the up, down and uplift forces and the shape of the hysteresis curve should be considered in order to detect and diagnose faults.

These results demonstrate that degradation of the pantograph affects the hysteresis curve. And the hysteresis test accomplished by the developed test rig is able to detect changes to the pantograph. Even though the pre-overhaul pantograph shows some changes compared to a new one, this does not necessarily indicate a fault. Therefore, in order to understand various fault features and realise pantograph fault diagnosis, the new pantograph is tested with various faults and changes deliberately introduced in Chapter 5.

4.2.4 Hysteresis of the pantograph under various excitation speeds

4.2.4.1 Pantograph nonlinearities

The stiffness in each joint and damping and inherent hysteresis of the pneumatic actuator vary the up and down contact forces influencing the pantograph hysteresis. The measured contact force is the sum of the uplift force, the friction in each joint, the damping force of the pneumatic actuator and inertial force, and can be described as:

$$\begin{gathered} F_{Contact} = F_{Static} + F_{Friction} + F_{Damping} + F_{Inertial} \\ F_{Inertial} = ma \end{gathered} \tag{4.1}$$

As the excitation speed of a hysteresis test can be considered as constant, the acceleration a is zero and the inertial force $F_{Inertial}$ can be neglected in Equation (4.1). The acceleration when the direction of travel reverses is not zero, but this is not important for the hysteresis test.

A faultless pneumatic actuator is able to maintain its pressure at a relatively constant level; therefore, the uplift force, F_{Static}, of the new pantograph is approximately constant. The direction of the uplift force is always upward which is assumed as the positive direction in this work.

Friction consists of stiction and kinetic friction (Haug et al., 1986). Stiction results in short spike in force when the pantograph reverses its direction of motion; however, as the reversing corners are smoothed on the excitation profiles, the stiction does not show up well in the measurement of hysteresis and is not taken into account in Equation (4.1). Kinetic friction is mainly generated in each joint, and its value varies with greasing level and wear. Hysteresis tests carried out on the same pantograph under similar degradation conditions are considered to have the same kinetic friction level.

Therefore, variation in the contact force principally results from changes in the damping force. The damping force that is generated by the pneumatic actuator can be written as Equation (4.2):

$$F_{Damping} = -c\dot{x} \tag{4.2}$$

where c is the damping coefficient, and $\dot{x}$ is the excitation speed applied to the pantograph head.

In Equation (4.2), it can be observed that as the excitation speed increases, the absolute value of the damping force grows. Considering the upward direction as the positive direction, in Equation (4.1), as the excitation speed grows, the up force decreases, and the down force increases correspondingly. As a result, hysteresis appears to increase as the excitation speed grows.

4.2.4.2 Feature extraction of the hysteresis tests at various excitation speeds

In this thesis, the excitation speeds of the hysteresis test were varied from 50 to 400 mm/s with a step of 50 mm/s. If the excitation speed is any lower than 50 mm/s, the hysteresis at that speed remains essentially the same as that at 50 mm/s. If the excitation speed is any higher than 400 mm/s, the high acceleration and deceleration result in fluctuation in and overshoot of the contact force, which is not accepted during a test. The time taken for hysteresis tests at various excitation speeds are shown in Table 4.2. The faster the speed, the shorter the test.

Table 4.2 Time taken for hysteresis test

Excitation speed (mm/s)	50	100	150	200	250	300	350	400
Time (s)	83.6	43.8	30.6	23.9	19.9	17.4	15.4	14.1

Hysteresis of the new Pendolino high-speed pantograph under different excitation speeds is shown in Figure 4.5. It verifies the assumption that the pantograph hysteresis grows as the excitation speed increases. Furthermore, all the hysteresis loops are concentric, which illustrates that the uplift force is almost the same while the pantograph is excited with different excitation speeds. These features characterise a faultless pantograph and will be used as references in Chapter 5 for pantograph fault detection and diagnosis.

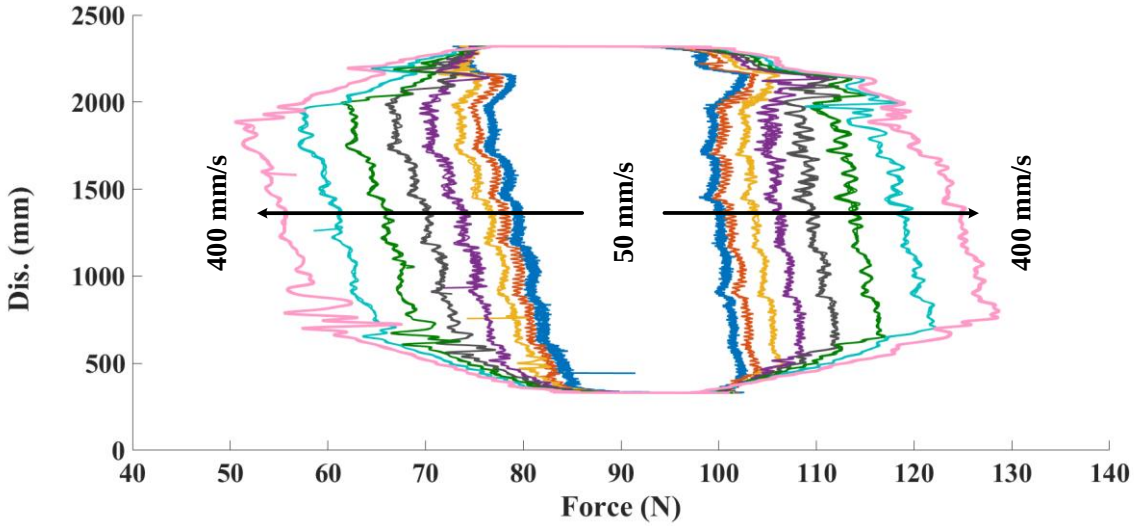

Figure 4.5 Hysteresis of the new pantograph at different speeds

The average up, down and uplift forces with respect to the excitation velocities are shown in Figure 4.6, and the values of these parameters are shown in Appendix A, Table A.1.

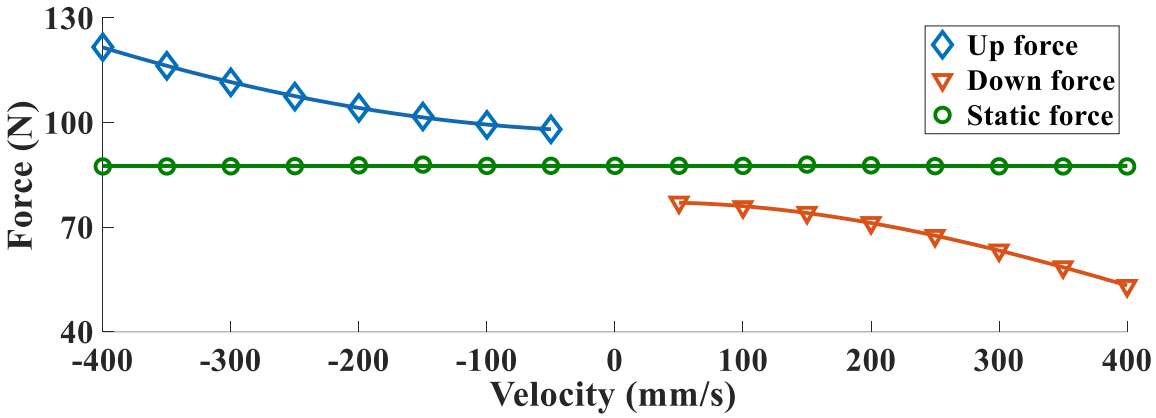

Figure 4.6 Up, down and uplift forces measured at different excitation speeds

The variation in the up and down forces is not proportional to the excitation velocities, which shows either that the damping force is nonlinear with speed, or the hysteresis in the pneumatic pressure control system varies with speed. In either case, the apparent damping coefficient varies with excitation speed. As the friction of the pantograph is difficult to measure and is relatively constant for the similar degradation level of the pantograph, the friction is neglected while looking at the variation in the damping coefficient as the excitation speed is varied. According to Equations (4.1) and (4.2), the damping coefficient can be described as:

$$c = (-F_{Contact} + F_{Static} + F_{friction})/\dot{x}$$

Using the measured contact force and uplift force in Appendix A, Table A.1, the damping coefficients can be worked out and are shown in Figure 4.7; the values of the damping coefficient are shown in Appendix A, Table A.1. The results demonstrate that the damping coefficient of the pantograph decreases significantly as the excitation speed increases in the low-speed range; the damping coefficients obtained under an excitation speed in the range of 200 to 400 mm/s are relatively similar. The values and trend of the damping coefficient in terms of different excitation speeds are used as references to detect and diagnose pantograph faults in Chapter 5.

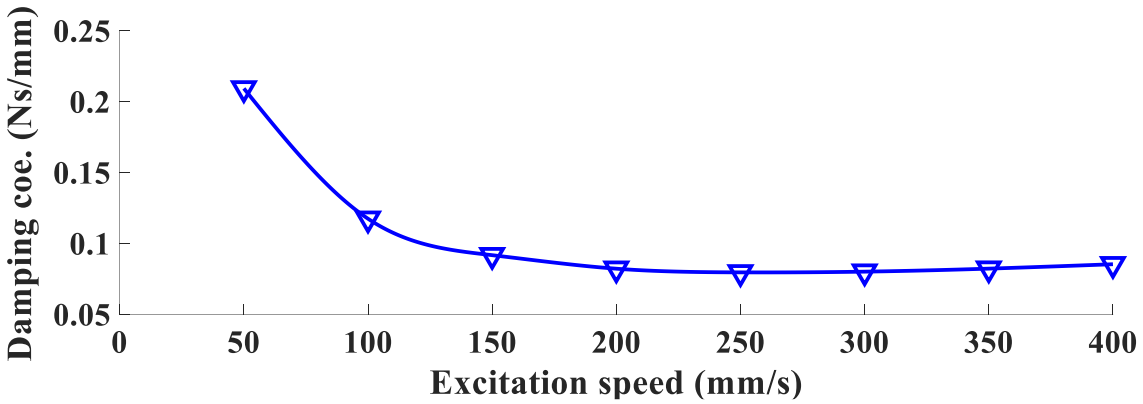

Figure 4.7 Damping coefficient at different speeds

4.3 Frequency-response Test

4.3.1 Introduction of frequency-response test

The second dynamic test applied in this work to detect and diagnose pantograph faults is a frequency-response test. Frequency-response methods were developed in the 1930's and 1940's by Nyquist, Bode, Nichols, and many others (Ogata, 1970). These methods have been widely used in many fields to investigate system behaviour by analysing the response of the tested system to an applied sinusoidal input over a range of frequencies (Seering et al., 1983). The relation between the output and the input signals is normally expressed by the frequency-response function (FRF) in the frequency domain (Lang et al., 2007).

Analysing the dynamic behaviour of a pantograph by measuring and analysing its FRF was proposed by O'Connor (1984) in the 1980's, and became a commonly used testing method applied by railway operators and manufactures (SNCF, 1991, Cullingford, 1993).The advantage of this approach is that it is able to realise system identification using actual measurement data without deriving the parameterised mathematical models that cannot sufficiently represent the dynamic behaviour and degradation of pantographs. Details of the natural modes of vibration, including the shapes of the resonances, resonant frequencies, and damping ratios from FRF measurements, describe the dynamic behaviour of the tested system. This analysis technique determines that variation in the masses, stiffness and damping of the

tested pantograph changes the appearance of the FRFs. Accordingly, by comparing the measured FRFs to the references, the differences indicate the occurrence of change or fault in the pantograph. By identifying the features of common pantograph faults, it is possible to detect and diagnose pantograph faults using the frequency-response tests. However, in previous studies, the FRFs of pantographs were used in particular to work out the parameters for lumped-mass models (Bruni et al., 2012a). In this work, a novel application of the frequency-response test is proposed to characterise pantograph dynamic behaviour, and therefore, to detect and diagnose pantograph faults.

4.3.2 Pantograph frequency-response test

4.3.2.1 Excitation strategies of the frequency-response test

A commonly used excitation signal for the frequency-response test is a stepped sine wave, which chains together tests at single frequencies to obtain the whole frequency response (Ogata, 1970). During the frequency-response test, the frequency of the input signal is varied over the range of interest. This range and the step sizes were chosen according to the requirements in EN 50317 (CENELEC, 2012a), '*the measurement of the applied force and the measured force shall be taken at frequencies from 0.5 up to 20 Hz in 0.5 Hz steps, with reduced intervals at resonant frequencies. The frequency steps near the resonant frequencies shall be specified'*. In order to fully inspect the pantograph dynamics, in this work, the step was selected as 0.1 Hz in the entire frequency range.

The relationship between the input and the resulting measurements was used to obtain the FRF of the tested system. In order to work out the FRF using the measurements, the first step is to perform a Fourier transform on the input and output data at each excitation frequency individually. The Fourier transform requires the data to be obtained while the system is under steady–state conditions. When the frequency of the input is increased to the next value,

transients are inevitably generated. Therefore, transients should be allowed to die away before the measurements are taken (Storer, 1991). In this work, 30 cycles of the sine wave at each frequency are applied: the first 5 cycles were to allow the transients to die away, and the remaining 25 cycles were used to calculate the FRFs, as shown in Figure 4.8.

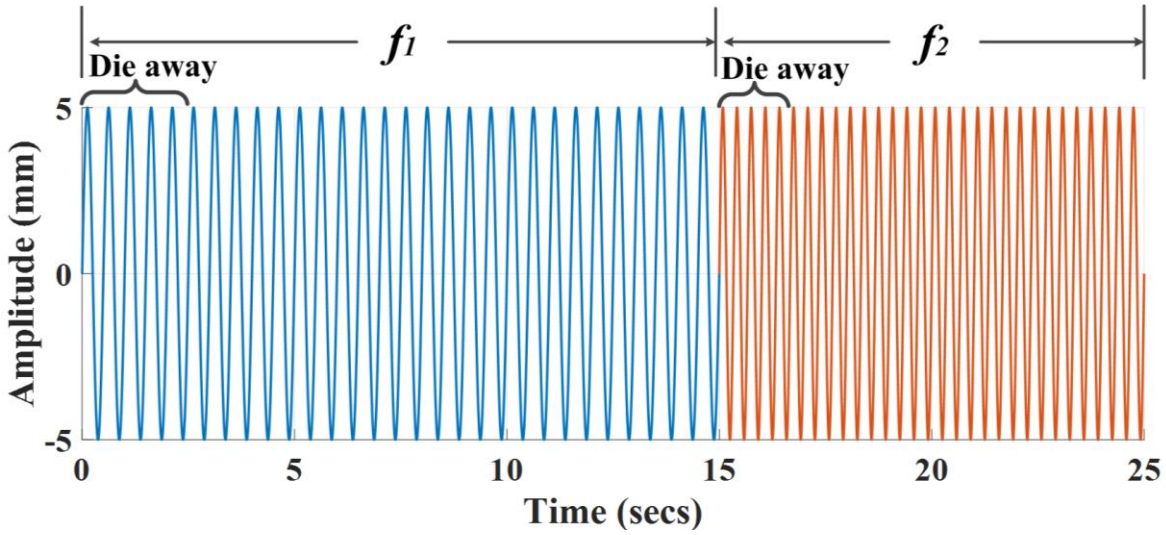

Figure 4.8 Stepped-sine wave excitation

The derivation of the frequency-response function refers to the standard model shown in Figure 4.9. In this work, the input $x(t)$ is the measured contact force, and $\mathrm{y}(t)$ is the accelerations collected from the pantograph head, the top and bottom end of the upper arm, and the top end of the lower arm. Therefore, for each frequency-response test, five response functions can be worked out.

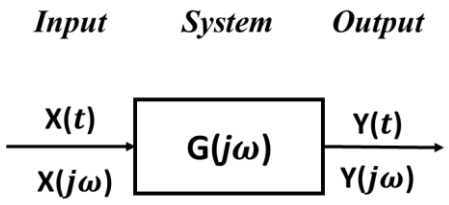

Figure 4.9 Standard frequency-response model

The mathematical expression for the frequency-response analysis in the frequency domain is:

$$Y(j\omega) = G(j\omega)X(j\omega) \tag{4.3}$$

where $X(j\omega)$ and $Y(j\omega)$ are the Fourier transforms of the contact force and the acceleration, respectively. $Y(j\omega)$ can be the accelerations measured by any accelerometer shown in Figure 3.15. $G(j\omega)$ is the response function of the tested pantograph. The unit of the contact force and the acceleration are Newton (*N*) and metres per squared second (m/s^2), respectively; therefore the unit of the magnitude of $G(j\omega)$ is kg^{-1}. $G(j\omega)$ is also named as 'accelerance' function (Ewins, 1984).

On the basis of Equation (4.3), it is possible to look the gain and phase shift at each frequency:

- $|G(j\omega)| = \left|\frac{Y(j\omega)}{X(j\omega)}\right| =$ magnitude ratio of the output to the input (gain);
- $\angle G(j\omega) = \angle \frac{Y(j\omega)}{X(j\omega)} =$ phase shift of the output with respect of the input.

Therefore, it is possible to represent the FRF by plotting magnitude and phase angle in separate figures against excitation frequency, named a Bode plot. The frequency-response method is strongly frequency selective, and, is therefore able to reject noise at frequencies different from the excitation (Schmitz and Smith, 2008). However, in practice, the input and output signals are corrupted to some degree by the interaction of the tested system and the excitation system, as well as by environmental noise. The noise influences the results of the FRFs, particularly the magnitude (Storer, 1991). Therefore, in this work, the variation in the phase plot is considerably more important than that of the magnitude plot in representing the dynamic behaviour of the pantograph.

4.3.2.2 Excitation levels for the frequency-response test

When using a frequency-response test to investigate the behaviour of a nonlinear system, the FRFs varies with the amplitude of the sinusoidal excitation signals. A pantograph is a system that contains several kinds of nonlinearities generated by the friction joints and the pneumatic

actuator (Cho, 2008). It is therefore necessary to choose the amplitude of sinusoidal input signals carefully for detecting different faults. In order to excite all the critical vibration modes of an Italian high-speed pantograph, Bruni et al. (2012a) carried out frequency-response tests at the Politecnico di Milano (POLIMI) using three excitation amplitudes, as shown in Table 4.3. The measurement is valid only while the excitation bar and the pantograph head remain in contact; otherwise, the force signal becomes unusable, and new transients are introduced when contact is restored.

Table 4.3 Excitation levels of frequency-response tests applied at POLIMI

Amplitude (mm)	Frequency range (Hz)
20	0.5–2
5	0.5–7
1	0.5–20

Referring to Table 4.3, various fixed-amplitude excitations, including 0.3, 0.5, 1, 2, 5 and 10 mm, were tested on the Pendolino high-speed pantograph using the test rig developed in this work. The FRFs with respect to various excitation levels in Figure 4.10. In this figure, the FRFs are worked out using the contact force and acceleration of the pantograph head as the input and output, respectively. For excitations with an amplitude lower than 0.3 mm, the test rig does not generate the displacement accurately, mainly because of a small amount of elasticity in the drive belt. When the excitation level is greater than 5 mm, such as at 10 mm, the valid measurement does not contain any resonance which describes the pantograph dynamics sufficiently. Therefore, excitation levels were varied between 0.3 and 5 mm in this work. Larger displacements are explored by the hysteresis and changing-gradient tests.

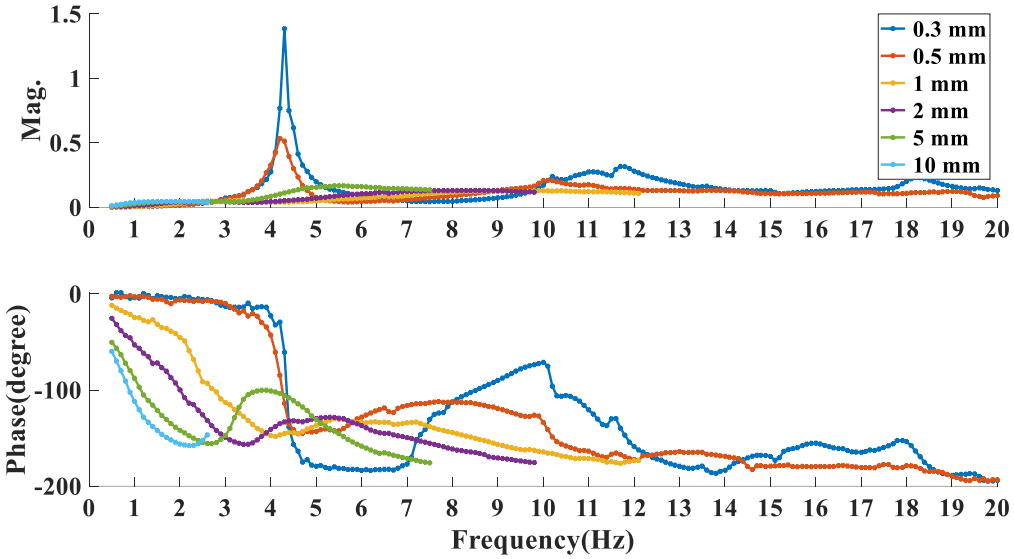

Figure 4.10 Head FRFs under different fixed-amplitude excitations. Input: contact force, output: acceleration of the head.

In Figure 4.10, it can be seen that the FRF is significantly affected by the use of different excitation amplitudes, which indicates nonlinearities are actuated in each profile. In order to excite the pantograph nonlinearities in the entire frequency range within a test; and therefore, to accomplish quick primary fault detection, an alternative excitation method is developed: the excitation amplitude is decreased as the frequency increases. In order to detect and diagnose different pantograph faults effectively, the excitation levels of the fixed-amplitude excitations are chosen according to the results obtained using the decreasing-amplitude excitation.

The mathematical function of the decreasing-amplitude excitation is described in Equation (4.4):

$$A = 5\ [mm], if\ f\ \leq 1\ Hz$$

$$A = {}^{5}/_{f}, if\ f\ \geq 1\ Hz \tag{4.4}$$

where f is the excitation frequency and varies from 0.5 to 20 Hz, and A is the amplitude of the sinusoidal excitation.

A demonstration of the fixed and decreasing-amplitude excitation with respect to frequency is shown in Figure 4.11.

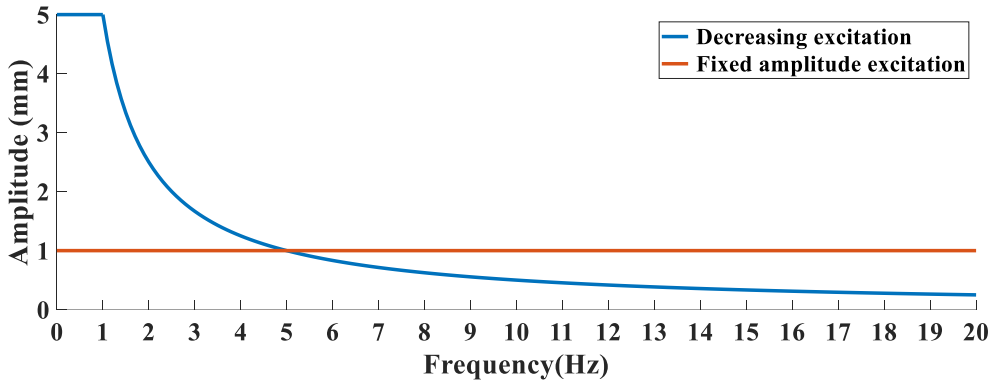

Figure 4.11 Fixed– and decreasing-amplitude excitations against frequency

While using the decreasing-amplitude excitation, a relatively high displacement is applied in the low-frequency range to actuate all the component of the tested pantograph; to allow the test to run through the entire frequency range of interest, the excitation amplitude decreases as the frequency of excitation increases. This decreasing-amplitude excitation approach can be considered as a combination of the various fixed-amplitude excitations. The FRF of the pantograph head obtained using this decreasing-amplitude excitation is shown in Figure 4.12.

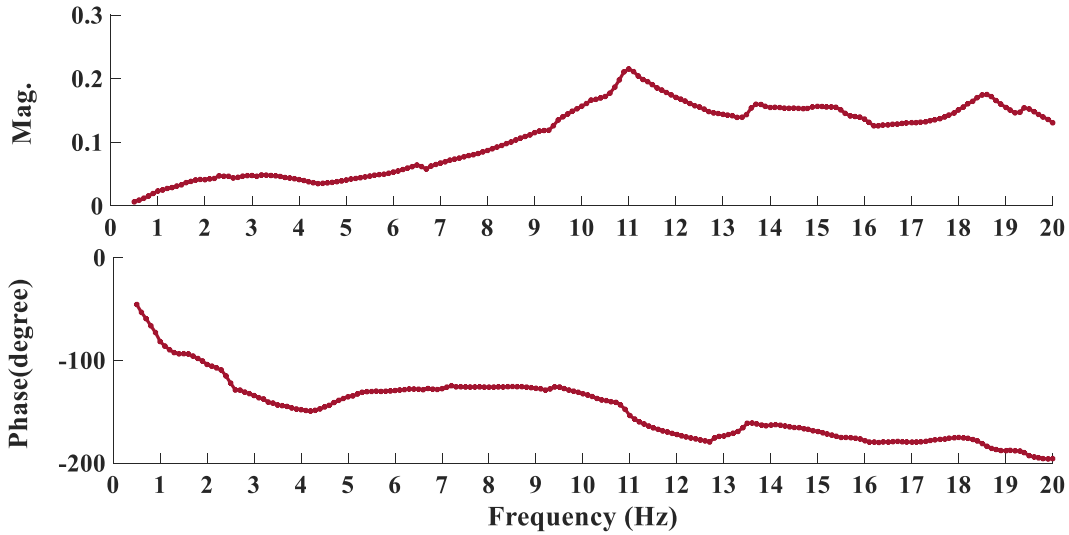

Figure 4.12 Head FRF under decreasing excitation. Input: contact force, output: acceleration of the head.

The FRFs measured using different excitations show that the frequency-response tests with an excitation amplitude of 0.3 and 0.5 mm are able to cover the entire frequency range of interest, and, excite the lightly damped resonance at 4.3 and 4.2 Hz, respectively. Moreover, the phase profiles under these the two excitation levels start from zero; meanwhile, the gradient of this

phase shift is steep. The first resonance of the FRFs collected using the 1 mm and higher excitation levels are successively more heavily damped; and therefore, the resonances cannot be observed clearly from the magnitude profiles, but they can from the phase angle profiles. Furthermore, the phases of these FRFs start at negative values. The frequency ranges can be covered by different excitation levels and the corresponding time taken for the tests are shown in Table 4.4.

Table 4.4 Excitations of frequency-response tests applied in this work

Excitations	Decreasing	0.3 mm	0.5 mm	1 mm	2 mm	5 mm
Frequency range (Hz)	0.5–20.0	0.5–0.0	0.5–20.0	0.5–12.0	0.5–9.8	0.5–7.5
Test time (s)	1138.5	1138. 5	1138. 5	985.7	925.2	845.4

4.3.2.3 Feasibility study of the FRFs for pantograph fault diagnosis

Measurement of frequency-response is meant to explore the variation in pantograph dynamics caused by degradation, changes or faults; and, consequently to realise pantograph fault diagnosis. In order to check the applicability of this method, frequency-response tests were carried out on new and pre-overhaul pantographs of the same type. As the proposed decreasing-amplitude excitation is a combination of the various fixed-amplitude excitations, it is used to verify the feasibility of the frequency-response test for pantograph fault detection. The FRFs of the head of the two pantographs are shown in Figure 4.13; the blue and red profiles represent the FRFs of the new and pre-overhaul pantographs, respectively.

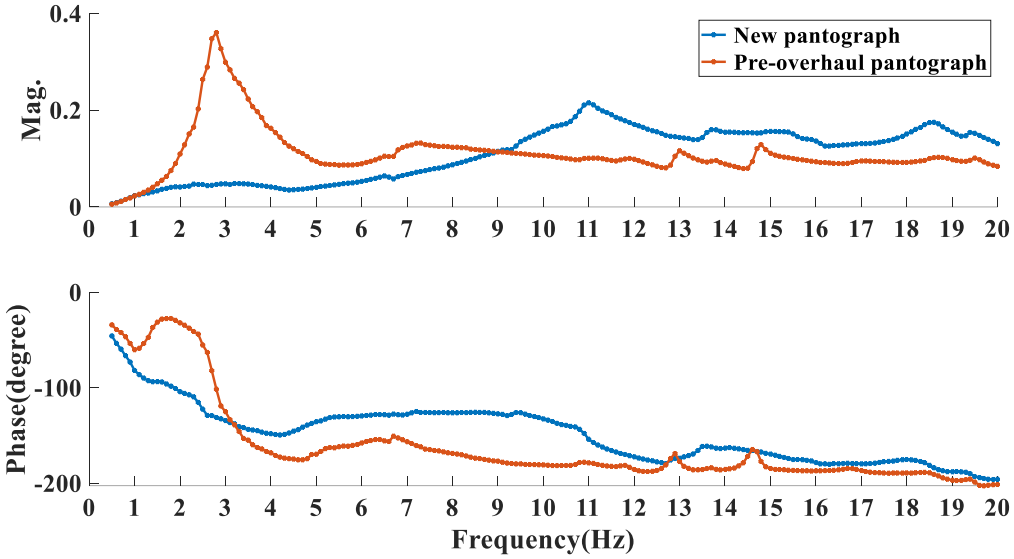

Figure 4.13 Head FRFs: new and pre-overhaul pantograph. Input: contact force, output: acceleration of the head.

In Figure 4.13, a lightly damped resonance shows up on the FRF profile of the pre-overhaul pantograph (red) at 2.8 Hz; no other obvious resonance appears at higher frequencies. The new pantograph only produces a heavily damped resonance at around 3.0 Hz. The differences show that the degradation and changes to the pantograph can be represented in the FRFs. Therefore, the frequency-response test is able to be used to detect the condition of a pantograph.

4.3.3 Feature extraction in the frequency domain

4.3.3.1 System identification in the frequency domain

On the FRF profiles, the critical traits that characterise the mode of vibration include resonant frequency and peak, damping ratio, and stiffness etc. (Ogata, 1970). The dynamic behaviour of the pantograph is also characterised by these features. In order to extract these features to represent the health status of the pantograph, a system identification approach is applied to process the FRF in the frequency domain. The lumped-mass models are used to reproduce the FRF measured using the test rig; an example of the FRF of a tested pantograph with a fault as shown in Figure 4.14. The critical traits can be worked out with identifying all the parameters of the lumped-mass model. In order to estimate the unknown parameters, a curve fitting technique is adopted by minimising the difference between the experimental and estimating

FRF. To represent the dynamic behaviour of the pantograph more accurately, the magnitudes and phase angles of the points close to the resonant peak have more heavily weighted.

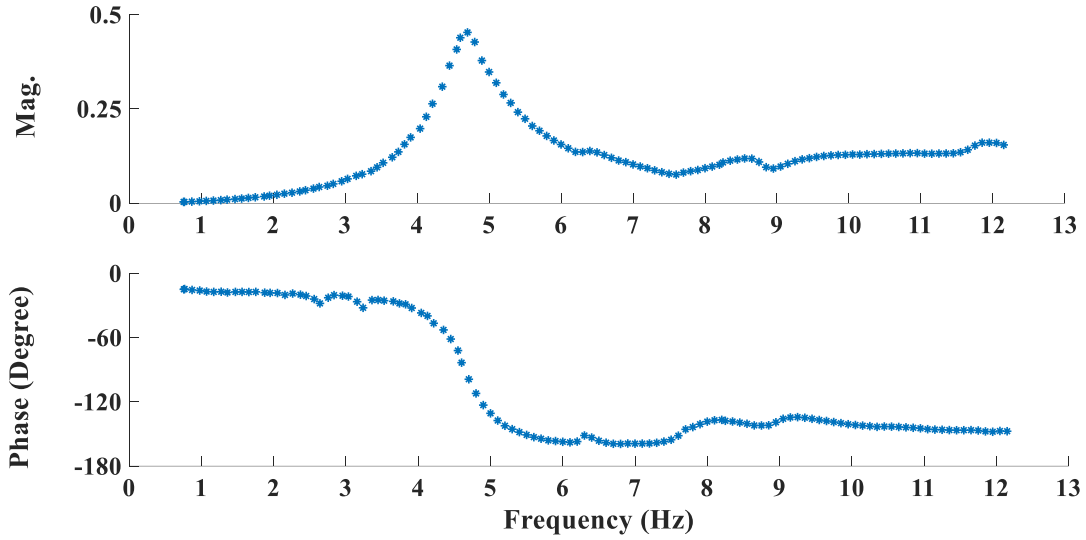

Figure 4.14 Bode plot of a pantograph

To work out the unknown parameters of a lumped-mass model that is able to reproduce the measured FRF of the pantograph, both the magnitude and phase angle curves need to be matched. The difference between the FRF of the estimated lumped-mass model and the actual measurement is minimised using the weighted least squares algorithm (Kerschen et al., 2006). The points closer to the resonant peak have relatively greater weights; and the points far from the resonance have lesser weights (Fessler, 1994). Therefore, the objective function can be written as Equation (4.5):

$$J = \sum_{i=1}^{n} w_i (y_i - \hat{y}_i)^2 \tag{4.5}$$

where y_i and $\hat{y}_i$ is the actual measurement and estimated output at the i^{th} point, respectively; and w_i is the weight of this point.

In Equation (4.5), the weight, w_i, follows a Gaussian distribution.

$$w(i|N, \sigma^2) = \frac{1}{\sqrt{2\pi\sigma^2}} e^{-\frac{(i-N)^2}{2\sigma^2}} \tag{4.6}$$

where N^{th} point is the resonant peak.

To reproduce this mode of vibration, 5 points (each point representing 0.1 Hz step) on the left and right of the resonance peak respectively are considered have more weights.

The total objective function to be minimised is the sum of the residuals of the magnitude and the phase,

$$J_{Total} = J_{mag.} + J_{phase} \tag{4.7}$$

where the phases are in radians.

To avoid the local minimum being found instead of the global minimum, a Monte Carlo algorithm is adopted to initialise the minimisation process (Gilks et al., 1995). By minimising the final objective function, all the parameters in the lumped-mass model are found.

4.3.3.2 Application I

The above system identification method is applied to estimate a lumped-mass model that reproduces the FRF in Figure 4.14. As only one resonance shows up, a one-mass model is able to reproduce the FRF in theory. However, as the actual measurement contains nonlinearities, in order to achieve better matching between the FRFs of the estimation model and experimental result, one– and two-mass models were both used. The state-space function of a one-mass model is simple and not given here. The differential function of a two-mass model is:

$$\begin{bmatrix} m_2 & 0 \\ 0 & m_1 \end{bmatrix} \begin{Bmatrix} \ddot{x}_2 \\ \ddot{x}_1 \end{Bmatrix} + \begin{bmatrix} C_2 & -C_2 \\ -C_2 & C_2 + C_1 \end{bmatrix} \begin{Bmatrix} \dot{x}_2 \\ \dot{x}_1 \end{Bmatrix} + \begin{bmatrix} k_2 & -k_2 \\ -k_2 & k_2 + k_1 \end{bmatrix} \begin{Bmatrix} x_2 \\ x_1 \end{Bmatrix} = F(t) \tag{4.8}$$

where x_1 and x_2 are the displacement of the bottom and top mass, respectively.

The state-space function of the system with single input and single output can be written as:

$$\dot{\boldsymbol{x}}(t) = \boldsymbol{A}\boldsymbol{x}(t) + \boldsymbol{B}u(t)$$

$$y(t) = \boldsymbol{C}\boldsymbol{x}(t) + \boldsymbol{D}u(t) \tag{4.9}$$

Referring Equation (4.9), the state-space function of the two-mass model that considers the contact force and acceleration of the pantograph head as the input and output can be described by Equation (4.10):

$$\begin{bmatrix} \ddot{x}_2 \\ \dot{x}_2 \\ \ddot{x}_1 \\ \dot{x}_1 \end{bmatrix} = \begin{bmatrix} -c_2/m_2 & -k_2/m_2 & c_2/m_2 & k_2/m_2 \\ 1 & 0 & 0 & 0 \\ c_2/m_1 & k_2/m_1 & -(c_1+c_2)/m_1 & -(k_1+k_2)/m_1 \\ 0 & 0 & 1 & 0 \end{bmatrix} \begin{bmatrix} \dot{x}_2 \\ x_2 \\ \dot{x}_1 \\ x_1 \end{bmatrix} + \begin{bmatrix} 1/m_2 \\ 0 \\ 0 \\ 0 \end{bmatrix} F(t)$$

$$\ddot{x}_2 = [-c_2/m_2 \quad -k_2/m_2 \quad c_2/m_2 \quad k_2/m_2] \begin{bmatrix} \dot{x}_2 \\ x_2 \\ \dot{x}_1 \\ x_1 \end{bmatrix} + [1/m_2\,]F(t) \tag{4.10}$$

Therefore,

$$\boldsymbol{A} = \begin{bmatrix} -c_2/m_2 & -k_2/m_2 & c_2/m_2 & k_2/m_2 \\ 1 & 0 & 0 & 0 \\ c_2/m_1 & k_2/m_1 & -(c_1+c_2)/m_1 & -(k_1+k_2)/m_1 \\ 0 & 0 & 1 & 0 \end{bmatrix}$$

$$\boldsymbol{B} = [1/m_2 \quad 0 \quad 0 \quad 0]^T$$

$$\boldsymbol{C} = [-c_2/m_2 \quad -k_2/m_2 \quad c_2/m_2 \quad k_2/m_2]$$

$$\boldsymbol{D} = [1/m_2]$$

where m_2 is the mass of the pantograph head, 8.5 kg. This parameter is also applied in the one–mass model estimation. The unknown parameters, $\theta = [m_1, k_1, k_2, c_1, c_2]^T$, are to be estimated. The flowchart of the system identification procedure shows in Figure 4.15.

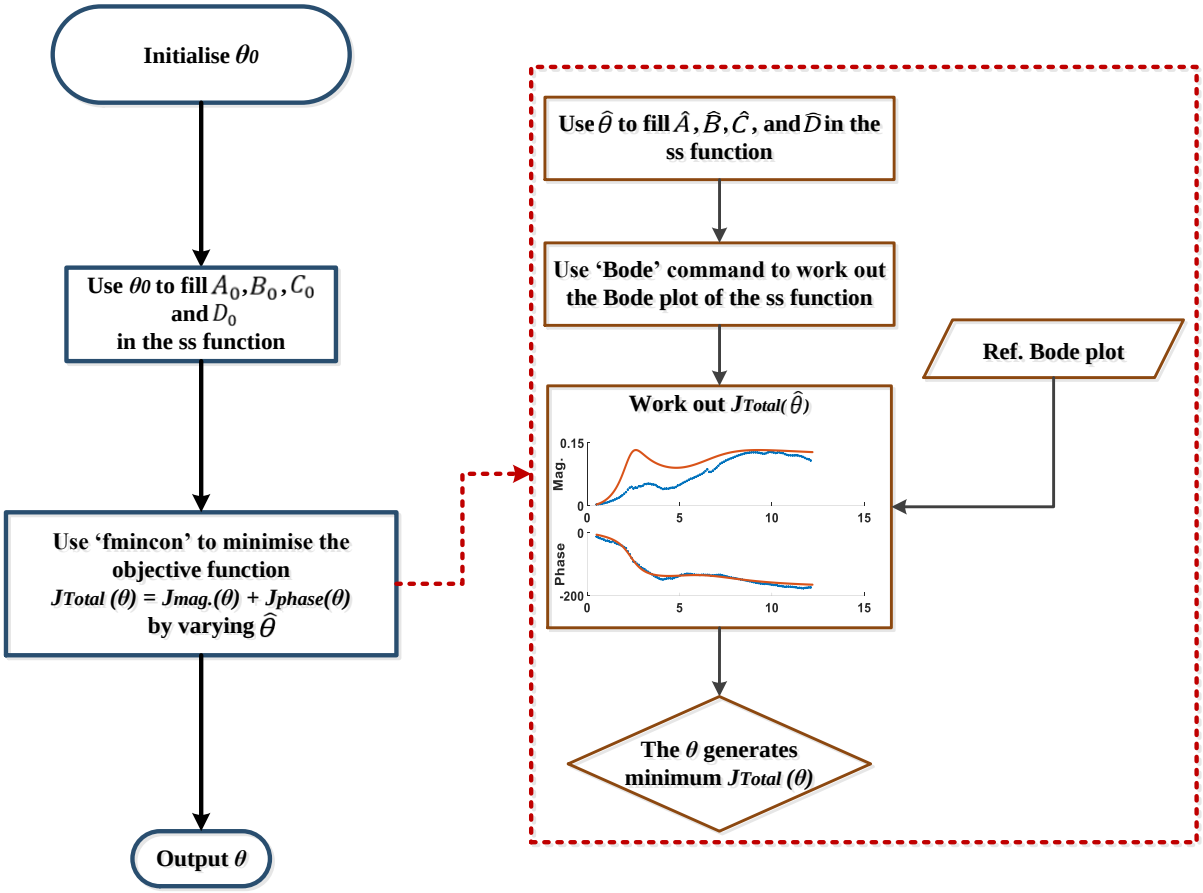

Figure 4.15 Procedure of system identification using the experimental data collected by frequency-response tests.

System identification to estimate the unknown parameters uses the command 'fmincon' in MATLAB Optimisation Toolbox to minimise the objective function described by Equation (4.7); internally, the command 'Bode' in MATLAB Control Toolbox was used to produce the FRF of the system estimated. The differences between the estimated and experimental Bode plot are described by the objective function. The values of the parameters in the θ that generates the minimum J_{Total} are the final values of m_1, k_1, k_2, c_1, and c_2.

The FRF and the output of the estimated one– and two-mass models that reproduce the FRF of a pantograph with a fault are shown in Figure 4.16. The results demonstrate that the two-mass model is able to reproduce the measured FRF much better than the one–mass model. The estimated parameters of the two-mass model are provided in Table 4.5. Note that the resulting

linear model fits the results only where the excitation level follows the prescribed amplitude profile – the linear model does not fit the behaviour for different amplitude profiles.

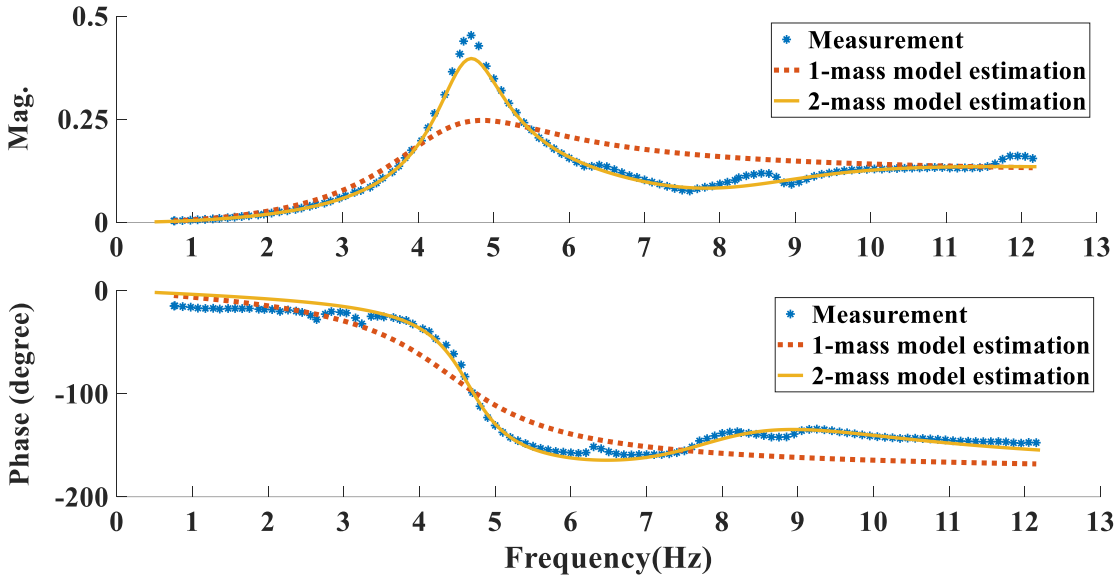

Figure 4.16 Comparison of FRF measurement and estimation. Input: contact force, output: acceleration of the head.

Table 4.5 Parameter estimation for a 2-mass model

Parameters	m_1 (kg)	m_2 (kg)	k_1 (N/m)	k_2 (N/m)	C_1 (Ns/m)	C_2 (Ns/m)
Values	23.9	8.5	40060.5	10923.3	73.6	180.4

Following this, fault detection can be carried out by comparing the parameters in the lumped-mass models estimated using the FRFs obtained in different conditions but using the same excitation amplitude profile. The use of the FRF for fault detection and diagnosis is continued in Chapter 6.

4.3.3.3 Application II: comparison to the model identified by RSSB

In 2016, RSSB identified a lumped-mass model for a healthy Brecknell Willis high-speed pantograph of the same type as the ones tested in this work by using the DB test rig that mentioned in Chapter 2 (Conway, 2016). All the parameters for the three-mass model were

worked out. However, the excitation amplitude used to obtain this lumped-mass model is not clarified in the report.

In this section, the system identification method applied in §4.3.3.2 is applied to estimate the 3-mass models that reproduce the experimental FRFs obtained using 0.3 and 1 mm excitations (blue and yellow curves in Figure 4.10). The parameters for the three-mass models are detailed in Table 4.6.

Table 4.6 Parameter comparison of the 3-mass models

	m (kg)			k (N/m)			C (Ns/m)		
	m_1	m_2	m_3	k_1	k_2	k_3	C_1	C_2	C_3
RSSB testing	3.42	7.0	8.6	26.3	7800	3000	39.4	0	5.0
0.3 mm excitation	19.1	1.9	8.5	26148	31259	32009	0.01	0.01	904
1 mm excitation	14.8	3.9	8.5	8930	16226	6103	259	16.8	732

The FRFs for the three lumped-mass models are shown in Figure 4.17. The blue triangles and the yellow stars represent the FRFs of the pantograph measured using 0.3 and 1 mm excitations, respectively; and the red and purple solid lines are the output of the estimated three-mass models. The green solid line is the output of the three-mass model identified by RSSB.

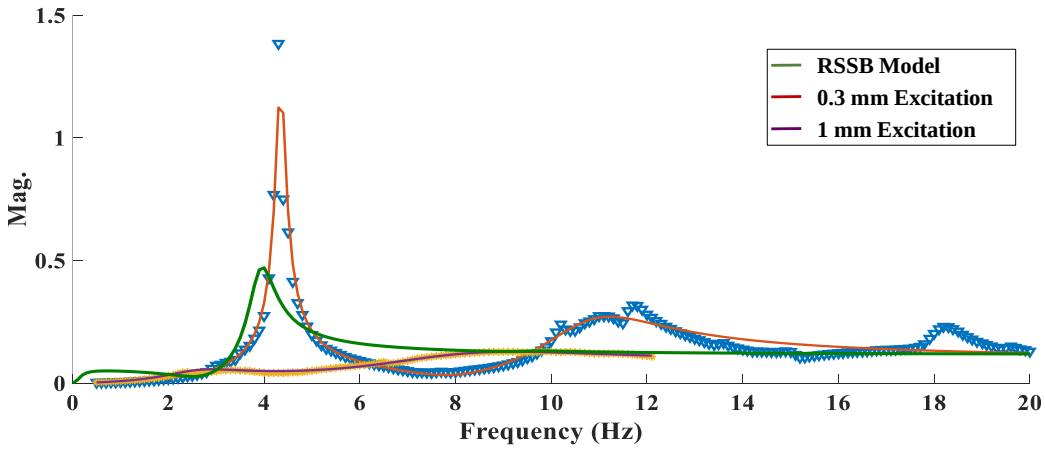

Figure 4.17 FRFs of the three-mass models. Input: contact force, output: acceleration of the head.

In Figure 4.17, the RSSB model (green line) generates two resonances. The 1st resonance is around 0.2 Hz. According to the standard BS EN 50317:2012 (CENELEC, 2012), the frequency of interest for measuring the dynamic behaviour of the pantograph is 0.5 – 20 Hz. At the frequencies lower than 0.5 Hz, the pantograph cannot be accelerated significantly. Therefore, the 1st resonance shown on the output of the RSSB model does not represent a sensible behaviour of the pantograph. The 2nd resonance of the RSSB model is at around 4.0 Hz that is close to the 1st resonance that appears on the red line. At higher frequencies, the RSSB model does not generate any clear resonance. Accordingly, the 3-mass RSSB model generates one representative resonance at around 4.0 Hz. As the pantograph is a nonlinear system, the FRF varies with different excitations. Therefore, the parameters for the lumped-mass models that reproduce the experimental FRFs obtained using various excitations can be significantly different. Furthermore, RSSB report does not illustrate the amplitude of the excitations that applied to obtain the FRFs of the tested pantograph. As there is not enough information in the RSSB report, it is difficult to explain the reasons for the differences in the parameters in Table 4.6.

Accordingly, in order to detect and diagnose various pantograph faults or changes, only the parameters for the lumped-mass models that reproduce the FRFs measured using the same excitation amplitude profile can be compared. As mentioned in Chapter 2, for a lumped-mass model, only the mass of the top block and the spring and damper that connect to the top mass have a relationship to the physical quantities of the pantograph (Antunes, 2012). The mass of the top block is the actual mass of the pantograph head that can be measured accurately. By comparing the stiffness and damping coefficient of the top mass for the lumped-mass models, pantograph fault detection and diagnosis can be realised.

4.4 Changing-gradient test

4.4.1 Introduction to the changing-gradient test

The third test applied in this work to realise pantograph fault detection and diagnosis is a novel changing-gradient test, also called a 'V' test. The purpose of this test is inspired by the pantograph response to the stiffness variation of the contact wire. As mentioned in Chapter 2, as both ends of a span are clamped at the masts, the stiffness of the contact wire near the masts is at its maximum, while, in the middle of a span it is at its minimum (Wu and Brennan, 1999). The stiffness of the catenary is in the range of 2200 to 6200 N/m (Bruni et al., 2015). The pantograph is only allowed to lift the contact wire at the supporting masts around 48 to 55 mm and 55 to 65 mm at operating speeds of 250 and 300 km/h, respectively (CENELEC, 2002). At the operating speeds lower than 250 km/h, the allowed uplift at the masts is less. As the pantograph slides along the contact wire, the variation in the stiffness produces periodic excitations to the pantograph head that results in fluctuations in contact force.

The frequencies of the oscillations resulted by the masts and droppers can be described as:

$$f_{Mast} = v/l_{Mast}$$

$$f_{Dropper} = v/l_{Dropper} \tag{4.11}$$

where v is the operational speed; l_{Mast} and $l_{Dropper}$ are the length of a span and distance between two adjacent droppers, respectively.

In line with EN 50318, the length of a span can be designed as 60 m in the UK, and 9 droppers are used within a span (CENELEC, 2002). Assuming that the space between two adjacent droppers is equal, that is 6.67 m. If the operational speed of the train is 180 km/h, the frequencies of oscillations resulted by the masts and droppers are 0.8 and 7.5 Hz, respectively. These frequencies increase as the operational speed increases. Therefore, the interaction

between the pantograph and catenary is affected by the operational speed significantly. At relatively low operating speeds, the pantograph is able to absorb the oscillation and maintain the contact with contact wire; however, at high speeds, the high-frequency oscillation propagates along the contact wire that differs both the interaction between the pantograph and catenary and the behaviour of the pantograph from those at lower speeds (Zhang et al., 2011).

While the train operates at walking speed, a relatively constant uplift force can be supplied by the pneumatic actuator; therefore, the pantograph lifts the contact wire to different levels with respect to the stiffness of the wire. As the pantograph approaches a mast point, the stiffness of the contact wire increases that forces the pantograph to travel downwards. After the pantograph passes the mast, it extends increasingly to the next lowest stiffness point. Accordingly, the vertical displacement of the pantograph head is equivalent to a 'V' shape, and the lowest position is at the mast. The vertical displacement of the pantograph head is plotted in red dash line in Figure 4.18. The high stiffness at the mast results in overshooting of the contact force, therefore contact loss is more likely (O'Connor et al., 1997). Accordingly, exciting the pantograph using a 'V'–shape profile can reproduce the pantograph response to the masts at low operational speeds.

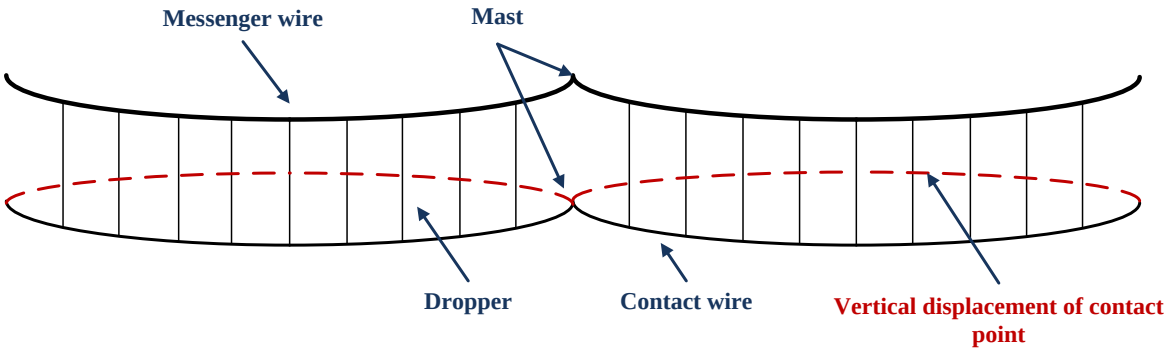

Figure 4.18 Displacement of the contact point at low operational speeds

If the train operates at other speeds, loss of contact is more likely near the middle of a span. A benchmark was held that concerns the pantograph-catenary interaction at the operational speed

of 320 km/h (Bruni et al., 2015). The contact force and the vertical displacement of the pantograph-catenary contact point as a function of distance were calculated using different simulation tools and are shown in Figure 4.19 *a* and *b*, respectively. The vertical dashed lines are the locations of the masts.

Figure 4.19 shows that the contact force between the pantograph and contact wire is variable. As the pantograph approaches a mast, the contact force increases; meanwhile, the vertical displacement of the contact point increases to the highest position then drops down. The variation in the vertical displacement can be reproduced by the left half of the 'V'–shape excitation. After the pantograph passes the mast, the displacement of the contact point and contact force decrease and reach the lowest values between two masts. The low contact force is more likely to result in contact loss. Therefore, the response of the pantograph to this 'V'–shape excitation can be studied in this work using the novel changing-gradient test.

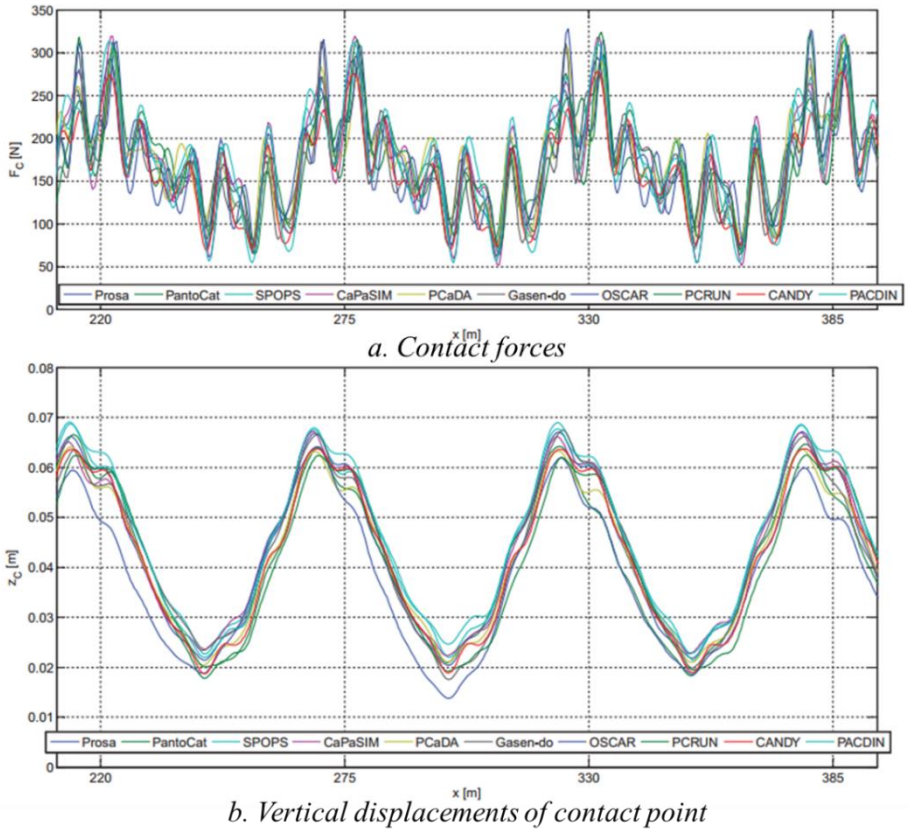

Figure 4.19 *a*. Contact force, *b*. vertical displacement of the contact point at 320 km/h (Bruni et al., 2015)

Features that characterise pantograph health conditions are extracted from the measurement of the changing-gradient test using system identification in the time domain; and a deep learning technique, a sparse stacked autoencoder, is also applied to classify the measurements corresponding to various pantograph faults.

4.4.2 Design of the changing-gradient test

The changing-gradient test aims to reproduce the scenario of the pantograph changing direction from downwards to upwards motion where loss of contact is most likely. While a 'V'–shaped excitation was applied to the tested pantograph, the contact force was measured during the test. The excitation speed was one of 50, 100, 200, 300, 400 or 500 mm/s. For each individual test, one excitation speed was applied; the excitation profiles with respect to time are shown in Figure 4.20, apart from the 50 mm/s excitation which is too long to fit on the figure. In order to avoid contact loss and extra oscillation in the contact force, the highest excitation is selected as 500 mm/s, and the reversing corners are smoothed over 0.5 s to avoid overshoot.

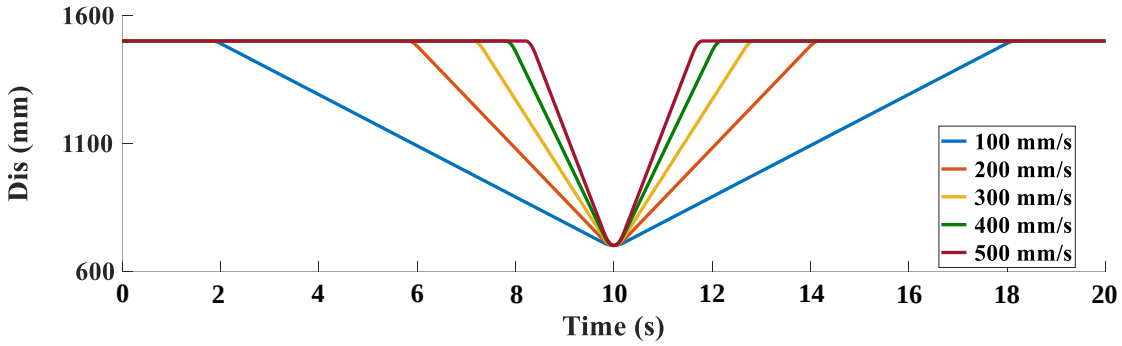

Figure 4.20 Excitation profiles of changing-gradient Test

The excitation always begins at a constant height for some time, then the excitation bar presses the pantograph in a downwards direction at the required speed. When the pantograph has moved down 800 mm, the excitation changes direction until the original height has been reached. The excitation height of the changing-gradient was chosen in the range of 700 to 1500 mm, but can be applied over other ranges. The hysteresis test height range was 330 to 2320 mm, but the excitation profiles of the changing-gradient test are a smaller range of those of the hysteresis

test at the same speed. The changing-gradient focuses on the performance of the pantograph to a sudden change in direction. The time taken for the changing-gradient tests at different excitation speeds is shown in Table 4.7.

Table 4.7 Time taken for changing-gradient test

Excitation speed (mm/s)	50	100	200	300	400	500
Time (s)	32.3	16.4	8.4	5.7	4.4	3.6

4.4.2.1 Data smoothing with spline functions

As the sensor cables are located near to those of the three-phase servo motor, the raw signals carry noise. The measurements obtained from the changing-gradient test are used to extract features in the time domain; therefore, the signals need to be smoothed without changing the phase and the oscillation trend. A smoothing spline is used as a commonly recognised efficient method for approximating highly dynamic shapes (Craven and Wahba, 1978). The spline functions are formed by joining piecewise polynomials with boundary constraints at fixed breaks. On an interval [a, b], supposing that $l+1$ jointing breaks have been specified as t_1, t_2,$\cdots$,t_{l+1} , and meet the constraint of $a = t_1 < t_2 < \cdots < t_{l+1} = b$. These breaks (knots) divide the original line into l pieces. A spline function of degree n can be defined in the form of piecewise polynomials (Ahlberg et al., 1967):

$$S(x) = P_i(x), x \in (t_i, t_{i+1}) \tag{4.12}$$

where

$$P_i(x) = \sum_{k=1}^{n} p_k^i (x - t_i)^{k-1}, i = 1, 2 \cdots, l \tag{4.13}$$

and p_k^i is the local polynomial coefficient (Gu, 2013). In this work, cubic polynomials were used to smooth the original signals using MATLAB. An example of a measurement smoothed

by a cubic spline function is shown in Figure 4.21, the yellow and red curves are the raw and filtered signals, respectively. The smoothed signal was used for pantograph system identification to help extract fault features. In this work, all signals obtained were smoothed using the spline function.

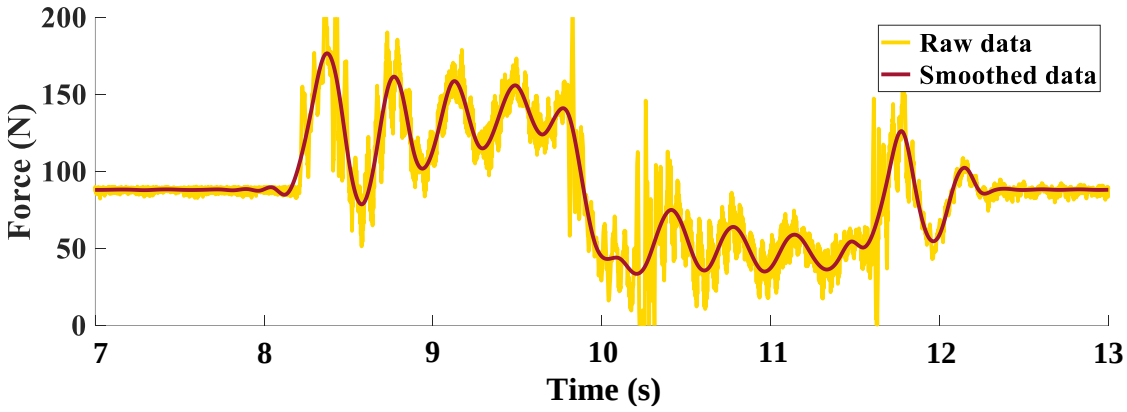

Figure 4.21 Raw and spline function smoothed signals

4.4.3 Changing-gradient test for fault diagnosis

The proposed novel changing-gradient test is used to realise pantograph fault detection and diagnosis assuming that the response varies with the health conditions of the pantograph. In order to ensure that this approach is able to detect faults or changes in the pantograph, the changing gradient tests were carried out in the normal and faulty condition, respectively. The excitation speeds of the tests were varied from 50 to 500 mm/s. An example of the contact forces measured using the novel test in the two conditions at a speed of 500 mm/s are shown in Figure 4.22.

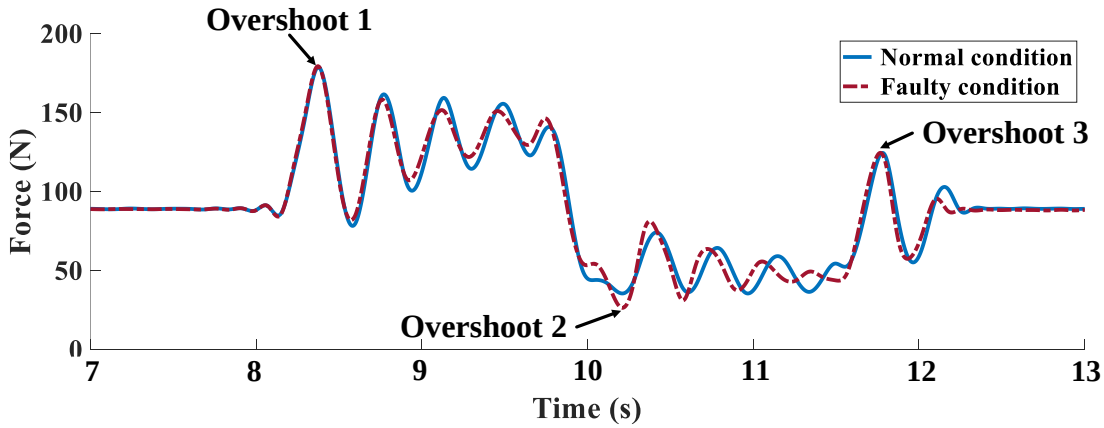

Figure 4.22 Results of changing-gradient tests at 500 mm/s: normal and faulty condition

In Figure 4.22, the two measurements have visible differences in the time domain. The differences include the overshoots, oscillation frequency and damping ratio. This particular test demonstrates that the changing-gradient test may be useful to detect faults or changes that happen to the pantograph.

4.4.4 Feature extraction in the time domain

The overshoots of the contact force can be read directly from the figure. To extract the values of the oscillation frequency and damping ratio, a system identification method is applied to identify parameters for a lumped-mass model from the experimental data. During the changing-gradient test, the tested pantograph was pressed downwards from a constant height at the required speed to the predetermined lowest point. Following this, the pantograph goes up to the original height at the same speed. The excitation speed increases or decreases to the required value over 0.5 s. As the excitation reverses direction in the lowest position, the pantograph response to the descent and ascent of the 'V'–shape excitation were analysed separately. Therefore, the result of a changing-gradient test can be considered as two step responses (step in the speed). The system identification was carried out to reproduce the experimentally–obtained step responses by estimating lumped-mass models. The input and output of the estimation system are considered as the contact force and speed, respectively. Similar to the system identification approach described in §4.3.3, the lumped-mass model was estimated by

matching the experimental signal with the output of the estimated model; however, in this case, the curve fitting was carried out in the time domain.

A lumped-mass model can be described by the transfer function in Equation (2.2) in Chapter 2. Given the step–response of a system, the transfer function can be estimated. As the pantograph is a nonlinear system, a higher-order model may be used while reproducing the experimental data measured for different pantograph health conditions. The dynamic behaviour of a higher-order spring-mass model can be described as the sum of the responses of several first– and second-order systems, as described in Equation (2.3) in Chapter 2. The dynamic behaviour of a higher-order system is dominated by the poles that are nearest to $j\omega$ axis (Schilders et al., 2008). The oscillation frequency and damping ratio can be worked out using the dominant poles. In order to estimate the transfer function, MATLAB System Identification Toolbox was applied with the assumed number of the poles of the estimated system, N_{pole}, varied from 2 to 10, and the number of zeros varied from 0 to N_{pole} The system identification is carried out with MATLAB using the System Identification Toolbox, the procedure as shown in Figure 4.23.

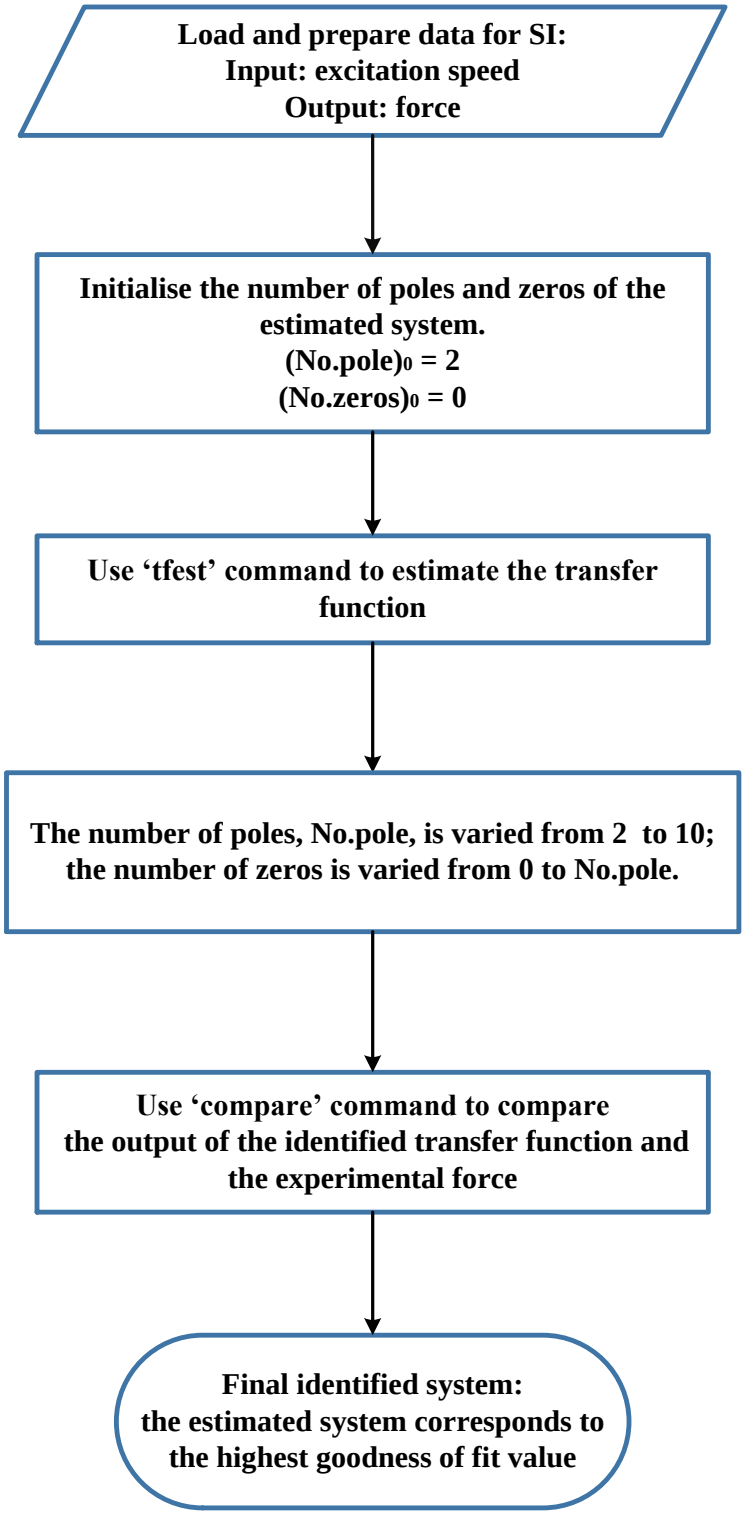

Figure 4.23 Procedure of system identification using the data obtained by the changing-gradient tests

In this section, the system identification method is applied to reproduce the raw and smoothed signals in Figure 4.21. The input and output for the system identification process are the excitation speed and the contact force measured, respectively. The signal is divided into two

parts: (i) the response under descent excitation (in Figure 4.24 and Figure 4.25), and (ii) that under ascent excitation (in Figure 4.26 and Figure 4.27). In these figures, the raw data and its corresponding step response estimation are represented by black and blue solid lines, respectively, and the smoothed data and its corresponding step response are plotted by black dash line and red dot line respectively. The responses of the estimated models using the raw data during descent and ascent (in Figure 4.24 and Figure 4.26, respectively) are not in good agreement with the experimental data, and the fitness are 58.49% and 49.24%; meanwhile, the output of the estimated models using the smoothed data (in Figure 4.25 and Figure 4.27) are in good agreement with the original data with the fitness of 95.09% and 98.64% during descent and ascent excitations, respectively. Therefore, in order to extract the oscillation frequency and damping ratio that represent the dynamic behaviour of the pantograph, the smoothed data is preferred to use for the system identification process.

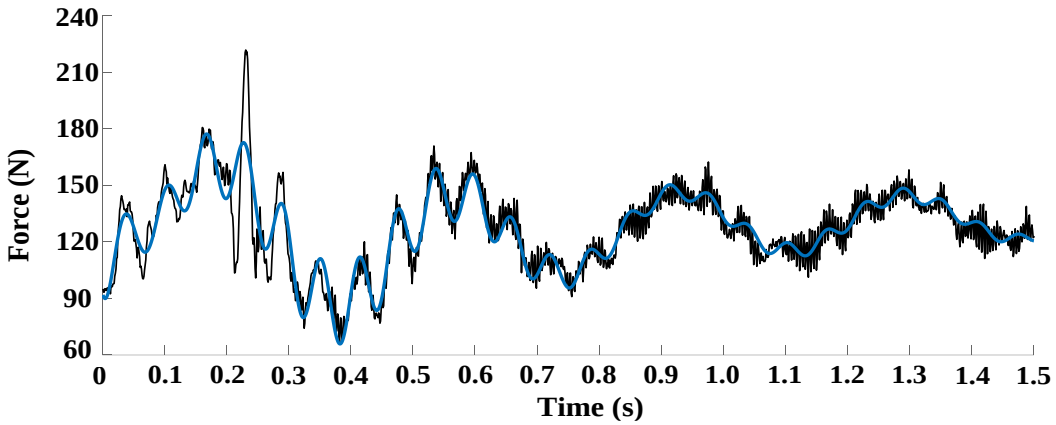

Figure 4.24 Raw data and the corresponding estimated output during descent excitation. (Input of the estimated model: excitation speed, output: contact force)

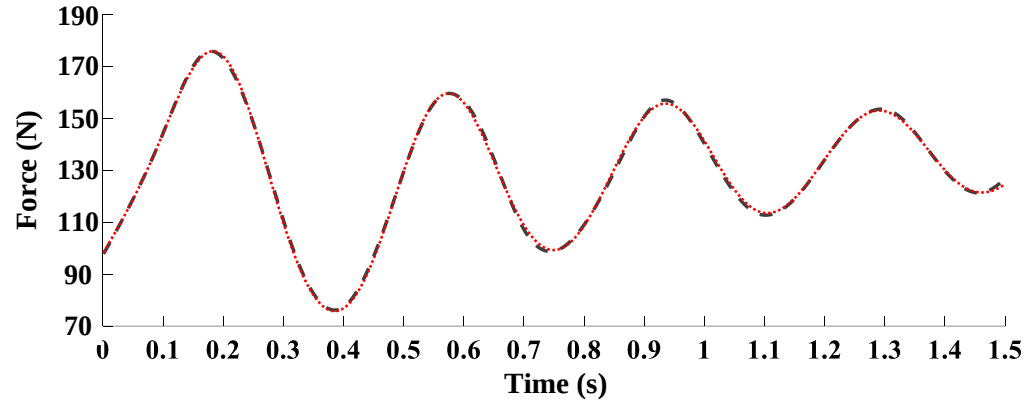

Figure 4.25 Smoothed data and the corresponding estimated output during descent excitation. (Input of the estimated model: excitation speed, output: contact force)

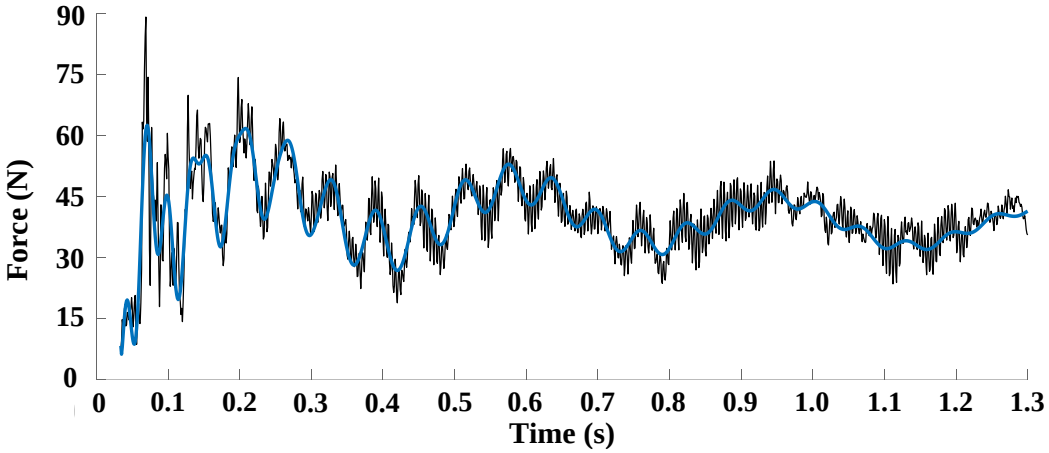

Figure 4.26 Raw data and the corresponding estimated output during ascent excitation. (Input of the estimated model: excitation speed, output: contact force)

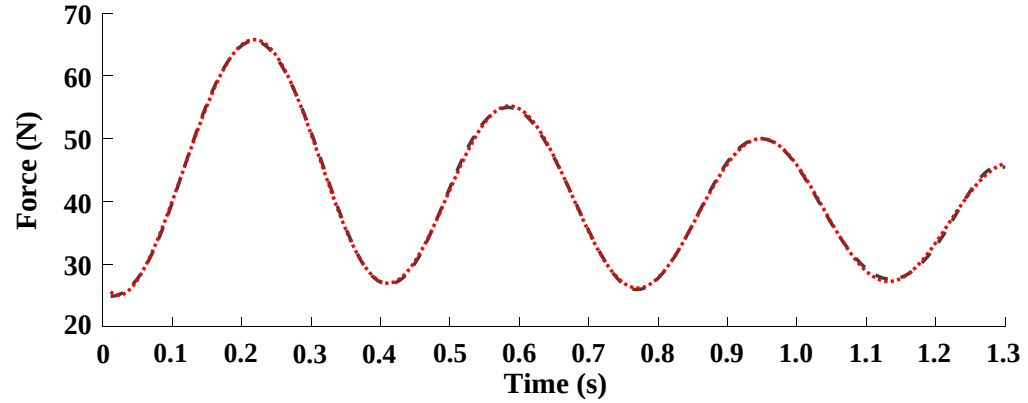

Figure 4.27 Smoothed data and the corresponding estimated output during ascent excitation. (Input of the estimated model: excitation speed, output: contact force)

The above system identification method is also applied to estimate the transfer function of the lumped-mass model that is able to reproduce the faulty signal in Figure 4.22 (red dash line).

The comparison of some features extracted from the healthy and faulty signals shown in Figure 4.22 is detailed in Table 4.8.

Table 4.8 Features extracted from the measurements collected by the changing-gradient test

Condition	Descent excitation			Ascent excitation			
	Damping ratio	Oscillation frequency (Hz)	Over-shoot 1	Damping ratio	Oscillation frequency (Hz)	Over-shoot 2	Over-shoot 3
Normal	0.07	2.9	177.9	0.08	3.4	25.3	125.2
Faulty	0.05	2.8	177.5	0.03	2.8	34.4	125.5
Difference	28.57 %	1.7 %	0.22 %	62.5 %	19.4 %	36.0 %	0.2 %

The results demonstrate that the pantograph response to the 'V'–shape excitation varies with its health condition. The features extracted from the signal that measured under normal condition were considered as references. By comparing the features extracted from other condition to the references, faults can be detected and diagnosed. Application of this method is continued in Chapter 7.

4.4.5 Fault classification using a deep learning method

In some cases, the signals obtained using changing-gradient test with different pantograph faults or changes are similar in the time domain. The oscillation frequencies and damping ratios extracted from the experimental data cannot distinguish, detect and diagnose different types of faults or changes. Given this, a deep learning algorithm, a stacked sparse autoencoder (SSAE), was adopted to classify and diagnose various faults or changes in the pantograph. Compared to the conventional feature excitation approach, the main advantage of the SSAE is that it can automatically learn features from the original experimental data without data pre-processing and selecting features (Zhao et al., 2017).

4.4.5.1 Introduction of stacked sparse autoencoder (SSAE)

- **Autoencoders**

An autoencoder is a neural network that is trained to minimise the discrepancy between the input and its reconstruction (Hinton et al., 2012). It was firstly introduced by Rumelhart et al. (1986). Autoencoders were traditionally used for dimensionality reduction or feature learning (Goodfellow et al., 2016). The training process of the autoencoder is based on optimisation of the cost function that evaluates the error between the actual input and reconstructed output. Autoencoders have the ability to extract good features from the input data thanks to their deep architectures. Shallow architecture has very few layers of compositions, for example, linear models and one hidden layered neural network. Compared to a shallow architecture, a deep architecture with more hidden layers is able to represent higher-order features more accurately (Verma et al., 2013). Previous related studies have shown that deep architecture is capable of representing a highly varying function with many nonlinearities, producing tiny errors (Ahmed et al., 2015, Jia et al., 2016).

An autoencoder is a deep network with several hidden layers, where the nonlinear transformation of the previous layer is computed. Assuming that an autoencoder has a hidden layer h that describes an internal representation code used to reproduce the input. The network of the autoencoder can be decomposed into two parts: an encoder function $h = f(x)$ and a decoder, $r = g(h)$, that produces a reconstruction (Goodfellow et al., 2016). The general structure of an autoencoder is shown in Figure 4.28.

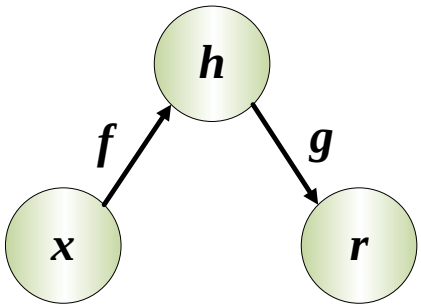

Figure 4.28 General structure of an autoencoder

A detailed structure of an autoencoder network with one hidden layer *h* is shown in Figure 4.29.

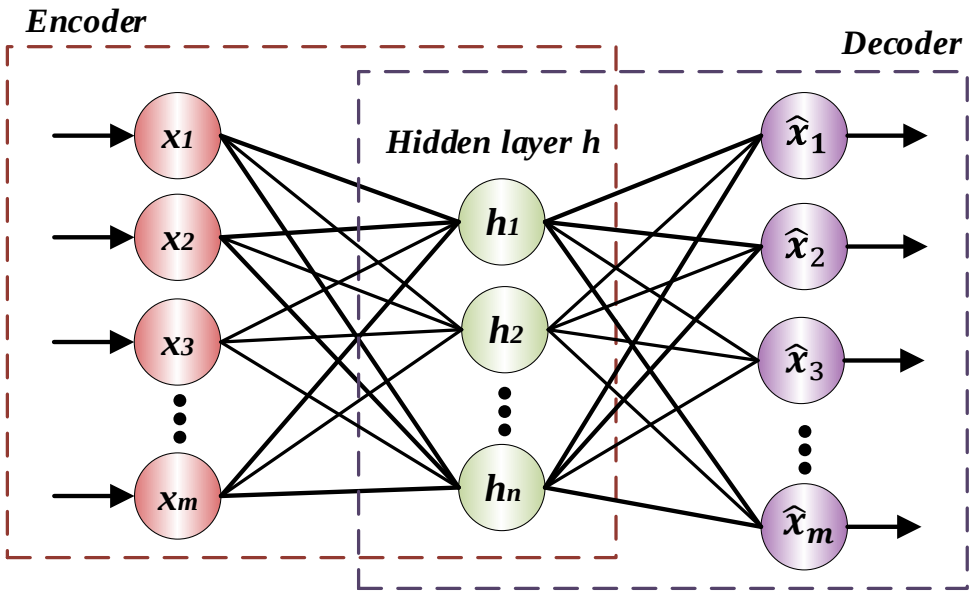

Figure 4.29 Structure of an autoencoder network with one hidden layer *h*

In the previous sections, the conventional system identification techniques extracted the features by specifying them in advance, which is highly dependent on prior signal processing and feature selection. The advantage of an autoencoder is that it is able to extract the features from the raw data and then classify the experimental data without predefining any features (Jia et al., 2016, Khan and Yairi, 2018). Therefore, various faults or changes can be classified and diagnosed by designing the structure and parameters of the autoencoder network properly. An overview of fault diagnosis by the conventional approach and the deep learning algorithm is shown in Figure 4.30 *a* and *b*, respectively.

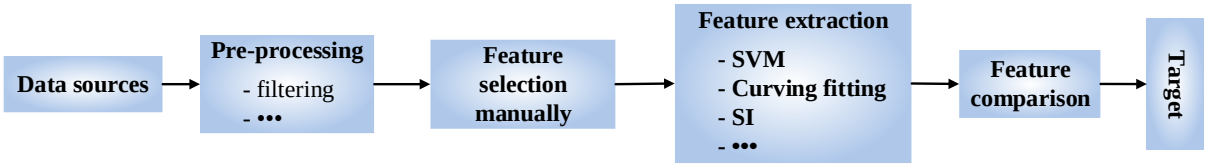

a. Conventional fault diagnosis method

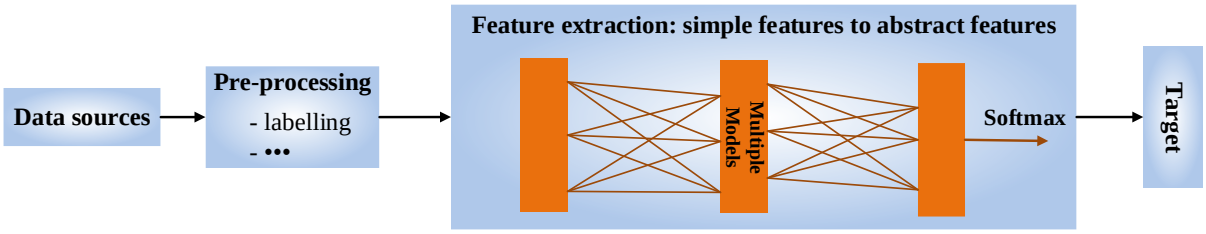

b. Deep learning algorithm

Figure 4.30 Procedure overview: *a*. conventional fault diagnosis; *b*. deep learning.

- **Sparse autoencoder**

There are two motivations for sparse representations: (i) the evidence shows that neural activity in the brain seems to be sparse, which inspired the work of Olshausen and Field (1996) on sparse coding; (ii) the dense compressed representations of a traditional autoencoder tend to entangle information, whereas sparse representations are able to learn relatively sparse features and be used for a subsequent classifier (Ranzato et al., 2007). The autoencoders have some intrinsic problems, e.g. simply copying an input layer to a hidden layer; therefore, under some circumstances, it is not effective to extract useful features even though the reconstructed output is able to reproduce the input admirably (Vincent et al., 2010).

The sparse autoencoder is an extension of the autoencoder with introducing a sparsity penalty, $\Omega(h)$, into the autoencoder. Following this, the cost function of a sparse autoencoder can be described as:

$$L' = L\left(x, g\left(f(x)\right)\right) + \Omega(h) \tag{4.14}$$

where $h = f(x)$, and $g(h)$ is the output of the decoder, and $L\left(x, g\left(f(x)\right)\right)$ is the cost function of the conventional autoencoder.

The sparsity penalty is used to average the output-activation value of a neuron by controlling the numbers of 'active' and 'inactive' neurons in each hidden layer (Sun et al., 2016). When the output of a neuron is close to one (the highest value), the neuron is considered to be 'active'; if that of a neuron is close to zero (the lowest value), it is considered as 'inactive'. In practice, it is better to keep the neurons 'inactive', as a low output-activation value means that this neuron in the hidden layer fires in response to a small number of the training data. If each individual neuron focuses on responding to the features that are presented by this small training group, effective feature representations can be learned (Olshausen and Field, 1997). The sparsity penalty improves the behaviour of a conventional autoencoder to deal with more practical issues and already shows good results in fault classification for rotating machinery (Sun et al., 2016).

- **Stacked sparse autoencoder**

Previous related studies have shown that one of the efficient ways to learn features from high–dimensional data is to couple a number of autoencoders (Sun et al., 2016). A stacked sparse autoencoder consists of multiple layers of basic sparse autoencoders (Xu et al., 2015). Each autoencoder performs a nonlinear transformation on the input, and then the output generated by each encoder is used as the input of the next autoencoder. Each successive autoencoder represents the original input in a more abstract form than the previous one (Ng, 2011). Finally, a required number of features are extracted from the inputs and then received by a Softmax classifier to categorise (Liu et al., 2018). The combination of a stacked autoencoder and Softmax regression is able to obtain a high degree of accuracy for fault diagnosis (Tao et al., 2015).

- **Softmax classifier (SMC)**

Softmax regression is a classification method that is a generalisation of logistic regression for solving multiclass problems. In logistic regression, the labels are binary: $y_n \in \{0,1\}$ (Ng and

Jordan, 2002). Comprised to the logistic regression, Softmax regression provides more possible values for labelling, $y_n \in \{0, \cdots, k\}$, instead of two (Tao et al., 2015). A Softmax classifier is a supervised model that has been commonly applied in fault classification and diagnosis (Lu et al., 2017). While training the model, the training data were labelled up front. For a give training set $\{(x_1, y_1), \cdots, (x_m, y_m)\}$, $y_n \in \{1, \cdots, k\}$ are the class labels that indicate different types of faults. For a given input x, the corresponding classification probability is

$$p(y = j|x) \tag{4.15}$$

where $j = 1, \cdots, k$.

The probability of each class label is estimated by the Softmax classifier (Verma et al., 2013). If the possibility p achieves the largest value in the class of i, the set of data is recognised with the label of i.

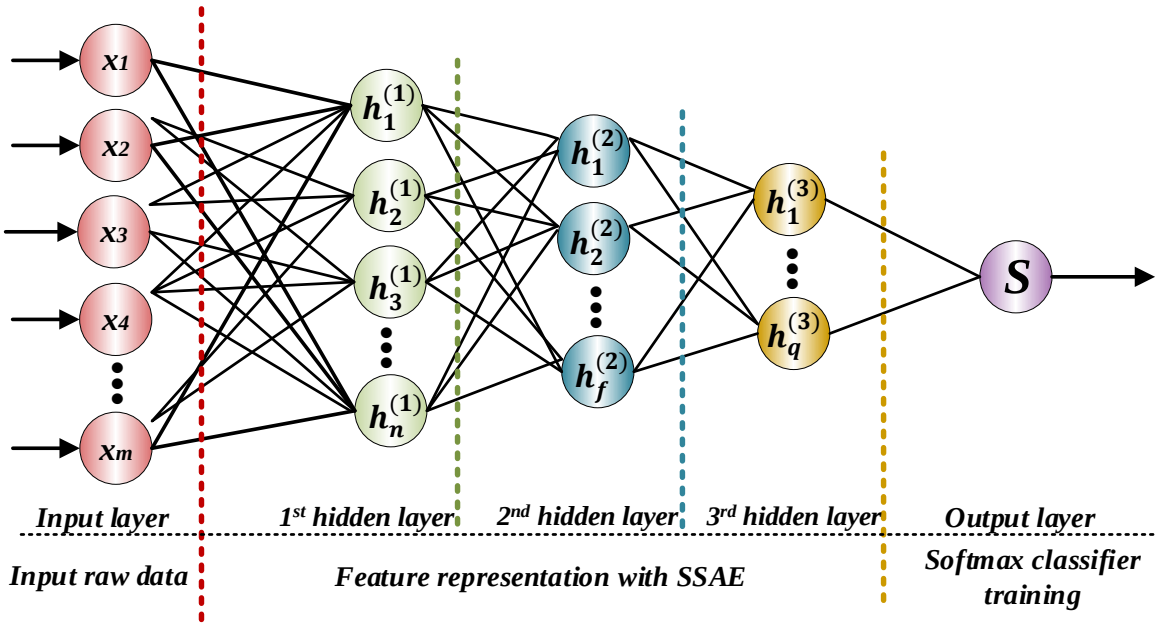

Figure 4.31 A SSAE with three autoencoders stacked plus a SMC

A stacked sparse autoencoder with three autoencoders stacked plus a Softmax Classifier is shown in Figure 4.31. In this work, each autoencoder contains one hidden layer. For simplicity, the decoder parts of each sparse autoencoder are not shown.

In this work, the SSAE was used to classifying and diagnosing various pantograph faults or changes using the experimental data collected using the changing-gradient test.

4.4.5.2 Application of the stacked sparse autoencoder

In order to validate the applicability of the SSAE in pantograph faults classification and diagnosis, the measurements obtained from the normal and faulty condition using the changing-gradient test at 500 mm/s (in Figure 4.22) were used to the train the deep learning network. The parameters measured with the same fault or change in the pantograph were labelled the same. The parameters include the contact force, the accelerations of the pantograph head, the top and bottom end of the upper arm, and the top end of the lower arm. As mentioned in §3.3, two load cells and five accelerometers are used. Two of the accelerometers are one-axis versions attached to the pantograph head; three of those are two-axis versions and are attached to the arms. Accordingly, ten signals were recorded during the test. The labelled experimental data were used to train and validate the deep learning network for fault classification and diagnosis.

A simple example using the SSAE to classify the normal and faulty condition at an excitation speed of 500 mm/s is presented. In this work, the experimental data sets used to train and validate the SSAE were collected while the test rig excites the pantograph and for another1 s after the motion of the test rig stops, as shown in Figure 4.32. As the pantograph still oscillates after the test rig stops, the oscillation should be collected and analysed.

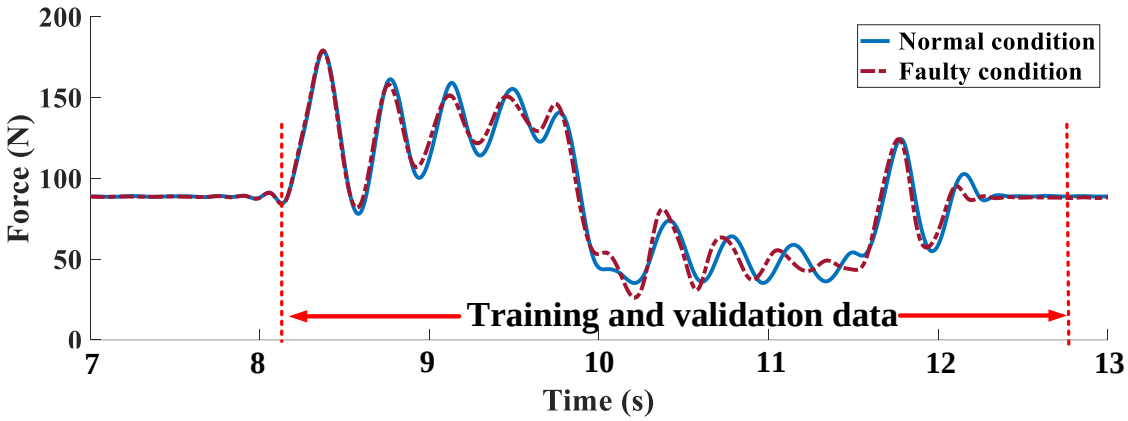

Figure 4.32 Experimental data used for training and validating the SSAE

As mentioned in §3.2.2, the test rig is capable of sampling at 1 kHz. As the machinery oscillates at a relatively low frequencies, for example at around 2.5 Hz in Figure 4.32, to decrease the computational cost, in this work the experimental data sets measured to train and validate the SSAE were collected at the sampling rate of 200 Hz that is the lowest sampling rate required in EN 50317(CENELEC, 2012a) for pantograph testing.

Typically, about 80% of the data for training and 20% for validation (Goodfellow et al., 2016). Since the SSAE performs better with more data sets, the changing-gradient test with one fault or change at each excitation speed was repeated 100 times: 80 of the data sets were used to train the deep learning network, and the remaining 20 data sets were for validating the model.

The SSAE model applied in this work has three sparse autoencoders stacked with the neurons in each autoencoder are 300, 100 and 3, respectively. The SSAE is formed by three encoders from the autoencoders and a Softmax classifier; the diagram of the SSAE network is shown in Figure 4.33.

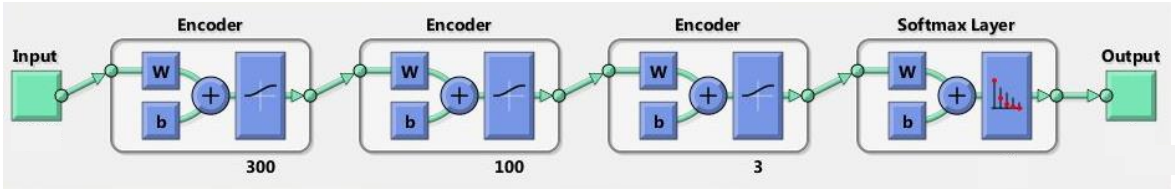

Figure 4.33 Structure of the SSAE network used in this work

Three features were learned by the last autoencoder and sent to the Softmax classifier. Two of the features learned by the SSAE, in this case, are plotted in Figure 4.34. It is shown that the features for the experimental data recorded under the normal and faulty conditions are well clustered. This demonstrates that the SSAE is applicable in classifying pantograph health conditions. The use of the SSAE for pantograph fault classification and diagnosis is continued in Chapter 7.

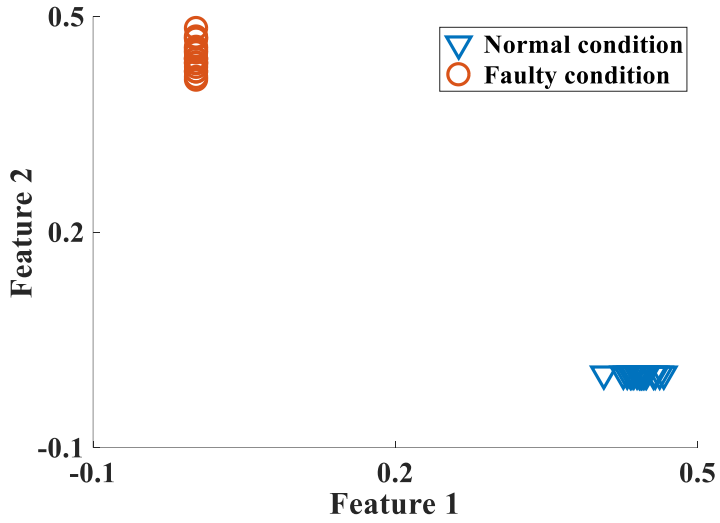

Figure 4.34 Features for normal and faulty conditions

4.5 Summary

In this chapter, the methodology of pantograph fault detection and diagnosis is detailed. In order to diagnose various faults in the pantograph and develop a fault diagnosis testing procedure, three dynamic tests are proposed: (i) a hysteresis test, (ii) a frequency-response test, and (iii) a novel changing-gradient test. The applicability of these tests being able to detect and maybe even diagnose common pantograph faults has been demonstrated.

The results of the static hysteresis test (50 mm/s only) show the degradation of pantographs can be detected by inspecting the up, down and uplift force, and the shape of the hysteresis loops. Furthermore, the hysteresis tests were extended to be carried out at different speeds to highlight

the relationship between the health status of the pantograph and the measurements of the hysteresis by exciting different nonlinearities.

A frequency-response test that is commonly used for estimating the parameters for the lumped-mass model was adapted for detecting and diagnosing pantograph faults innovatively, but with an amplitude profile chosen to suit the pantograph under test. An example of comparing the FRFs of a new and a pre-overhaul pantograph showed that the frequency-response test is capable of detecting changes to pantographs. In this work, decreasing- and various fixed-amplitude excitations were proposed to excited pantograph nonlinearities in different levels, therefore to accomplish the high accuracy and efficiency of fault detection and diagnosis. Lumped-mass models were also adopted to extract features that are able to detect pantograph status by identifying the parameters for the lumped-mass models (again, based on the chosen amplitude profile).

The changing-gradient test is a novel test proposed in this work. It aims to reproduce the response of the pantograph to the variation in stiffness of the contact wire. 'V'-shaped profiles were designed to excite pantograph at various speeds. Critical parameters, including the damping ratio, oscillation frequencies, and overshoots of contact forces, were extracted using the conventional system identification approach in the time domain. However, as some of the faults do not vary the response of the pantograph significantly in the time domain, in order to classify all types of faults, a stacked sparse autoencoder was adapted.

Common pantograph faults were inspected by hysteresis, frequency-response and changing-gradient tests in Chapters 6, 7, and 8, respectively.

CHAPTER 5 HYSTERESIS TEST

5.1 Introduction

In this chapter, in order to realise pantograph fault detection and diagnosis, hysteresis tests are discussed which emulate common pantograph faults. Only one fault or change was made to the pantograph at a time. The measurements obtained, and features extracted from a healthy pantograph at various excitation speeds are considered as a reference. By comparing the measurements and features obtained in a faulty or abnormal condition to the reference, the corresponding fault or change can be characterised. The faults and changes were made to a number of pantograph components, including the head and frame suspensions, and elbow joint. The fault features will be used to develop a testing routine for pantograph fault detection and diagnosis, which is described in Chapter 8.

5.2 Changes to the head suspension

5.2.1 Hysteresis test with changes to the head suspension

The head suspension links the pantograph head and upper arm aims to track the high-frequency irregularities of the contact wire seen by the pantograph head (Gil-Vera, 2000). Since it is close to the pantograph head to which excitations are applied, its characteristics critically affect the performance of the pantograph. As mentioned in §3.2, the head suspension acts as a spring-damper system, and its dynamic behaviour is related to the stiffness of the bearings and the stiffness and damping of the torsion bar. In order to investigate the relationship between the hysteresis and these parameters, hysteresis tests were carried out with two changes made to the head suspension. In Case 1, the head suspension was taken apart, the bearings greased, and the

suspension reassembled. In Case 2, the original torsion bar was replaced with another one 30% less stiff. The stiffness of the original torsion bar is about 4.6 kN/m (equivalent at the head). The two torsion bars are the same size. Hysteresis tests were carried out under the two conditions at excitation speeds of 50 to 400 mm/s with a step size of 50 mm/s.

The measurements obtained at 50, 200 and 400 mm/s are shown in Figure 5.1 *a*, *b* and *c*, respectively; those at other excitation speeds are shown in Appendix A, Figure A.1. The blue profile is the hysteresis of the pantograph in its healthy condition, and the red and yellow profiles are those where the head suspension has been greased and the torsion bar replaced, respectively. The values of the average up and down forces, the static uplift forces, and hysteresis obtained at different excitation speeds in Cases 1 and 2 are shown in Appendix A, Table A.2. Greasing the head suspension reduces the stiffness of the bearings; it is difficult to restore the stiffness to its original level. Therefore, the measurements and features extracted from the experimental data in Case 1 are considered as references for the tests carried out later.

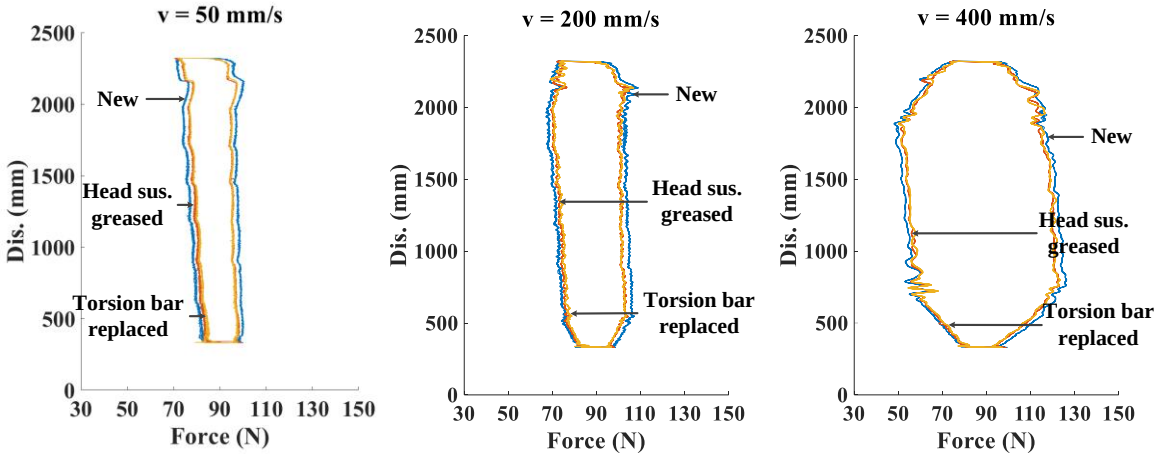

Figure 5.1 Hysteresis tests: normal and changes to the pantograph head

In Figure 5.1, the yellow and red curves almost overlap at all excitation speeds, which indicates that the stiffness and damping of the torsion bar do not affect the hysteresis of the pantograph. The head suspension is designed to absorb high-frequency oscillation; however, the hysteresis

test is equivalent to a static test that cannot excite the dynamics of the torsion bar. Therefore, the hysteresis test is invalid for inspecting changes to the torsion bar.

Comparing the hysteresis in Case 1 (red profile) to that in the healthy condition (blue profile), greasing the head suspension increases and decreases the up and down forces, respectively, and therefore reduces the overall hysteresis. Hysteresis loops for the three conditions with respect to excitation speed are shown in Figure 5.2. However, the hysteresis loops for the healthy pantograph and Case 1 are almost concentric, and the uplift forces at different excitation speeds are similar. Moreover, in Figure 5.2, the hysteresis profiles for healthy pantograph (blue stars) and Case 1 (red circles) are almost identical, but offset from one another. This indicates that the differences in hysteresis that resulted from greasing the head suspension do not vary with the excitation speed. Accordingly, variations in the greasing level of the pantograph head suspension can be detected by the hysteresis test at any excitation speed.

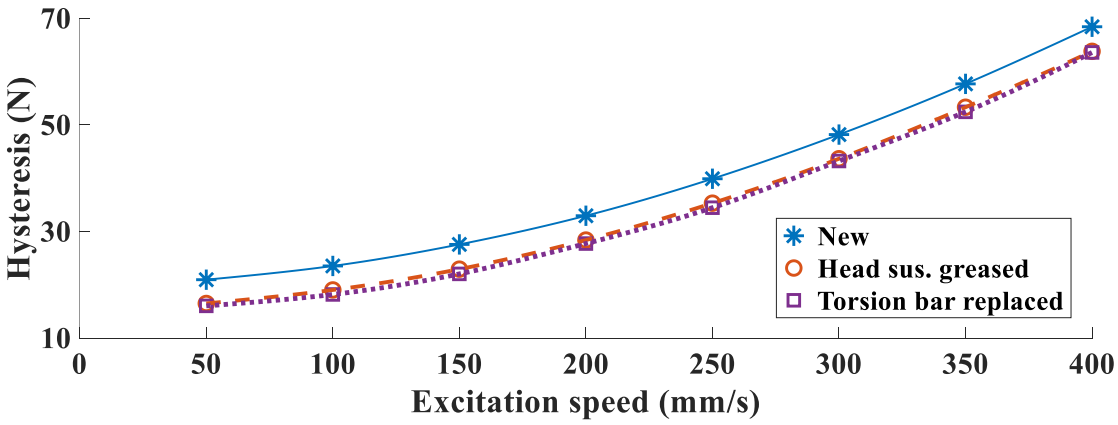

Figure 5.2 Hysteresis for normal and changes to the pantograph head conditions

5.2.2 Comments

According to the results of the hysteresis tests carried out, it was concluded that the hysteresis test cannot be used to inspect the variation in stiffness and damping of the torsion bar. However, the hysteresis test can be used to detect the variation in greasing level of the head suspension. The testing results show that an increased level of greasing results in less hysteresis; meanwhile,

the hysteresis curve loops for the normal and head suspension greased conditions are concentric, and the uplift force remains the same. As the hysteresis test does not excite the dynamics of the head suspension, the variation in greasing level of the head suspension can be inspected by the hysteresis test at any excitation speed.

5.3 Loosening the elbow joint outer chain

The elbow joint connects the upper and lower sections of a pantograph through three chains lying on the eccentric cam, one centre chain and two outer chains. The tightness of the chains varies the extension ratio of the upper arm. The chains may become loose as a result of vibration while the train operates. Currently, the degree of tightness of the chains is checked manually. Even though static hysteresis measurement devices are used at some depots, it cannot be used to look at the state of the chains because the relationship between the measurement of the hysteresis and the tightness of the elbow joint chains has not been addressed.

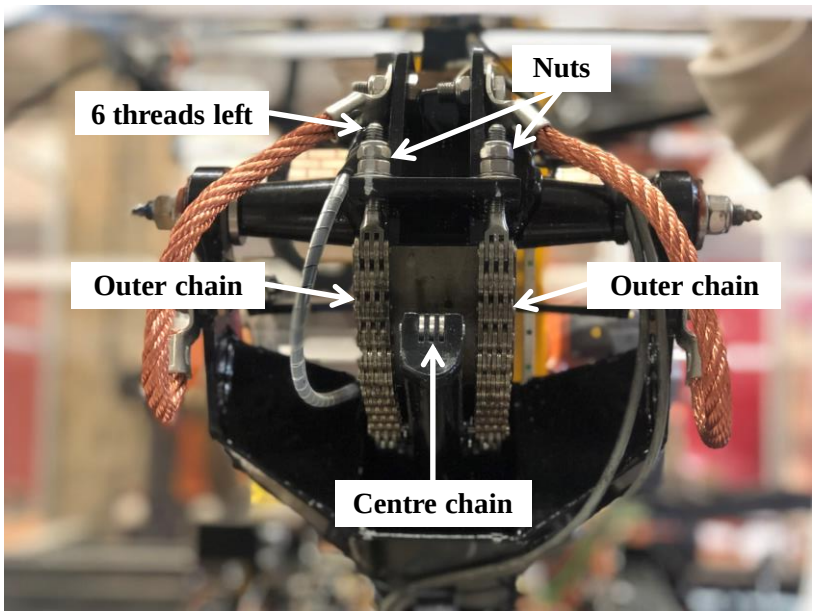

Figure 5.3 Pantograph elbow joint

In this section, hysteresis tests at different excitation speeds were carried out with varying the degree of tightness of one elbow joint outer chain. As lateral excitation is not applied during the hysteresis test, it is safe to loosen one of the outer chains, and even to remove it. The degree

of tightness of the outer chains is varied by changing the attachment point of the nut that fixes one end of the outer chain to the eccentric cam, the attachment point of the nut is shown in Figure 5.3. On the healthy pantograph, the nut can be loosened by 6 turns before it comes off. Four cases were tested: loosening the nut by one, three and five turns, and removing the outer chain entirely.

5.3.1 Static hysteresis tests with varying degrees of tightness of one outer chain

Firstly, hysteresis was measured at a speed of 50 mm/s; the results are shown in Figure 5.4 *a*. The blue profile, which is the outermost, is the hysteresis in the normal condition and is considered as the reference; the other four profiles correspond to different degrees of tightness of the outer chain.

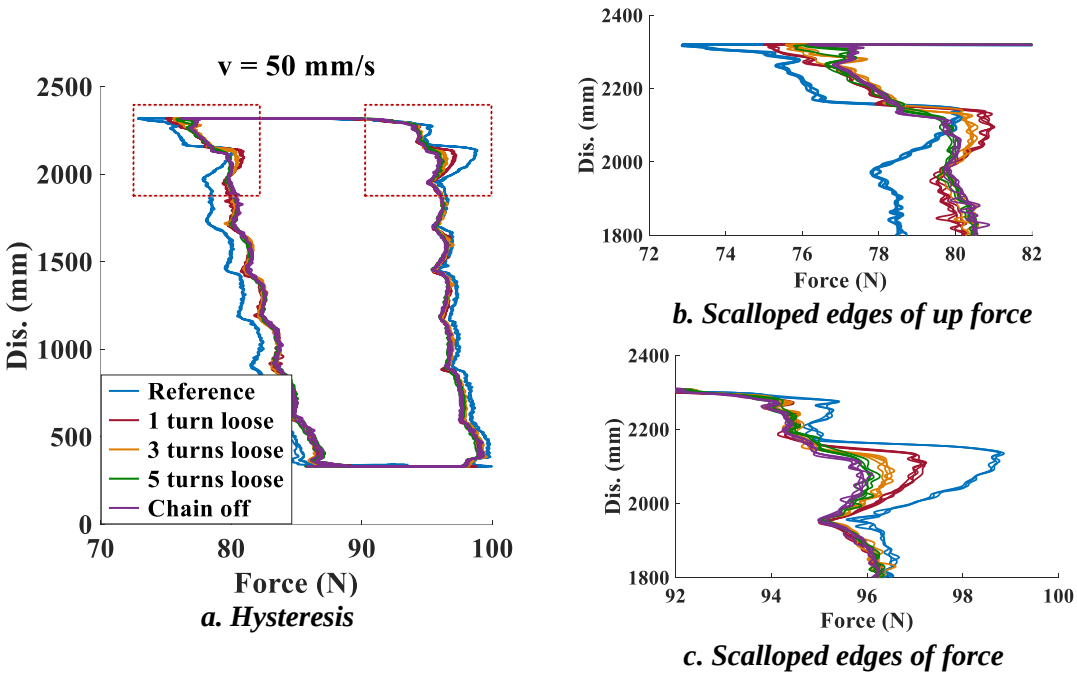

Figure 5.4 Hysteresis for healthy condition and various tightness of the chain at 50 mm/s

Compared to the reference, the hysteresis curves obtained with reducing the degree of tightness of the outer chain are narrower. This illustrates that hysteresis decreases when the outer chain does not fit tightly. However, the hysteresis loops for the four faulty conditions are almost overlapping, other than the extension range where the large scalloped edge (or ripple) appears.

The zoomed–in scalloped edges of up and down forces under different degrees of tightness of the outer chain are shown in Figure 5.4 *b* and *c*, respectively. It can be observed that the hysteresis loops are most different at the highest pantograph extent. The large scalloped edge shrinks successively as the degree of tightness of the outer chain decreases. After the outer chain is taken off, the sizes of the large scalloped edges to the up and down forces are about the same as the regular ripples. In order to describe the variability in the big scallop edges of the up and down forces under different degrees of tightness of the outer chain, standard deviations (SDs) of the up and down forces were calculated; these are presented in Table 5.1. In Table 5.1, SDs of the up and down force both decrease as the tightness of the outer chain decreases.

Table 5.1 Static hysteresis under different degrees of tightness of the outer chain

Conditions		Avg. up force (N)	SD of up force	Avg. down force (N)	SD of down force	Uplift force (N)	Hysteresis (N)
Reference		80.8	0.75	97.2	0.82	89.0	16.5
Outer chain loose	1 T	82.1	0.63	96.6	0.58	89.4	14.5
	3 T	82.2	0.50	96.6	0.49	89.4	14.4
	5 T	82.2	0.42	96.5	0.46	89.4	14.3
Outer chain off		82.3	0.41	96.5	0.45	89.4	14.2

In Table 5.1, the average up, down and uplift forces of the four loosened chain conditions are similar to each other, but different from the reference. It can be concluded that if the elbow joint chain is loose, the hysteresis of the pantograph is less than the reference, while the uplift force is close to the reference and the scalloped edges on the hysteresis loop shrinks. Therefore, in this case, different degrees of tightness of the outer chain can be inspected from the size of the scalloped edges. Accordingly, the large scalloped edges on the hysteresis curves are related to

the health of the elbow joint, and the appearance of scalloped edges could be considered as one of the criteria for evaluating the performance of the elbow joint.

5.3.2 Hysteresis tests with various degrees of tightness of one outer chain

In order to extract more features to distinguish different degrees of tightness of the outer chain, hysteresis tests were carried out at higher excitation speeds. The excitation speeds were in the range of 100–400 mm/s with a step of 50 mm/s. The measurements collected at the speeds of 200 and 400 mm/s are shown in Figure 5.5 *a* and *b*, respectively; those under other excitation speeds are shown in Appendix A, Figure A.2.

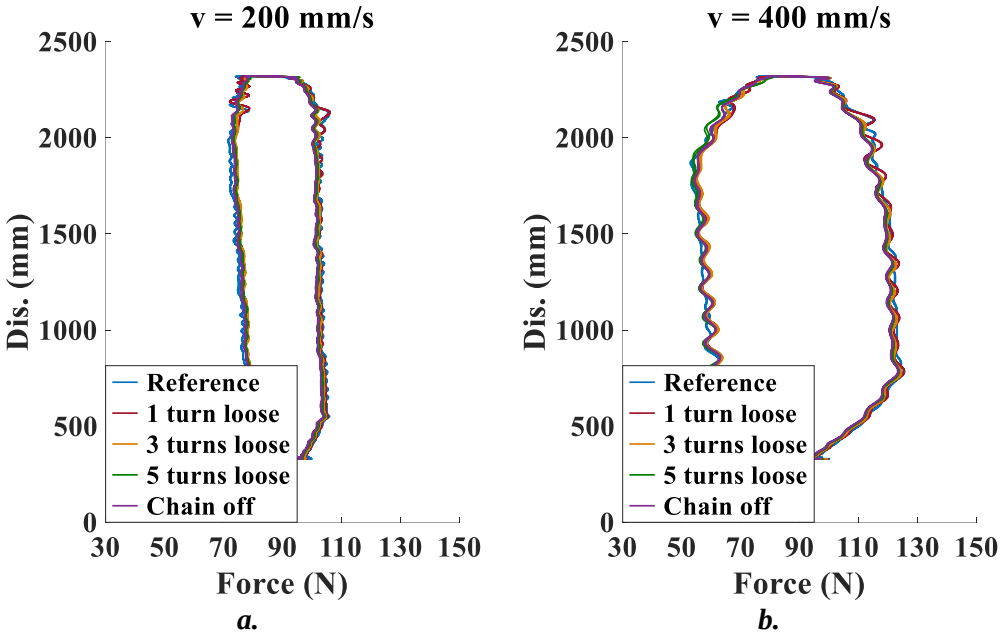

Figure 5.5 Hysteresis measurements with changes to elbow chains

In Figure 5.5 *a* and *b*, the hysteresis under four different tightness conditions is almost the same at the excitation speeds of 200 and 400 mm/s, except for the large scalloped edged areas. Observing the hysteresis measured at the excitation speeds varied from 100 to 400 mm/s in Figure 5.5 and Figure A.2, as the excitation speed increases, the large scalloped edges are not visible. As the excitation speed increases, higher acceleration or deceleration are required to speed up or slow down the excitation to the expected speed within 1 second. Higher acceleration

and deceleration generated more fluctuation to the contact force. Therefore, the large scalloped edges cannot be observed using the hysteresis tests at higher speeds. Accordingly, the hysteresis at the lowest speed, 50 mm/s, can be used to detect the variation in the degree of tightness of the outer chain.

5.3.3 Comments

In this section, in order to detect and diagnose the health of the elbow joint chain using the hysteresis test, the hysteresis tests were carried out at different excitation speeds with various degrees of tightness of the elbow joint outer chain. The results of the static hysteresis test (50 mm/s) show that the hysteresis decreases if the outer chain is loose; however, the hysteresis measured when the chain is loosened by different degrees does not vary significantly. Different degrees of tightness of the outer chain can be detected by the appearance and size of the large scallops in the waveforms that occur at high extension height. The large scallops shrink as the degree of tightness of the chain decreases. The measurements also show that the hysteresis obtained with varying degrees of tightness of the outer chain is close to the reference at excitation levels higher than 100 mm/s, and tests carried out at the speeds higher than 200 mm/s do not result in large scallops in the resulting waveforms. Therefore, a hysteresis test at a speed of 50 mm/s can be used to detect the tightness of the elbow joint outer chain and to diagnose the health of the elbow joint, particularly at the highest pantograph extension.

5.4 Changes to the pneumatic actuator

The pneumatic actuator supplies the uplift force to maintain the contact between the pantograph and contact wire. It dominates the dynamic behaviour of the frame suspension. According to the working principle of the pneumatic actuator detailed in §3.2, common pneumatic actuator faults are: wrong levels of air pressure, leakage, and blocked venting plug. Leakages and blocked venting plug may vary the nonlinearities of the pneumatic actuator. The pneumatic

actuator behaves in two ways: as a supplier of constant force while the excitation applied to it is at relatively low frequency or speed, and as a nonlinear spring-damper system while the excitation is at a high frequency or speed. Therefore, the dynamic behaviour of the pneumatic actuator is sensitive to excitation amplitude. In order to detect the dynamic behaviour of the pneumatic actuator in various faulty conditions and extract fault features, the hysteresis tests were carried out at different speeds.

5.4.1 Incorrect levels of air pressure

The pneumatic actuator is connected to an air reservoir through a pressure regulator that maintains the pressure relatively constantly. For the Pendolino high-speed pantograph tested in this work, a 5.5 bar pressure is required to provide an uplift force of 90 ± 3 N (ERG, 2012a). Excessive air pressure generates too much uplift force that may reduce the life cycle of the pantograph-catenary system; too little pressure could result in an increase in the percentage of contact force loss. The air pressure level can be detected by measuring the static uplift force (Cullingford, 1993). In this section, to inspect the effect of an incorrect pressure level on the pantograph hysteresis curves, static hysteresis was measured while adjusting the outlet of the pressure regulator to 5.0 and 6.0 bar. Measurements of static hysteresis under different pressure levels are shown in Figure 5.6; the values of the up, down and uplift forces and hysteresis are detailed in Table 5.2.

Table 5.2 Hysteresis measured at different pressures

Pressure (bar)	Avg. up force (N)		Avg. down force (N)		Uplift force (N)		Hysteresis (N)	
	Force	difference	Force	difference	Force	difference	Force	difference
5.0	69.2	–10.4	90.3	–10.3	79.8	–10.3	21.0	0.10
5.5	79.6	0.0	100.6	0.0	90.1	0.0	20.9	0.0
6.0	88.6	9.0	109.3	8.7	98.9	8.8	20.7	–0.2

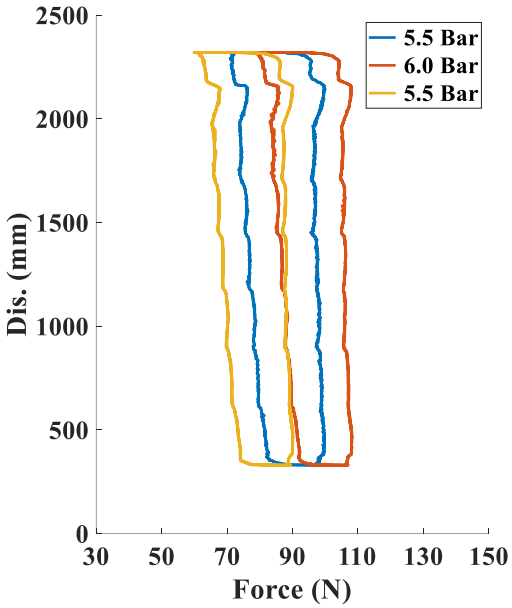

Figure 5.6 Hysteresis measured at different air pressures

In Figure 5.6, the shapes of the hysteresis loops obtained at the three pressure levels are approximately the same. In Table 5.2, it is shown that the differences in the up, down and uplift forces between the reference and the experimental data at 5.0 bar are close to each other; this is the same for measurements obtained at 6.0 bar. Furthermore, the hysteresis measured at 5.0 and 6.0 bar are close to that obtained at normal pressure level. Accordingly, the hysteresis curves obtained with the lower or higher pressure levels can be equivalent to translating the reference to the left or right, respectively.

Therefore, wrong pressure levels do not vary the values of pantograph hysteresis and the shape of the hysteresis loops significantly but translate the regular hysteresis loop to the left or right. Based on this feature, the wrong pressure levels resulting from an abnormal output from the pressure regulator can be inspected using the static hysteresis test.

5.4.2 Leakage within the pneumatic actuator

In the real operating circumstances, leakage may occur within the pneumatic actuator that decreases the uplift force and varies the dynamic behaviour of the pantograph. In this section,

in order to explore the features of a leaking pneumatic actuator, the original (new) pneumatic actuator was replaced by another one that had a leak at a particular extension height.

5.4.2.1 Static hysteresis test with a leaking actuator

Firstly, static hysteresis with the leaking actuator was measured at an excitation speed of 50 mm/s, the result as shown in Figure 5.7. The hysteresis results obtained with the original and leaking pneumatic actuator are plotted in blue and red, respectively. Figure 5.7 shows that the up and down forces of the hysteresis loops for the normal and leaking cases are similar, except for the sudden drop on the red curve at the excitation height of approximately 1910 mm. This is because that when the piston reaches the leakage point, the pressure inside the pneumatic actuator drops significantly; due to the limited size of the orifice, air cannot flow into the pneumatic actuator rapidly enough to sustain the required pressure. Therefore, the leakage results in a sudden reduction in the contact force.

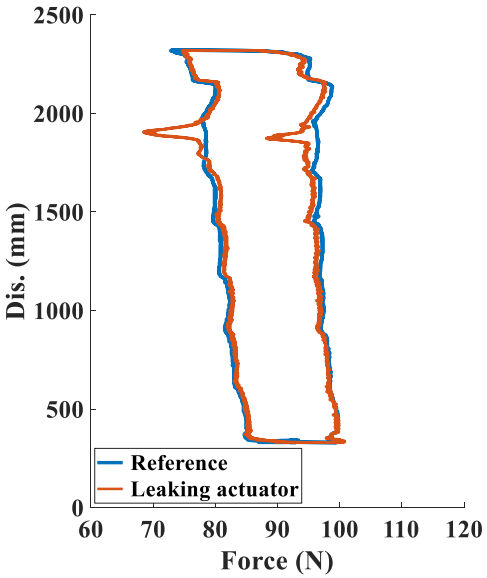

Figure 5.7 Static hysteresis: normal and leaking actuator conditions

It is clear, that leakage of the pneumatic actuator varies the shape of the hysteresis loop. The SDs of the up and down forces measured with the original and leaking actuator are compared in Table 5.3. The SDs of the up and the down forces with the leaking pneumatic actuator were

113.3% and 40.8% higher than the references, respectively. Whereas, other parameters did not vary significantly. As a result, it can be concluded that static hysteresis is efficient in detecting the leakage occurring in the pneumatic actuator by monitoring the sudden drop in the contact force.

Table 5.3 Hysteresis measured with the normal and leaking pneumatic actuators

Conditions	Avg. up force		Avg. down force		Uplift force (N)	Hysteresis (N)
	Force (N)	SDs	Force (N)	SDs		
Reference	81.8	0.75	98.3	0.81	90.1	16.5
Leaking actuator	81.5	1.60	96.8	1.14	89.1	15.3
Differences	0.4%	113.3%	1.5%	40.8%	1.0%	6.9%

5.4.2.2 Hysteresis tests with a leaking pneumatic actuator

In order to detect the more features of the leaking pneumatic actuator, hysteresis tests were carried out at higher excitation speeds; the results are shown in Figure 5.8.

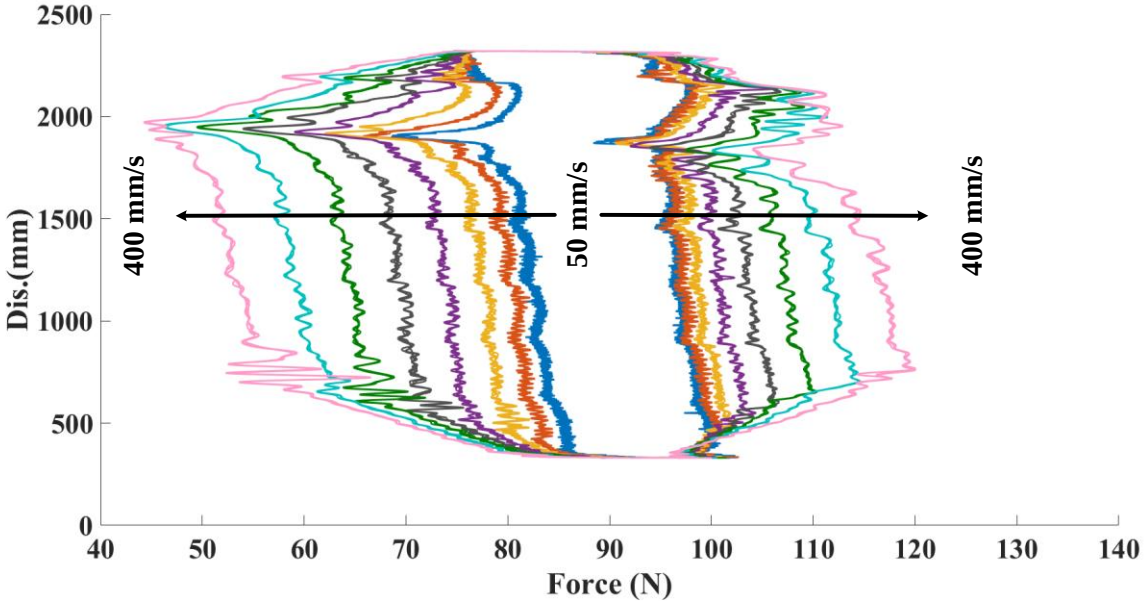

Figure 5.8 Hysteresis of a leaking actuator

Compared to the hysteresis loops for the normal condition (in Figure 4.5), these obtained with the leaking pneumatic actuator not only drops at the extension height where the piston reaches

the leakage point, but also is not centred with a constant uplift force. The hysteresis loops move to the left as the speed increases, which indicates that the uplift force decreases as the excitation speed increases.

The up, down and uplift forces at different speeds are detailed in Table A.3 in Appendix A and presented in Figure 5.9. The triangles and diamonds represent the average up and down forces, respectively, and the circles represent the uplift forces. The references and parameters obtained with the leaking actuator are plotted as blue solid lines and red dashed lines, correspondingly. In this figure, as the excitation speed increases, the up and down forces obtained with the leaking pneumatic actuator become increasingly lower than the references, which is caused by the successively weaker uplift force, whereas the original actuator is able to maintain the uplift force at a relatively stable level at any excitation speed.

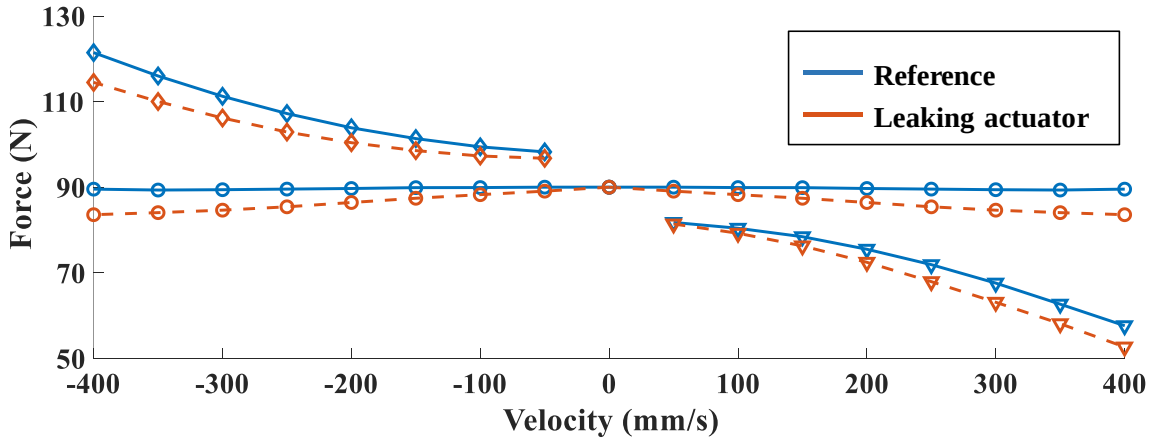

Figure 5.9 Up, down and uplift forces with original and leaking pneumatic actuators

The equivalent damping coefficients of the pantograph with the leaking pneumatic actuator at different speeds are compared to the reference in Figure 5.10. The damping coefficients with the leaking actuator are lower than that of the reference at the same excitation speed.

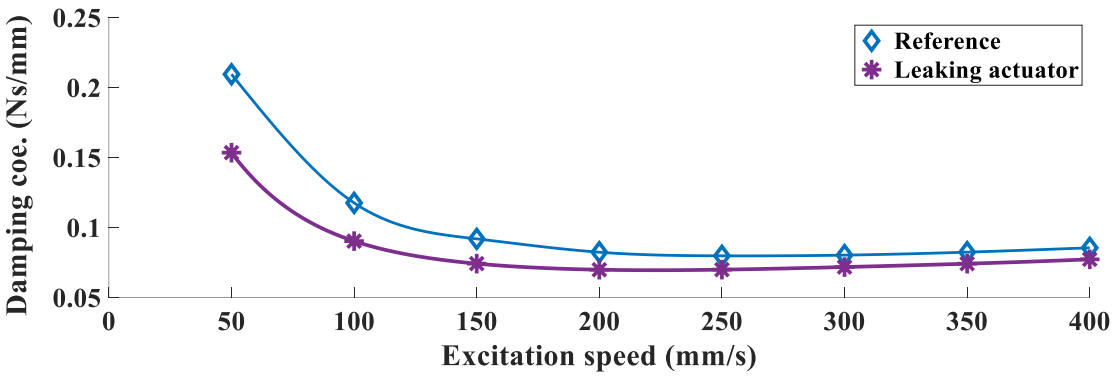

Figure 5.10 Damping coefficients with original and leaking pneumatic actuators

Additionally, the weaker contact force and sudden drop in force result in a greater likelihood of contact loss and a decrease in current collection quality (Collina et al., 2007b). Therefore, the leakage within the pneumatic actuator must be detected and diagnosed. The hysteresis test at 50 mm/s is able to show the sudden drop in contact force caused by leakage and indicate the leakage point. However, if the leaking problems do not create an obvious drop in the contact force, static hysteresis may not be appropriate. Accordingly, hysteresis tests at higher speeds need to be used, as the behaviour of the pneumatic actuator varies with excitation speed significantly. If leakage happens, the uplift force should decrease as the excitation speed increases.

5.4.3 Changes to the venting plug

When the pneumatic actuator is compressed, excess air is expelled through an orifice which is protected by a venting plug. As mentioned in §3.2, the cleanliness of the venting plug varies the permeability of the orifice, and therefore affects the dynamic behaviour of the pneumatic actuator and the pantograph. However, degradation on the top of the venting plug is difficult to check manually and visually. In order to develop the new approach to detect the condition of the venting plug, in this section, hysteresis tests were carried out while blocking half of the top piece of the venting plug (‘half sealed’) and then blocking it entirely (‘sealed’) to emulate its degradation; a venting plug is shown in Figure 3.10. Accordingly, pantograph performance with

different permeability levels of the venting plug can be inspected. The hysteresis tests were carried out at 50, 200 and 400 mm/s to explore the variation in hysteresis loops at low, medium and high excitation speeds. The results are shown in Figure 5.11.

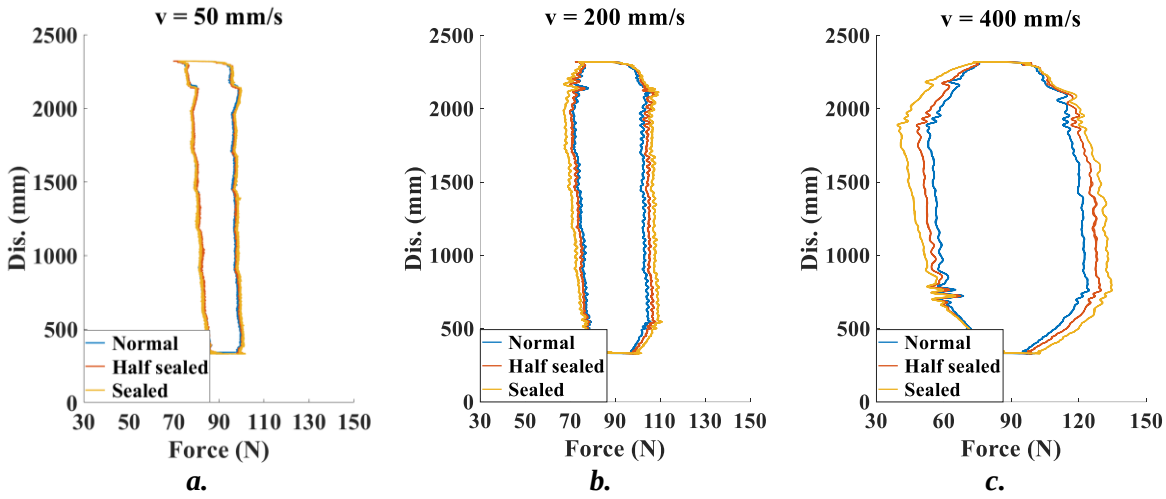

Figure 5.11 Hysteresis measured for different degrees of permeability of the venting plug

At a speed of 50 mm/s (Figure 5.11 *a*), the hysteresis of the normal, half and entirely sealed conditions are approximately the same. At a speed of 200 mm/s (Figure 5.11 *b*), it is shown that the sealed venting plug (yellow profile) generates the highest hysteresis; the hysteresis loop with the half–sealed venting plug (red profile) is in the middle, and the normal condition has the lowest hysteresis. Hysteresis measured at a speed of 400 mm/s is shown in Figure 5.11 *c*. The features are similar to those at 200 mm/s, but the differences in the hysteresis loops recorded under the three conditions show up more clearly. Details of the measurement of the hysteresis tests are shown in Table 5.4.

Table 5.4 Hysteresis under various degradation status of the venting plug

Speed (mm/s)	Conditions	Avg. up force (N)	Avg. down force (N)	Uplift force (N)	Hysteresis (N)
50	Reference	81.8	98.5	90.1	16.5
	Half-sealed	81.5	98.4	90.1	16.6
	Sealed	81.8	98.4	90.0	16.7
200	Reference	75.6	103.9	89.5	28.4
	Half-sealed	73.9	105.6	89.8	31.7
	Sealed	71.5	107.9	89.7	36.4
400	Reference	57.7	121.5	89.6	63.8
	Half-sealed	53.1	126.1	89.6	73.0
	Sealed	47.6	130.3	88.9	82.8

According to the above results, the uplift forces of the three conditions measured at the same excitation speed are close to each other, which explains why all the hysteresis loops in the three subfigures in Figure 5.11 are concentric. The degradation of the venting plug can be detected by observing the increase in hysteresis under high-speed excitations. Compared to the hysteresis recorded at the excitation speed of 200 mm/s, that recorded at 400 mm/s is able to show the rise in hysteresis more clearly. Therefore, for the purpose of detecting the status of the venting plug using the hysteresis test, 400 mm/s excitation is more applicable.

5.5 Conclusions

In this chapter, the static hysteresis test was extended to be carried out at higher speeds to detect common pantograph faults. Some pantograph faults may vary pantograph nonlinearities; therefore, different excitation speeds were expected to actuate the nonlinearities by different amounts. Following this, fault features were extracted, and pantograph fault detection and diagnosis were realised. With the test rig, the hysteresis test could be carried out with excitation

speeds varied in the range of 50 to 400 mm/s, whereas commercial measuring devices can only be used at a single excitation speed of 50 mm/s.

In order to understand the characteristics of common pantograph faults on hysteresis loops, faults and changes were emulated in the pantograph head and frame suspension and at the elbow joint. Two changes were made to the head suspension: greasing the head suspension and replacing the torsion bar with a less stiff one. The results show that a higher greasing level reduces hysteresis without changing the shape of the hysteresis curves at any excitation speed. However, the hysteresis test is not able to detect the change in the torsion bar.

The hysteresis tests were also carried out to detect different degrees of tightness of one elbow joint outer chain. The tightness of the outer chain can be varied by changing the tightness of the nut that secures the chain. The experimental results of the static hysteresis test show that as the tightness of the outer chain decreases, the large scallops on the hysteresis loops diminish. When the outer chain was removed from the pantograph, the large scallops disappeared. Furthermore, the hysteresis of a loosened chain condition is lower than the reference. Hysteresis tests under higher excitation speeds cannot show the variation in hysteresis and the size of the large scallops clearly. Therefore, the hysteresis test at a speed of 50 mm/s can be used to detect the tightness of the elbow joint outer.

Finally, three changes were made to the pneumatic actuator and tested by the hysteresis test. Wrong pressure levels that translate the normal hysteresis profile can be detected by the static hysteresis test. Leakage of the pneumatic actuator generates a sudden drop in the contact force and reduces the uplift force as excitation speed grows. It is preferable to check the degradation of the venting plug with a hysteresis test under the highest excitation speed.

The fault features obtained using the hysteresis tests at various speeds are summarised in Table 5.5. These features will be used to develop the testing routine for rapid pantograph fault detection and diagnosis in Chapter 8.

Table 5.5 Hysteresis tests for fault detection and diagnosis

Faults	Suitable hysteresis test	Features
Greasing head suspension	Hysteresis test at any excitation speed	Hysteresis loops are in the same shape, but the hysteresis decreases.
Torsion bar replaced	/	/
Elbow joint chain loose	Hysteresis test at 50 mm/s	Size of the large scallop at high pantograph extent decreases, or the large scallop disappears.
Incorrect pressure levels	Hysteresis test at 50 mm/s	Hysteresis loops translate in the force direction.
Leakage in the pneumatic actuator	Hysteresis test at any excitation speed	Static hysteresis test: a sudden drop in contact force. Higher speeds: hysteresis loops move to the left successively.
Degradation of venting plug	Hysteresis test at high excitation speeds, but 400 mm/s excitation is preferred.	Hysteresis loops are concentric, but hysteresis increases.

CHAPTER 6 FREQUENCY RESPONSE FUNCTION

In order to characterise common pantograph faults or changes using frequency-response test, in this chapter, the FRFs were measured with various faults or changes made to the critical components of the pantograph, including head and frame suspensions, and elbow joint. The FRFs obtained from the pantograph under the original condition are considered as references. By comparing the faulty measurement to the reference, the differences between them are defined as the features of this particular fault or change. The input and output used to calculate the FRFs are the contact force and the vertical accelerations measured on various pantograph components. The faults feature extracted in this chapter will be used to develop the pantograph fault-diagnosis testing routines in Chapter 8.

6.1 Dynamic behaviour of the pantograph

As mentioned in §4.3, the FRFs of the pantograph vary with the excitation levels significantly as the nonlinearities are actuated at different amplitudes. In order to understand the appearance of the pantograph nonlinearities with respect to various excitation amplitudes, in this section, the FRFs measured at different pantograph parts under various excitations are analysed.

6.1.1 FRF test using decreasing-amplitude excitation

Since the decreasing-excitation is a combination of a sequence of fixed-amplitude excitations, it is applied to detect the occurrence of changes or faults to the pantograph prior to the frequency response tests under fixed-amplitude excitations. The FRFs obtained from different parts of the pantograph under decreasing-amplitude excitation are shown in Figure 6.1. Purple profiles represent head accelerance; the blue and red curves are the accelerance of the top and bottom

end of the upper arm, respectively; and, the yellow curves are the accelerance of the top of the lower arm. According to the consistency of the phases with respect to excitation frequency, the Bode plot in Figure 6.1 can be divided into three ranges: low, medium and high frequency.

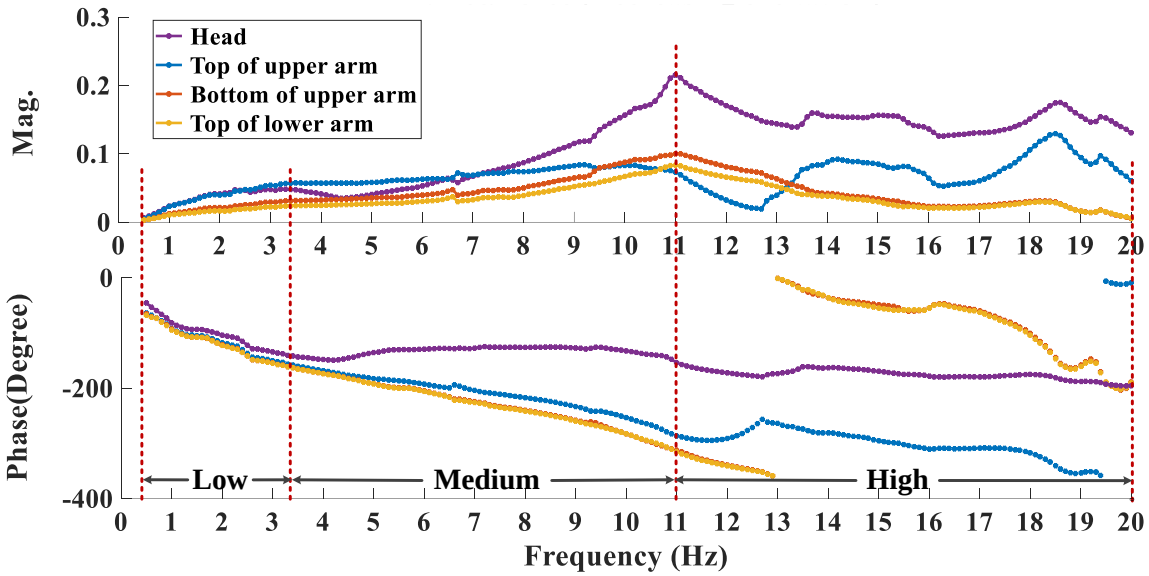

Figure 6.1 FRFs of the pantograph under decreasing excitation

The low-frequency range is from 0.5 to 3.3 Hz, where the phase angle curves of the pantograph head and arms are approximately identical. This indicates that all the pantograph parts move in-phase. Regarding descending gradient of the phase curves in this frequency range, a heavily damped resonance that is hard to observe from the magnitude curve appears.

The medium-frequency range is from 3.3 to 11.0 Hz. In this area, the phase curve of the pantograph head splits out from these of the arms. As the frequency increases, the gap between the phase curve measured from the pantograph head and other curves increases. Therefore, the dynamic behaviour appearing in this range is dominated by the freedom of the head suspension.

The high-frequency range is between 11.0 and 20.0 Hz, where the phase of the top of the upper arm separates from those of the bottom of the upper arm and the top of the lower arm. Within this range, the top and bottom ends of the upper arm move out-of-phase due to the bending

mode of the upper arm. Thus, the FRFs in the high-frequency range are related to the properties of the upper arm, which are not considered in this work.

Additionally, the phase curves of the bottom of the upper arm (red) and the top of the lower arm (yellow) are overlapping at all frequencies; meanwhile, the magnitude of the bottom of the upper arm is slightly larger than that of the top of the lower arm. This demonstrates that the top and bottom of the elbow joint always move in-phase for small movements, rather than in opposite directions.

6.1.2 FRF test using 0.3 mm excitation

A 0.3 mm excitation was applied to the pantograph; the results are shown in Figure 6.2. Similar to the FRFs for decreasing-amplitude excitation, the FRFs in Figure 6.2 can also be categorised into low, medium and high-frequency sections in the ranges 0.5–6.9 Hz, 6.9–12.2 Hz, and 12.2–20.0 Hz, respectively.

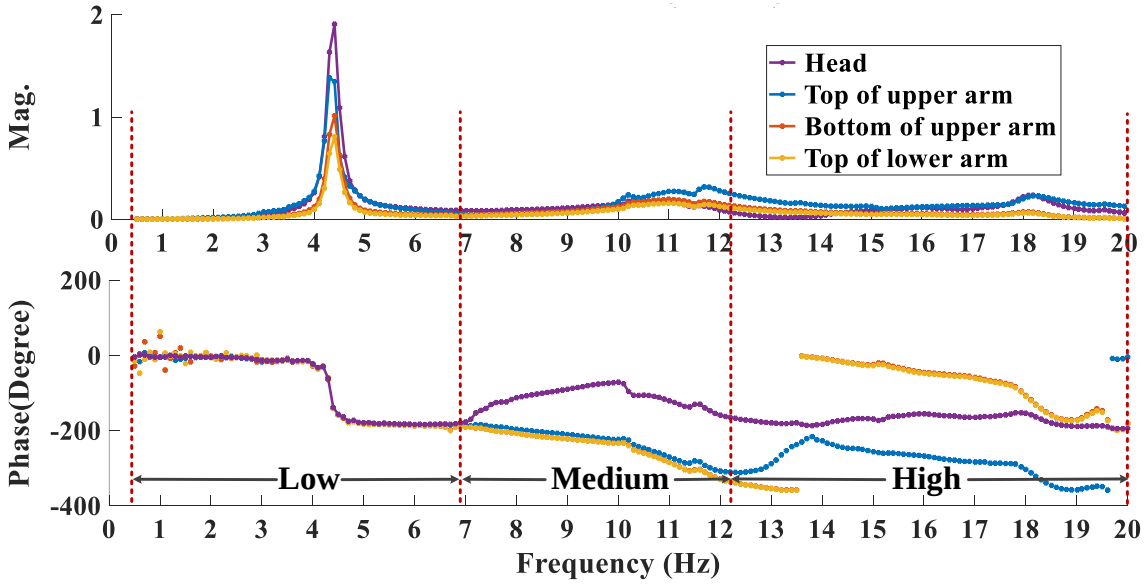

Figure 6.2 FRFs of the pantograph under 0.3 mm excitation

In the low-frequency area, the phase curves of the head and arms are the same, other than several noisy phase points. A lightly damped resonance appears, whose resonant frequency is about 4.4 Hz. The peak magnitudes decrease successively from the pantograph head to the lower arm.

Different from the phase curves starting from negative values as shown in Figure 6.1, when using 0.3 mm excitation, the phases are around zero before the first resonance occurs. Moreover, the phase shift of this resonance is around 180º. As the motion ratio that is defined as the travel distance of the piston and that of the pantograph head is designed as 1:17, low excitation level barely excites the pneumatic actuator. Therefore, it is assumed that the resonance in the low-frequency range is dominated by the behaviour of the head suspension and elbow joint. Accordingly, it can also be assumed that the heavily damped resonance shown in the low-frequency range in Figure 6.1 is mainly generated by the pneumatic actuator, while the head suspension and elbow joint are excited.

The medium-frequency range is from 6.9 to 12.2 Hz, where the phase of the pantograph head moves out from those of the arms. Therefore, the dynamic behaviour presented in this range is mainly generated by the freedom of the head suspension. The high-frequency range is from 12.2 to 20.0 Hz, where the phase of the top of the upper arm splits out from those of the remaining two locations. The dynamic behaviour shows up in the medium- and high-frequency ranges using 0.3 mm excitation is the same as that using decreasing excitation.

The FRFs measured with using 0.5 mm excitation are similar to those under 0.3 mm; the results are shown in Appendix A, Figure A.3.

6.1.3 FRF test using 1 mm excitation

A higher excitation level, 1 mm, was applied to the pantograph to inspect its dynamic behaviour; the FRFs are shown in Figure 6.3. According to the analysis principle applied above, the FRFs were also broken down into three parts in terms of the consistency of the phase curves.

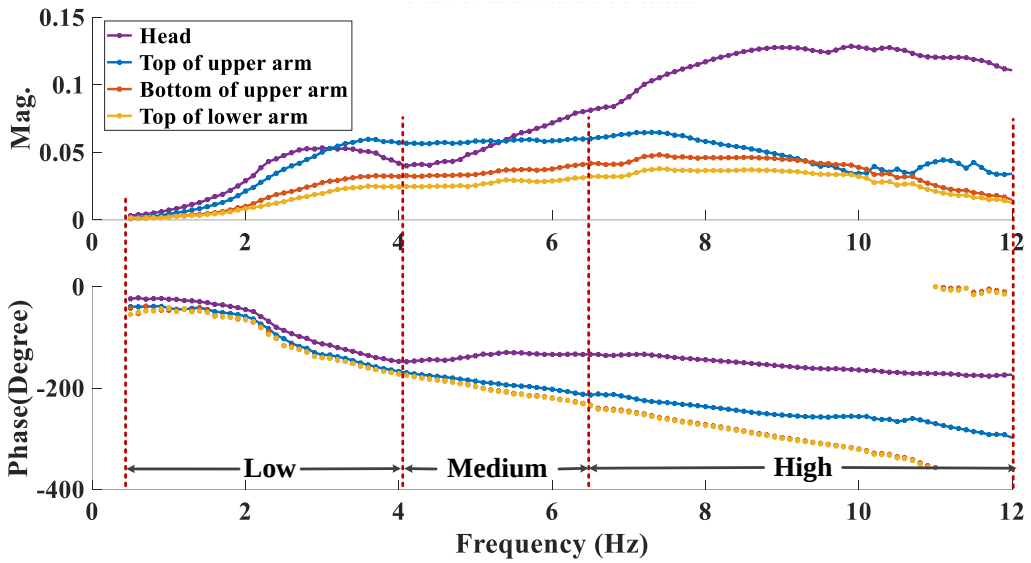

Figure 6.3 FRFs of the pantograph under 1 mm excitation

In the low-frequency range, from 0.5 to 4.0 Hz, all the parts move in-phase. A heavily damped resonance appears, where the variation in the phases and the magnitudes is gentle. Furthermore, the phase curves start with negative values. This phenomenon indicates that the nonlinear pneumatic actuator is excited. The variation in the FRF in medium- and high-frequency ranges is similar to that recorded under decreasing and 0.3 mm excitation. The dynamic behaviour of the pantograph in medium- and high-frequency ranges is dominated by the flexibility of the head suspension and the bending mode of the upper arm, respectively.

The characteristics of the dynamic behaviour of the pantograph in normal condition under 2 and 5 mm excitation levels are similar to those under 1 mm; the FRFs obtained using 2 and 5 mm excitations are shown in Appendix A, Figures A.4 and A.5.

In this thesis, the FRFs worked out using the accelerations of the pantograph head divided by the contact force that is named ‘head FRFs’.

6.1.4 Comments

In order to understand the dynamic behaviour of the pantograph under different excitation levels, in this section, the frequency-response tests were carried out on a healthy Pendolino high-speed

pantograph. The measurement data are only considered valid when the excitation arm and the pantograph head remain in contact. The frequency ranges covered by different excitations and the corresponding time consumption are detailed in Table 6.1

Table 6.1 Excitation strategies of and time taken for frequency-response tests

Excitations	Decreasing	0.3 mm	0.5 mm	1 mm	2 mm	5 mm
Frequency range (Hz)	0.5–20.0	0.5–20.0	0.5–20.0	0.5–12.0	0.5–9.8	0.5–7.5
Research profiles: time consumption (s)	1138.5	1138. 5	1138. 5	985.7	925.2	845.4

According to the variation in the phase profiles collected from different pantograph parts, FRFs can be divided into three sections: low, medium and high-frequency ranges. Various excitations actuate the pantograph parts differently; details are shown in Table 6.2.

Table 6.2 Frequency ranges with respect to different excitations

Excitations		Low-frequency		Medium-frequency		High-frequency	
		Fre. range (Hz)	Excited parts	Fre. range (Hz)	Excited parts	Fre. range (Hz)	Excited parts
Decreasing–amplitude		0.5–3.3	All parts	3.3–11.0	Head suspension mainly	11.0–20	Bending mode of the upper arm
Fixed–amp. (mm)	0.3	0.5–6.9	Except for the pneumatic actuator	6.9–12.2	Head suspension mainly	12.2–20	Bending mode of the upper arm
	0.5	0.5–4.5	Except for the pneumatic actuator	4.5–9.7	Head suspension mainly	9.7–20	Bending mode of the upper arm
	1	0.5–4.0	All parts	4.0–6.5	Head suspension mainly	6.5–12	Bending mode of the upper arm
	2	0.5–3.4	All parts	3.4–6.3	Head suspension mainly	6.3–9.8	Bending mode of the upper arm
	5	0.5–2.6	All parts	2.6–5.4	Head suspension mainly	5.4–7.5	Bending mode of the upper arm

When using the excitation levels of 0.3 and 0.5 mm, the low-frequency range presents the dynamic behaviour of the pantograph parts other than the pneumatic actuator. While using higher excitation levels, the pneumatic actuator is excited, and its behaviour can be inspected from the magnitude and phase curves in the low-frequency range. The dynamic behaviour of the tested pantograph displayed in the medium-frequency range is dominated by the flexibility of the head suspension under all excitations. The dynamics in the high-frequency range are generated by bending mode of the upper arm, which are not studied in this work. Thus, in this work, the FRFs in the low- and medium-frequency ranges are analysed for pantograph fault detection and diagnose purpose.

In the following sections, common pantograph faults or changes were emulated, tested and characterised using frequency-response test.

6.2 Changes to the head suspension

The pantograph head suspension connects the head to the upper parts. Any excitation applied to the pantograph head transmits to other parts through the head suspension. In this section, two changes were made to the pantograph head suspension, and then frequency-response tests were carried out to investigate the corresponding variation in FRFs. The two changes emulated: (i) Case 1, greasing the head suspension; and, (ii) Case 2, replacing the original torsion with another one 30% less stiff. The cases are the same as those tested by hysteresis tests in §5.2. In order to detect the changes to the head suspension using frequency-response test, it is better to avoid activating other parts. Therefore, relatively low-level excitations are suitable. However, in order to understand the variation in FRFs under all excitations resulting from faults or changes to the head suspension, and therefore to help with diagnosing other pantograph faults, all excitation strategies were used in this section.

6.2.1 FRF test using decreasing-amplitude excitation

Firstly, the decreasing excitation method was applied. Comparison of head FRFs in the conditions of greasing the head suspension and replacing the torsion bar to the reference is shown in Figure 6.4; the FRFs for other pantograph parts are shown in Figures A.6 to A.8 in Appendix A. The blue profile is the head FRF of the normal condition; the red and yellow profiles are the FRFs for Cases 1 and 2, respectively. Segmentation of the frequency ranges refers to the consequences in Table 6.2.

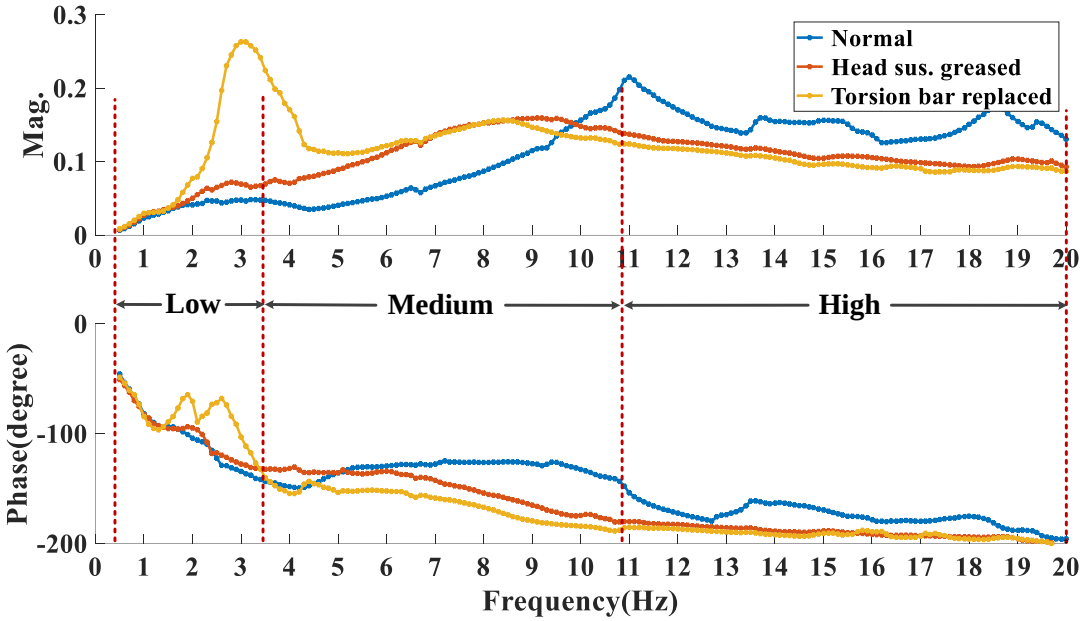

Figure 6.4 Head FRFs with changes to head suspension using decreasing–amp. excitation

In the low-frequency range (up to 3.3 Hz), the three FRFs were identical at frequencies lower than 1.6 Hz approximately. For frequencies higher than 1.6 Hz, differences appear in both the magnitude and phase curves. As changes were made to the head suspension, it can be assumed that the head suspension is excited above this frequency. Compared to the reference (blue), the condition of the greased head suspension (red) generates greater magnitudes. Therefore, the reduced friction in the head suspension produces less heavily damped resonance in the low-frequency range under decreasing excitation and varies the FRFs at the frequencies higher than 1.6 Hz. As the head is excited at the frequencies above 1.6 Hz, the variation in FRFs resulting from higher greasing level shows up in every frequency range.

Compared to the greased head suspension condition (red), the less stiff torsion bar condition (yellow) generates a much more lightly damped resonance at around 3.1 Hz in the low-frequency range. The resonance peak is approximately four times the magnitude with the head suspension greased. The variation in phase corresponding to this resonance is steep. In the medium-frequency range, as the condition of the head suspension is varied by the 'softer' torsion bar, the FRFs for the greased head suspension condition and replaced torsion bar

condition are still different. However, since the FRFs in the high-frequency range are dominated by the bending mode of the upper arm that is not varied in this case, the two FRFs tend to draw closer.

6.2.2 FRF test using 0.3 mm excitation

As analysed in §6.1, the excitation level of 0.3 mm is able to detect the dynamic behaviour of the head suspension without exciting the nonlinearities of the pneumatic actuator, therefore it is the prefered choice for detecting changes to the head suspension. The head FRFs measured under 0.3 mm excitation with two different changes made to the head suspension separately are shown in Figure 6.5; the FRFs of the pantograph arms are shown in Appendix A, Figures A.9 to A.11.

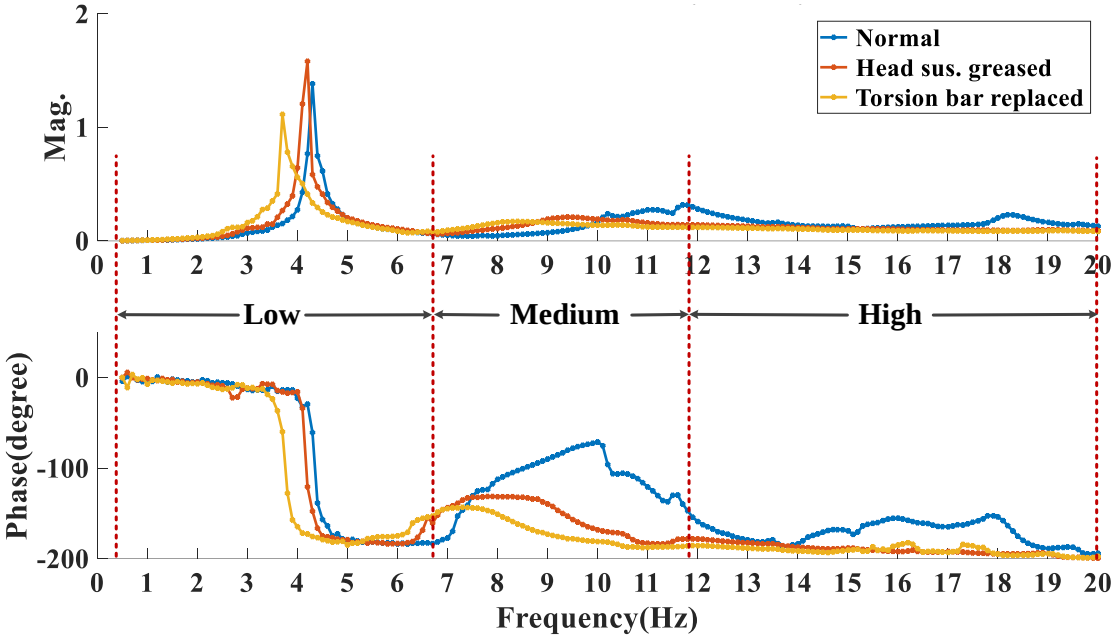

Figure 6.5 FRFs of the head with changes to head suspension using 1 mm excitation

In the low-frequency range, the resonant frequencies under the normal, greasing head suspension, and torsion bar replaced cases are at 4.3, 4.2 and 3.7 Hz, respectively. The oscillation frequency of a second-order system is given by:

$$f = \frac{1}{2\pi}\sqrt{\frac{k}{m}} \tag{6.1}$$

where k and m are stiffness and mass, respectively.

As the mass of the pantograph remains the same, the resonant frequency is altered by the stiffness of the head suspension. Greasing the head suspension and replacing the torsion bar both decrease the stiffness of the head suspension. The differences in the FRFs in the medium-frequency range in Figure 6.5 demonstrate changes to the pantograph suspension. In the high-frequency range, the differences in FRFs are similar to those obtained using decreasing excitation.

The conditions of head suspension greased and replacing torsion bar both decrease the frequency of the resonance in the low-frequency range, meanwhile vary the dynamic behaviour of the pantograph significantly in medium-frequency range. However, it is difficult to distinguish the two changes in this case. Therefore, a system identification approach is used to detect the variation in the stiffness and damping of the head suspension quantitatively.

6.2.2.1 Parameter estimation to lumped-mass models

As mentioned in Chapter 2, lumped-mass models are commonly used to reproduce the dynamic behaviour of the pantograph. However, only the parameters describing the top mass are related to the physical parameters of the pantograph head and head suspension. In this case, as the pneumatic actuator was not excited and the tests were carried out with changes only made to the head suspension, the variation in stiffness and damping ratio of the head suspension on greasing the bearings and replacing the torsion bar can be quantified by the estimation models that reproduce the recorded FRFs. In order to reproduce the lightly damped and anti-mode resonances in the low- and medium-frequency ranges on the FRFs in Figure 6.5, two-mass models were used.

The mass of the top block in the two-mass model, m_2, was considered as the actual mass of the pantograph head, 8.5 kg. The curve fitting technique applied to estimate the unknown

parameters, including m_1, k_1, k_2, c_1, and c_2, have been detailed in §4.3.3. Comparisons of the estimated outputs and measured FRFs are shown in Figure 6.6, the separate symbols and solid lines representing the actual measurements and the outputs of the estimation models, respectively.

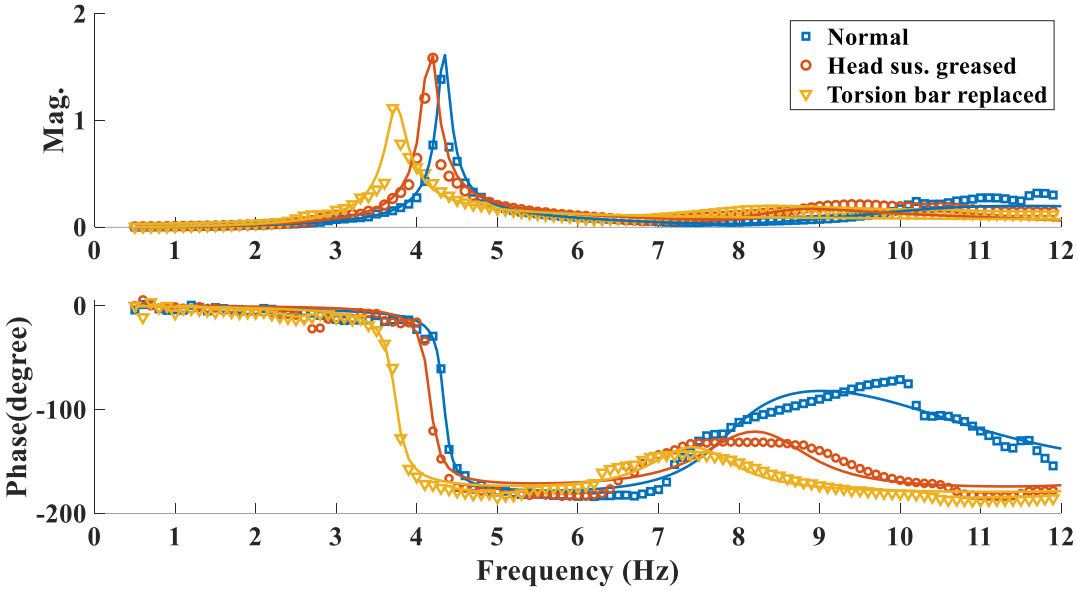

Figure 6.6 Comparison of measured and estimated FRFs for the pantograph head

The estimated parameters for the two-mass models that reproduce the three FRFs are presented in Table 6.3, where k_2 and c_2 represent the actual stiffness and damping coefficient of the head suspension respectively, and they are mainly affected by the greasing level of the head suspension and the material properties of the torsion bar. The values of m_1, k_1, and c_1 represent the characteristics of the pantograph parts below the head suspension. As changes only emulated to the head suspension, the values of m_1, k_1, and c_1 in Table 6.3 for the three conditions are relatively close to each other.

Table 6.3 Parameter estimation for pantograph 2-mass models

	Normal	Case 1: Head suspension greased	Case 2: Torsion bar replaced
m_2 (kg)	8.5	8.5	8.5
m_1 (kg)	15.7	13.7	13.5
k_2 (N/m)	20111	9593	6858
k_1 (N/m)	20687	24058	21945
c_2 (N·s/m)	81.1	14.4	2.8
c_1 (N·s/m)	31.1	87.3	99.8

Compared to the stiffness and damping coefficient of the head suspension for the normal condition, those for Case 1 decrease significantly. Accordingly, this system identification approach can be used to detect the variation in the greasing level of the head suspension. Comparing the values of k_2 and c_2 for Case 2 to those for Case 1, the 'softer' torsion bar reduces both the stiffness and the damping coefficient of the head suspension as well. As Case 1 and Case 2 were tested with the same greasing level, it is assumed that variation in k_2 and c_2 is affected by the torsion bar only. The stiffness of the original torsion bar is about 4.6 kN/m (equivalent at the contact point), and that of the 'softer' torsion bar is 30% less. In Table 6.3, the value of k_2 for Case 2 is 28.5% less than that for Case 1. Accordingly, the system identification approach used in this section is able to detect the variation in the stiffness of the head suspension resulting from the torsion bar accurately.

6.2.3 FRF test using 1 and 2 mm excitations

The head FRFs collected using 1 and 2 mm excitations with the head suspension greased and torsion bar replaced are shown in Figure 6.7 and Figure 6.8, respectively. The FRFs for other parts are shown in Appendix A, Figures A.12 to A.17. While using excitations greater than 1 mm, the pantograph head and frame suspensions and elbow joint are all excited in the low-

frequency range. Therefore, the FRFs in the low-frequency range is able to present the characteristics of all the critical connections. When the frame suspension is actuated, the phase curves start from negative angles.

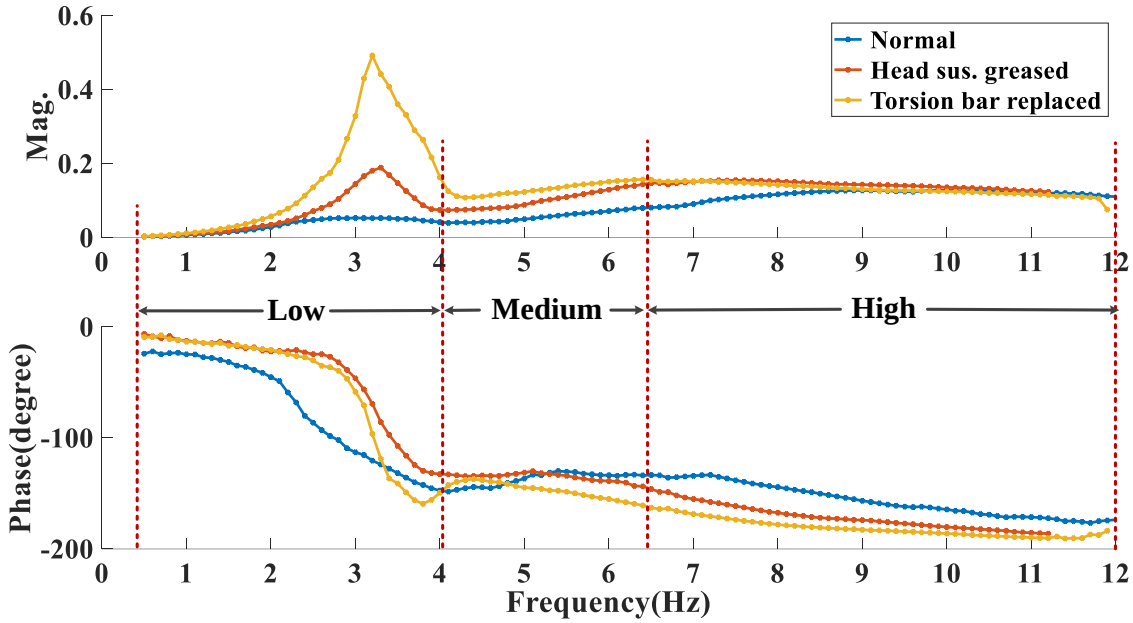

Figure 6.7 FRFs of the head with changes to head suspension using 1 mm excitation

According to the results in Table 6.3, the stiffness and damping coefficients for Cases 1 and 2 decrease successively. Therefore, in Figure 6.7, the resonance appearing in the low-frequency range for the normal condition (blue), Case 1 (red) and Case 2 (yellow) becomes increasingly lightly damped. Compared to Cases 1 and 2, the phase angles of the normal condition are lower. This indicates that the pneumatic actuator is excited less after the head suspension is greased; and therefore the pantograph becomes lightly damped.

In the medium- and high-frequency ranges, there is no obvious mode of vibration. Therefore, features cannot be extracted to detect and diagnose changes to the head suspension in these two frequency ranges. The FRFs for Cases 1 and 2 are similar to each other and not distinguishable in the whole frequency range of interest. Accordingly, the frequency test carried out with 1 mm excitation cannot be used to detect variation in the head suspension.

The FRFs recorded using 2 mm excitation, as shown in Figure 6.8, are able to represent the variations in FRF caused by changes to the head suspension apparently in both the low and

medium-frequency ranges. In the low-frequency range, similar to the results in Figure 6.7, the resonant peak for the normal condition and Cases 1 and 2 increases successively. In the medium-frequency range, the peak of the anti-mode resonance also increases successively as the stiffness of the head suspension decreases. However, the 2 mm excitation makes the pneumatic actuator more active. For the purposes of detecting the dynamic behaviour of the head suspension, the pneumatic actuator is not expected to be excited to avoid any unwanted variation in the FRFs.

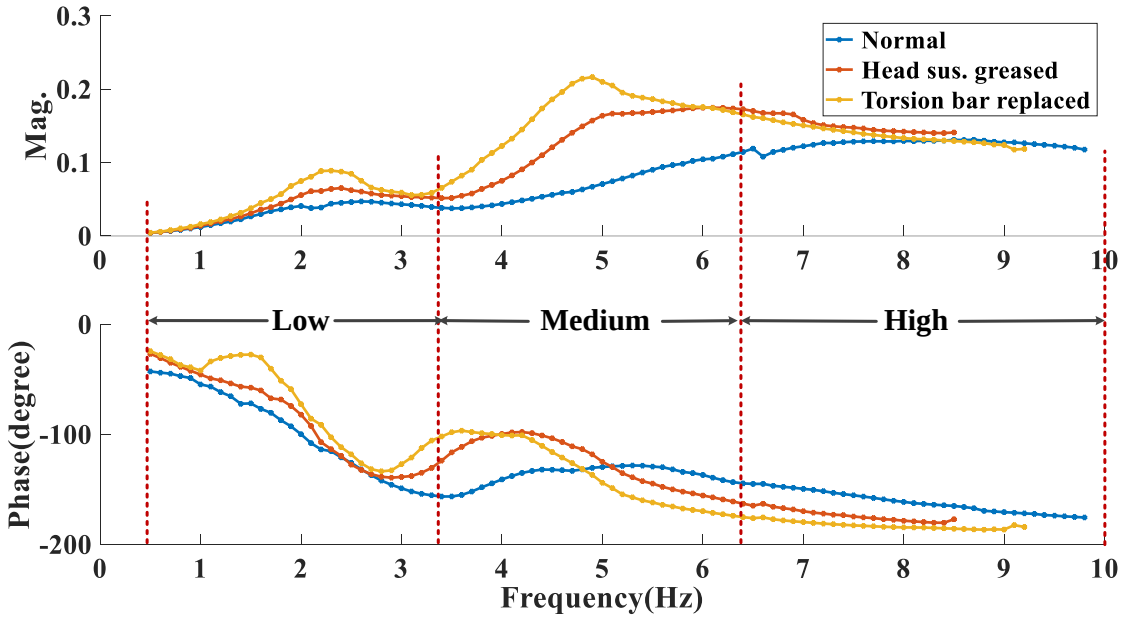

Figure 6.8 FRFs of the head with changes to head suspension using 2 mm excitation

6.2.4 FRF test using 5 mm excitation

When using 5 mm excitation to measure FRFs, contact loss happens at very low frequencies after changes made to the head suspension. The FRFs for Cases 1 and 2 in Figure 6.9 are not able to show sufficient features to detect and distinguish fault. As the variation in the greasing level is not easily reversible, in the following tests, 5 mm excitation therefore no longer operates.

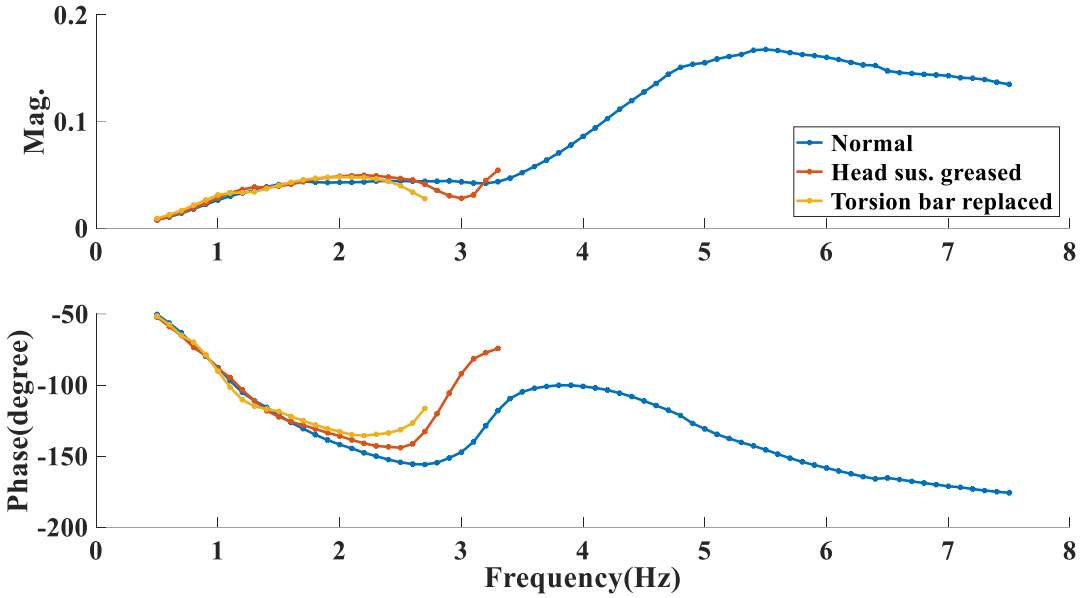

Figure 6.9 FRFs of the head with changes to head suspension using 5 mm excitation

6.2.5 Comments

In this section, various faulty features corresponding to the conditions of greasing the head suspension and replacing the torsion bar on FRFs were analysed. The changes to the head suspension vary the FRFs measured with decreasing and 0.3, 1 and 2 mm fixed-amplitude excitations. First of all, decreasing-amplitude excitation was applied to scan the dynamic behaviour of the pantograph in the entire frequency range of interest; then, fixed-amplitude excitations were used to address the most efficient excitation for fault detection and diagnosis.

The results show the variation in FRFs resulting from greasing the head suspension and replacing the torsion bar can be detected by frequency-response tests using any excitation levels. However, to avoid the dynamics of the pneumatic actuator being excited during the investigation of the status of the head suspension, the 0.3 mm excitation level is preferable.

6.3 Changes to the elbow joint chain

In Chapter 5, various degrees of tightness of the elbow joint outer chain have been detected using a static hysteresis test by observing the appearance and shape of the large scallops. However, if the large scallops do not appear on the hysteresis of a healthy pantograph, the

approach proposed in §5.3 cannot be used to inspect the condition of the outer chain. In order to develop a universal fault detection and diagnosis method to investigate the condition of the elbow joint, frequency-response tests were carried out. The cases tested in this section are the same as those in §5.3. The outer chain was loosened one, three and five turns, and then completely removed from the elbow joint. The features related to the different degrees of tightness of the outer chain can be extracted by comparing the FRFs for different cases to the reference.

6.3.1 FRF test using decreasing-amplitude excitation

Similar to the fault detection procedure used above, decreasing-amplitude excitation was applied firstly to detect whether fault or change to the pantograph exists; the recorded FRFs for the head are shown in Figure 6.10, and those for the pantograph arms as shown in Figures A.18 to A.20 in Appendix A. In Figure 6.10, the differences between the FRFs for different degrees of tightness of the outer chain are mainly shown in the low-frequency range and the initial area of the medium-frequency range. In the second half of the medium and high-frequency ranges, the FRFs are almost identical. It can be observed that as the tightness of the outer chain decreases, the resonant peak of the first resonance increases successively; meanwhile, the variation in phase corresponding to this resonance becomes steeper. This indicates that the pantograph becomes increasingly lightly damped.

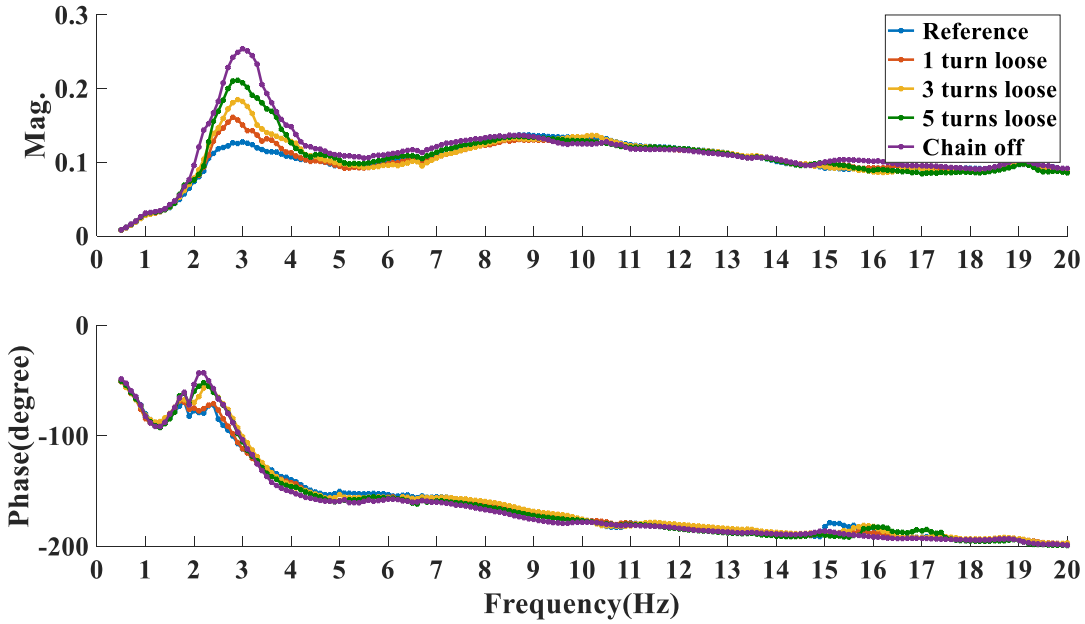

Figure 6.10 Head FRFs with changes to the outer chain under decreasing–amp. excitation

However, this variation in Figure 6.10 is similar to that in the FRFs obtained with less stiff torsion in Figure 6.4. As the pantograph is a nonlinear system, various excitations actuate different dynamics. Therefore, in order to extract the features that are able to distinguish the conditions of loosening the outer chain and replacing the torsion bar conditions, frequency-response tests using different fixed-amplitudes excitations were carried out.

6.3.2 FRF test using fixed-amplitude excitations

6.3.2.1 FRFs measured using 0.3 mm excitation

Excitation of 0.3 mm was applied to detect changes to the outer chain; the FRFs of the pantograph head are shown in Figure 6.11, and those of the arms are shown in Figures A.21 to A.23 in Appendix A. In Figure 6.11, the magnitude and phase curves almost overlap, and so cannot indicate any features clearly. Therefore, 0.3 mm excitation is not valid for detecting the condition of the elbow joint outer chain.

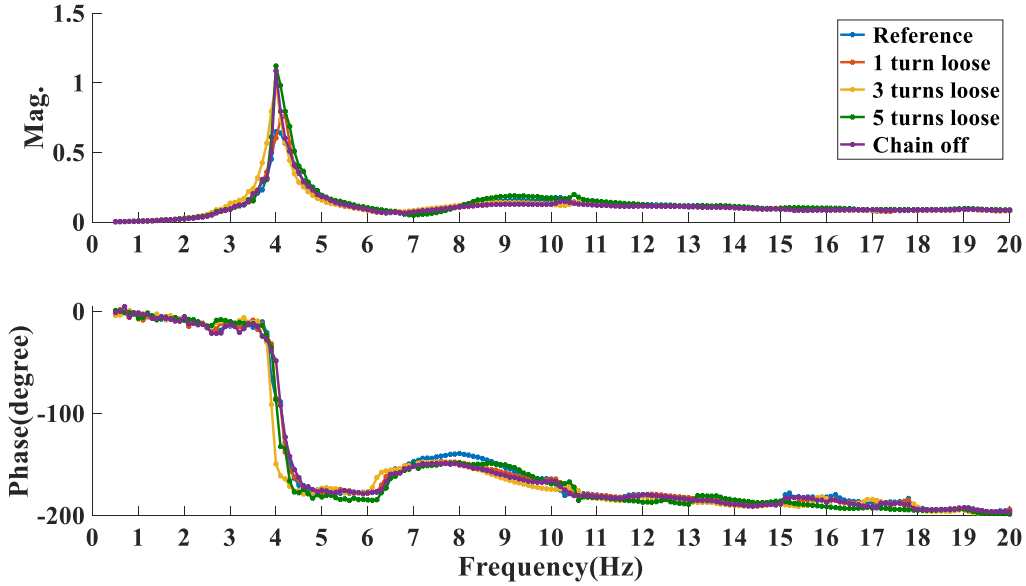

Figure 6.11 FRFs of the head with changes to the outer chain under 0.3 mm excitation

6.3.2.2 FRFs measured using 1 and 2 mm excitation

Excitations of 1 and 2 mm were applied to detect changes to the elbow joint outer chain; the FRFs of the head are shown in Figure 6.12 and Figure 6.13, and those for the pantograph arms are shown in Figures A.27 to A.32 in Appendix A.

6.3.2.2.1 1 mm excitation

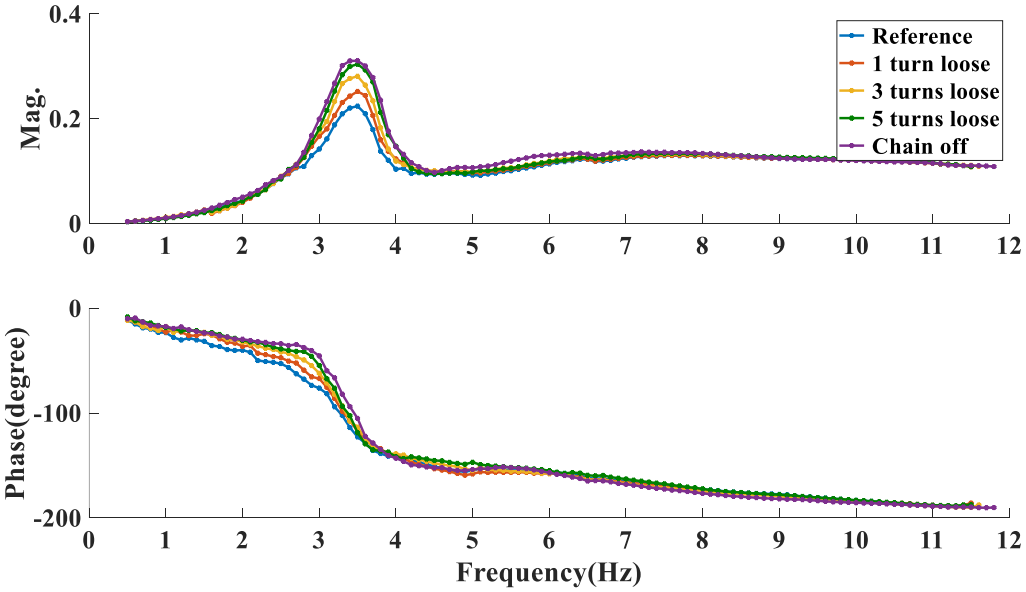

Figure 6.12 FRFs of the head with changes to the outer chain under 1 mm excitation

In Figure 6.12, the obvious differences in FRFs caused by varying the tightness of the outer chain appear in the low-frequency range. The successive decrease in the tightness of the outer

chain results in higher values of the resonant peak and steeper variation in phase angles. In the medium- and high-frequency ranges, the FRFs of the faulty conditions and the reference are almost identical. This phenomenon is similar to that for the FRFs obtained using decreasing excitation.

6.3.2.2.2 2 mm excitation

In Figure 6.13, the differences in FRFs occur in the low-frequency range and the front area of the medium-frequency range. The features in the low-frequency range are the same as those under decreasing and 1 mm excitation. Unlike the FRFs for changes to the head suspension conditions as previously shown in Figure 6.8, the tightness of the outer chain does not change the behaviour in the medium-frequency range significantly.

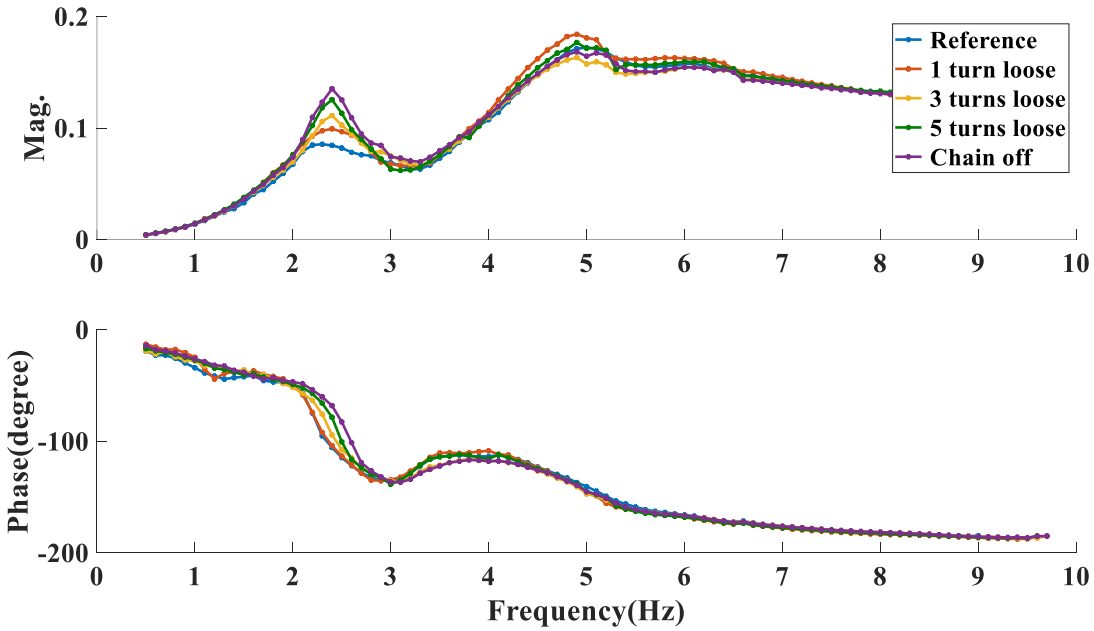

Figure 6.13 FRFs of the head with changes to the outer chain under 2 mm excitation

6.3.3 Comments

In this section, frequency-response tests were accomplished by varying the degree of tightness of the elbow joint outer chain. The results show that FRFs under any level of excitation, except for 0.3 mm, are able to detect variation in the degree of tightness of the outer chain. Furthermore, as the tightness of the outer chain decreases, the pantograph becomes increasingly

lightly damped. Variation in the FRFs shows clearly in the low-frequency range. Different from the FRFs for the conditions with changes to the head suspension, the tightness of the elbow joint outer chain does not affect the dynamic behaviour in the medium-frequency range significantly. In the real world, the worst case of the elbow joint outer chain is breakage, which is equivalent to the testing condition of removing the chain. However, the differences between the FRFs for this condition and the reference are not significant. Furthermore, having the outer chain with a few turns loose does not vary the magnitude and phase curves significantly. As the FRF is sensitive to any changes in the pantograph and environmental factors, the variation in FRFs satisfy the features extracted in this section may be caused by other reasons. Consequently, the frequency-response test is able to investigate the tightness of the elbow joint, but not robustly.

6.4 Changes to the pneumatic actuator

The pneumatic actuator is the major component of the frame suspension. It supplies the uplift force to maintain the contact between the pantograph and contact wire. Fault diagnosis for the pneumatic actuator has been accomplished efficiently using the hysteresis test in §5.4. However, to address the most efficient approach for detecting and diagnosing the condition of the pneumatic actuator, in this section, the FRFs were measured while varying the condition of the pneumatic actuator under different excitation strategies. Two types of condition were tested: the first by replacing the original pneumatic actuator with a leaking one, and the second by sealing the top of the venting plug to different extents.

6.4.1 FRFs obtained with a leaking actuator

The pneumatic actuator is far from the head of a pantograph. In order to explore its dynamic behaviour, relatively large excitation levels should be applied to excite the pneumatic actuator during frequency-response tests. Therefore, the 0.3 and 0.5 mm excitation levels were not used.

6.4.1.1 FRF test using decreasing excitation

Similar to the frequency-response testing procedure described above, decreasing excitation was applied firstly, to accomplish a quick scan of the FRFs through the entire frequency range of interest; the FRFs for the pantograph head are shown in Figure 6.14, and those for other parts are shown in Figures A.30 to A.32 in Appendix A.

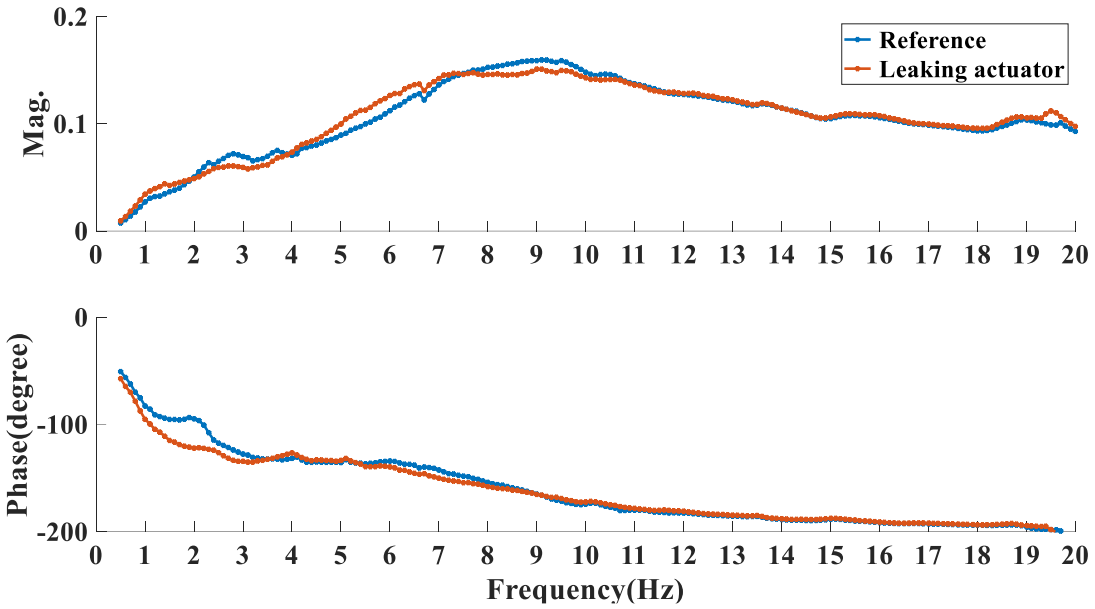

Figure 6.14 FRFs of the head using decreasing excitation: reference and leaking actuator

Regarding the conclusions made in the previous sections, while using decreasing excitation, the dynamics of the frame suspension mainly show up in the low-frequency range, 0.5–3.3 Hz. In Figure 6.14, the phase curve for the leaking pneumatic actuator (red) is obviously lower than the reference (blue). However, the difference between the magnitude curves is modest. The differences in magnitude and phase in the medium-frequency range indicate that the pneumatic actuator is still excited in this frequency range. Within the high-frequency range, the phase profiles of the two tend to be close.

6.4.1.2 FRF test using fixed-amplitude excitations

Ideally, higher excitation levels activate the pneumatic actuator more, and therefore allow variation in FRF to be inspected clearly. In order to address the most efficient excitation

methods for detecting the leakage within the pneumatic actuator, 1 and 2 mm excitations were applied; the head FRFs under the two excitation levels are shown in Figure 6.15 and Figure 6.16, respectively. The other FRFs are shown in Figures A.33 to A.38 in Appendix A.

6.4.1.2.1 FRFs measured using 1 mm excitation

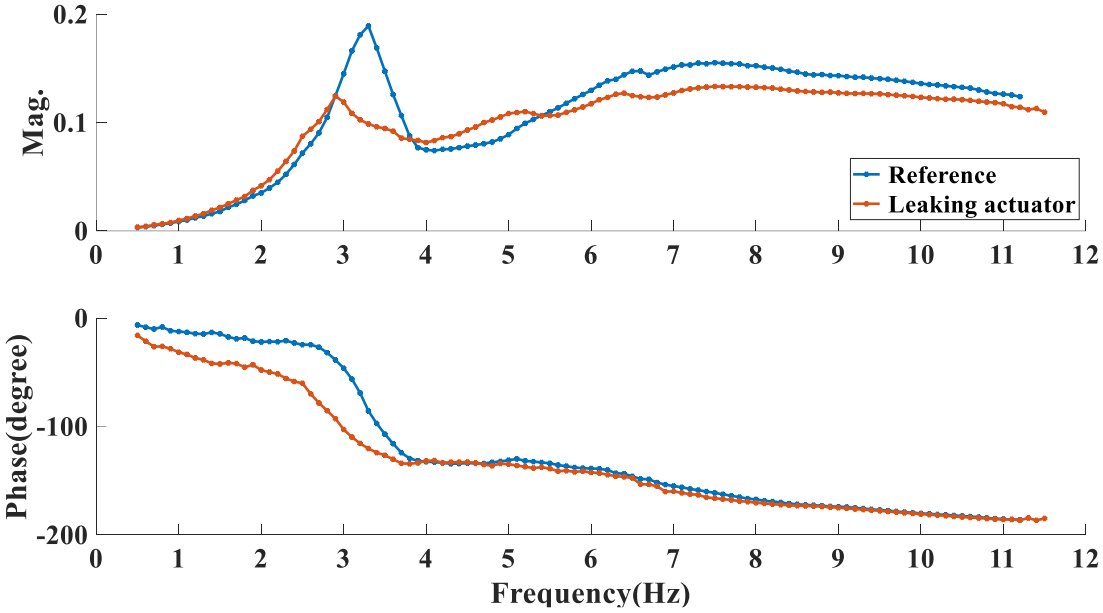

Figure 6.15 FRFs of the head using 1 mm excitation: reference and leaking actuator

In Figure 6.15, the phase angle for the actuator leakage condition (red) is less than that of the reference (blue) in the low-frequency range (0.5–4.0 Hz); in the medium- (4.0–6.5 Hz) and high-frequency (6.5–12.0 Hz) ranges, the phase profiles in the two situations are nearly the same. As the magnitude is more sensitive, the variations of the magnitude profiles in the medium- and high-frequency ranges are not considered as fault features. Accordingly, 1 mm excitation actuates the pneumatic actuator adequately in the low-frequency range, but not in the medium and high-frequency ranges.

The frequency of the first resonance dropped from 3.3 to 3.0 Hz after the original pneumatic actuator was replaced by the leaking one; meanwhile, the magnitude dropped by 34.2%. Furthermore, the variation in the phase curve corresponding to the resonance under the leakage condition is less steep than that under the normal condition. This demonstrates that leakage

increases the damping of the pantograph, and therefore the pantograph becomes heavily damped. Based on the features shown in Figure 6.15, the frequency-response test using 1 mm excitation is able to detect leakage of the pneumatic actuator effectively.

6.4.1.2.2 FRFs measured using 2 mm excitation

The head FRFs measured using a 2 mm excitation level are shown in Figure 6.16. As the 2 mm excitation actuates the pneumatic actuator more deeply, the differences between the reference (blue) and the FRF for the leaking actuator show in both low- and medium-frequency ranges. However, the medium-frequency range was used to detect and diagnose the changes to the head suspension. Therefore, 2 mm excitation is not practical for investigating the dynamic behaviour of the frame suspension.

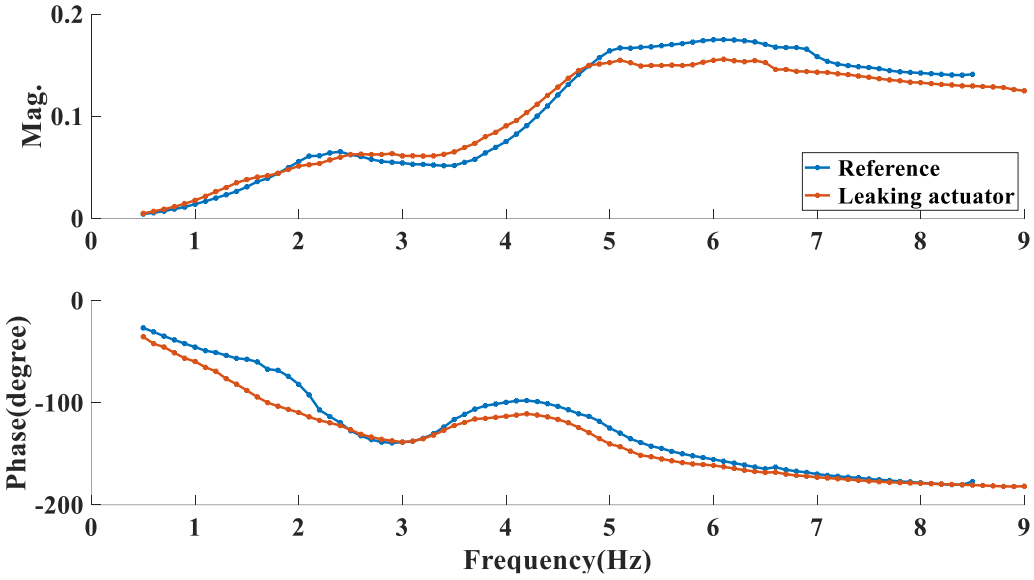

Figure 6.16 FRFs of the head using 2 mm excitation: reference and leaking actuator

6.4.1.3 Comments

In this section, frequency-response tests were implemented to investigate leakage of the pneumatic actuator. Three levels of excitations were applied, decreasing excitation, 1, and 2 mm excitation amplitudes. By comparing the FRFs for the leakage condition to the reference, it was shown that all three excitations are able to detect the fault. However, as a pantograph is a nonlinear system, actuation of different nonlinearities depends on the excitation amplitude.

The FRFs recorded under 1 mm excitation is able to show the features of leakage distinctly in the low-frequency range without involving the features of other issues. Therefore, when using FRFs to evaluate the performance of a pneumatic actuator after decreasing excitation is accomplished, the 1 mm excitation strategy is the best choice.

6.4.2 FRFs obtained by sealing the venting plug

The permeability of the venting plug affects the dynamic behaviour of the pneumatic actuator and therefore modifies the dynamic behaviour of the pantograph when the pneumatic actuator is excited. If the permeability of the venting plug is lower than expected, air cannot be expelled from the pneumatic actuator properly. Therefore, the pneumatic actuator is more resistant to motion. In §5.4, changes to the venting plug were detected by hysteresis tests carried out at high speeds. In this section, the same cases were tested using a frequency-response method. Two cases were considered: half and entire sealing of the top piece of the venting plug. Regarding the conclusion made in the previous section, the 1 mm excitation is most efficient for investigating changes to the pneumatic actuator. Therefore, this excitation level was applied to detect the variation in the dynamic behaviour of the tested pantograph caused by different permeabilities of the venting plug; the head FRFs are shown in Figure 6.17, and the FRFs for the other parts are shown in Figures A.39 to A.41 in Appendix A.

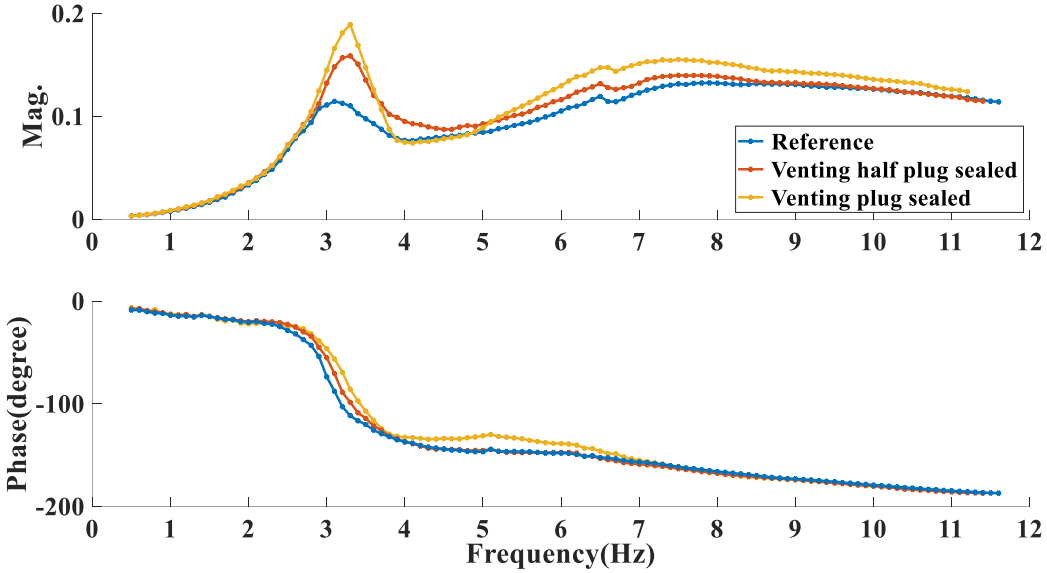

Figure 6.17 FRFs of the head with changes to the venting plug under 1 mm excitation

In Figure 6.17, the magnitude of the resonant peak decreases as the venting plug is half and entirely sealed successively in the low-frequency range. This demonstrates that the damping ratio of the pantograph decreases as the permeability of the venting plug decreases. However, the variations in phase angles are not significant. Furthermore, compared to the hysteresis test, the frequency-response test is time-consuming. Therefore, so far, it is better to explore the degradation of the venting plug using the hysteresis test.

6.5 Conclusions

In this chapter, in order to extract the features corresponding to common pantograph faults or changes in the frequency domain, and therefore realise pantograph fault diagnosis, frequency-response tests were carried out under various excitations. As the pantograph is a nonlinear system, its dynamic behaviour varies with excitation amplitude. In this chapter, different fixed-amplitude sine waves in the frequency range of 0.5–20 Hz were used. Other than using conventional fixed-amplitude excitation, a new decreasing-amplitude excitation method is proposed to realise a primary detection for the occurrence of fault or change to the pantograph. Following this, selected fixed-amplitude tests can be carried out to diagnose the fault or change.

In order to understand the dynamic behaviour of the pantograph with respect to different excitation strategies, the FRFs were collected for all the critical parts of the pantograph, including the head and frame suspensions and elbow joint. FRFs under any excitation strategy can be divided into three sections regarding the consistency of the phase curves of the pantograph head, the top and bottom end of the upper arm, and the top end of the lower arm.

The low-frequency range presents the dynamic behaviour of the head suspension and the elbow joint while using 0.3 and 0.5 mm excitations. When using other excitations, the low-frequency range represents the dynamic behaviour of all the critical pantograph parts. The medium- and high-frequency ranges suggest the performance of the head suspension and the bending mode of the upper arm, respectively. According to this principle and the features extracted for different faults or changes, the frequency-response tests can be used to detect and diagnose pantograph faults.

The 0.3 mm excitation level is preferable to detect changes to the head suspension. The variation in the degree of tightness of the elbow joint outer chain can be detected by the frequency-response tests under the excitation levels above 0.3 mm or the decreasing amplitude test. The 1 mm excitation level works efficiently to inspect leakage of the pneumatic actuator. However, compared to hysteresis test, frequency-response test is not efficient in detecting the degradation of the venting plug.

The observations made in this chapter using frequency-response tests will be used in Chapter 8 to develop a rapid testing procedure for detecting and diagnosing common pantograph faults or changes.

CHAPTER 7 CHANGING-GRADIENT TEST

7.1 Introduction

As mentioned in §4.4, the changing-gradient test is proposed to reproduce the pantograph response to the periodic 'V'-shape excitation that results from the variation in stiffness of the contact wire. Contact loss is more likely when the excitation reverses direction (O'Connor et al., 1997). Changes or faults to the pantograph vary its dynamic behaviour and therefore may result in a higher percentage of contact loss. Therefore, it is necessary to understand the impacts of different changes and faults to the pantograph on its response to the 'V'-shape excitations. Regarding this, the changing-gradient tests were carried out with various common faults or changes were made to the pantograph. The oscillation frequencies and damping ratios of the measured contact force can be extracted using the conventional system identification technique that has been detailed in §4.4.4. By comparing the features extracted from the faulty measurements to the references, some of the decisive faults or changes can be detected and diagnosed.

However, in some cases, the responses of the pantograph with different faults or changes may be similar in the time domain. The oscillation frequencies and damping ratios extracted for these conditions are close to each other, in which case the conventional system identification method cannot distinguish and diagnose these faults or changes. Accordingly, a sparse stacked autoencoder was applied to classify the measurement without extracting physical features. The results of the sparse stacked autoencoder algorithm show a high degree of accuracy for fault classification.

7.2 Feature analysis

7.2.1 Results of the changing-gradient test for a new pantograph

In this section, changing-gradient tests were carried out on a new Pendolino high-speed pantograph at the excitation speeds of 50, 100, 200, 300, 400 and 500 mm/s. The contact forces were smoothed by cubic spline functions as detailed in §4.4.2. The smoothed signals are shown in Figure 7.1 (apart from the contact force measured at 50 mm/s excitation which is too long to fit on the figure).

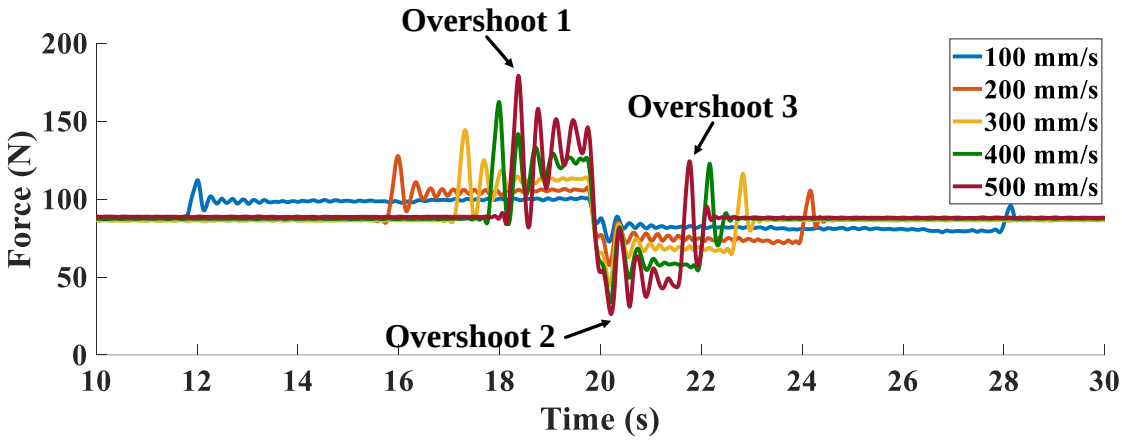

Figure 7.1 'V' test under the normal condition

The excitation begins at a constant height for some time; then the excitation bar presses the pantograph in a downwards direction at the required speed. When a sudden excitation is applied to the pantograph, the stiction on each joint and bearing results in an overshoot of the contact force, named as 'Overshoot 1' in Figure 7.1. After the pantograph is actuated, the contact force oscillates around a relatively constant value. As the excitation speed increases, the overshoot of the contact forces grows significantly.

When the pantograph has moved down 800 mm, the excitation changes direction until the original height has been reached. As kinetic energy exists in the pantograph, the pantograph cannot change the direction of motion immediately. Therefore, the contact force decreases to the lowest value, called 'Overshoot 2'. Following this, the contact force oscillates around

another relatively constant value until the excitation bar reaches the original height. When the excitation bar stops at the original height, the pantograph is forced to change its state of motion that results in another overshoot of contact force, 'Overshoot 3'.

For each changing-gradient test, the excitation speed is a single value but reverses direction at the lowest height. Therefore, the response of the pantograph to a 'V'-shape profile can be considered as two step responses during the descent and ascent of the excitation. The force overshoots, oscillation frequency and damping ratio are determined by the dynamic behaviour of the system (Ogata, 1970). In order to work out the values of these parameters accurately, system identification was accomplished by reproducing the measured contact forces with lumped-mass models using the technique has been detailed in §4.4.4. The input of the estimation model is the excitation speed signal. By comparing the contact force overshoots, oscillation frequencies and damping ratios extracted for different conditions, the fault features can be defined.

7.2.2 Feature extraction by system identification

The changing-gradient tests were performed on the new pantograph at various excitation speeds. The critical features extracted from the smoothed experimental data are considered as references. The overshoots in contact force, oscillation frequencies and the damping ratios are detailed in Table 7.1 and plotted with respect to the excitation speed in Figure 7.2 *a* and *b*, respectively.

Table 7.1 Feature extraction for the new pantograph using changing-gradient tests

Excitation speed (mm/s)	Down			Up			
	Damping ratio	Oscillation frequency (Hz)	Over-shoot 1 (N)	Damping ratio	Oscillation frequency (Hz)	Over-shoot 2 (N)	Over-shoot 3 (N)
50	0.01	4.87	104.4	0.05	4.99	80.0	89.1
100	0.03	4.75	112.2	0.06	4.85	72.6	95.5
200	0.12	3.74	122.9	0.14	4.20	59.1	101.8
300	0.14	2.81	144.6	0.15	3.52	44.6	116.42
400	0.10	2.65	161.9	0.11	3.44	33.7	121.7
500	0.07	2.88	177.9	0.08	3.41	25.3	125.2

In Figure 7.2, it shows that the trends of the oscillation frequency with respect to speed under downwards and upwards excitation are similar, and the same is true for the damping ratio. For excitation speeds lower than 300 mm/s, the oscillation frequencies decrease while the damping ratios increase; when the pantograph is excited at higher speeds, the oscillation frequencies stay in a relatively similar range and the damping ratios decrease.

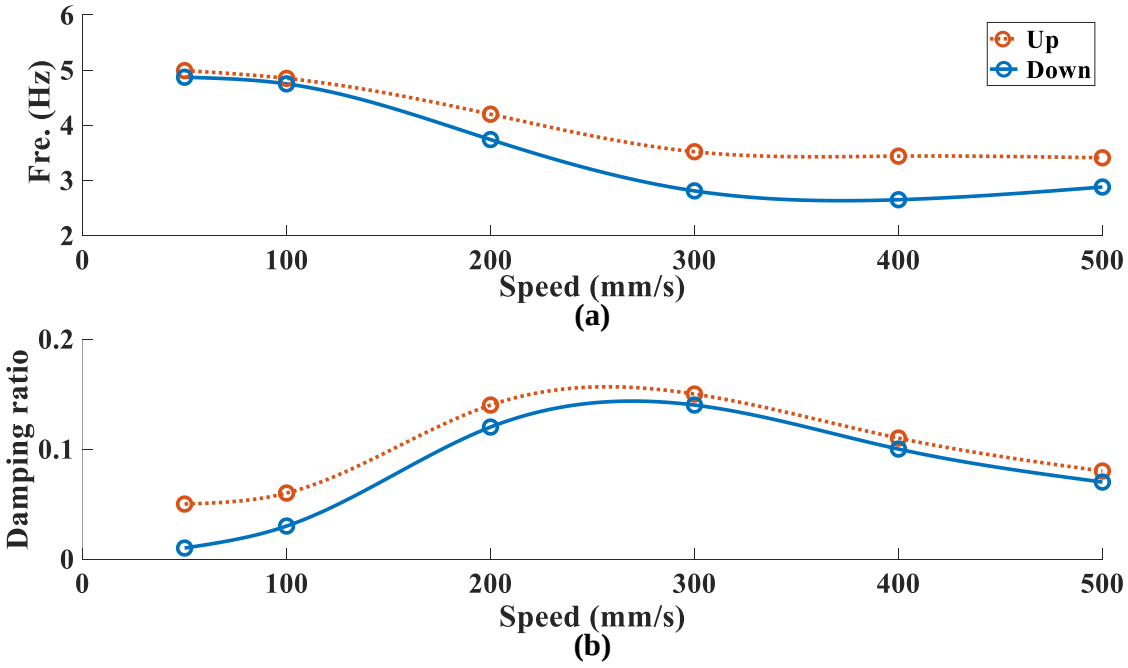

Figure 7.2 Oscillation frequency and damping ratio under the normal condition

The contact force overshoots with respect to excitation speed are shown in Figure 7.3. As the excitation speed grows, the values of Overshoot 1 and 3 increase, and that of Overshoot 2 decreases. Furthermore, the overshoots of contact force are proportional to excitation speed approximately.

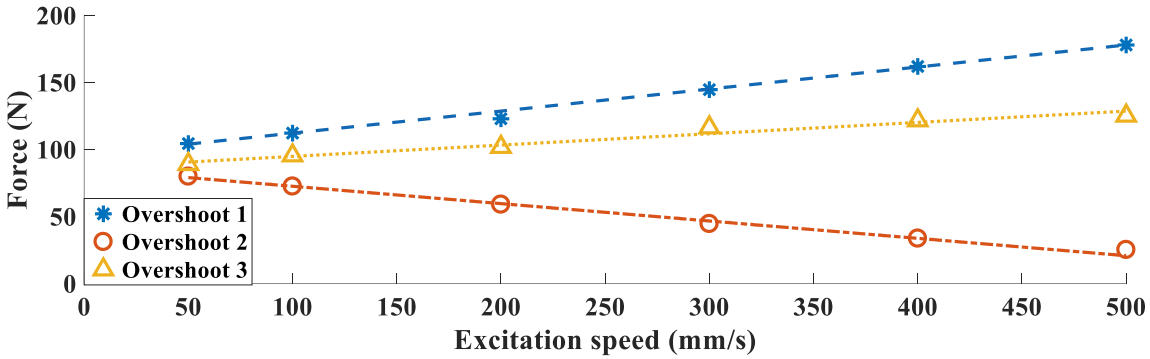

Figure 7.3 Overshoot forces for the reference case

7.3 Changing-gradient tests under faulty conditions

The overall research objective of this work is to develop a rapid testing procedure for pantograph fault detection and diagnosis. In order to achieve this purpose, different tests need to be carried out to inspect the same faults, so that the efficiency of each test can be compared, and it is therefore possible to work out the most efficient testing procedure. In this section, some of the pantograph faults or changes emulated in Chapters 5 and 6 were tested using the changing-gradient test. Features that can be used to detect and diagnose faults are extracted and then compared to the reference.

7.3.1 Replacing the torsion bar and pneumatic actuator

7.3.1.1 Testing results in the time domain

The hysteresis and frequency-response tests were carried out by replacing the original torsion bar with a less stiff one and changing the original pneumatic actuator to a leaking one in Chapters 5 and 6. In this section, the novel changing-gradient tests were applied under these

two circumstances. The filtered experimental data of the changing-gradient tests at different speeds are shown in Figure 7.4 and Figure 7.5, respectively.

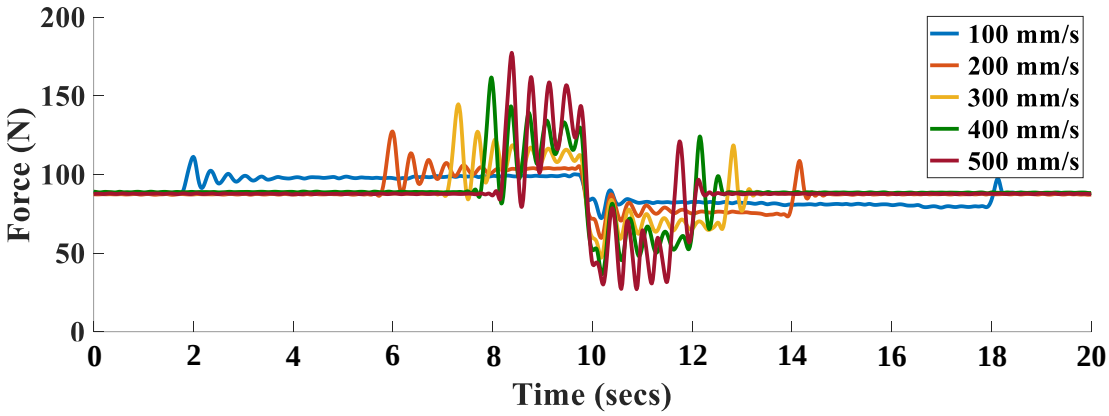

Figure 7.4 Results of changing-gradient test with less stiff torsion bar

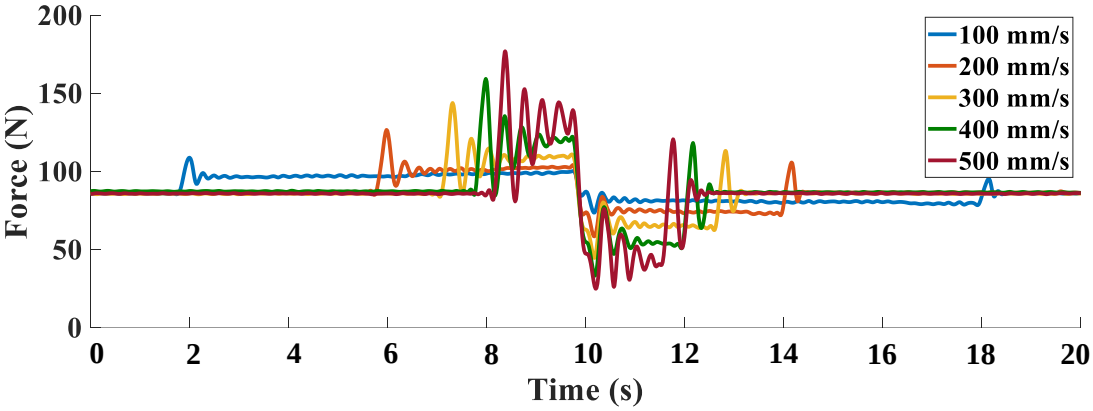

Figure 7.5 Results of changing-gradient test with leaking actuator

The results of the changing-gradient tests under the original condition and on replacing the torsion bar and the pneumatic actuator are similar in the time domain. To diagnose the different conditions of the pantograph, the contact force overshoots, oscillation frequencies and damping ratios were extracted by system identification and compared to the reference.

7.3.1.2 Feature extraction

The values of the overshoot contact forces, oscillation frequencies and damping ratios extracted for the conditions of replacing the torsion bar and changing the pneumatic actuator are shown in Appendix A, Tables A.5 and A.6, respectively. The ‘Overshoot 1’ for the three conditions with respect to the excitation speed is shown in Figure 7.6. It shows that the ‘Overshoot 1’ for

the faulty conditions are close to each other and still proportional to the excitation speed and similar to the references. The overshoot forces recorded at the same excitation speed for the three conditions are close (in Tables A.5 and A.6). Therefore, in this case, the force overshoot is not able to be used to diagnose faults.

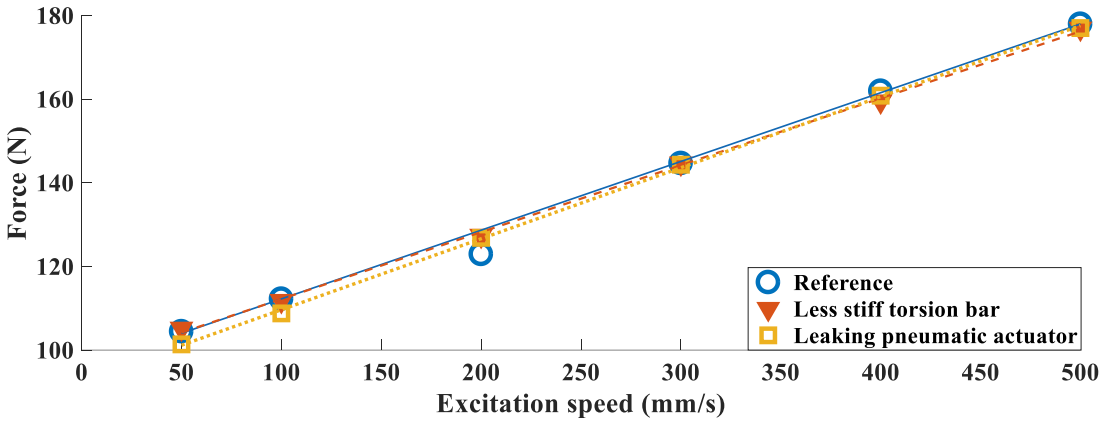

Figure 7.6 Values of Overshoot 1 for the three conditions

The oscillation frequencies and the damping ratios for each excitation speed during descent and ascent are plotted in Figure 7.7 and Figure 7.8, respectively. The trends of the oscillation frequencies and damping ratios for the condition with leaking actuator (yellow squares) are similar to the references (blue circles). However, the values of the oscillation frequencies with the leaking actuator are slightly lower than the references at excitation speeds lower than 300 mm/s; at other excitation speeds, the oscillation frequencies with the leaking actuator and the references are similar. Meanwhile, the damping ratios with the leaking actuator are higher than the reference results, particularly while the pantograph goes up. The results indicate that the leakage problem slows the pantograph response slightly when the pantograph is excited at a relatively low speed; moreover, the leaking pneumatic actuator makes the pantograph less lightly damped.

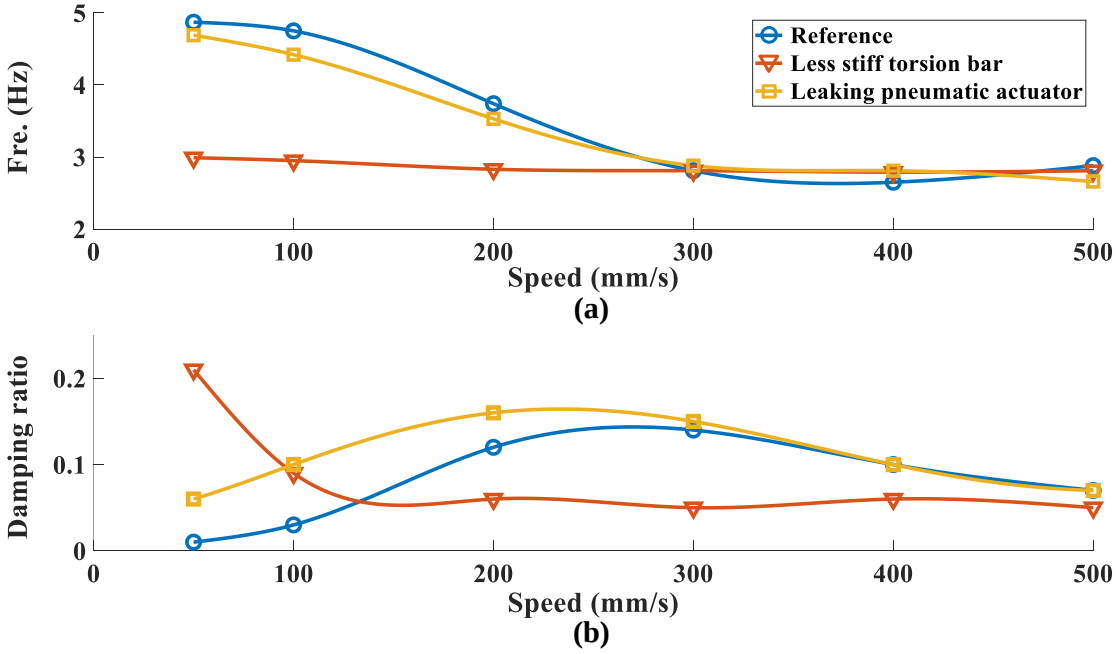

Figure 7.7 Oscillation frequencies and damping ratios during descent

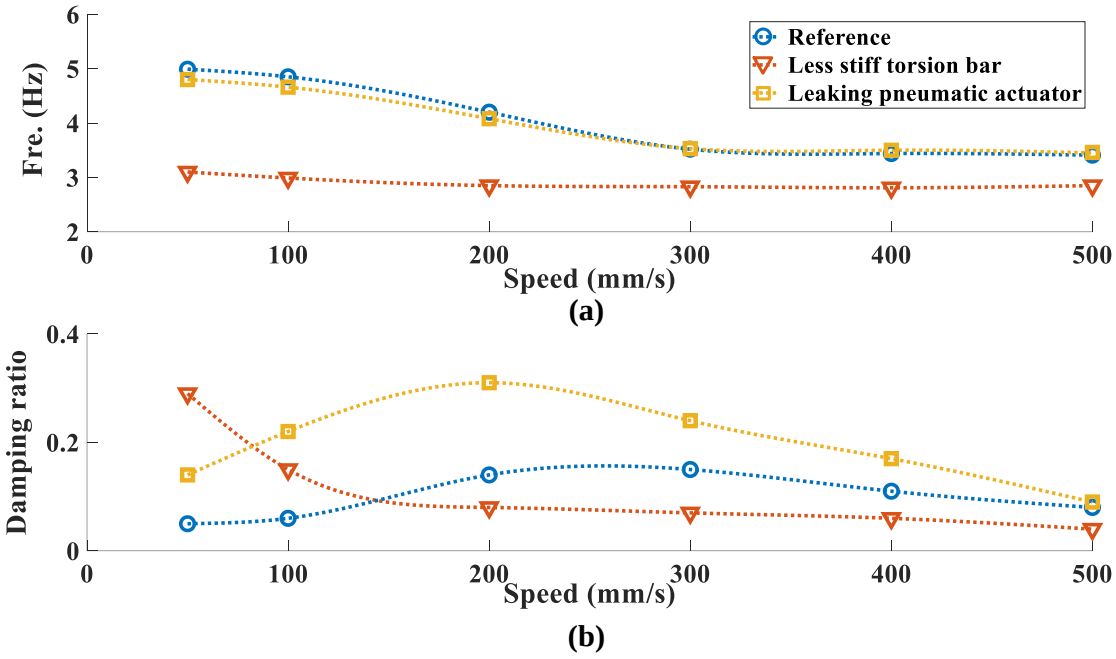

Figure 7.8 Oscillation frequencies and damping ratios during ascent

The trends of the oscillation frequencies and damping ratios for the condition with less stiff torsion bar (red triangles) are different from those for the normal condition. The oscillation frequencies under different speeds vary within a small range no matter whether the pantograph is pressed down or raised up. The damping ratio decreases as the speed increases at low excitation speeds. For the excitation speeds higher than 200 mm/s, damping ratios are

maintained at a relatively steady value. Accordingly, the 'soft' torsion bar decelerates the pantograph response, particularly when the pantograph goes up. Meanwhile, it turns the pantograph into a less lightly damped system under relatively low-speed excitation speeds, and turns the pantograph into a more lightly damped system under high-speed excitations. As a result, the less stiff torsion bar significantly varies the response of the pantograph to sudden or high-frequency excitations that happen commonly in actual operating conditions.

7.3.2 Venting plug sealed

In order to detect the effect of degradation of the venting plug on the response of the pantograph to the variation in stiffness of the contact wire, the changing-gradient tests were carried out with the top of the venting plug half and entirely sealed. The experimental results in the time domain for these two circumstances are shown in Figure A.42 in Appendix A and Figure 7.9, respectively. In Figure 7.9, it is shown that with the venting plug sealed, while the pantograph is suppressed, the contact force oscillates across the trend that increases slowly. While the pantograph goes up, the contact force oscillates across the trend that decreases significantly. A similar phenomenon appears while the venting plug is half-sealed (in Figure A.42). Accordingly, the degradation of the venting plug affects the up force more than the down force.

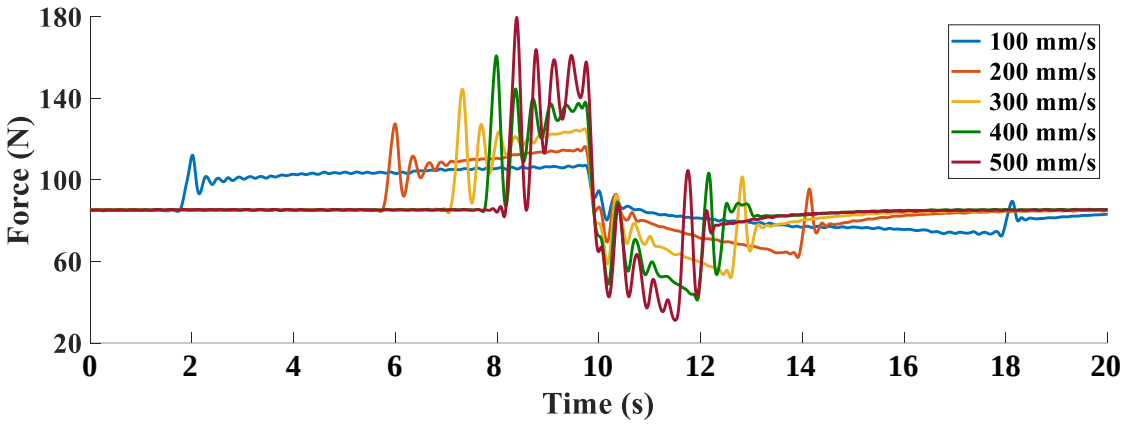

Figure 7.9 Results of changing-gradient test with venting plug sealed

As the contact force oscillates around the increasing and decreasing trends while the pantograph is compressed and goes up, linear lumped-mass models cannot reproduce the contact forces shown in Figure 7.9. Therefore, the conventional system identification approach used in the section above are not suitable for this case. However, degradation of the venting plug can be detected by the hysteresis tests under relatively high excitation speeds as mentioned in §5.4.

7.3.3 Changes to the elbow joint chain

The changing-gradient tests were also accomplished by differing the attachment point of the elbow joint outer chain. Changes to the tightness of the outer chain can be detected by the static hysteresis and frequency-response tests described in Chapters 5 and 6. However, the hysteresis test is only valid when large scallops show up on the hysteresis curve of a healthy pantograph; while variation in FRF with loosening the outer chain is not quite noticeable on the phase curves. In order to find a universal and robust testing method for detecting the tightness of the elbow joint chain, changing-gradient tests were carried out.

The contact forces measured with the outer chain loosened by one turn and totally removed at an excitation speed of 500 mm/s are shown in Figure 7.10. In this figure, the measurements for the two conditions are almost identical. Accordingly, it is difficult to use the conventional system identification method to extract the features for diagnosing different degrees of tightness of the outer chain. Therefore, an advanced technique, deep learning, was applied to classify the measurements recorded with different degrees of tightness.

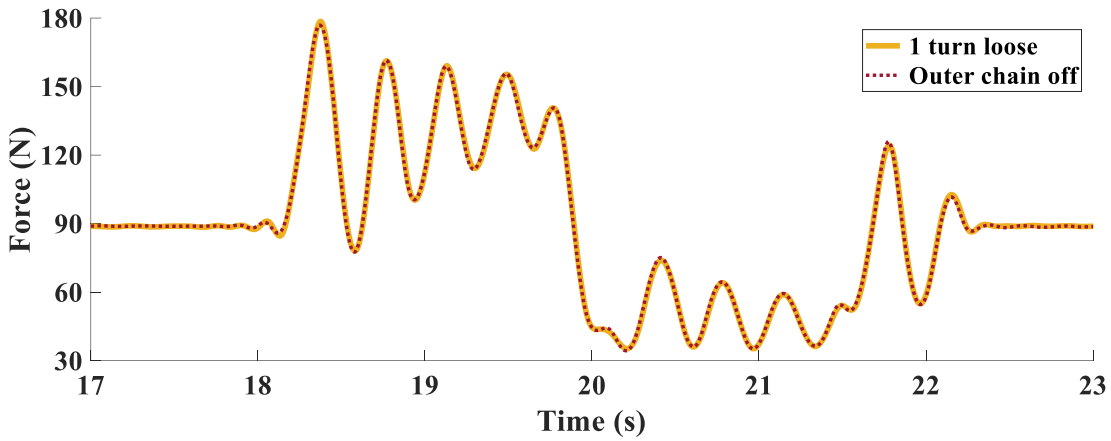

Figure 7.10 Changing-gradient tests with loosening the outer chain under 500 mm/s

7.4 Fault classification using stacked sparse autoencoder

The conventional feature extraction method used in this chapter is only efficient in detecting some faults or changes that significantly change the responses of the pantograph to the 'V'-shape excitations, for example when the stiffness of the torsion bar is reduced by 30%. However, such extreme cases seem unlikely to happen in the real world. More practical faults or changes in the pantograph, such as looseness of the elbow joint chains, are difficult to diagnose using the conventional feature extraction approach. Therefore, in order to classify and diagnose all types of pantograph faults, a deep learning approach, the stacked sparse autoencoder, was used.

In this section, two cases are considered: (i) the first case is to classify different degrees of tightness of the outer chain, (ii) the second case is to classify the faults in different pantograph parts. Since the stacked sparse autoencoder (SSAE) performs better with more sets of input data, each test is (one fault and one test speed) repeated 100 times: the results of 80 randomly chosen tests are used to train the deep neural network, and those of the remaining 20 tests are used to validate the network.

7.4.1 SSAE for detecting tightness of the outer chain

In this section, the SSAE was adopted to classify the different degrees of tightness conditions: the outer chain loosened by one, three and five turns, and totally removed, respectively. In this case, the experimental data in the normal condition were labelled as '1'; those in the conditions of the outer chain loosened by one, three and five turns, and totally removed were labelled as '2', '3', '4', and '5', respectively.

Firstly, the labelled data were used to train the stacked sparse autoencoders. As the length of the training data must be in the same length, the labelled data recorded at the same excitation speed were used to train one deep learning network. As the changing-gradient tests were carried out at six speeds, six individual deep learning networks were trained separately. The SSAE model applied in this work has three sparse autoencoders stacked with the hidden layers of 300, 100 and 3, respectively (in Figure 4.33). Therefore, each layer can learn features at a different level of abstraction.

The results of the training and validation can be visualised with a confusion matrix (Cireşan et al., 2012). The training results using the data recorded at an excitation speed of 500 mm/s are shown in Figure 7.11 *a*. The rows and columns of the confusion matrix correspond to the predicted class (Output Class) and true class (Target Class), respectively. The diagonal squares correspond to data sets that are correctly classified. The other squares correspond to data sets that incorrectly classified. The overall accuracy of this training process is 100%. Following this, the trained deep learning network was validated by the remaining 20 data sets. The confusion matrix of the validation is shown in Figure 7.11 *b*.

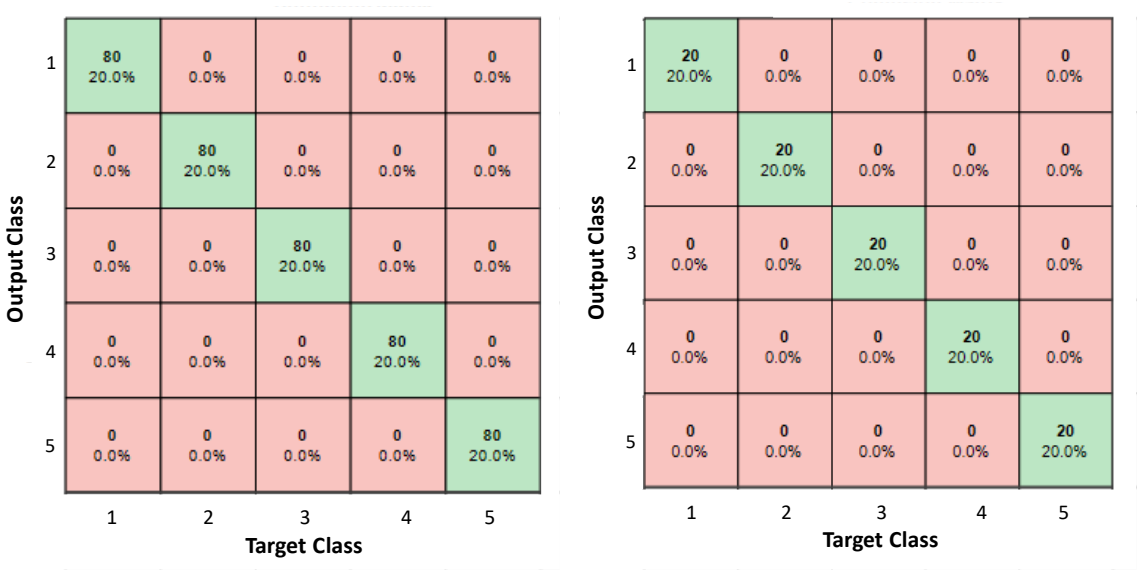

a. Training *b. Validation*

Figure 7.11 Confusion matrices with changes to outer chain: (a) training; (b) validation

The SSAEs in the same structure were also applied to classify the data sets recorded with various degrees of tightness of the outer chain at other excitation speeds. The confusion matrices for the results of the training and validation the data measured at a speed of 50 mm/s are shown in Figure A.43 in Appendix A. High accuracies of the training and validation process were achieved.

Therefore, the SSAE can be used to classify various degrees of tightness of the elbow joint outer chain, even though the experimental contact force signals are nearly identical in the time domain.

7.4.2 SSAE for detecting common pantograph faults

In order to ensure the applicability of the SSAE for classifying the faults happening to different components of the pantograph, in this section, the experimental data recorded in six different conditions were classified using the SSAE. The conditions were: (i) normal, (ii) greasing the head suspension, (iii) replacing the torsion bar with a less stiff one, (iv) one outer chain loosened by one turn, (v) outer chain removed, and (vi) replacing the pneumatic actuator with a leaking one.

Similar to the section above, fault classification using the SSAEs was run six times separately using the experimental data for six different excitation speeds. The results of the training and validation process using the experimental data recorded at a speed of 200 mm/s are shown in Figure 7.12 *a* and *b*, respectively. It is shown that the trained SSAE is able to classify the different common faults accurately. Another example of 300 mm/s is shown in Appendix A, Figure A.44. The data classification also achieved a high degree of accuracy.

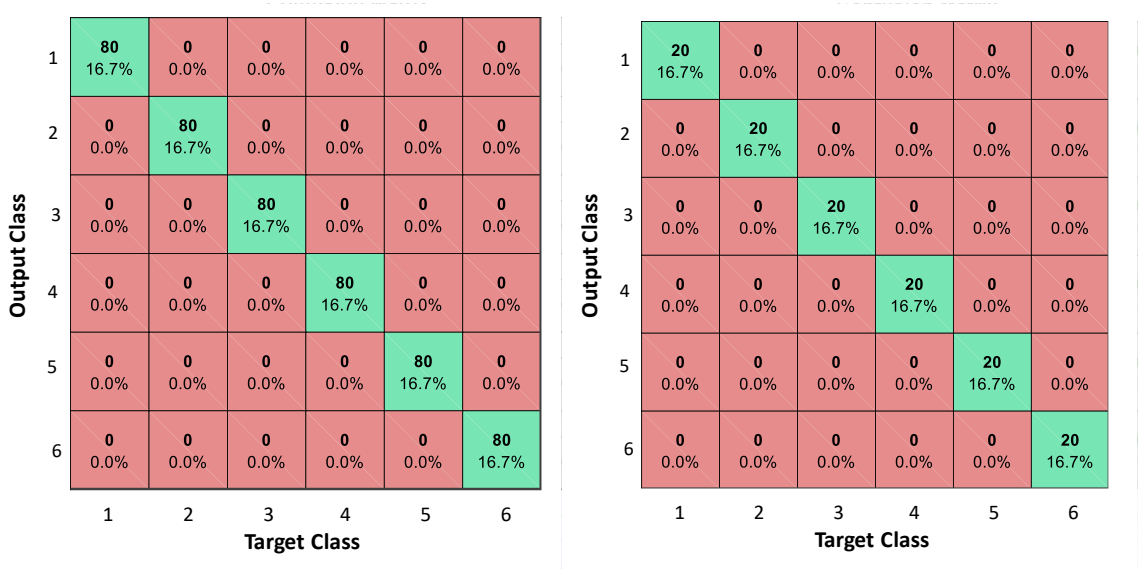

a. Training ***b. Validation***

Figure 7.12 Confusion matrices with common faults: (a) training; (b) validation

7.4.3 Comments

In this section, the SSAE was used to classify the experimental data recorded with different faults or changes in the pantograph. In the first case, the SSAE was applied to classify and diagnose different degrees of tightness of the outer chain. In the second case, the SSAE was used to classify and diagnose faults happening to different parts. The results show that the SSAE is efficient for classifying and diagnosing the common pantograph faults that were emulated in the laboratory. However, this approach requires plenty of data to train and validate the deep learning networks. Therefore, SSAE can be applied to practice after the pantograph fault database is developed with long-term testing data in the next stage of this project.

7.5 Conclusions

In this chapter, a novel changing-gradient test was proposed to reproduce the response of a pantograph to the variation of the stiffness of the contact wire. In order to explore the relationship between faults or changes in the pantograph and its response to the 'V'–shape excitations, some common faults were emulated to the pantograph. Firstly, the conventional feature extraction method was adapted to extract the oscillation frequencies and damping ratios from the contact forces recorded at various excitation speeds. The results show that this technique is able to detect and diagnose some major faults, including replacement of the torsion bar and leakage of the pneumatic actuator. However, it cannot work with some minor and practical faults or changes, such as variation in the tightness of the elbow joint chain.

In order to diagnose various faults or changes to the pantograph with the measurements obtained using the changing-gradient tests, the stacked sparse autoencoder (SSAE) was applied. The results show that the SSAE achieved high accuracy in fault classification. It is not only able to recognise different degrees of tightness of the outer chain, but also efficient in classifying the faults happen to different parts. However, as the SSAE requires plenty of testing data to train and validate the deep learning network, it is more applicable to long-term testing or operating data.

CHAPTER 8 DEVELOPMENT OF A PANTOGRAPH FAULT DETECTION AND DIAGNOSIS PROCEDURE

8.1 Introduction

In this chapter, a condition-based pantograph fault diagnosis testing procedure is proposed that combines the three dynamic tests detailed in previous chapters. The procedure is developed using decision tree analysis by considering the various fault features extracted from the three tests presented in this work. In order to develop a practical testing procedure that meets the requirements of the railway industry, a minimum sensor plan is proposed where sensors are only attached to the test rig. Another concern of engineers, namely the need to have a fast procedure, is addressed by adopting fewer cycles in the frequency-response test, which shortens the testing time significantly.

8.2 Optimisation of sensor configuration

In this work, a condition-based pantograph fault diagnosis testing procedure is proposed to realise efficient pantograph fault detection and diagnosis. The Birmingham pantograph test rig requires the pantograph to be removed from the roof of the train. In order for the same tests to be carried out in a depot environment, it is best if all the measuring devices are incorporated into the test rig and do not need to be attached to a pantograph under test. In this way, train maintenance engineers do not have to go onto the roof of the train to attach additional sensors, which saves time and avoids trailing cables. In order to achieve this, the sensors that were

previously attached to the pantograph should not be used and diagnosis of pantograph faults should rely only on the sensors remaining on the test rig.

Recalling the tests carried out in the previous four chapters, the hysteresis and changing-gradient tests only use the contact force and displacement of the pantograph head for analysing different features and diagnosing faults. Meanwhile, the frequency-response test only uses the FRFs from the pantograph upper and lower arms to understand the internal dynamic behaviour of the pantograph: the sensors on the arms are not required for fault diagnosis. The fault diagnosis using the frequency-response test in Chapter 7 was realised by observing the FRFs obtained from the pantograph head.

Therefore, for the pantograph fault detection and diagnosis procedure proposed for use in depots, the data from the sensors on the pantograph arms in the laboratory-based prototype are excluded. Meeting the requirement of depot managers yet still collecting sufficient information for pantograph fault detection and diagnosis, the final configuration of the lab-based pantograph test rig is shown in Figure 8.1, with all sensors mounted on the test rig.

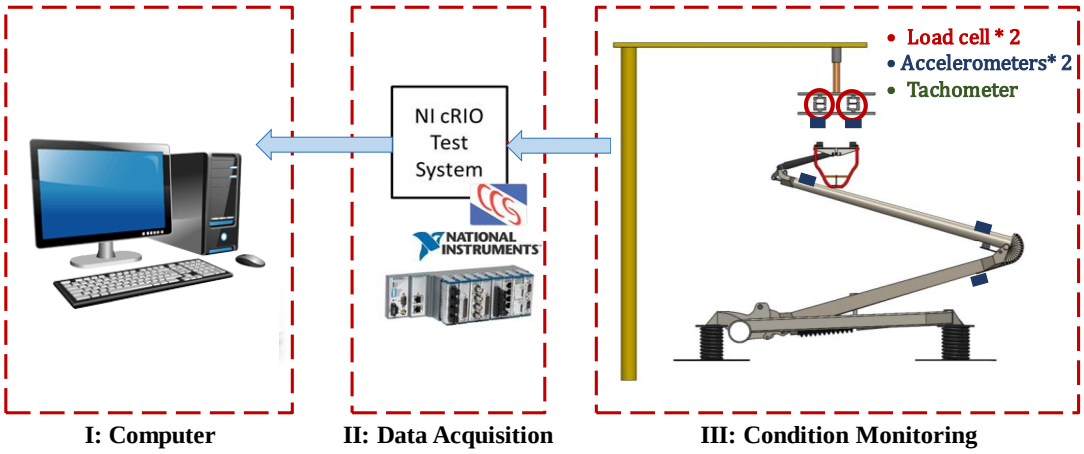

Figure 8.1 Architecture of the lab-based pantograph test rig with no sensors on the pantograph

8.3 Optimisation of excitations for the frequency-response test

The FRFs of the tested Pendolino high-speed pantograph were unknown before the frequency-response tests were carried out in this work. In order to understand the dynamic behaviour of the pantograph, the testing step was set to 0.1 Hz over the whole frequency range of interest. By analysing the differences between the reference and measurements, the features of the common faults of interest in this work mainly show up in the low- and medium-frequency ranges. The high-frequency range represents the bending mode of the upper arm, which is not included in this work. As the response in the high-frequency range (as defined in Table 6.2) is not that important for developing a rapid pantograph fault detection and diagnosis testing procedure, a step of 0.5 Hz is applied in this range: the standard step size in EN 50317 (CENELEC, 2012a). The testing time is shortened accordingly.

Furthermore, the number of sinusoidal wave cycles applied at each frequency within the frequency range swept can be reduced. The frequency-response tests previously used 30 cycles of the sinusoidal wave at each frequency: the first five cycles were to allow any transient effects to die away, and the remaining 25 cycles were used to calculate the FRFs. Typically, the sinusoidal wave with 10 cycles at each frequency is used to measure the FRF of the pantograph (Bruni et al., 2012a). Therefore, the number of cycles is reduced to 15 cycles of the sinusoidal wave at each frequency for use in depots: the first 5 cycles to allow the transients to die away, and the remaining 10 cycles to calculate the FRFs. The time taken for the reduced–cycle frequency-response test is shown in Table 8.1.

Table 8.1 Excitations of frequency-response tests

Excitations		Decreasing	0.3 mm	0.5 mm	1 mm	2 mm	5 mm
Frequency range (Hz)		0.5–20.0	0.5–20.0	0.5–20.0	0.5–12.0	0.5–9.8	0.5–7.5
Time consumption (s)	Research profiles	1138.5	1138. 5	1138. 5	985.7	925.2	845.4
	Depot used profiles	498.2	507.9	483.0	421.6	413.9	385.5

In each case, the testing time is reduced by more than 50%.

8.4 Development of pantograph fault detection and diagnosis testing procedure using a decision tree

For the purposes of developing the fault detection and diagnosis testing procedure, a decision tree was constructed. The testing procedure is proposed with the assumption that only one fault or change happens to the tested pantograph. The decision tree is a compromise between the accuracy of the decision and the time taken to accomplish the proposed tests. A tree structure was established, which is able to classify pantograph faults based on the features extracted by the three tests that have been carried out. Therefore, based on the architecture of the decision tree, condition-based fault detection and diagnosis can be realised.

8.4.1 Introduction to decision trees

Decision trees have been proved to be valuable tools for a wide range of classification and generalisation problems (Friedl and Brodley, 1997). Generally, a decision tree is composed of a root node and a number of interiors and terminal nodes. The root node and interior nodes are connected to different decision stages, while the final classifications are denoted by terminal nodes (Swain and Hauska, 1977). Following this structure, diagnostic decision trees (DDTs) have been developed for system fault detection and diagnosis by applying related diagnostic

rules (Lee et al., 2005). For a diagnostic decision tree, each interior node corresponds to a test, and the branches to the interior or terminal nodes handling the features obtained from this test; then, the decision is made by applying the diagnostic rules (Stein et al., 2005). The tests to be carried out next are determined by the decision made in the previous layer. The decision tree grows with more layers until each branch finished with a terminal node where the diagnosis is complete and corresponding maintenance can be carried out. The advantage of diagnostic decision trees is to break down a complex decision-making process into a collection of simpler decisions (Safavian and Landgrebe, 1991). By applying this method, the complicated multiple–features problem for a condition-based pantograph diagnostic procedure is simplified into a number of dynamic tests.

8.4.2 A diagnostic decision tree for pantograph fault diagnosis

The basic rule for building the condition-based pantograph fault diagnosis testing procedure is to ensure the accuracy of the diagnostic decision tree while minimising time consumption. By combining the various fault features obtained by the three dynamic tests, the testing procedure proposed is shown in Figure 8.2; the corresponding explanation is in Table 8.2.

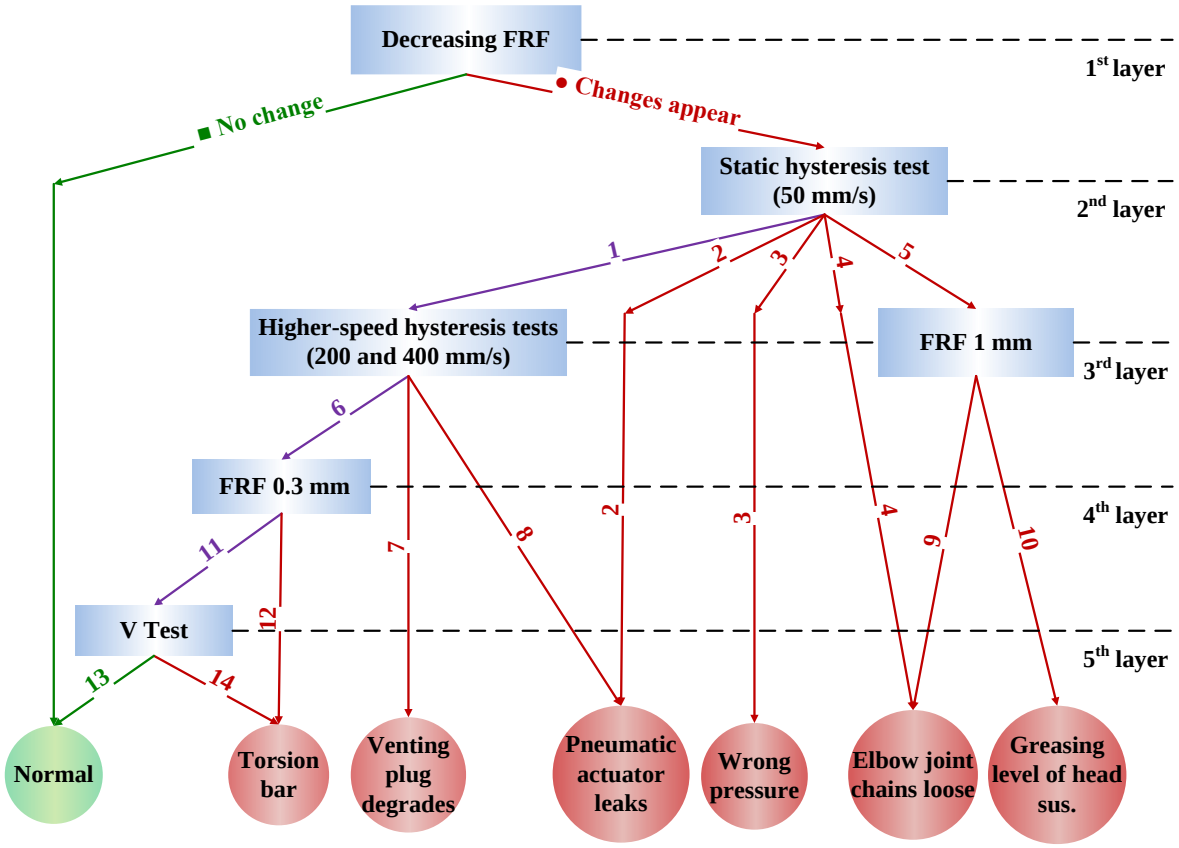

Figure 8.2 Pantograph fault diagnostic decision tree

Table 8.2 Details of the decision tree for pantograph fault detection and diagnosis

Layer	No.	Phenomenon	Possible issues	Time consumption (s)
1st	■	No change.	Normal.	497.5
	●	Changes appear.	Normal, or; Faulty.	
2nd	1	No obvious change.	Normal, or; Stiffness and/or damping of torsion bar vary, or; Pneumatic actuator leaks, or; Venting plug is degraded.	581.1
	2	Contact force plunges.	Pneumatic actuator leaks.	
	3	Hysteresis loop translates only, and the shape of the loop is almost identical to the reference.	Wrong level of pressure supply.	
	4	Large scallops shrink or disappear.	Elbow joint chains loose.	
	5	Overall hysteresis decreases, but the shape of the hysteresis loop is almost identical to the reference.	Elbow joint chains loose, or; Greasing level on head suspension.	
3rd	6	No obvious change.	Normal, or; Properties of torsion bar vary.	619.1
	7	Loops are centred to the same static force, but hysteresis increases.	Venting plug is degraded.	
	8	Loops translate, and uplift force decreases successively.	Pneumatic actuator leaks.	
	9	Phase is different from the reference in the low- and first half of the medium-frequency range.	Elbow joint chains loose.	1002.7
	10	Phase is different from the reference in the entire frequency range of interest.	Greasing level of head suspension is varied.	
4th	11	No obvious change.	Normal, or; Torsion bar properties vary.	1112.0
	12	Both the phase and magnitude of the first resonance are changed.	Torsion bar properties vary.	
5th	13	Difference between the measurements and references are acceptable.	Normal (acceptable condition).	1182.9
	14	The trend of the frequencies and damping ratios varies.	Torsion bar properties vary slightly.	

8.4.2.1 First layer

Decreasing-amplitude excitation is proposed to accomplish the primary fault detection. As mentioned in Chapter 6, decreasing-amplitude excitation is able to excite every critical pantograph component in the low-frequency range, and the head suspension in the medium-frequency range. Additionally, the FRF is sensitive to any change or fault happening in the pantograph. Therefore, decreasing-amplitude excitation is the root test that is carried out to investigate the condition of the tested pantograph prior to other tests.

The testing procedure for fault detection and diagnose starts with the frequency-response test under decreasing-amplitude excitation. By comparing the measured head FRF to the reference, if there is no variation in either the magnitude or phase curve, this pantograph is counted as in a normal condition; otherwise, a fault or degradation has probably occurred. Possible methods to quantify the differences between the FRFs include dynamic time warping (Eamonn and Ratanamahatana, 2005), Euclidean vector distance (Xinsheng and Loparo, 2004), etc. The thresholds will be set based on results of dynamic tests that will be carried out to more pantographs in the type. In order to identify the status of the pantograph, tests need to be accomplished in the next layer.

8.4.2.2 Second layer

The target of the second layer is to recognise the possible conditions assumed in the first layer as much as possible. The static hysteresis test, which is able to separate some faults within one test, is carried out. Another benefit of using the static hysteresis test is the time saving, as the time consumed by this test is 83.6 s.

Comparing the measured hysteresis loops to the reference, by applying the diagnostic rules extracted in Chapter 5, the result indicates one of five possible circumstances. Referring to Table 8.2, if Phenomenon 2, ‘contact force plunges’, happens, leakage of the pneumatic actuator

is diagnosed. If Phenomenon 3, 'hysteresis loop translates only, and the shape of the loop is almost identical to the reference', occurs, it indicates that the level of pressure supply needs to be adjusted. If Phenomenon 4, 'large scallops shrink or disappear', appears, the elbow joint chain(s) are loose.

If no obvious variation can be spotted in the static hysteresis measurement, as described by Phenomenon 1 in Table 8.2, there are four possibilities: the condition of the pantograph is acceptable, the stiffness and/or damping of the torsion bar varies, the pneumatic actuator is leaking, or the venting plug is degraded. If Phenomenon 5 occurs, 'overall hysteresis decreases, but the shape of the hysteresis loop is almost identical to the reference', there are two possible faults: loose elbow chains or variation in the greasing or wear level of the head suspension. To distinguish the potential faults corresponding to Phenomena 1 and 5, the decision tree grows one layer deeper.

8.4.2.3 Third layer

- **Hysteresis test at 200 and 400 mm/s**

The tests applied in the third layer to distinguish possible faults correlating to Phenomenon 1 are hysteresis tests under higher excitation speeds. In Chapter 5, it was concluded that the hysteresis tests are able to detect different types of fault in the pneumatic actuator. As two of the four possible faults are in the pneumatic actuator, the hysteresis tests are carried out at 200 and 400 mm/s, which are the medium and highest speeds applied in this work. These two tests are able to excite different nonlinearities of the pneumatic actuator. Another benefit of using the hysteresis tests is that they are rapid. The time consumed by the hysteresis at these two speeds is 23.9 and 14.1 s, respectively. Therefore, the decisions corresponding to Phenomenon 6, 7 and 8 are made with a testing time of 619.1 s.

If the hysteresis loops of the tested pantograph collected at speeds of 50, 200 and 400 mm/s are centred to approximately the same static force while the hysteresis increases successively, corresponding to Phenomenon 7, the fault is that the top piece of the venting plug is degraded. The condition of Phenomenon 8 is that the loops move to the left under the three excitation speeds successively, which demonstrates a decrease in the uplift force resulting from the leakage in the pneumatic actuator.

If no obvious variation can be detected in the hysteresis loops, the pantograph is in two possible conditions: an acceptable normal condition or the stiffness and/or damping of the torsion bar vary slightly. To discriminate these two circumstances, a test is chosen in the fourth layer of the decision tree.

- **Frequency-response test under the excitation of 1 mm**

In order to categorise the two possible circumstances corresponding to Phenomenon 5, loose elbow joint chains and variation in the greasing or wear level of the head suspension, the frequency-response test under 1 mm excitation level is implemented. If the FRFs measured is different from the reference in the low- and first half of medium-frequency range, the fault is looseness of the elbow joint chains, whereas if the difference between the measurement and the reference is shown up in the entire frequency range of interest, the level of greasing or wear of the head suspension is changed. The time consumption for making these two decisions is 1002.7 s.

8.4.2.4 Fourth layer

In the fourth layer, the target is to distinguish the acceptable normal status and abnormality of the torsion bar. The frequency-response test is accomplished with an excitation level of 0.3 mm, which is able to inspect the behaviour of the head suspension without exciting nonlinear behaviour of the frame suspension. As the dynamic behaviour of the head suspension mainly

appears in the low- and medium-frequency range, to reduce testing time, the response in the high-frequency range is not measured, and the time consumption is reduced to 492.9 s.

If the stiffness or/and damping of the torsion bar are varied due to cracks or other reasons, both the resonant peak and frequency should vary. By investigating the difference between the FRF obtained and the reference, a decision can be made. Until now, the time consumed to achieve this decision is 1112.0 s. However, if the fault on the torsion bar does not vary the FRF significantly, the condition of the pantograph is still unsure. Therefore, another test is carried out in the fifth layer.

8.4.2.5 Fifth layer

In the fifth layer, changing-gradient tests at various excitation speeds are carried out to investigate the occurrence of the fault to the torsion bar by extracting the features using a classic system identification approach. The features include the damping ratios and oscillation frequencies at different excitation speeds. By inspecting the trend of the feature curves with respect to the excitation speed, some faults can be diagnosed. Referring to the studies in Chapter 7, variation in the stiffness or/and damping of the torsion bar changes the trend of the feature profiles significantly. If the difference between the trend of the references and measurements is acceptable, the circumstance will be recognised as ‘normal’; otherwise, a fault in the torsion bar is diagnosed.

Following this procedure, the common pantograph faults considered in this work can be detected and diagnosed. Then, appropriate maintenance activities can be carried out based on the actual condition of the tested pantograph.

8.5 Conclusions

In this chapter, a decision tree for a pantograph fault detection and diagnosis is proposed by combining the three dynamic tests described in detail in this work. A simplified sensor plan is proposed by having sensors only on the pantograph test rig, which meets the requirements from the depot managers while being able to obtain the critical parameters for fault detection and diagnosis. Furthermore, in order to develop the rapid diagnostic testing procedure, the time consumption of the frequency-response tests is reduced by using the minimum number of cycles (15 cycles) measured at each frequency.

The root test of the proposed condition-based procedure is the frequency-response test under decreasing excitation, which is able to excite all important pantograph parts. Then, to distinguish the possible faults considered, a static hysteresis test is adopted, which is able to diagnose some faults directly. In the deeper layers of the decision tree, other tests are applied based on the possible faults diagnosed from the monitoring data. Finally, all the faults are identified. However, the decision tree for pantograph fault detection and diagnosis developed in this work is based on the experiments carried out on only one pantograph. The applicability of this decision tree needs to be verified using the experimental data collected from other pantographs of the same type. Further modifications for this decision tree may be required.

CHAPTER 9 CONCLUSIONS AND FURTHER WORK

9.1 Introduction

In this chapter, the conclusions developed as part of the research are presented. This chapter also lists further work that needs to be carried out to allow condition-based pantograph fault-diagnosis method to play its full role in enhancing the safety and reliability of the railway network.

There is interest in the railway industry to investigate the possibility of intelligent maintenance of pantographs at depots. In order to make progress on this ambition, a hypothesis was made that it is possible to develop a pantograph dynamic behaviour measurement device that is able to implement condition-based fault detection and diagnosis. This thesis provides a response to this hypothesis by developing a laboratory-based pantograph test rig and implementing three dynamic tests to characterise common pantograph faults or changes. At the end of this thesis, a testing procedure for pantograph fault detection and diagnosis was proposed by merging three dynamic tests. The efficiency and time consumption of each test were taken into account. Therefore, a reliable fault diagnosis decision can be to be obtained rapidly.

9.2 Conclusions

Currently, the maintenance activities for pantographs implemented in depots is based on a fixed time or operating distance and tends to rely on visual and manual checks. This approach is only capable of determining some obvious faults. Static hysteresis tests are carried out at some depots but are not adequate to investigate the condition of the pantographs tested. Condition-based pantograph evaluations are accomplished by using on-board and trackside systems, but

these devices are only able to inspect a limited number of pantographs. Even if a suspicious pantograph is identified by the on-board and trackside systems, the depot needs ways to identify the actual problem. Accordingly, in this work, a laboratory-based pantograph test rig was developed to carry out various dynamic tests for pantograph fault detection and diagnosis. This can be adapted for use in a depot where the tests can be carried out without removing the pantograph from the roof of the train.

Prior to choosing the dynamic tests and related critical parameters for investigating the dynamic behaviour of pantographs, it is necessary to understand its working principle. A 3D multibody model of a Pendolino high-speed pantograph and a simplified test rig were developed with SolidWorks and simulated with MATLAB Simscape Multibody Toolbox. Following this, in order to detect and diagnose common pantograph faults or changes in pantograph head and frame suspensions and elbow joint, three distinct dynamic tests have been identified, which are explained and formalised in this thesis: (i) a hysteresis test; (ii) a frequency-response test; and (iii) a novel changing-gradient test. Various common pantograph faults or changes were emulated and tested by these three tests.

The development of the hysteresis test carried out at various excitation speeds was inspired by the existing static hysteresis test (50 mm/s). The results in this thesis show that the extended hysteresis test (Chapters 5) is able to detect the variation in the greasing level of the head suspension and faults or changes in the pneumatic actuator efficiently, including incorrect air pressure, leakage of the pneumatic actuator and degradation of the venting plug. The hysteresis test can also potentially be used to detect the different degrees of tightness of the elbow joint chain; however, this test is quite experimental.

The frequency-response test (Chapter 6) is proposed to investigate the steady-state response of the pantograph in the frequency domain presented in a Bode plot. A decreasing-amplitude and

various fixed-amplitude excitations were tested on a Pendolino high-speed pantograph in the frequency range of 0.5–20 Hz as required in EN 50317. The testing results show that the frequency-response test under decreasing-amplitude excitation is able to detect all pantograph faults or changes considered in this work. Therefore, it was used as the root test of the decision tree proposed in Chapter 8 for pantograph fault detection and diagnosis. According to the consistency of the phase angle curves for different pantograph parts, the Bode plot can be divided into three ranges: low, medium and high frequency. The dynamic behaviour shown in each frequency range is dominated by different pantograph parts. The fault detection and diagnosis using the frequency-response test were realised by characterising the differences between the FRFs recorded with fault or change to the reference in the low- and medium-frequency ranges with respect to the excitation amplitude.

A novel changing-gradient test (Chapter 7) aims to reproduce the response of a pantograph to the variation in the stiffness of the contact wire. This test is much faster than the frequency-response test and faster than the hysteresis test. Conventional feature extraction using a system identification method can diagnose limited types of faults. In order to use the rapid changing-gradient test to diagnose all types of common faults or changes in the pantograph, a deep learning algorithm, a stacked sparse autoencoder (SSAE), was adapted to classify the experimental data. The efficiency of this method has been proved by classifying different degrees of tightness of the elbow joint outer chain, and faults in different pantograph parts. However, since the SSAE requires plenty of experimental data sets to train and validate the deep learning network, this method can only be implemented in practice after long-term operating data has been collected.

As none of the three dynamic tests is able to detect and diagnose all types of common pantograph faults or changes alone, a testing procedure that combines the three tests was

proposed in Chapter 8. This procedure for pantograph fault detection and diagnosis was developed using a decision tree analysis method considering the various fault features and diagnostic rules extracted from the three tests. In order to develop a practical testing procedure that meets the requirements of the railway industry, a minimum sensor configuration and a faster frequency-response test were proposed. The decision tree starts with the root test: frequency-response test under decreasing–amplitude excitation. In each layer, the decision for fault detection or diagnosis is made by analysing the feature monitored by a specific test. The decision tree grows with more layers until the decision for fault diagnosis is made. Following the decision tree, common pantograph faults or changes considered in this work can be diagnosed. Following this, appropriate maintenance activities can be carried out based on the actual condition of the tested pantograph.

Throughout this work, the author has been in dialogue with railway operators and depot managers, thus helping to identify common pantograph faults and clarify the requirements for the test rig that will be later installed in depots, while also informing the industry about the most advanced and appropriate approaches to pantograph condition monitoring for fault detection and diagnosis.

Some of the work presented in this thesis has also been published at the 10th IFAC SafeProcess conference, and Proceedings of the Institution of Mechanical Engineers, Part F: Journal of Rail and Rapid Transit; details can be found in Appendix B.

9.3 Further work

To reach a point where condition-based pantograph maintenance can actively contribute to increased reliability, maintainability and safety of the railway network in a cost-effective manner, the pantograph test rig developed in this thesis must be developed further. The plans

for further work are presented under two headings: improvement of the test rig and making the proposed fault detection and diagnosis method more robust, including the testing of more pantographs.

9.3.1 Improvement of the test rig

The test rig proposed in this work is able to excite the pantograph in both vertical and lateral directions. However, lateral excitation was not applied in this work, as the friction between the excitation bar and the carbon strips would potentially damage the pantograph without the longitudinal motion normally present. In order to minimise lateral friction, the excitation bar could be replaced by two separated rollers which contact the two carbon strips. Thus, lateral excitation could be applied to the pantograph head to reproduce the effect of catenary staggers without lateral drag.

Furthermore, a real-time analysis server needs to be developed. By using this server, the pantograph fault diagnosis testing routine can be applied automatically, and a report of the potential faults in the tested pantograph will be generated that gives recommendations for pantograph maintenance.

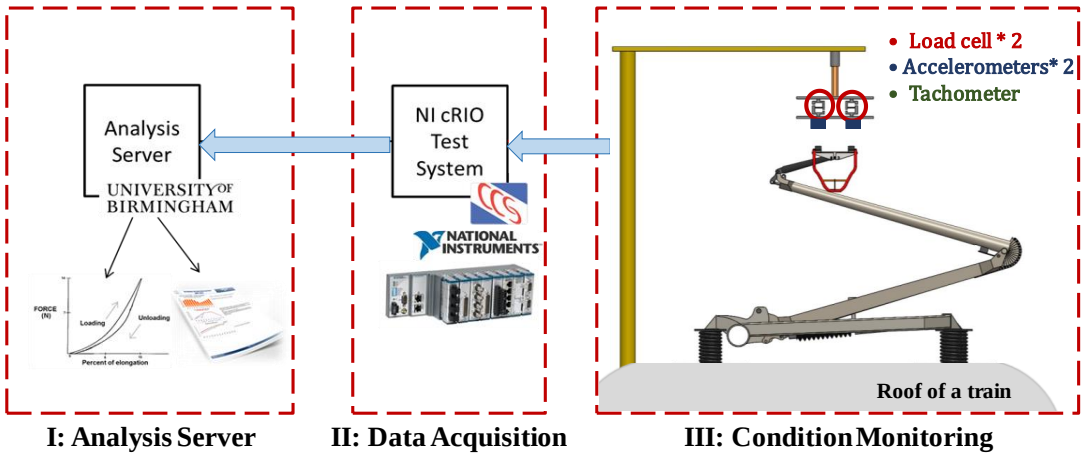

Figure 9.1 Future architecture of the pantograph test rig to be used in depots

Finally, in order to install the test rig in depots, the architecture of the actuation subsystem needs to be redesigned with higher supports. Currently, the tested pantograph is placed on the floor. As the test rig is proposed to test a pantograph without removing it from the roof of the train, trains are allowed to pass underneath the test rig. Accordingly, higher supports are required before installing the test rig in a train maintenance depot.

9.3.2 Data from additional pantographs

In this work, the experiments were carried out on one Pendolino high-speed pantograph with one fault or change at each time. In order to develop a robust testing procedure for fault detection and diagnosis, long-term experimental data needs to be collected from more pantographs with multiple faults.

The dynamic behaviour of healthy pantographs of the same type may not all be identical. Accordingly, the experiments need to be carried out on more pantographs to investigate the variation in the dynamic behaviour of different healthy pantographs. Therefore, the tolerances and threshold for pantograph fault detection and diagnosis can be worked out.

In this work, to obtain faulty experimental data, the faults or changes were emulated on the pantograph. The features were extracted by comparing the faulty measurement to the reference. The thresholds for various faults are not detailed. In the next phase, long-term operating data will be recorded that could be used to select the values of thresholds and analyse degradation of the pantographs.

REFERENCES

[1]. Ahlberg, J.H., Nilson, E.N. & Walsh, J.L. (1967) *The Theory of Splines and Their Applications*. New York: Academic Press.

[2]. Ahmed, E., Jones, M. & Marks, T.K. (2015) An improved deep learning architecture for person re-identification. *Proceedings of the IEEE Conference on Computer Vision and Pattern Recognition.* Boston, UK. pp. 3908-3916.

[3]. Ambrósio, J. & Pombo, J. (2013) Minimal requirements of multibody pantograph models for high-speed railway applications. *10th World Congress on Railway Research (WCRR).* Sydney, Australia.

[4]. Ambrósio, J., Pombo, J., Antunes, P. & Pereira, M. (2015) PantoCat statement of method. *Vehicle System Dynamics: International Journal of Vehicle Mechanics and Mobility (Special Issue: The Pantograph-Catenary interaction Benchmark)*, 53 (3), pp. 314-328.

[5]. Ambrósio, J., Pombo, J. & Pereira, M. (2013) Optimization of high-speed railway pantographs for improving pantograph-catenary contact. *Theoretical and Applied Mechanics Letters*, 3 (1), pp. 9-013006.

[6]. Ambrósio, J., Pombo, J., Pereira, M., Antunes, P. & Mósca, A. (2012) A computational procedure for the dynamic analysis of the catenary-pantograph interaction in high-speed trains. *Journal of theoretical and applied mechanics*, 50 (3), pp. 681-699.

[7]. Ambrósio, J., Rauter, F., Pombo, J. & Pereira, M.S. (2011). A Flexible Multibody Pantograph Model for the Analysis of the Catenary–Pantograph Contact. *In:* Arczewski, K., Blajer, W. & Fraczek, J. (eds.) *Multibody Dynamic.* Dordrecht, Netherlands: Springer, pp. 1-27.

[8]. Ambrósio, J.A.C., Pombo, J., Rauter, F. & Pereira, M. (2009). A Memory Based Communication in the Co-simulation of Multibody and Finite Element Codes for Pantograph-Catenary Interaction Simulation. *In:* Arczewski, K., Blajer, W. & Fraczek, J. (eds.) *Multibody Dynamics.* Dordrecht, Netherlands: Springer, pp. 231-252.

[9]. Ambrósio, J.A.C., Rauter, F., Pombo, J. & Pereira, M. (2010) Dynamics of High-Speed Train Pantograph-Catenary Co-Simulation of Finite Element and Multibody Codes. *Theoretical and Applied Mechanics Letters*, 3 (1), pp. 9-013006.

[10]. Antunes, P., Mósca, A., Ambrósio, J., Pombo, J. & Pereira, M. (2012) Development of a Computational Tool for the Dynamic Analysis of the Pantograph-Catenary Interaction for High-Speed Trains. Topping, B. H. V., (ed.) *The 11th International Conference on Computational Structures Technology.* Dubrovnik, Croatia. pp. 1-25.

[11]. Antunes, P.C. (2012) *Development of multibody pantograph and finite element catenary models for application to high-speed railway operations.* Master of Science. School of Mechanical Engineering, Instituto Superior Técnico, Universidade Técnica de Lisboa. Lisboa, Portugal.

[12]. Aschauer, G., Schirrer, A., Kozek, M. & Jakubek, S. (2017) Realtime-capable FE-based railway catenary emulation via pantograph test rig impedance control. *IFAC Papers OnLine*, 50 (1), pp. 636–641.

[13]. Aydin, İ., Karaköse, E., Karaköse, M., Gençoğlu, M.T. & Akın, E. (2013) A new computer vision approach for active pantograph control. *Innovations in Intelligent Systems and Applications (INISTA), 2013 IEEE International Symposium on.* Albena, Bulgaria. pp. 1-5.

[14]. Aydin, I., Karakose, M. & Akin, E. (2014) A New Contactless Fault Diagnosis Approach for Pantograph-Catenary System Using Pattern Recognition and Image Processing Methods. *Advances in Electrical and Computer Engineering*, 14 (3), pp. 79-88.

[15]. Aydin, I., Karaköse, M. & Akin, E. (2012) A New Contactless Fault Diagnosis Approach for Pantograph-Catenary System *15th International Conference MECHATRONIKA.* Prague, Czech Republic. pp. 1-6.

[16]. Balestrino, A., Bruno, O., Landi, A. & Sani, L. (2000) Innovative solutions for overhead catenary-pantograph system: wire actuated control and observed contact force. *Vehicle System Dynamics*, 33 (2), pp. 69-89.

[17]. Barmada, S., Raugi, M., Tucci, M. & Romano, F. (2014) Arc detection in pantograph-catenary systems by the use of support vector machines-based classification. *IET Electrical Systems in Transportation* 4(2), pp. 45-52.

[18]. Baxter, A. (2015) *Network Rail A Guide to Overhead Electrification*. Alan Baxter Ltd, London.

[19]. Benedetto, A., Pugi, L. & Bartolini, F. (2008) Design and experimental results of an active suspension system for a high-speed pantograph. *Mechatronics*, 13 (5), pp. 548-557.

[20]. Benet, J., Alberto, A., Arias, E. & Rojo, T. (2007) A Mathematical Model of the Pantograph-Catenary Dynamic Interaction with Several Contact Wires *IAENG International Journal of Applied Mathematics*, 37 (2).

[21]. Benet, J., Cuartero, N., Cuartero, F., Rojo, T., Tendero, P. & Arias, E. (2013) An advanced 3D-model for the study and simulation of the pantograph catenary system. *Transportation Research Part C:Emerging Technologies*, 36, pp. 138-156.

[22]. Betts, A.I., Hall, J. & Keen, P.M. (1989) *Condition monitoring of pantographs - development of Cheddington site*. British Rail, Derby, UK.

[23]. Bobillot, A., Delcourt, V., Demanche, P. & Massat, J.P. (2006) Pantograph-Catenary: Three Paths to Knowledge. *7th World Congress on Railway Research (WCRR).* Montreal, Canada. WCRR Management, Munich.

[24]. Bocciolone, M., Bucca, G., Collina, A. & Comolli, L. (2013) Pantograph–catenary monitoring by means of fibre Bragg grating sensors: Results from tests in an underground line. *Mechanical Systems and Signal Processing*, 41 (1-2), pp. 226-238.

[25]. Bocciolone, M., Lorenzo, C. & Pietro, C. (2012) A novel design of a compact S-shaped balance with FBG sensors for the pantograph-catenary contact force measurement. *Proceedings of SPIE - The International Society for Optical Engineering, 22nd International Conference on Optical Fiber Sensors.* Beijing, China.

[26]. Bocciolone, M., Resta, F., Rocchi, D., Tosi, A. & Collina, A. (2006) Pantograph aerodynamic effects on the pantograph–catenary interaction. *Vehicle System Dynamics*, 44 (sup1), pp. 560-570.

[27]. Boffi, P., Cattaneo, G., Amoriello, L., Barberis, A., Bucca, G., Bocciolone, M., Collina, A. & Martinelli, M. (2009) Optical Fiber Sensors to Measure Collector Performance in the Pantograph-Catenary Interaction. *Sensors Journal*, 9 (6), pp. 635-640.

[28]. Boglietti, A., Cavagnino, A., Tenconi, A., Vaschetto, S. & di Torino, P. (2009) The safety critical electric machines and drives in the more electric aircraft: A survey. *35th Annual Conference of IEEE Industrial Electronics.* Porto, Portugal. pp. 2587-2594.

[29]. Bolton, J.S. & Dyne, M. (1984) *Improved Technique for the Valuation of Structural Dynamic Response*. Purdue University, Purdue, Ray W. Herrick Laboratories

[30]. Bruni, S., Ambrosio, J., Carnicero, A., Cho, Y.H., Finner, L., Ikeda, M., Kwon, S.Y., Massat, J.-P., Stichel, S., Tur, M. & Zhang, W. (2015) The results of the pantograph–catenary interaction benchmark. *Vehicle System Dynamics*, 53 (3), pp. 412-435.

[31]. Bruni, S., Ambrosio, J. & Pombo, J. (2012a) *PantoTRAIN-PANTOgraph and catenary interaction: Total Regulatory Acceptance for the Interoperable Network*. Internal Politecnico di Milano report. Unpublished.

[32]. Bruni, S., Bucca, G., Carnevale, M., Collina, A. & Facchinetti, A. (2017) Pantograph–catenary interaction: recent achievements and future research challenges. *International Journal of Rail Transportation*, 6 (2), pp. 1-26.

[33]. Bruni, S., Bucca, G., Collina, A. & Facchinetti, A. (2012b) Numerical and Hardware-In-the-Loop Tools for the Design of Very High Speed Pantograph-Catenary Systems. *Journal of Computational and Nonlinear Dynamics*, 7 (4), pp. 1-8.

[34]. Bruni, S., Bucca, G., Collina, A., Facchinetti, A. & Melzi, S. (2004) Pantograph-catenary dynamic interaction in the medium-high frequency range. *The Dynamics of Vehicles on Roads and on Tracks. Proceedings of the 18th Iavsd Symposium.* Kanagawa, Japan. pp. 697-706.

[35]. Bruni, S., Facchinetti, A., Kolbe, M. & Massat, J.-P. (2011) Hardware-in-the-Loop testing of pantograph for homologation. *9th World Congress on Railway Research WCRR.* Lille, France.

[36]. Bruno, O., Landi, A., Papi, M. & Sani, L. (2001) Phototube sensor for monitoring the quality of current collection on overhead electrified railways. *Proceedings of the Institution of Mechanical Engineers, Part F: Journal of Rail and Rapid Transit*, 215 (3), pp. 231-241.

[37]. Bucca, G. & Collina, A. (2009) A procedure for the wear prediction of collector strip and contact wire in pantograph–catenary system. *Wear*, 266 (1-2), pp. 46–59.

[38]. Bucca, G., Collina, A., Manigrasso, R., Mapelli, F. & Tarsitano, D. (2011) Analysis of electrical interferences related to the current collection quality in pantograph–catenary interaction. *Proceedings of the Institution of Mechanical Engineers, Part F: Journal of Rail and Rapid Transit*, 225 (5), pp. 483-500.

[39]. Bucca, G., Collina, A. & Tanzi, E. (2017). Experimental Analysis of the Influence of the Electrical Arc on the Wear Rate of Contact Strip and Contact Wire in A.C. System. *In:* Boschetti G. & Gasparetto A. (eds.) *Advances in Italian Mechanism Science.* Cham: Springer pp. 449-456.

[40]. Burgess, A. (1988) *Transient Response of Mechanical Strucures Using Modal Analysis Techniques.* Doctor of Philosophy. Department of Mechanical Engineering, University of London. London

[41]. Butcher, L. (2017) *Rail electrification*. Transport Policy, London, The House of Commons Library.

[42]. Carnevale, M., Facchinetti, A. & Rocchi, D. (2017) Procedure to assess the role of railway pantograph components in generating the aerodynamic uplift. *Journal of Wind Engineering and Industrial Aerodynamics*, 160, pp. 16-29.

[43]. CENELEC.(2002) BS EN 50318:2002. *Railway applications-Current collection systems-Validation of simulation of the dynamic interaction between pantograph and overhead contact line*. London, BSI Standards Ltd.

[44]. CENELEC.(2009) BS EN 50119:2009+A1:2013. *Railway applications-Fixed installations-Electric traction overhead contact lines*. London, BSI Standards Ltd.

[45]. CENELEC.(2010) BS EN 50206-1:2010. *Railway applications. Rolling stock. Pantographs. Characteristics and tests. Part 1: Pantographs for main line vehicles*. London, BSI Standards Ltd.

[46]. CENELEC.(2012a) BS EN 50317: 2012. *Railway applications-Current collection systems-Requirements for and validation of measurements of the dynamic interaction between pantograph and overhead contact line*. London, BSI Standards Ltd.

[47]. CENELEC.(2012b) BS EN 50367:2012 +A1:2016. *Railway applications-Current collection systems-Technical criteriafor the interaction between pantograph and overhead line*. BSI Standards Ltd

[48]. CENELEC.(2012c) BS EN 50206-1:2010. *Railway applications - Rolling stock - Pantographs: Characteristics and tests. Part 1: Pantographs for main lines vehicles*. London, BSI Standards Ltd.

[49]. CENELEC.(2013) BS EN 50119:2009+A1:2013. *Railway applications. Fixed installations. Electric traction overhead contact lines*. London, BSI Standards Ltd.

[50]. Cho, C.J. & Park, Y. (2016) New Monitoring Technologies for Overhead Contact Line at 400km/h. *Engineering* 2(3), pp. 360-365.

[51]. Cho, Y. (2008) Numerical simulation of the dynamic responses of railway overhead contact lines to a moving pantograph, considering a nonlinear dropper. *Journal of Sound and Vibration*, 315 (3), pp. 433-454.

[52]. Cho, Y.H. (2015) SPOPS statement of methods. *Vehicle System Dynamics*, 53 (3), pp. 329-340.

[53]. Cireşan, D., Meier, U. & Schmidhuber, J. (2012) Multi-column Deep Neural Networks for Image Classification. *arXiv preprint arXiv:1202.2745*.

[54]. Cléon, L.M., Bobillot, A., Collina, A., Mohamed, O. & Loverre, V. (2006) Pantograph-Catenary: A European Couple. *7th World Congress on Railway Research (WCRR).* Montréal, Canada.

[55]. Collina, A. & Bruni, S. (2002) Numerical simulation of pantograph-overhead equipment interaction. *Vehicle System Dynamics*, 38 (4), pp. 261-291.

[56]. Collina, A., Bruni, S., Facchinetti, A. & Zuin, A. (2015) PCaDA statement of methods. *Vehicle System Dynamics*, 53 (3), pp. 347-356.

[57]. Collina, A., Facchinetti, A., Fossati, F. & Resta, F. (2004) Hardware in the Loop Test-Rig for Identification and Control Application on High Speed Pantographs. *Shock and Vibration*, 11 (3-4), pp. 445-456.

[58]. Collina, A., Facchinetti, A., Fossati, F. & Resta, F. (2005) An Application of Active Control to the Collector of an High-Speed Pantograph: Simulation and Laboratory Tests. *44th IEEE Conference on Decision and Control.* Seville, Spain. pp. 4602-4609.
[59]. Collina, A., Facchinetti, A. & Resta, F. (2007a) A feasibility study of an aerodynamic control for a high speed pantograph. *2007 IEEE/ASME international conference on advanced intelligent mechatronics.* Zurich, Switzerland. pp. 1-6.
[60]. Collina, A., Fossati, F., Papi, M. & Resta, F. (2007b) Impact of overhead line irregularity on current collection and diagnostics based on the measurement of pantograph dynamics. *Proceedings of the Institution of Mechanical Engineers, Part F: Journal of Rail and Rapid Transit*, 221 (4), pp. 547-559.
[61]. Conway, S. (2014) *Statistical distribution of pantograph characteristics*. RSSB, London.
[62]. Conway, S. (2016) *Lump mass models for legacy pantographs on GB mainline (T1105 Report)*. RSSB, London.
[63]. Craven, P. & Wahba, G. (1978) Smoothing noisy data with spline functions. *Numerische mathematik*, 31 (4), pp. 377-403.
[64]. Cullingford, S. (1993) *TMST pantogrpah type test*. Brecknell Willis, Millfield Chard, U.K.
[65]. Daadbin, A. & Rosinski, J. (2010) Development, Testing And Implementation Of The Pantograph Damage Assessment System (PANDAS). *WIT Transactions on The Built Environment*, 114, pp. 573-578.
[66]. Deml, J. & Baldauf, W. (2001) A new test bench for examinations of the pantograph-catenary interaction. *World Congress Railway Research (WCRR).* Koln, Germany
[67]. DepartmentforTransport. (2017) *High Speed Two From Concept to Reality*. Department for Transport, London.
[68]. Eamonn, K. & Ratanamahatana, C.A. (2005) Exact indexing of dynamic time warping. *Knowledge and information systems*, 7 (3), pp. 358-386.
[69]. Eppinger, S.D. (1984) *An Experimental and Analytical Study of Pantograph Dynamics.* Master of Science. Department of Mechanical Engineering, Massachusetts Institute of Technology.
[70]. ERG. (2012a) *Vehicle Instruction.* Eversholt Rail Group, London. EV/VI9142.
[71]. ERG. (2012b) *Vehicle Maintenance & Overhaul Instruction.* Eversholt Rail Group, London. GP0101.
[72]. Evans, J.R., Johnson, T. & Clark, R.A. (1990) *Dewirement Dynamics-Final Report*. British Rail Research, Derby.
[73]. Ewins, D.J. (1984) *Modal Testing: Theory and Practice*. Letchworth: Research studies press.
[74]. Facchinetti, A. & Bruni, S. (2012) Hardware-in-the-loop hybrid simulation of pantograph–catenary interaction. *Journal of Sound and Vibration*, 331 (12), pp. 2783-2797.
[75]. Facchinetti, A., Gasparetto, L. & Bruni, S. (2013) Real-time catenary models for the hardware-in-the-loop simulation of the pantograph–catenary interaction. *Vehicle System Dynamics*, 51 (4), pp. 499-516.
[76]. Facchinetti, A. & Marco, M. (2008) Hardware in the loop test-rig for pantograph active control evaluation. *IEEE International Symposium on Industrial Electronics.* Cambridge. pp. 2171-2176.
[77]. Facchinetti, A. & Mauri, M. (2009) Hardware-in-the-Loop Overhead Line Emulator for Active Pantograph Testing. *IEEE Transactions on Industrial Electronics,*, 56 (10), pp. 4071-4078.
[78]. Farrington-Darby, T., Pickup, L. & Wilson, J.R. (2005) Safety culture in railway maintenance. *Safety Science*, 43 (1), pp. 39-60.
[79]. Fessler, J.A. (1994) Penalized weighted least-squares image reconstruction for positron emission tomography. *IEEE transactions on medical imaging* 13 (2), pp. 290-300.
[80]. Finner, L., Poetsch, G., Sarnes, B. & Kolbe, M. (2015) Program for catenary–pantograph analysis, PrOSA statement of methods and validation according EN 50318. *Vehicle System Dynamics*, 53 (3), pp. 305-313.
[81]. Friedl, M.A. & Brodley, C.E. (1997) Decision tree classification of land cover from remotely sensed data. *Remote sensing of environment*, 61 (3), pp. 399-409.
[82]. Fumi, A. & Forgione, A. (2001) A new complete system for catenary's checking. *World Congress on Railway Research (WCRR).* Brussels, Belgium.

[83]. Gabbott, M.A. (2007) Catenary and pantograph design and interface. *3rd IET Professional Development Course on Railway Electrification Infrastructure and Systems.* Birmingham, UK. pp. 115-121.

[84]. Galeotti, G., Galanti, M., Magrini, S. & Toni, P. (1993) Servo Actuated Railway Pantograph for High-Speed Running with Constant Contact Force. *Proceedings of the Institution of Mechanical Engineers, Part F: Journal of Rail and Rapid Transit*, 207 (1), pp. 37-49.

[85]. Gil-Vera, J.A. (2000) *Modelling and Simulation of A Modified Brecknell Willis Pantograph for High Speed Rail in Britain.* Masters of Science. Department of Mechanical Engineering University of Sheffield. Sheffield, U.K.

[86]. Gilks, W.R., Richardson, S. & Spiegelhalter, D. (1995) *Markov chain Monte Carlo in practice*. London: Chapman & Hall/CRC.

[87]. Giuseppe, B., Marco, C., Andrea, C., Felice, A., Gianfranco, B. & Claudio, S. (2016) A diagnostic system for overhead lines and pantographs: Results from first installation on commuter and high speed commercial trains. *World Congress on Railway Research (WCRR).* Milan, Italy.

[88]. Goodfellow, I., Bengio, Y. & Courville, A. (2016) *Deep learning*. Cambridge: MIT press.

[89]. Gostling, R.J. (1979) *Brecknell Willis 'high-speed' pantograph*. British Railways Board, Derby, UK.

[90]. Gostling, R.J. & Hobbs, A.E.W. (1983) The Interaction of Pantograph and Overhead Equipment: Practical Applications of A New Theoretical Method. *Proceedings of the Institution of Mechanical Engineers, Part C: Journal of Mechanical Engineering Science*, 197 (1), pp. 61-69.

[91]. Gregori, S., Tur, M., Nadal, E., Aguado, J.V., Fuenmayor, F.J. & Chinestab, F. (2017) Fast simulation of the pantograph–catenary dynamic interaction. *Finite Elements in Analysis and Design*, 129, pp. 1-13.

[92]. Gu, C. (2013) *Smoothing spline ANOVA models*. Springer Science & Business Media.

[93]. Hamey, L.G.C., Watkins, T. & Yen, S.W.T. (2007) Pancam: In-Service Inspection of Locomotive Pantographs. *Digital Image Computing Techniques and Applications, 9th Biennial Conference of the Australian Pattern Recognition Society (DICTA 2007).* Glenelg, Australia. pp. 493-499.

[94]. Han, T., Liu, Y. & Liu, H. (2013) Research about high speed railway pantograph-catenary relations. *8th World Congress on Railway Research (WCRR)* Sydney, Australia.

[95]. Harell, P., Drugge, L. & Reijm, M. (2005) Study of critical sections in catenary systems during multiple pantograph operation. *Proceedings of the Institution of Mechanical Engineers, Part F: Journal of Rail and Rapid Transit* 219 (4), pp. 203-211.

[96]. Haug, E.J., Wu, S.C. & Yang, S.M. (1986) Dynamics of mechanical systems with Coulomb friction, stiction, impact and constraint addition-deletion—I theory. *Mechanism and Machine Theory*, 21 (5), pp. 401-406.

[97]. Hinton, G., Deng, L., Yu, D., Dahl, G., Mohamed, A.-r., Jaitly, N., Senior, A., Vanhoucke, V., Nguyen, P., Sainath, T. & Kingsbury, B. (2012) Deep Neural Networks for Acoustic Modeling in Speech Recognition: The Shared Views of Four Research Groups. *IEEE Signal Processing Magazine*, 29 (6), pp. 82 - 97.

[98]. Hobbs, A.E.W. (1977) Accurate prediction of overhead line behaviour. *Railway Gazette International* 133 (9), pp. 339-343.

[99]. Ikeda, K. (2008) Optimization of overhead contact lines for Shinkansen speed increases. *JR EAST Techical Review*, 12, pp. 64-69.

[100]. Jarzebowicz, L. & Judek, S. (2014) 3D machine vision system for inspection of contact strips in railway vehicle current collectors. *Applied Electronics (AE), 2014 International Conference on.* Pilsen, Czech Republic.

[101]. Jia, F., Lei, Y., Lin, J., Zhou, X. & Lu, N. (2016) Deep neural networks: A promising tool for fault characteristic mining and intelligent diagnosis of rotating machinery with massive data. *Mechanical Systems and Signal Processing*, 72-73, pp. 303-315.

[102]. Judek, S. & Jarzebowicz, L. (2014) Algorithm for automatic wear estimation of railway contact strips based on 3D scanning results. *Electrical and Power Engineering (EPE), 2014 International Conference and Exposition on.* Iasi, Romania.

[103]. Karakose, E. & Gencoglu, M.T. (2014) An investigation of pantograph parameter effects for pantograph-catenary systems. *IEEE International Symposium onInnovations in Intelligent Systems and Applications (INISTA)* Alberobello, Italy. pp. 338-343.

[104]. Karakose, E., Gencoglu, M.T., Karakose, M., Aydin, I. & Akin, E. (2017) A New Experimental Approach Using Image Processing-Based Tracking for an Efficient Fault Diagnosis in Pantograph–Catenary Systems. *IEEE Transactions on Industrial Informatics*, 13 (2), pp. 635-643.

[105]. Keen, P.M., Phillpotts, R.E. & Conway, S. (2008) An instrumented pantograph for high speed current collection measurements. *Railway Condition Monitoring, 4th IET International Conference on.* Derby, UK.

[106]. Kerschen, G., Worden, K., F.Vakakis, A. & Golinval, J.-C. (2006) Past, present and future of nonlinear system identification in structural dynamics. *Mechanical Systems and Signal Processing*, 20 (3), pp. 505-592.

[107]. Khan, S. & Yairi, T. (2018) A review on the application of deep learning in system health management. *Mechanical Systems and Signal Processing*, 107, pp. 241-265.

[108]. Kolbe, M. & Baldauf, D.-I.W. (2001) Compact contact force measurement system - online diagnosis of the overhead line system with regular trains. *World Congress Railway Research (WCRR)* Cologne, Germany.

[109]. Koyama, T., Ikeda, M., Kobayashi, S., Nakamura, K., Tabayashi, S. & Niwakawa, M. (2014) Measurement of the Contact Force of the Pantograph by Image Processing Technology. *Quarterly Report of RTRI*, 55 (2), pp. 73-78.

[110]. Koyama, T., Ikeda, M., Nakamura, K., Tabayashi, S. & Niwakawa, M. (2012) Measuring the contact force of a pantograph by image processing technology. *Computer in Railways XIII*, 127 (22), pp. 199 - 210.

[111]. Koyama, T., Usuda, T., Kawasaki, K., Nakamura, K. & Kawamura, T. (2016) Methods for Detecting Pantograph Defects Using Sensors Installed on Contact Lines. *Quarterly Report of RTRI*, 57 (3), pp. 207-212.

[112]. Kumaniecka, A. & Prącik, M. (2003) Modelling and Identifiation of Catenary-Pantograph System. *Journal of Theoretical and Applied Mechanices*, 41 (4), pp. 887-901.

[113]. Landi, A., Balestrino, A., Bruno, O., Sani, L., Masini, P., Mingozzi, E. & Papi, M. (2003) Infrared cameras for monitoring pantograph-catenary interactions. *World Congress on Railway Research (WCRR)* Edinburgh, UK.

[114]. Landi, A., Menconi, L. & Sani, L. (2006) Hough transform and thermo-vision for monitoring pantograph-catenary system. *Proceedings of the Institution of Mechanical Engineers, Part F: Journal of Rail and Rapid Transit*, 220 (4), pp. 435-447.

[115]. Lang, Z.Q., Billings, S.A. & R. Yue, J.L. (2007) Output frequency response function of nonlinear Volterra systems. *Automatica*, 43 (5), pp. 805–816.

[116]. Lee, C., Alena, R.L. & Robinson, P. (2005) Migrating fault trees to decision trees for real time fault detection on international space station. *IEEE conference on Aerospace Conference,*. pp. 1-6.

[117]. Liu, R., Yang, B., Zio, E. & Chen, X. (2018) Artificial intelligence for fault diagnosis of rotating machinery: A review. *Mechanical Systems and Signal Processing*, 108, pp. 33-47.

[118]. Lopez-Garcia, O., Carnicero, A. & Maron˜o, J.L. (2007) Influence of stiffness and contact modelling on catenary–pantograph system dynamics. *Journal of Sound and Vibration*, 299 (4), pp. 806-821.

[119]. Lu, C., Wang, Z.-Y., Qin, W.-L. & Ma, J. (2017) Fault diagnosis of rotary machinery components using a stacked denoising autoencoder-based health state identification. *Signal Processing*, 130, pp. 377-388.

[120]. Masini, P., Papi, M. & Puliatti, G. (1998) Virtual acquisition system for experimentation in pantograph-catenary interaction. *6th International Conference on Computer Aided Design, Manufacture and Operation in the Railway and Other Advanced Mass Transit Systems.* Lisbon, Portugal. pp. 827–836.

[121]. Massat, J.-P., Balmes, E., Bianchi, J.-P. & Kalsbeek, G.V. (2015) OSCAR statement of methods. *Vehicle System Dynamics*, 53 (3), pp. 370-379.

[122]. MATLAB. (2018) *Model and simulate multibody mechanical systems* [Online]. MATLAB. Available: https://uk.mathworks.com/products/simmechanics.html [Accessed 20/09/2018 2018].

[123]. Mochizuka, H., Kusumi, S., Mori, M. & Kobayashi, N. (2000) New measuring method of contact loss of pantograph in AC electric railroads. *Instrumentation and Measurement Technology Conference (IMTC 2000). Proceedings of the 17th IEEE.* Baltimore, MD, USA. pp. 1529-1533.
[124]. Morris, R.B. (1964) The Application of an Analogue Computer to a Problem of Pantograph and Overhead Line Dynamics. *Proceedings of the Institution of Mechanical Engineers*, 179 (1), pp. 782-808.
[125]. Murphy, D., Fielder, S., Chullingford, S. & Hoare, P. (2007) *Maintenance Manual*. Brecknell Willis, Somerset, U.K. TS4548.
[126]. NetworkRailLimited. (2017) *Railway Upgrade Plan: 2017-18*. Network Rail Limited, London.
[127]. Ng, A. (2011) *Sparse autoencoder*. Stanford University, Stanford, California.
[128]. Ng, A.Y. & Jordan, M.I. (2002). On discriminative vs. generative classifiers: A comparison of logistic regression and naive bayes. *In:* Jordan, M. I., LeCun, Y. & Solla, S. A. (eds.) *Advances in neural information processing systems.* Cambridge, Massachusetts, pp. 841-848.
[129]. O'Connor, D. (1984) *Modeling and simulation of pantograph-catenary systems.* Master of Science. Department of Mechanical Engineering, Massachusetts Institute of Technology. Cambridge, MA.
[130]. O'Donnell, C. (2003) *Development of a spatially varying stiffness model of the overhead contact system.* Masters of Science. Department of Mechanical Engineering, University of Sehffield. Sheffield, UK.
[131]. O'Donnell, C., Palacin, R. & Rosinski, J. (2006) Pantograph Damage and Wear Monitoring System. *Railway Condition Monitoring, 2006. The Institution of Engineering and Technology International Conference on.* Birmingham, UK.
[132]. O'Connor, D.N., Eppinger, S.D., Seering, W.P. & Wormley, D.N. (1997) Active Control of a High-Speed Pantograph. *Journal of Dynamic Systems, Measurement, and Control* 119 (1), pp. 1-4.
[133]. Ogata, K. (1970) *Modern Control Engineering*. Fifth Edition. London: Prentice Hall.
[134]. Olshausen, B.A. & Field, D.J. (1996) Emergence of simple-cell receptive field properties by learning a sparse code for natural images. *Nature*, 381, pp. 607-609.
[135]. Olshausen, B.A. & Field, D.J. (1997) Sparse Coding with an Overcomplete Basis Set: A Strategy Employed by V1. *Vision Research*, 37 (23), pp. 3311-3325.
[136]. Park, T.J., Han, C.S. & Jang, J.H. (2003) Dynamic sensitivity analysis for the pantograph of a high-speed rail vehicle. *Journal of Sound and Vibration*, 266 (2), pp. 235-260.
[137]. Phillpotts, R. (1995) *Strategic Project-Preventing Pantograph and OHL Line Damage: Part 4 - Optical Fibre Pantograph Auto Drop System*. Systems and Monitoring Group, British Railway Research Derby, UK.
[138]. Poetsch, G., Evans, J., Meisinger, R., Kortum, W., Baldauf, W., Veitl, A. & Wallaschek, J. (1997) Pantograph/Catenary Dynamics and Control. *Vehicle System Dynamics* 28 (2-3), pp. 159-195.
[139]. Pombo, J. & Ambrósio, J. (2012a) Influence of pantograph suspension characteristics on the contact quality with the catenary for high speed trains. *Computers and Structures*, 110-111, pp. 32-42.
[140]. Pombo, J. & Ambrósio, J. (2012b) Multiple Pantograph Interaction With Catenaries in High-Speed Trains. *Journal of Computational and Nonlinear Dynamics*, 7 (4), pp. 041008.
[141]. Pombo, J., Ambrósio, J., Pereira, M., Rauter, F., Collina, A. & Facchinetti, A. (2009) Influence of the aerodynamic forces on the pantograph–catenary system for high-speed trains. *Vehicle System Dynamics*, 47 (11), pp. 1327-1347.
[142]. Pombo, J. & Ambrósio, J.A.C. (2013) Environmental and track perturbations on multiple pantograph interaction with catenaries in high-speed trains. *Computer & Structures*, 124, pp. 88–101.
[143]. Pombo, J. & Antunes, P. (2013) A Comparative Study between Two Pantographs in Multiple Pantograph High-Speed Operations. *International Journal of Railway Technology*, 2 (1), pp. 83-108.
[144]. Pombo, J., Antunes, P. & Ambrósio, J. (2012) A Study on Multiple Pantograph Operations for High-Speed Catenary Contact *11th International Conference on Computational Structures Technology.* Stirlingshire, UK.
[145]. Profillidis, V.A. (2016) *Railway management and engineering*. New York, USA: Routledge.

[146]. Pugi, L., B.Allotta, F.Bartolini, M.Rinchi, Collina, A., F.Resta, G.Bucca, A.Facchinetti & R.Cheli (2008) Design and development of an active suspension system for T-2006 Pantograph. *8th World Congress on Railway Research (WCRR).* Seoul, Korea. pp. 1-9.

[147]. Qin, Y., Zhang, Y., Cheng, X., Jia, L. & Xing, Z. (2014) An analysis method for correlation between catenary irregularities and pantograph-catenary contact force. *Journal of Central South University*, 21 (8), pp. 3353-3360.

[148]. RAIB. (2013) *Rail Accident Report - Accident involving a pantograph and the overhead line near Littleport, Cambridgeshire 5 January 2012*. Rail Accident Ivestigation Branch, Derby.

[149]. Ranzato, M.A., Poultney, C., Chopra, S. & LeCun, Y. (2007) Efficient Learning of Sparse Representations with an Energy-Based Model. *19th International Conference on Neural Information Processing Systems.* Canada. pp. 1137-1144.

[150]. Rauter, F.G., POMBO, J., AMBRÓSIO, J., CHALANSONNET, J., BOBILLOT, A. & PEREIRA, M.S. (2007a) Contact Model for The Pantograph-Catenary Interaction. *Journal of System Design and Dynamics; Special Issue on The Third Asian Conference on Multibody Dynamics 2006*, 1 (3), pp. 447-457.

[151]. Rauter, F.G., Pombo, J., Ambrósio, J. & Pereira, M. (2007b). Multibody Modeling of Pantographs for Pantograph-Catenary Interaction. *IUTAM Symposium on Multiscale Problems in Multibody System Contacts.* Dordrecht: Springer, pp. 205-226.

[152]. Resta, F., Collina, A. & Fossati, F. (2001) Actively controlled pantograph: an application. *IEEE/ASME International Conference on Advanced Intelligent Mechatronics.* Como, Italy. pp. 243-248.

[153]. Resta, F., Facchinetti, A., Collina, A. & Bucca, G. (2008) On the use of a hardware in the loop set-up for pantograph dynamics evaluation. *Vehicle System Dynamics*, 46 (S1), pp. 1039-1052.

[154]. Rosero, J., Ortega, J., Aldabas, E. & Romeral, L. (2007) Moving towards a more electric aircraft. *IEEE Aerospace and Electronic Systems Magazine*, 22 (3), pp. 3-9.

[155]. RTSandTSLG. (2012) *The Future Railway*. RSSB, London.

[156]. Rumelhart, D.E., Hinton, G.E. & Williams, R.J. (1986) Learning representations by back-propagating errors. *Nature* 323 (9), pp. 533–536

[157]. Safavian, S.R. & Landgrebe, D. (1991) A survey of decision tree classifier methodology. *IEEE transactions on systems, man, and cybernetics*, 21 (3), pp. 660-674.

[158]. Sánchez-Rebollo, C., Carnicero, A. & Jiménez-Octavio, J.R. (2015) Candy statement of method. *Vehicle System Dynamics* 53 (3), pp. 392-401.

[159]. Schaub, M. & Simeon, B. (2001) Pantograph-Catenary Dynamics: An Analysis of Models and Simulation Technique. *Mathematical and Computer Modelling of Dynamical Systems: Methods, Tools and Applications in Engineering and Related Sciences*, 7 (2), pp. 225-238.

[160]. Schilders, W.H., Vorst, H.A.V.d. & Rommes., J. (2008) *Model order reduction: theory, research aspects and applications*. Berlin: Springer.

[161]. Schirrer, A., Aschauer, G., Talic, E., Kozek, M. & Jakubek, S. (2017) Catenary emulation for hardware-in-the-loop pantograph testing with a model predictive energy-conserving control algorithm. *Mechatronics*, 41, pp. 17-28.

[162]. Schmitz, T.L. & Smith, K.S. (2008) *Machining Dynamics: Frequency Response to Improved Productivity*. New York: Springer Science & Business Media.

[163]. Schröder, K., Ecke, W., Kautza, M., Willett, S., Jenzer, M. & Bosselmann, T. (2013) An approach to continuous on-site monitoring of contact forces in current collectors by a fiber optic sensing system. *Optics and Lasers in Engineering*, 51 (2), pp. 172-179.

[164]. Seering, W., Vesely, C., Armbruster, K. & Wormley, D. (1983) Experimental and Analytical Study of Pantograph Dynamics. *American Control Conference.* San Francisco, CA, USA. pp. 270-275.

[165]. Seo, J.-H., Sugiyama, H. & Shabana, A.A. (2005) Three-Dimensional Large Deformation Analysis of the Multibody Pantograph/Catenary Systems. *Nonlinear Dynamics*, 42 (2), pp. 199–215.

[166]. Shabana, A.A. (2013) *Dynamics of multibody systems*. New York: Cambridge University Press.

[167]. Shin, S.K., Eum, K.Y. & Um, J.H. (2006) Contact Force Control of Pantograph-Catenary System using Block Pulse Function. *World Congress on Railway Research (WCRR).* Montreal, Canada.

[168]. Sidorov, O., Goryunov, V., Salya, I. & Tomilov, V. (2016) Dynamic models choice for pantographs of high-speed railway transport. *Dynamics of Systems, Mechanisms and Machines (Dynamics).* Omsk, Russia. pp. 1-4.
[169]. SNCBandSNCF. (2007) *Maintenance document V AUX 07 37*. Internal the Eurostar International Maintenance Committee report Unpublished.
[170]. SNCF. (1991) *Brecknell Willis panographs type test report*. SNCF, France.
[171]. Soderstrom, T.S. & Stoica, P.G. (1989) *System Identification*. New Jersey, US: Prentice Hall.
[172]. Song, Y., Ouyang, H., Liu, Z., Mei, G., Wang, H. & Lu, X. (2017) Active control of contact force for high-speed railway pantograph-catenary based on multi-body pantograph model. *Mechanism and Machine Theory*, 115, pp. 35-59.
[173]. Stein, G., Chen, B., Wu, A.S. & Hua, K.A. (2005) Decision tree classifier for network intrusion detection with GA-based feature selection. *43rd annual Southeast regional conference*. pp. 136-141.
[174]. Storer, D.M. (1991) *Dynamic Analysis of Non-Linear Structures Using Higher Order Frequency Response Functions.* Doctor of Philosophy. Department of Engineering, University of Manchester. Manchester, UK.
[175]. Stoten, D., Yamaguchi, T. & Yamashita, Y. (2016) Dynamically substructured system testing for railway vehicle pantographs. *Journal of Physics: Conference Series.* pp. 012204.
[176]. Sun, W., Shao, S., Zhao, R., Yan, R., Zhang, X. & Chen, X. (2016) A sparse auto-encoder-based deep neural network approach for induction motor faults classification. *Measurement*, 89, pp. 171-178.
[177]. Swain, P.H. & Hauska, H. (1977) The decision tree classifier: Design and potential. *IEEE Transactions on Geoscience Electronics*, 15 (3), pp. 142-147.
[178]. Tao, S., Zhang, T. & Yang, J. (2015) Bearing fault diagnosis method based on stacked autoencoder and softmax regression. *34th Chinese Control Conference (CCC).* Hangzhou, China. pp. 6331-6335.
[179]. Tieri, R., Collina, A., Carnevale, M., Stichel, S. & Jönsson, P.-A. (2013) Pneumatic active control system for pantograph-catenary interaction. *10th World Congress on Railway Research.* Sidney. pp. 1-7.
[180]. Tur, M., Baeza, L., Fuenmayor, F.J. & García, E. (2015) PACDIN statement of methods. *Vehicle System Dynamics*, 53 (3), pp. 402-411.
[181]. Van, O.V. (2016) *Introduction of variability into pantograph-catenary dynamic simulations.* Doctor of Philosophy. l'École Nationale Supérieure d'Arts et Métiers. Paris.
[182]. Van, O.V., Massat, J.-P. & Balmes, E. (2017) Waves, modes and properties with a major impact on dynamic pantograph-catenary interaction. *Journal of Sound and Vibration*, 402, pp. 51-69.
[183]. Veitl, A. & Arnold, M. (1999) Coupled simulation of multibody systems and elastic structures. *Advances in Computational Multibody Dynamics*, pp. 635-644.
[184]. Verma, N.K., Gupta, V.K., Sharma, M. & Sevakula, R.K. (2013) Intelligent condition based monitoring of rotating machines using sparse auto-encoders. *Prognostics and Health Management (PHM), IEEE Conference on.* Gaithersburg, MD, USA.
[185]. Vincent, P., Larochelle, H., Lajoie, I., Bengio, Y. & Manzagol, P.-A. (2010) Stacked Denoising Autoencoders: Learning Useful Representations in a Deep Network with a Local Denoising Criterion. *Journal of machine learning research*, 11, pp. 3371-3408.
[186]. Walters, S., Rachid, A. & Mpanda, A. (2011) On Modelling and Control of Pantograph Catenary Systems. *Int. Conf. on Pantograph Catenary Interaction Framework for Intelligent Control PACIFIC.* Amiens.
[187]. Wann, L.-m. (1980) *Improvement of a Pantograph for High-speed Trains.* Master of Science Department of Mechanical Engineering Massachusetts Institue of Technology Massachusetts Institue of Technology
[188]. Wei, W., Zhidong, Y. & Ting, G. (2013) The development of pantograph-catenary dynamics testing rig for high-speed railway. *Mechatronic Sciences, Electric Engineering and Computer (MEC), Proceedings 2013 International Conference on.* Shenyang, China.
[189]. Weston, P., Stewart, E., Roberts, C. & Hillmansen, S. (2008) Analysis of electric shoegear dynamics. *8th World congress on railway research (WCRR).* Coex, Korea. pp. 748-752.

[190]. Weston, P. & Xin, T. (2016) *RSSB1751 deliverable D0.3 "Phase I interim progress report"*. Internal University of Birmingham report, Birmingham. Unpublished.
[191]. Weston, P. & Xin, T. (2017) *Pantograph test rig: Final report*. University of Birmingham Birmingham. RSSB project reference RSSB-1751.
[192]. Wolstenholme, A. (2017) *Environment Report 2017*. Crossrail, London.
[193]. Wu, T.X. & Brennan, M.J. (1999) Dynamic stiffness of a railway overhead wire system and its effect on pantograph–catenary system dynamics. *Journal of Sound and Vibration*, 219 (3), pp. 483-502.
[194]. Xinsheng, L. & Loparo, K.A. (2004) Bearing fault diagnosis based on wavelet transform and fuzzy inference. *Mechanical systems and signal processing* 18 (5), pp. 1077-1095.
[195]. Xu, J., Xiang, L., Liu, Q., Gilmore, H., Wu, J., Tang, J. & Madabhushi, A. (2015) Stacked Sparse Autoencoder (SSAE) for Nuclei Detection on Breast Cancer Histopathology Images. *IEEE Transactions on Medical Imaging*, 35 (1), pp. 119-130.
[196]. Zhang, W., Mei, G., Wu, X. & Shen, Z. (2002) Hybrid Simulation of Dynamics for the Pantograph-Catenary System. *Vehicle System Dynamics*, 38 (6), pp. 393-414.
[197]. Zhang, W., Zhou, N., Li, R., Mei, G. & Song, D. (2011) Pantograph and catenary system with double pantographs for high-speed trains at 350 km/h or higher. *Journal of Modern Transportation*, 19 (1), pp. 7-11.
[198]. Zhao, W., Meng, Q.-H., Zeng, M. & Qi, P.-F. (2017) Stacked Sparse Auto-Encoders (SSAE) Based Electronic Nose for Chinese Liquors Classification. *Sensors*, 17 (12).
[199]. Zhou, N., Lv, Q., Yang, Y. & Zhang, W. (2015) <TPL-PCRUN> Statement of methods. *Vehicle System Dynamics*, 53 (3), pp. 380-391.

APPENDIX A FIGURES AND TABLES

A.1 Tables referenced in Chapter 4

A.1.1 Hysteresis of the new pantograph under different excitation speeds

The measurements of hysteresis test for the pantograph in the new condition are shown in Table A.1.

Table A.1 Hysteresis of the tested pantograph

Speed (mm/s)	Avg. up force (N)	Avg. down force (N)	Static uplift force (N)	Hysteresis (N)	Damping. (Ns/mm)
50.00	79.6	100.6	90.1	20.9	0.21
100.00	78.3	101.9	90.9	23.5	0.12
150.00	76.7	104.3	90.5	27.6	0.09
200.00	73.8	106.7	90.3	32.9	0.08
250.00	70.1	110.0	90.0	39.9	0.08
300.00	65.9	114.1	90.0	48.2	0.08
350.00	61.1	118.8	89.9	57.7	0.08
400.00	55.7	124.1	89.9	68.4	0.09

A.2 Figures and Tables referenced in Chapter 5: Hysteresis Test

A.2.1 Hysteresis tests with changes to the head suspension

In §5.2, the hysteresis was measured with changes to the pantograph head suspension under various excitation speeds. Some of the hysteresis curves are shown in Figure A.1.

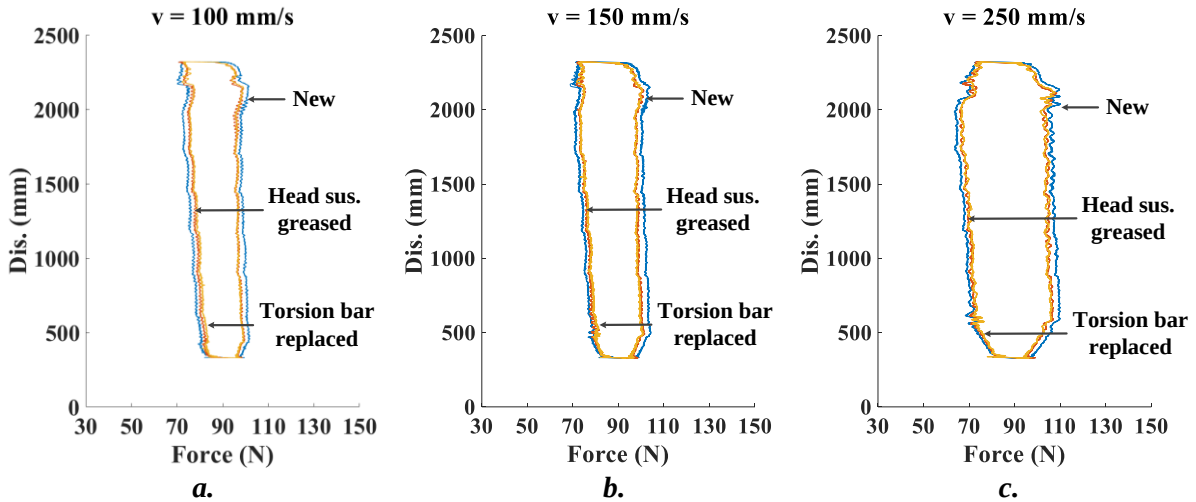

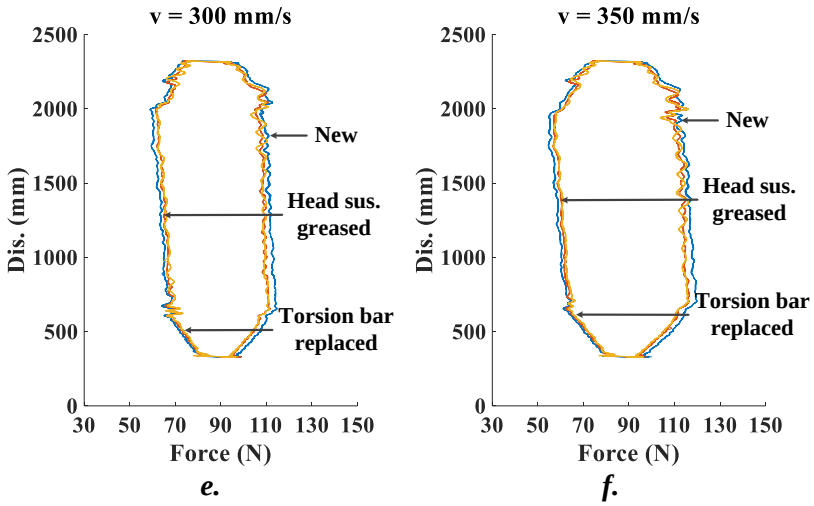

Figure A.1 Hysteresis comparison: new, head suspension greased, and torsion bar replaced

The measurements of the hysteresis tests with changes to the head suspension under different excitation speeds are shown in Table A.2.

Table A.2 Hysteresis with changes to pantograph head suspension

Parameters	Speed (mm/s)	Pantograph conditions		
		Healthy	Case 1	Case 2
Avg. up force (N)	50	79.64	81.8	82.0
	100	78.33	80.5	81.2
	150	76.69	78.5	78.9
	200	73.78	75.6	76.1
	250	70.08	71.9	72.3
	300	65.89	67.6	68.0
	350	61.10	62.7	63.2
	400	55.74	57.7	57.9
Avg. down force (N)	50	100.6	98.3	98.0
	100	101.9	99.5	99.3
	150	104.3	101.4	100.9
	200	106.7	103.9	103.8
	250	109.9	107.3	106.8
	300	114.1	111.3	111.3
	350	118.8	116.0	115.7
	400	124.1	121.5	121.5
Static uplift force (N)	50	90.1	90.1	90.0
	100	90.1	90.0	90.2
	150	90.5	89.9	89.9
	200	90.3	89.8	90.0
	250	90.0	89.6	89.6
	300	90.0	89.5	89.7
	350	89.9	89.4	89.4
	400	89.9	89.6	89.7
Hysteresis (N)	50	20.9	16.5	16.0
	100	23.5	19.0	18.1
	150	27.6	22.9	22.0
	200	32.9	28.3	27.7
	250	39.9	35.3	34.4
	300	48.2	43.6	43.2
	350	57.7	53.3	52.4
	400	68.4	63.7	63.6

A.2.2 Hysteresis tests with various tightness of one outer chain

The hysteresis tests were accomplished with different degrees of tightness of the outer chain. Some of the measurements are shown in Figure A.2.

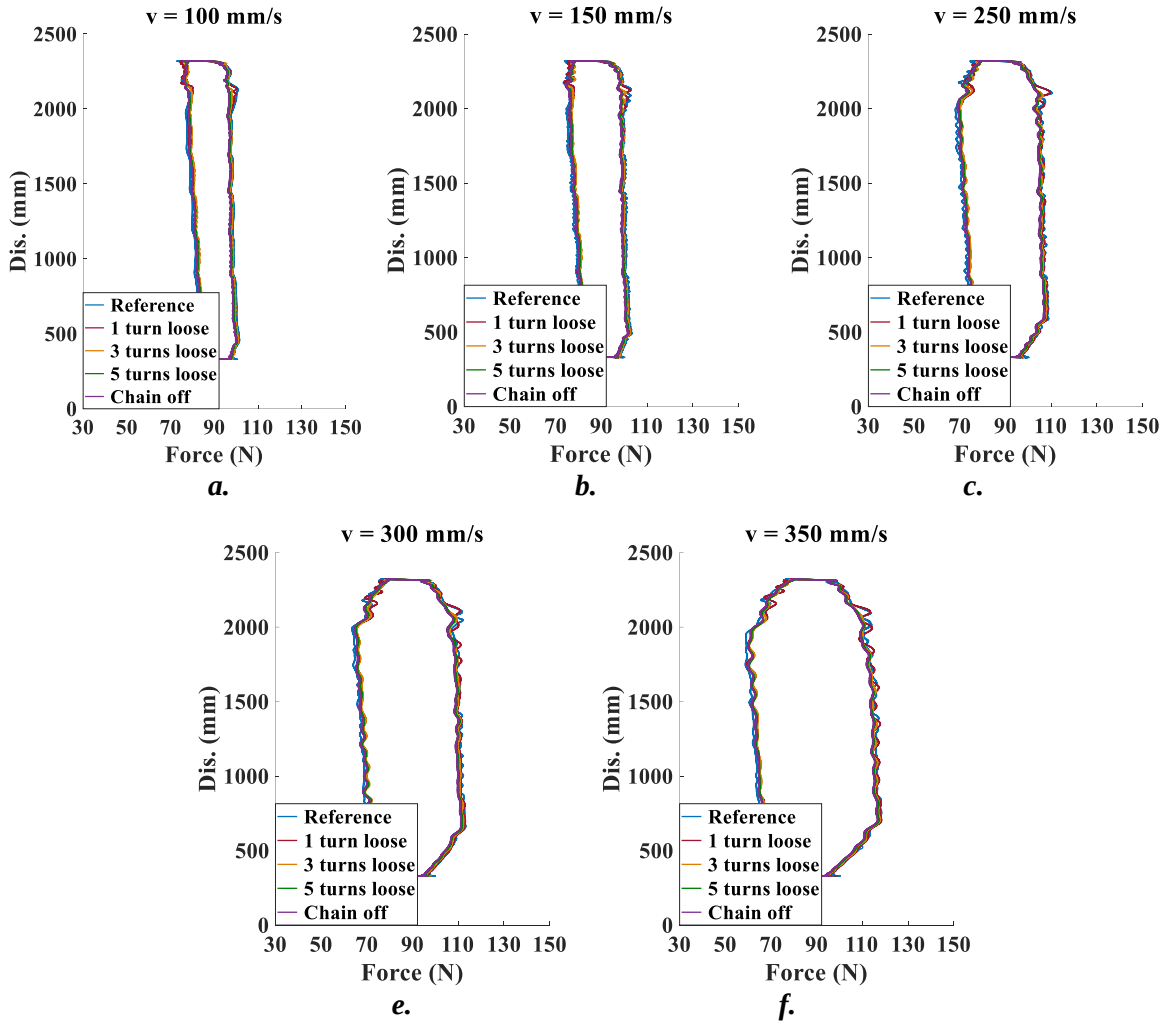

Figure A.2 Hysteresis comparison: reference and various tightness of the outer chain

A.2.3 Hysteresis tests with the leaking pneumatic actuator

The hysteresis tests were accomplished with replacing the original pneumatic actuator by a leaking one. The details of the measurements are shown in Table A.3.

Table A.3 Hysteresis with the leaking pneumatic actuator

Speed (mm/s)	Average up force (N)	Average down force (N)	Static uplift force (N)	Hysteresis (N)	Damping coefficient (Ns/mm)
50.00	81.5	96.8	89.1	15.4	0.15
100.00	79.3	97.3	88.3	18.1	0.09
150.00	76.3	98.6	87.5	22.3	0.07
200.00	72.5	100.4	86.5	27.9	0.07
250.00	67.9	102.9	85.5	34.9	0.07
300.00	63.2	106.2	84.7	43.1	0.07
350.00	58.2	110.1	84.1	51.9	0.07
400.00	52.7	114.5	83.6	61.8	0.08

A.3 Figures referenced in Chapter 6: Frequency Response Function

A.3.1 Dynamic Behaviour of the Pantograph

A.3.1.1 Frequency-response test of the new pantograph using 0.5 mm excitation

The FRFs of the new pantograph measured under 0.5 mm excitation are shown in Figure A.3.

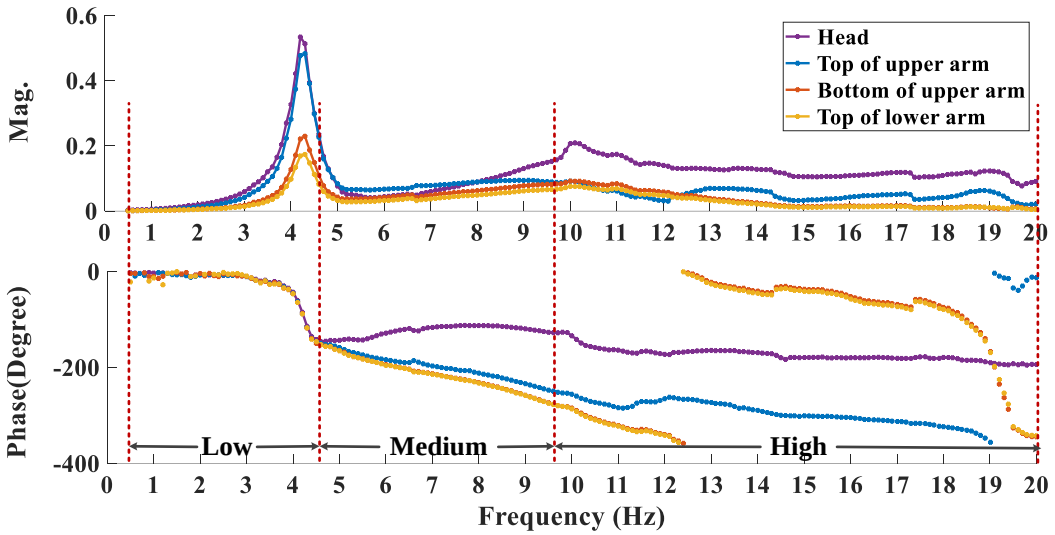

Figure A.3 FRFs of the new pantograph under 0.5 mm excitation

A.3.1.2 Frequency-response test of the new pantograph using 2 mm excitation

The FRFs of the new pantograph to measure under 2 mm excitation are shown in Figure A.4.

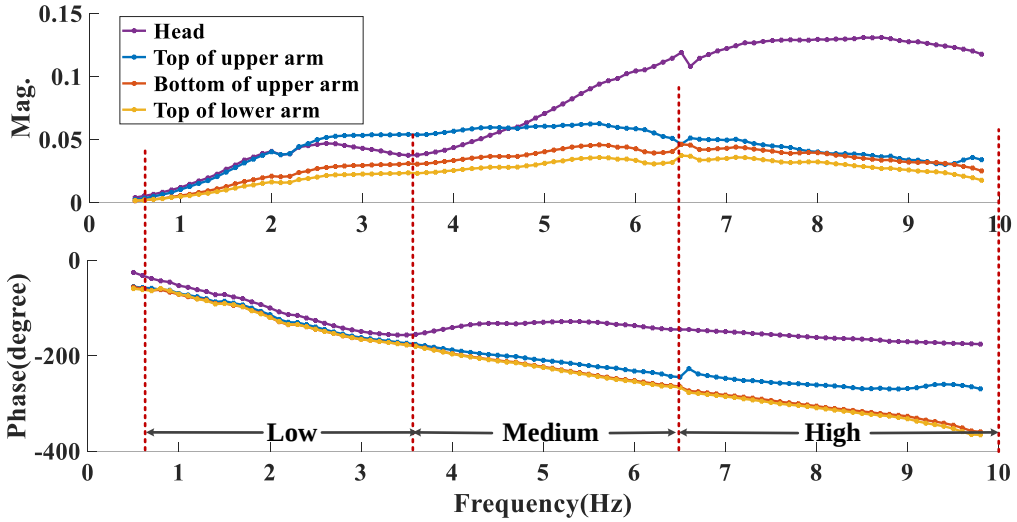

Figure A.4 FRFs of the new pantograph under 2 mm excitation

A.3.1.3 Frequency-response test of the new pantograph using 5 mm excitation

The FRFs of the new pantograph to measure under 5 mm excitation are shown in Figure A.5.

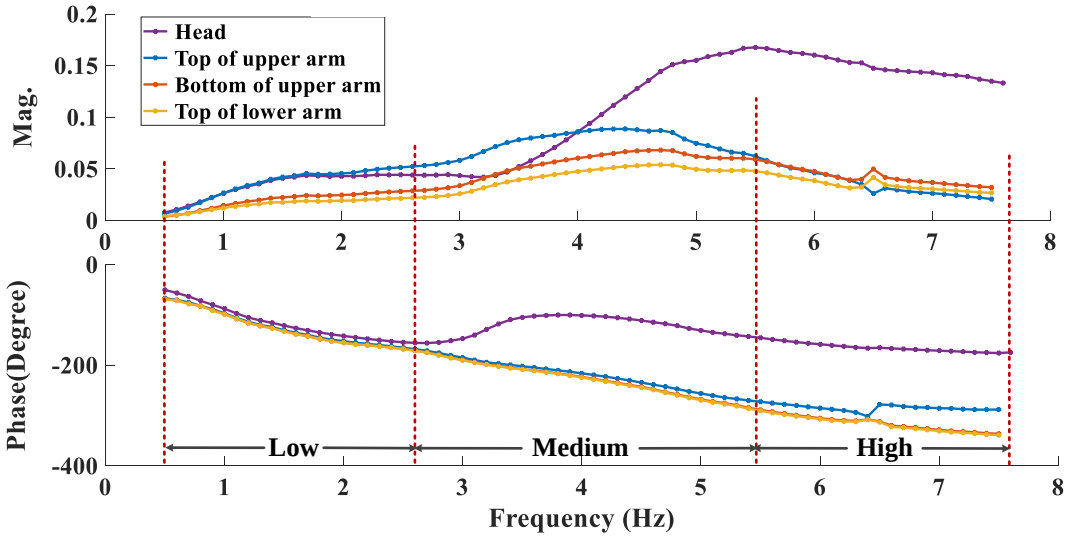

Figure A.5 FRFs of the new pantograph under 5 mm excitation

A.3.2 FRFs under changes to the Head Suspension

A.3.2.1 Frequency-response test using decreasing excitation

The decreasing-amplitude excitation method is applied to the obtained the FRFs with two changes to the pantograph head suspension. The FRFs of the pantograph arms are shown in Figures A.6 – A.8.

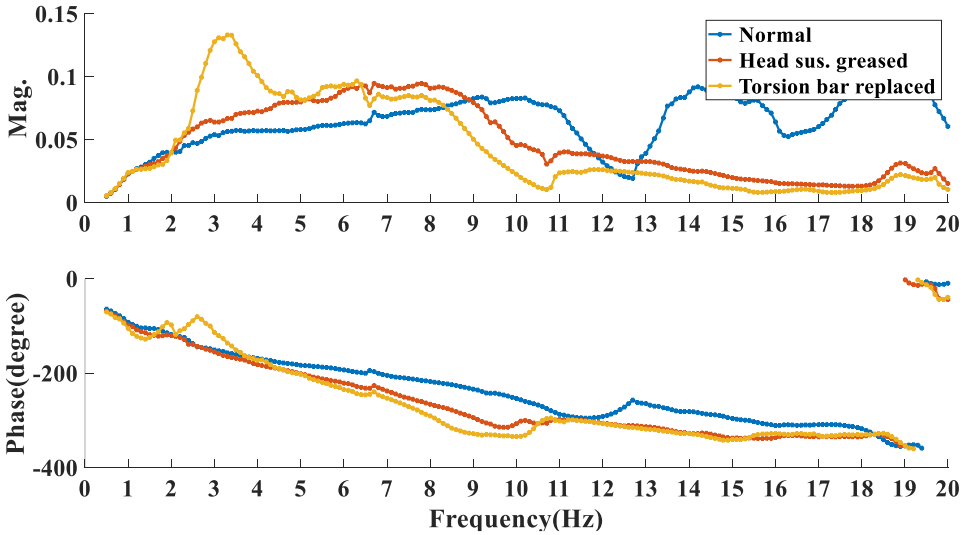

Figure A.6 FRFs of upper arm top with changes to head suspension using decreasing excitation

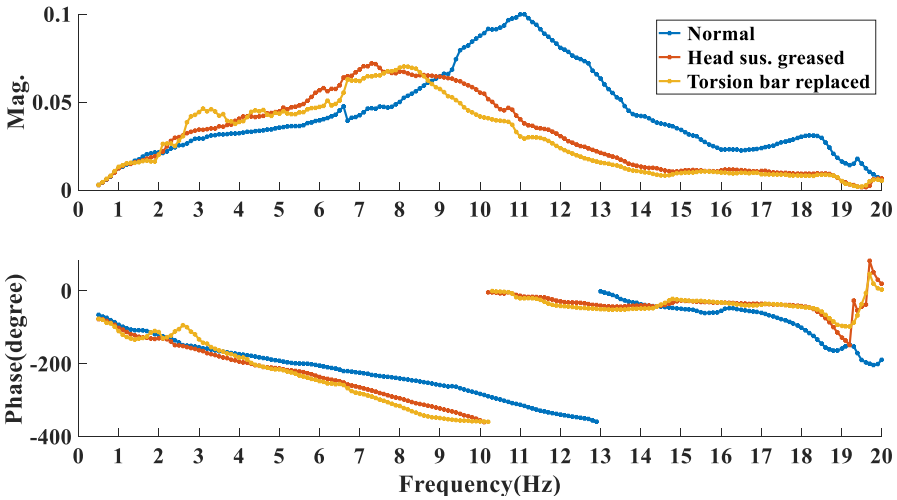

Figure A.7 FRFs of upper arm bottom with changes to head suspension using decreasing excitation

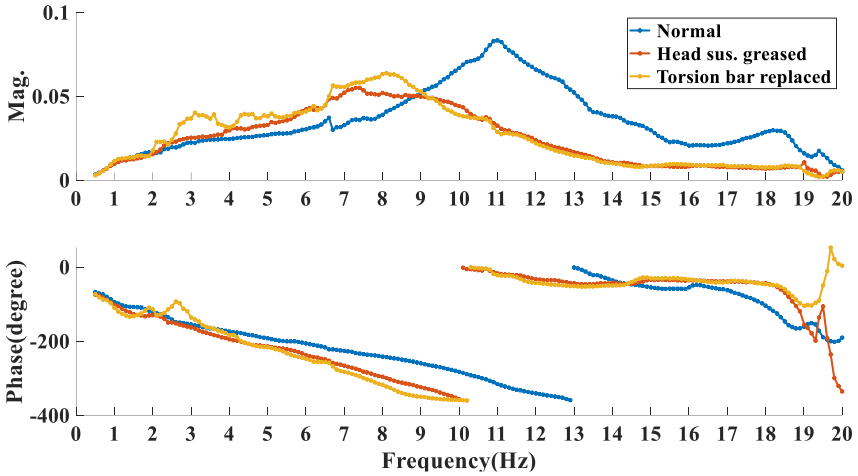

Figure A.8 FRFs of lower arm top with changes to head suspension using decreasing excitation

A.3.2.2 Frequency-response test using 0.3 mm excitation

The FRFs of the pantograph arms obtained with two changes made to the pantograph head suspension using 0.3 mm excitation are shown in Figure A.9 – A.11.

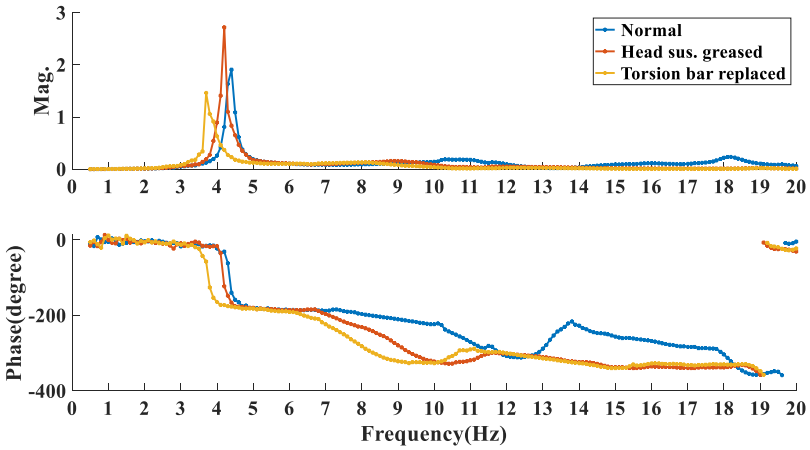

Figure A.9 FRFs of upper arm top with changes to head suspension using 0.3 mm excitation

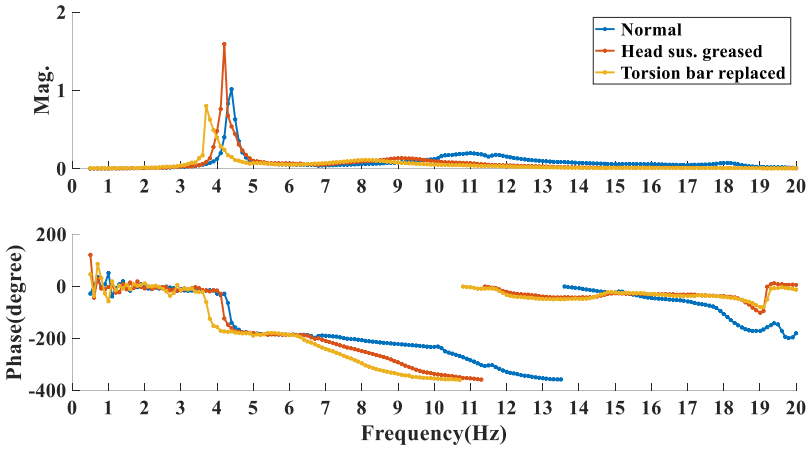

Figure A.10 FRFs of upper arm bottom with changes to head suspension using 0.3 mm excitation

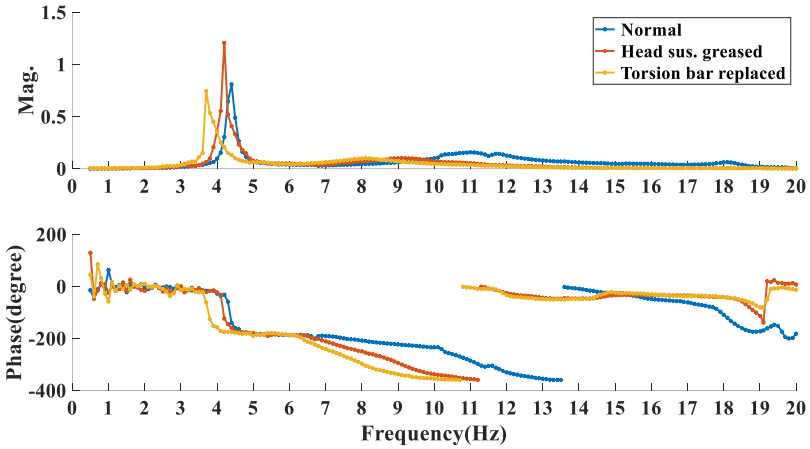

Figure A.11 FRFs of lower arm top with changes to head suspension using 0.3 mm excitation

A.3.2.3 Frequency-response test using 1mm excitation

The excitation level of 1 mm is applied to obtain the FRFs with two changes made to the pantograph head suspension; the results are shown in Figure A.12 – A.14.

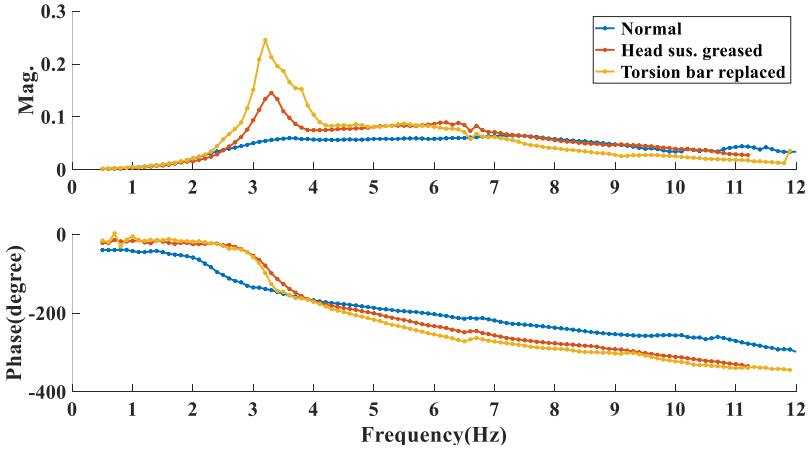

Figure A.12 FRFs of upper arm top with changes to head suspension using 1 mm excitation

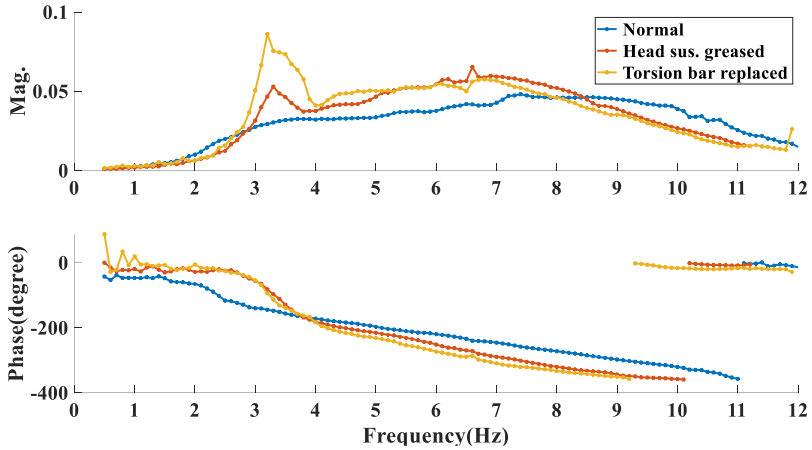

Figure A.13 FRFs of upper arm bottom with changes to head suspension using 1 mm excitation

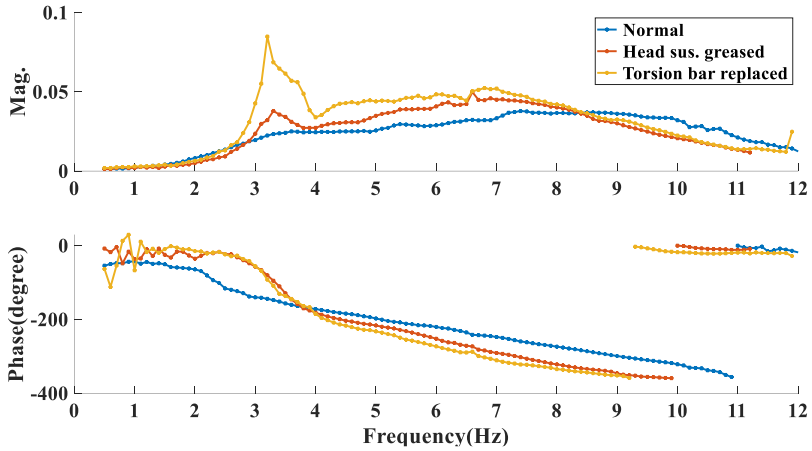

Figure A.14 FRFs of lower arm top with changes to head suspension using 1 mm excitation

A.3.2.4 Frequency-response test using 2 mm excitation

The FRFs of the pantograph arms under 2 mm excitation are shown in Figure A.15 –A.17.

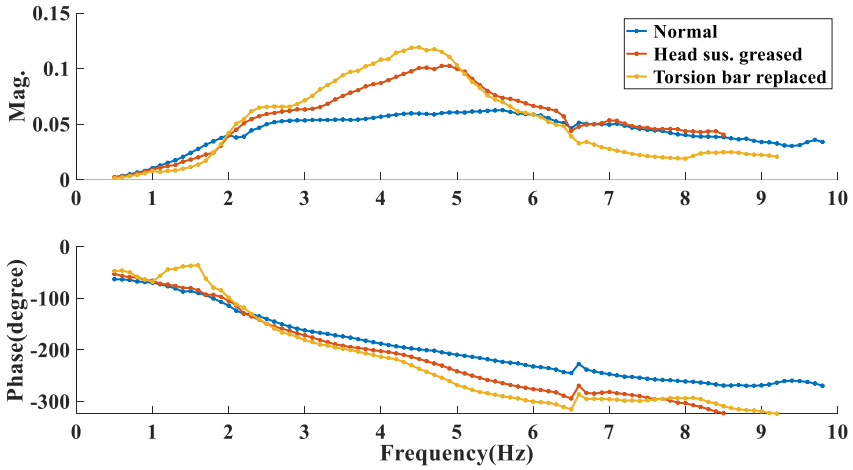

Figure A.15 FRFs of upper arm top with changes to head suspension using 2 mm excitation

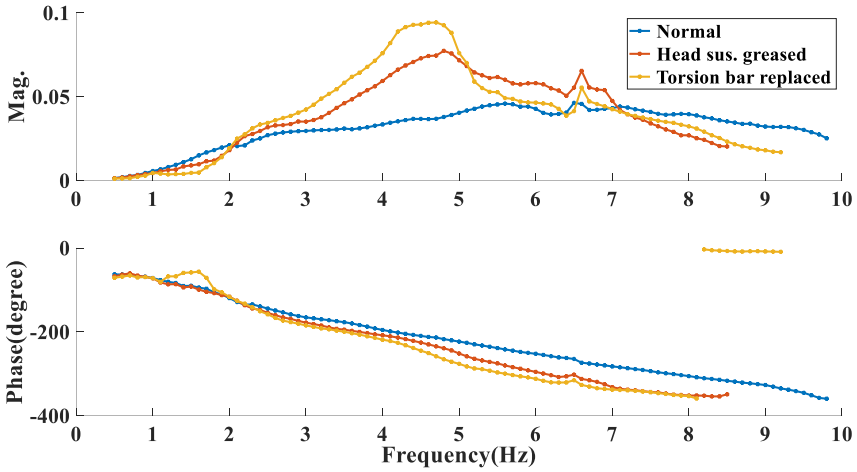

Figure A.16 FRFs of upper arm bottom with changes to head suspension using 2 mm excitation

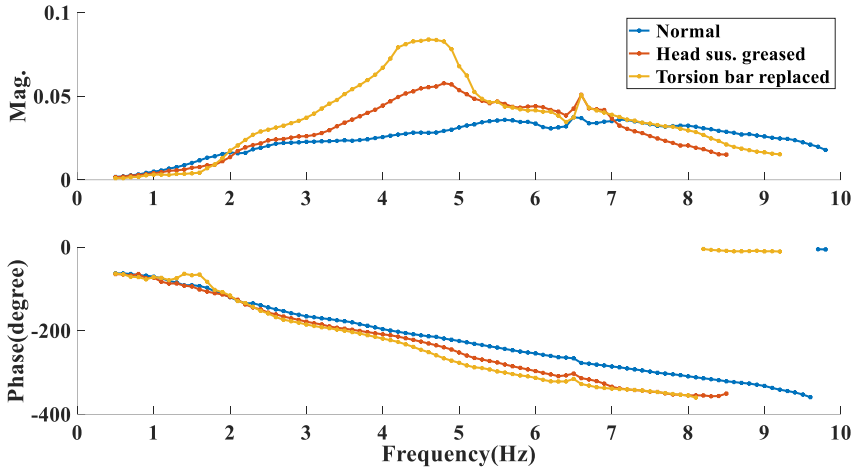

Figure A.17 FRFs of lower arm top with changes to head suspension using 2 mm excitation

A.3.3 FRFs with changes to elbow joint outer chain

A.3.3.1 Frequency-response test using decreasing excitation

The decreasing-amplitude excitation is applied to detect the changes to the outer chain, the FRFs of the pantograph arms as shown in Figure A.18- A.20.

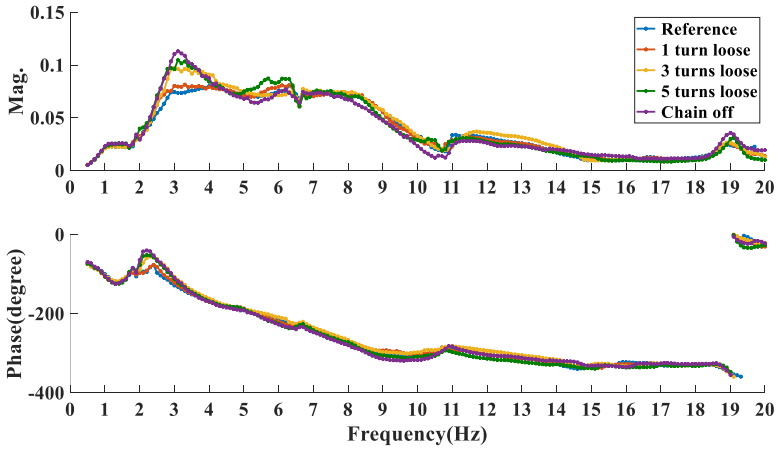

Figure A.18 FRFs of upper arm top with changes to outer chain under decreasing excitation

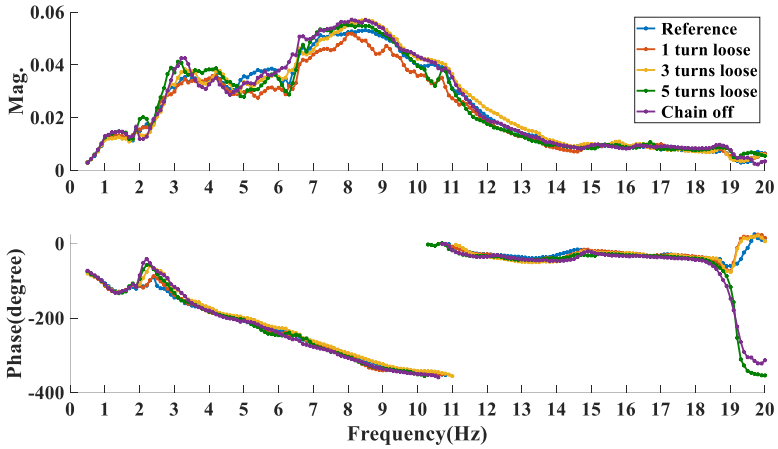

Figure A.19 FRFs of upper arm bottom with changes to outer chain under decreasing excitation

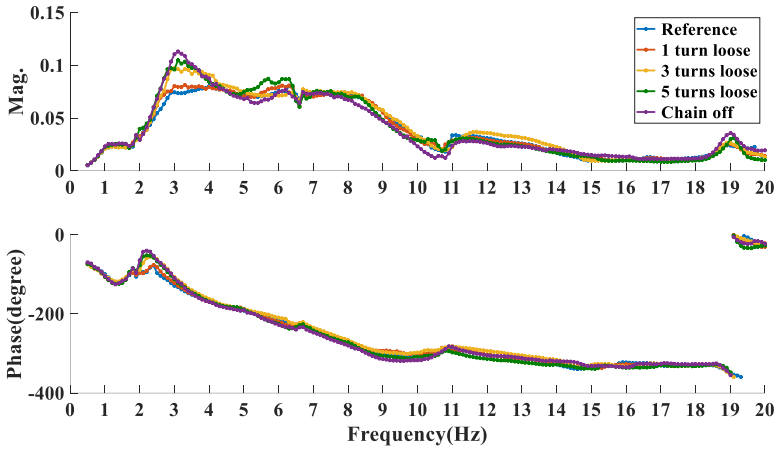

Figure A.20 FRFs of lower arm top with changes to outer chain under decreasing excitation

A.3.3.2 Frequency-response test using 0.3 mm excitation

The 0.3 mm excitation is applied to detect the changes to the outer chain, the FRFs of the pantograph arms as shown in Figure A.21 – A.23.

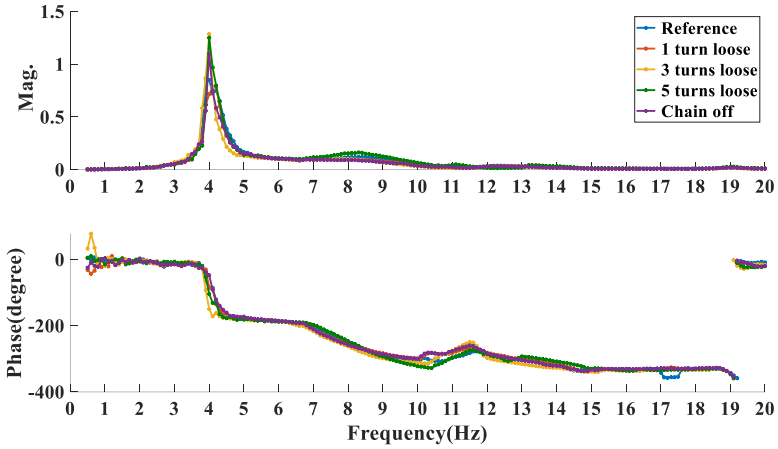

Figure A.21 FRFs of upper arm top with changes to outer chain under 0.3 mm excitation

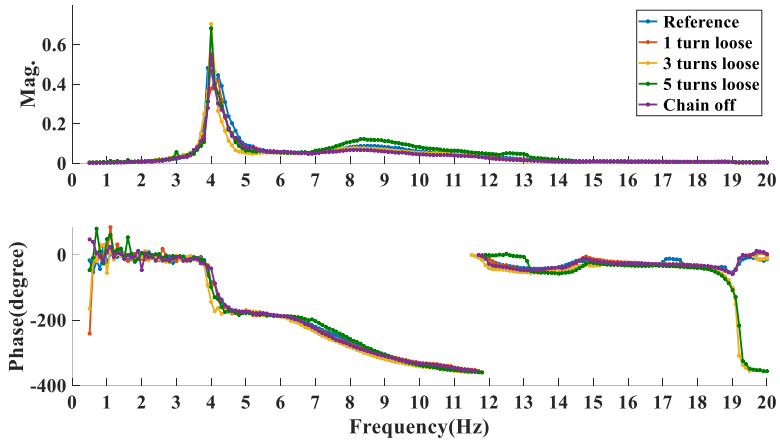

Figure A.22 FRFs of upper arm bottom with changes to outer chain under 0.3 mm excitation

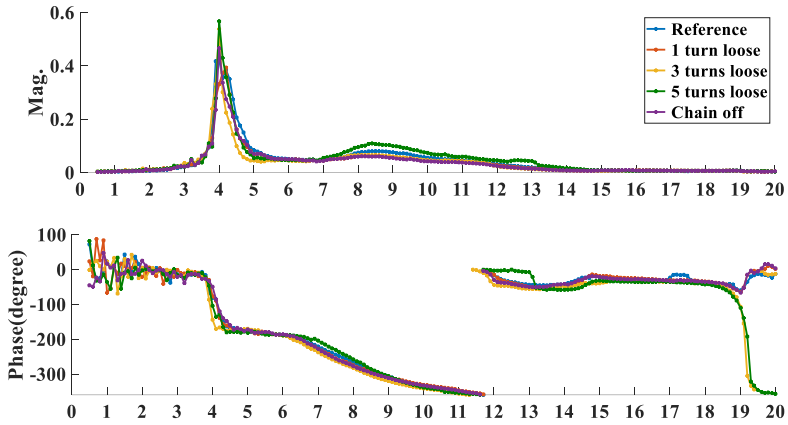

Figure A.23 FRFs of lower arm top with changes to outer chain under 0.3 mm excitation

A.3.3.3 Frequency-response test using 1 mm excitation

The 1 mm excitation is applied to detect the changes to the outer chain, the FRFs of the pantograph arms as shown in Figure A.24 – A.26.

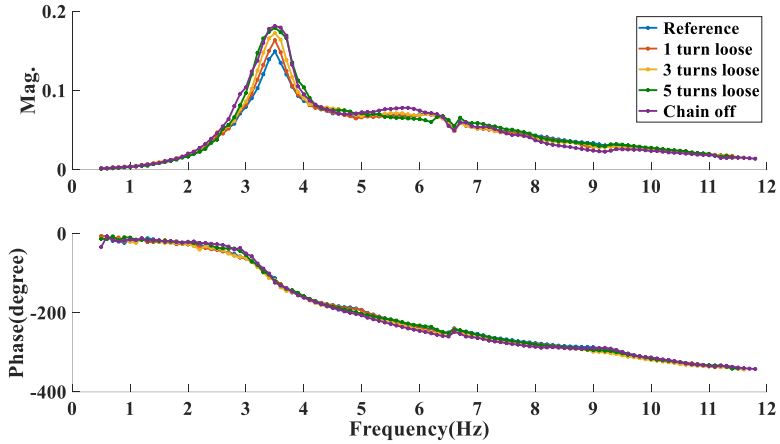

Figure A.24 FRFs of upper arm top with changes to outer chain under 1 mm excitation

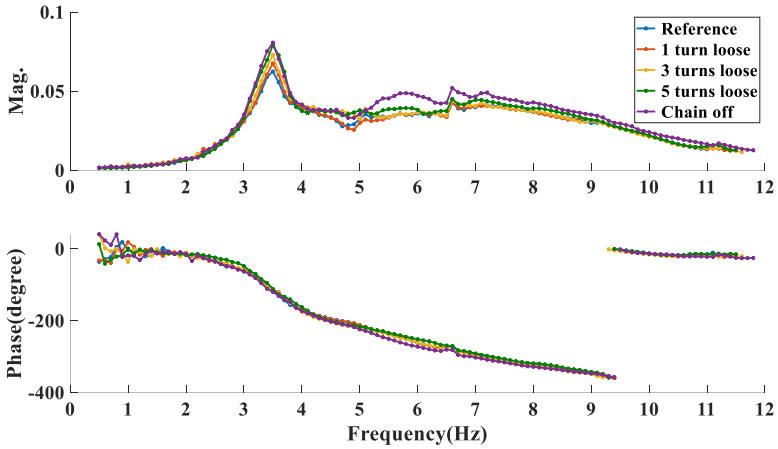

Figure A.25 FRFs of upper arm bottom with changes to outer chain under 1 mm excitation

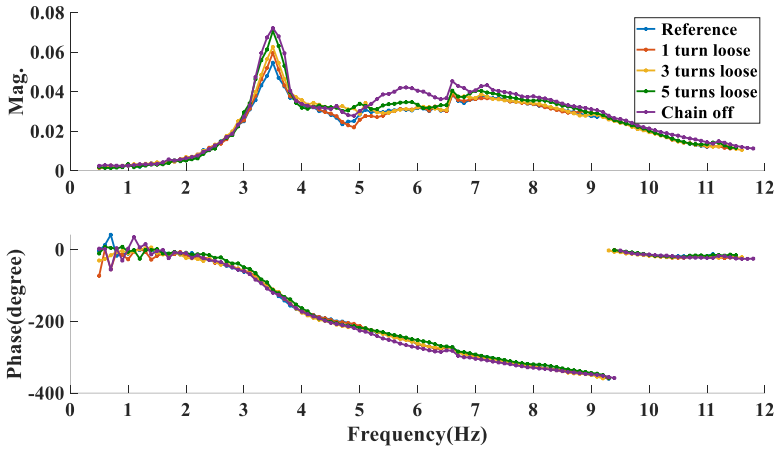

Figure A.26 FRFs of upper arm top with changes to outer chain under 1 mm excitation

A.3.3.4 Frequency-response test using 2 mm excitation

The 2 mm excitation is applied to detect the changes to the outer chain, the FRFs of the pantograph arms as shown in Figures A.27 – A.29.

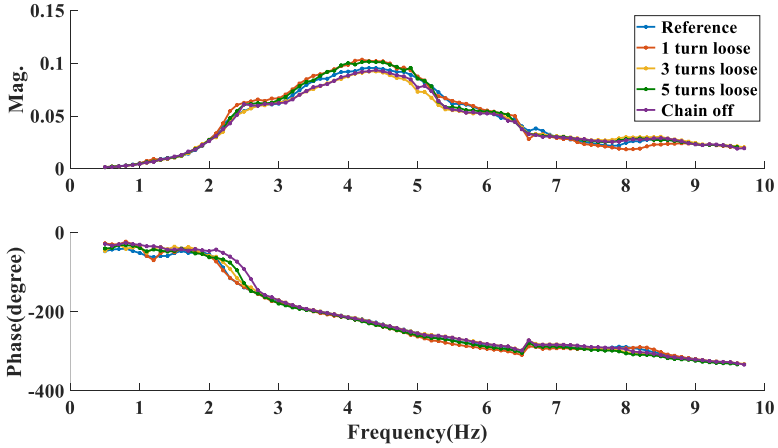

Figure A.27 FRFs of upper arm top with changes to outer chain under 2 mm excitation

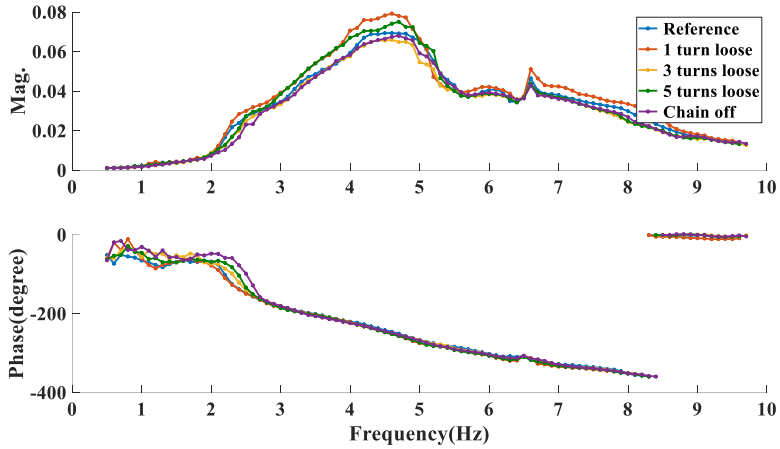

Figure A.28 FRFs of upper arm bottom with changes to outer chain under 2 mm excitation

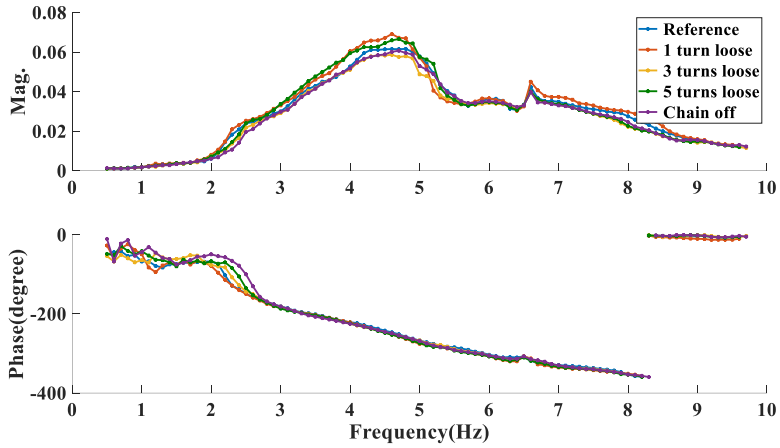

Figure A.29 FRFs of lower arm top with changes to outer chain under 2 mm excitation

A.3.4 FRFs with a leaking pneumatic actuator

A.3.4.1 Frequency-response test using decreasing excitation

The FRFs of the arms obtained with a leaking pneumatic actuator using decreasing excitation are shown in Figures A.30 – A.32.

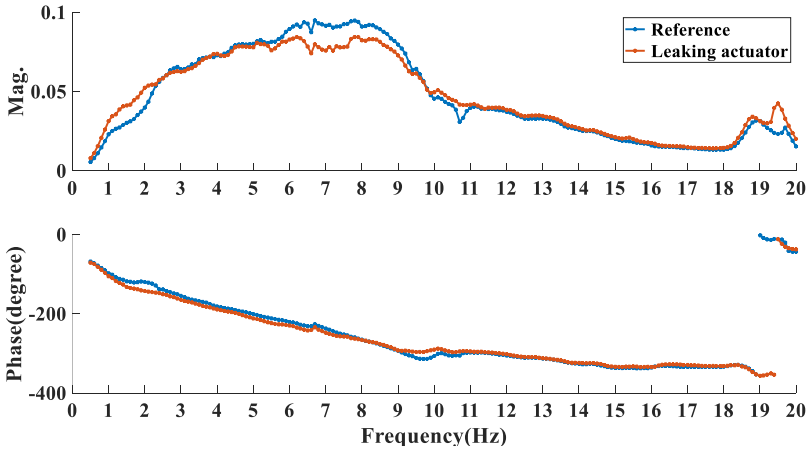

Figure A.30 FRFs of upper arm top using decreasing excitation: reference and leaking actuator

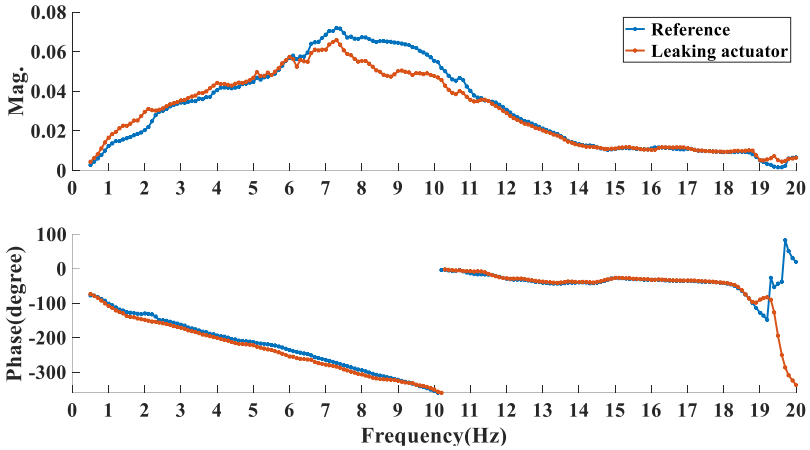

Figure A.31 FRFs of upper arm bottom using decreasing excitation: reference and leaking actuator

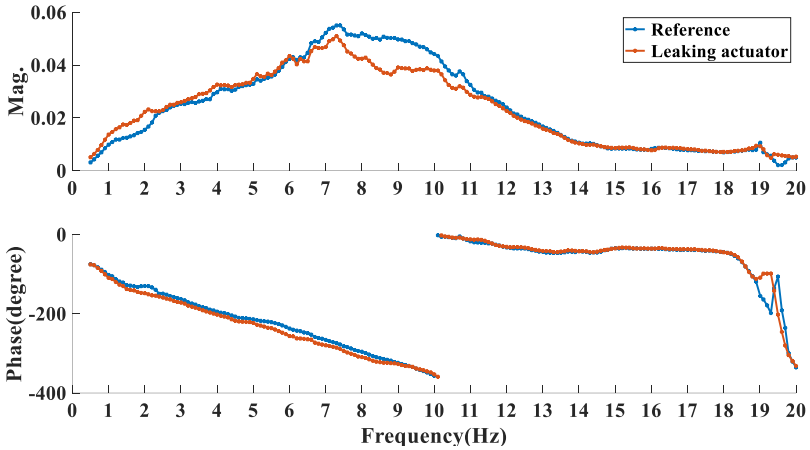

Figure A.32 FRFs of lower arm top using decreasing excitation: reference and leaking actuator

A.3.4.2 Frequency-response test using 1 mm excitation

The 1 mm excitation is applied to the obtained the FRFs with a leaking pneumatic actuator. The FRFs of the pantograph arms are shown in Figure A.33 – A.35.

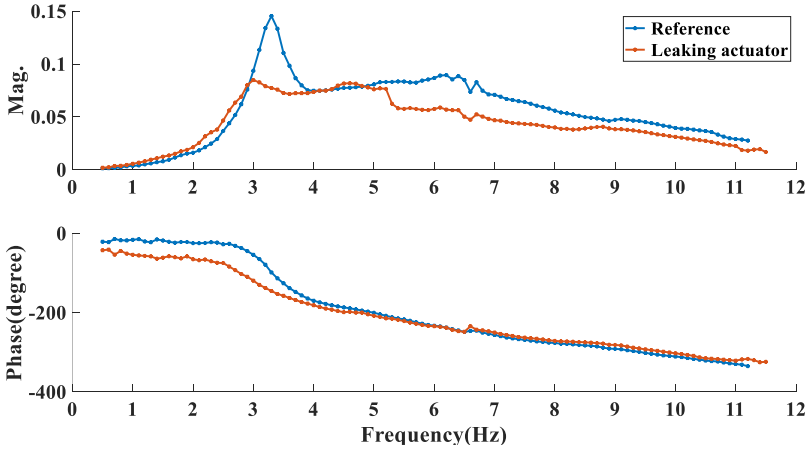

Figure A.33 FRFs of upper arm top using 1 mm excitation: reference and leaking actuator

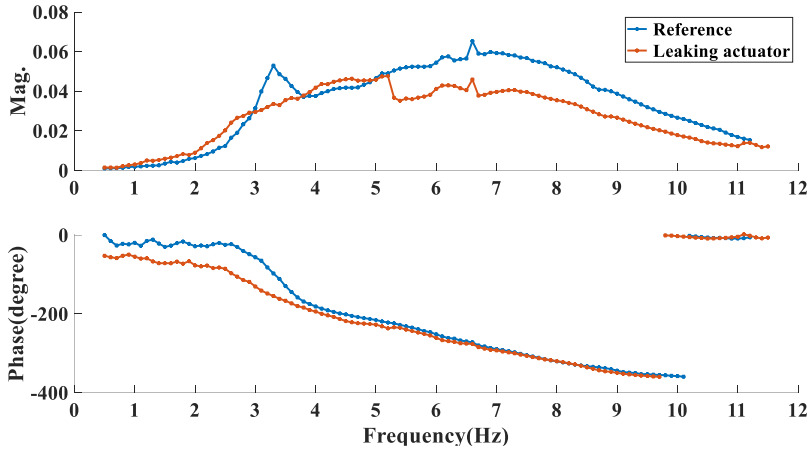

Figure A.34 FRFs of upper arm bottom using 1 mm excitation: reference and leaking actuator

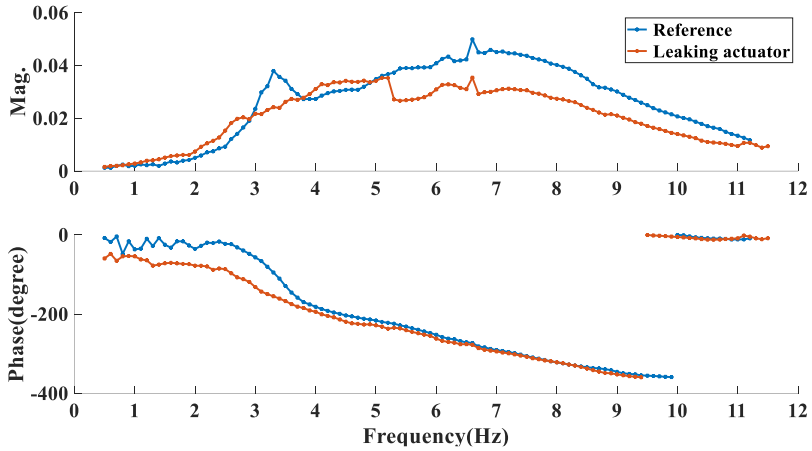

Figure A.35 FRFs of lower arm top using 1 mm excitation: reference and leaking actuator

A.3.4.3 Frequency-response test using 2 mm excitation

The 2 mm excitation method is applied to the obtained the FRFs with a leaking pneumatic actuator. The FRFs of the pantograph arms obtained with the leaking actuator and the references are shown in Figure A.36 – A.38.

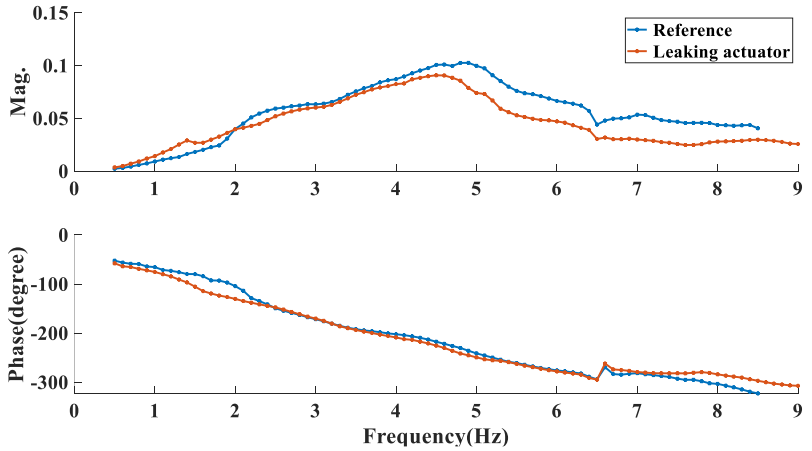

Figure A.36 FRFs of upper arm top using 2 mm excitation: reference and leaking actuator

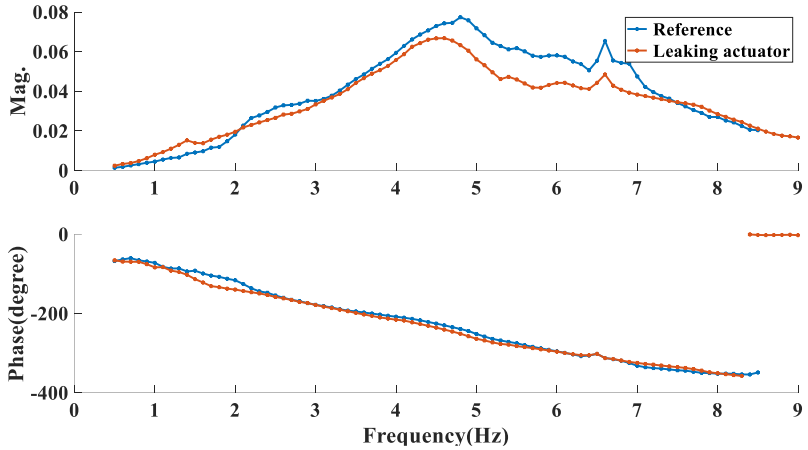

Figure A.37 FRFs of upper arm bottom using 2 mm excitation: reference and leaking actuator

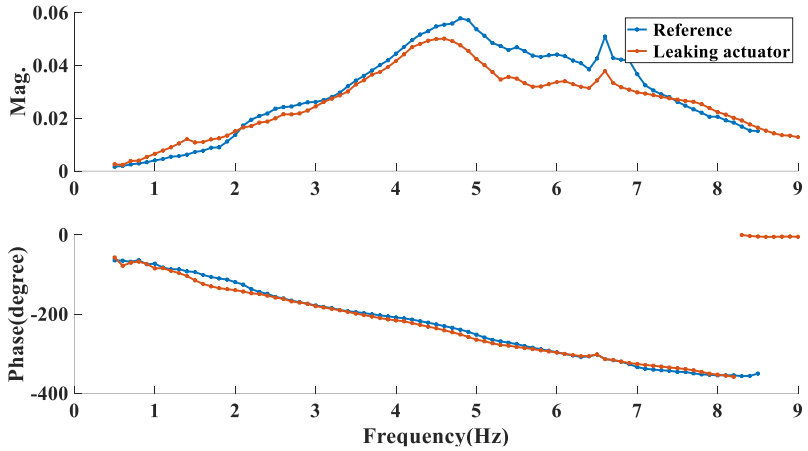

Figure A.38 FRFs of lower arm top using 2 mm excitation: reference and leaking actuator

A.3.5 FRFs with venting plug sealed differently

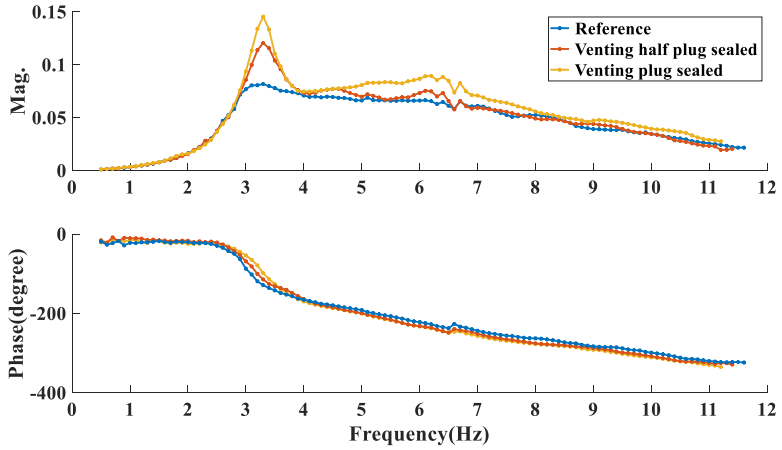

Figure A.39 FRFs of upper arm top with changes to venting plug under 1 mm excitation

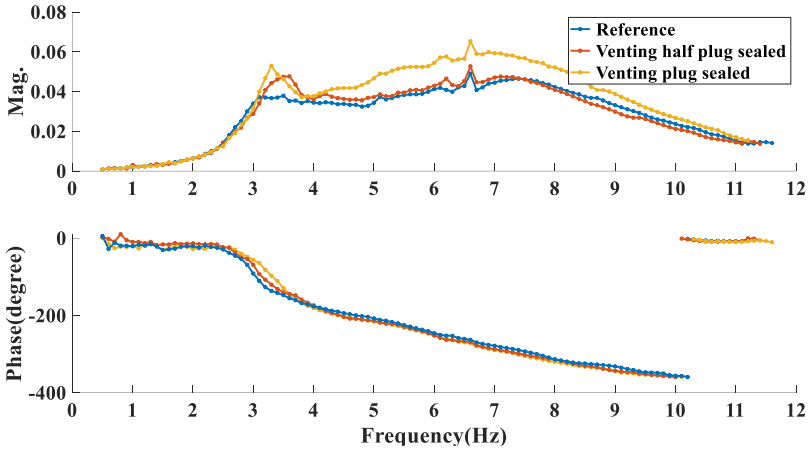

Figure A.40 FRFs of upper arm bottom with changes to venting plug under 1 mm excitation

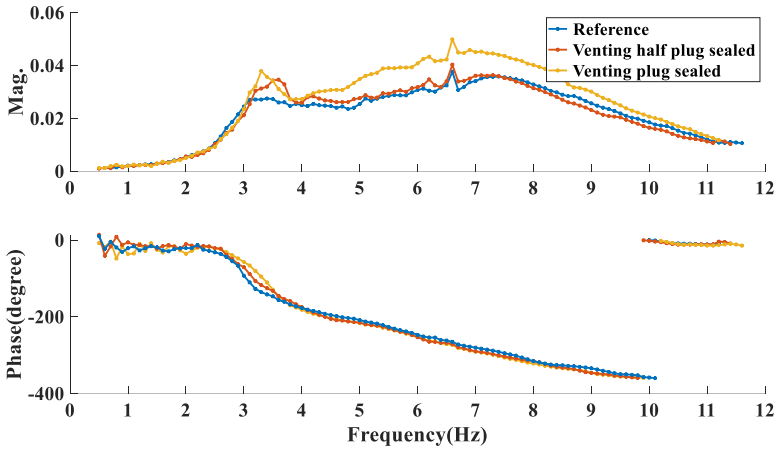

Figure A.41 FRFs of lower arm top with changes to venting plug under 1 mm excitation

A.4 Figures in Chapter 7

A.4.1 Changing gradient test with replacing torsion bar and pneumatic actuator

The features derived from the two conditions are shown in Table A.5 and Table A.6.

Table A.5 Feature extracted with less stiff torsion bar using 'V' tests

Excitation speed (mm/s)	Down			Up			
	Damping ratio	Oscillation fre. (Hz)	Over-shoot 1	Damping ratio	Oscillation fre. (Hz)	Over-shoot 2	Over-shoot 3
50	0.21	2.99	105.1	0.29	3.10	82.2	91.4
100	0.09	2.95	111.8	0.15	2.99	72.3	97.1
200	0.06	2.83	127.4	0.08	2.85	59.9	108.8
300	0.05	2.81	144.6	0.07	2.83	47.2	118.6
400	0.06	2.79	159.5	0.06	2.81	33.2	117.5
500	0.05	2.81	176.9	0.04	2.85	25.7	121.3

Table A.6 Feature extracted with leaking pneumatic actuator using 'V' tests

Excitation speed (mm/s)	Down			Up			
	Damping ratio	Oscillation fre. (Hz)	Over-shoot 1	Damping ratio	Oscillation fre. (Hz)	Over-shoot 2	Over-shoot 3
50	0.06	4.69	101.4	0.14	4.80	80.6	89.1
100	0.10	4.42	108.8	0.22	4.66	73.5	95.3
200	0.16	3.53	126.8	0.31	4.08	58.3	104.9
300	0.15	2.88	144.3	0.24	3.53	44.8	112.5
400	0.10	2.81	160.8	0.17	3.50	37.2	123.8
500	0.07	2.66	176.9	0.09	3.48	24.2	129.5

A.4.2 Changing gradient test with sealing the venting plug

The top of the venting plug is half sealed to accomplish the changing gradient test, the results as shown in Figure A.42.

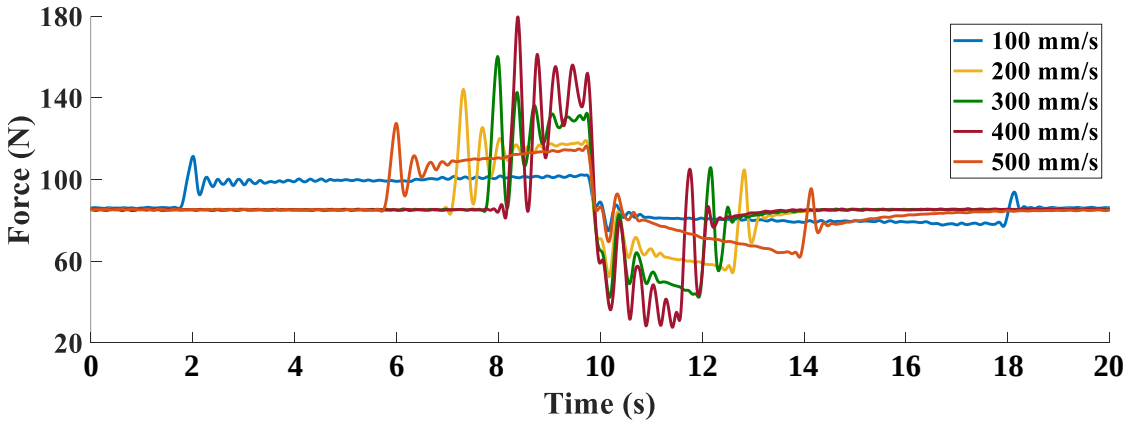

Figure A.42 Results of 'V' tests with venting plug half sealed

A.4.3 Results of SSAE in detecting tightness of the outer chain

The confusion matrices of the measurements under different tightness of the outer chain conditions at the excitation speed of 50 mm/s are shown in Figure A.43.

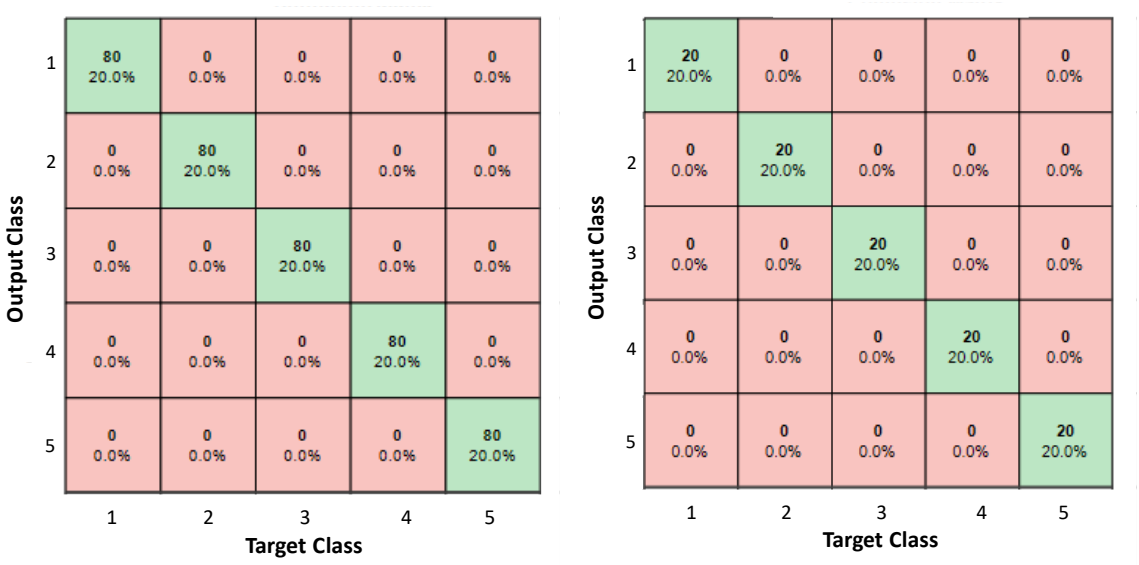

a. Training *b. Validation*

Figure A.43 Confusion matrices with changes to outer chain at 50 mm/s

A.4.4 Results of SSAE in detecting various faults

The confusion matrices of the measurements under the 5 conditions at other excitation speed of 300 mm/s are shown in Figure A.44.

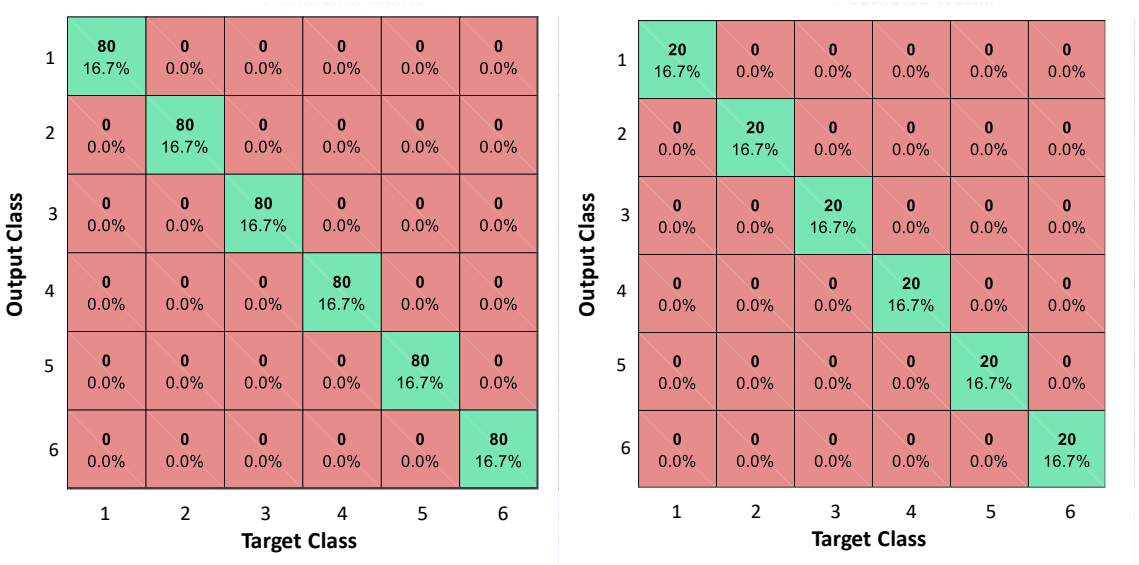

a. Training *b. Validation*

Figure A.44 Confusion matrices with common faults at 300 mm/

APPENDIX B PUBLISHED PAPERS

Papers that have been published during the course of the PhD study.

1. Xin, T., Roberts, C., Weston, P., Stewart, E. (2018) Condition Monitoring of Railway Pantographs to Achieve Fault Detection and Fault Diagnosis, *Proceedings of the Institution of Mechanical Engineers, Part F: Journal of Rail and Rapid Transit.*
2. Xin, T., Roberts, C., Weston, P., Stewart, E. (2018) Condition Based Railway Pantograph Dynamic Behaviour Measurement and Fault Diagnosis, *10th IFAC Symposium on Fault Detection, Supervision, and Safety for Technical Processes, SAFEPROCESS 2018*. Warsaw, Poland.